이학박사학위논문

Reconstruction of oceanographic properties and atmospheric circulation at the marginal regions of the Western Pacific Warm Pool during the late Quaternary

신생대 제 4기 동안의 서태평양 난수역의 해양학적 특성과 대기순환 복원

2016 년 2 월

서울대학교 대학원

지구환경과학부

서 인 아

Reconstruction of oceanographic properties and atmospheric circulation at the marginal regions of the Western Pacific Warm Pool during the late Quaternary

신생대 제 4기 동안의 서태평양 난수역의 해양학적 특성과 대기순환 복원

지도교수 이 용 일

이 논문을 이학박사 학위논문으로 제출함
2016 년 2 월

서울대학교 대학원
지구환경과학부
서 인 아

서인아의 이학박사 학위논문을 인준함
2016 년 2 월

위 원 장 최 영 숙 (인)
부위원장 이 용 일 (인)
위 원 안 진 호 (인)
위 원 최 기 성 (인)
위 원 정 대 교 (인)

Abstract

Reconstruction of oceanographic properties and atmospheric circulation at the marginal regions of the Western Pacific Warm Pool during the late Quaternary

Inah Seo

School or Earth and Environmental Sciences

The Graduate School

Seoul National University

Evolution of surface ocean environment in the eastern margin of the Western Pacific Warm Pool and its forcing mechanisms during the late Quaternary were investigated using various biogenic and lithogenic components in the northwestern and central equatorial Pacific where paleoclimatic records are rare due to paucity of sedimentary archives. To better understand the coupled behavior and interactions between the atmosphere and surface ocean dynamics, the provenance of eolian mineral dust and the composition of biogenic microfossils were investigated together.

For the last 600 kyr, eolian mineral dust deposited in the northwest Pacific, represented by a sediment core (12°30’N, 135°00’E) from the Philippine Sea, has

been supplied predominantly from the central Asian deserts (e.g., Taklimakan desert). It highlights that the prevailing wind system, rather than seasonal monsoon, has been the main transporting agent of eolian dust from Asian inland to the North Pacific. In contrast, eolian mineral dust deposited in a central equatorial Pacific site (5°53'N, 177°26'W) reveals Australian/South American dust affinity before 0.8 Ma but gradually increasing Asian dust signal after 0.8 Ma. The change in dust provenance was accompanied by an increased dust flux and a decrease in surface productivity and salinity. These changes can be explained by the southward movement of the Intertropical Convergence Zone (ITCZ) and North Equatorial Counter Current (NECC) and the direct influence of these features on the site after 0.8 Ma. The southward movement of the ITCZ is in phase with the warming trend observed in upwelling regions of the equatorial Pacific and Atlantic between 0.9 and 0.8 Ma. The southward movement of the ITCZ from 0.9 to 0.8 Ma indicates more significant cooling in the Northern Hemisphere (NH) than in the Southern Hemisphere across the Mid-Pleistocene Transition, which is supportive of the interpretation that the NH ice sheet expanded significantly and stabilized after 0.9 Ma.

For the last deglacial period, water column structure and temperatures were investigated in the central equatorial Pacific (6°40′N, 177°28′W) from a multiple-core by using oxygen isotopic compositions and Mg/Ca ratios of three planktplankticonic foraminifer species (*G. sacculifer*, *P. obliquiloculata*, and *G. tumida*) that dwell in mixed layer, upper thermocline, and lower thermocline, respectively. Only the upper thermocline temperatures have risen as high as 3°C during the last deglaciation between 18 and 12 ka, and then decreased to the present level since then. It can be explained by weakening of water column

stratification in the upper part of thermocline and shallowing of *P. obliquiloculata* habitat at this time. Such change coincides the period of decreased pole to equator temperature gradients in the SH and following NH cooling events, the Heinrich Stadial 1 (HS1) and Younger Dryas (YD), resulting in intensification of northeast Trades and southward migration of the ITCZ. Intensified wind-driven mixing and reduced precipitation during the last deglacial period likely had caused relatively nutrient-rich surface water condition without a significant surface cooling and migration of *P. obliquiloculata* to shallower depth. This interpretation leads to a conclusion that the ITCZ was placed far south to the study site during the last deglaciation and the study site was influenced by northeast Trades that prevails north of the ITCZ. This thesis emphasizes the strong control of atmospheric processes on the surface oceanography at the study site, i.e., north central equatorial Pacific, on the long-term global climate change.

Keywords : paleoceanography, late Pleistocene, inter-tropical convergence zone, equatorial Pacific, climate change

Student Number : 2011-30917

TABLE OF CONTENTS

LIST OF FIGURES

LIST OF TABLES

CHAPTER 1. INTRODUCTION

The buoyant warm water body with mean annual temperature exceeding 28°C and relatively low salinity (<35 psu) occupies approximately 11% of the Earth's surface ocean [*Gagan et al.*, 2004; *Webster*, 1994]. The largest expanse of this warm water, so called Western Pacific Warm Pool (WPWP), is located in the western equatorial Pacific (Figure 1-1). Easterly trade winds over the equator accumulate warm water to the west and induce equatorial upwelling off Peru and Ecuador, which maintains the zonal heat contrast between the eastern equatorial Pacific and WPWP. A subtle change, a fraction of a degree Celsius, in the zonal gradient of sea surface temperature (SST) across the equatorial Pacific causes a range of anomalous weather phenomena such as tropical storm activities, global patterns of flood and drought, and oceanic biological activity [e.g., *Rasmusson and Wallace*, 1983; *Schubert et al.*, 2004; *Siegert et al.*, 2001]. Because of its importance in the global climate system, the equatorial Pacific zonal SST gradient has been of great interest for past and future climate researches.

In the modern climate system, the fluctuation in the equatorial zonal SST gradient is manifested by two extremes: El Niño and La Niña (Figure 1-2). Therefore, a weakening of the zonal SST gradient and atmospheric circulation in the past and future climate research has been termed "El Niño-like," referring to modern analogy and a strengthening thereof has been termed ''La

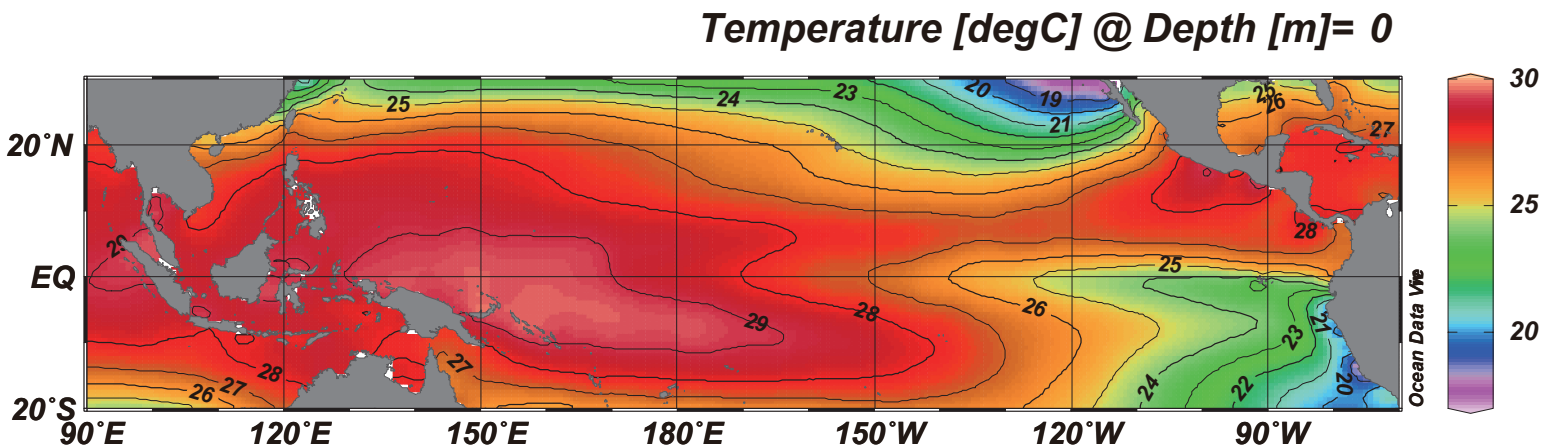

Figure 1-1. Annual mean surface temperature of the tropical-subtropical Pacific ocean (data source: World Ocean Atlas 2013).

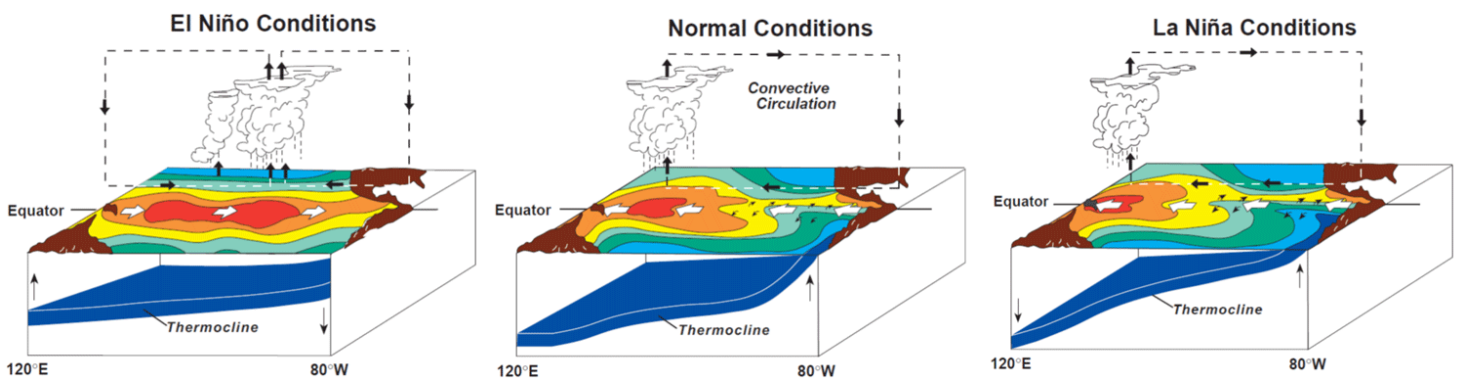

Figure 1-2. A schematic diagram showing an inter-annual variation of SST and water column structure in the tropical Pacific. Source: NOAA/PMEL/TAO Project Office, Dr. Michael J. McPhaden, Director

Niña-like'' in past and future climate studies [e.g., *Koutavas et al.*, 2002; *Vecchi et al.*, 2008; *Wara et al.*, 2005]. However, "El Niño-like" and "La Niña-like" conditions are defined solely based on the SST difference between the center of WPWP and East Pacific Cold Tongue (EPCT). Such simplified characterization of oceanographic and atmospheric states does not fully depict the mean state of tropical Pacific because forcing and feedback mechanisms in geologic past were likely different from those of the present. For example, oceanographic states of the Last Glacial Maximum (LGM) reveal the characteristics of both El Niño and La Niña of the modern climate system. In specific, the mean state of tropical Pacific during the LGM is often described as "El Niño-like" because of the decreased zonal SST difference between the centers of WPWP and EPCT regions [*Ford et al.*, 2015; *Koutavas et al.*, 2002], but also reveals faunal characteristics of the modern La Niña in the upwelling intensity in the EPCT region under the modern La Niña condition [*Feldberg and Mix*, 2002; *Martínez et al.*, 2003]. Thus, it is necessary to be supplemented with SST and water column structure data from multiple locations across the equator, in addition to two key locations (center of WPWP and EPCT), in order to better understand mean states of tropical Pacific in the geologic past.

The equatorial central Pacific near the date line is a critical location to monitor the climate state of tropical Pacific. For instance, weakened easterly winds under the El Niño condition induce the eastward expansion and/or migration of the WPWP, which causes cooling and shoaling in the western

Pacific and warming and deepening of thermocline in the central Pacific (Figure 1-2). In contrast, intensified easterly winds during La Niña shift the WPWP farther west and bring cold water to the central Pacific (Figure 1-2). For this reason, the zonal extent of WPWP has also been successfully used to describe the mean state of tropical Pacific during ENSO events [*Gill*, 1983; *McPhaden and Picaut*, 1990; *Picaut et al.*, 1996; *Picaut et al.*, 1997]. In addition, Central Pacific-type El Niño (El Niño "Modoki") and La Niña (La Niña "Modoki"), nontraditional ENSO variation, involve temperature anomalies arisen in the central Pacific [*Ashok et al.*, 2007; *Kao and Yu*, 2009; *Kug et al.*, 2009; *Yeh et al.*, 2009]. Thus, the central Pacific is one of the most plausible locations to understand the mean state of tropical Pacific in addition to the center of WPWP and EPCT.

Despite such climatic importance, paleo-extent and paleo-location of the eastern margin of WPWP and paleo-SST of the central equatorial Pacific have not been investigated so far partly because of the deficiency in sedimentary archives in this region. In the boundary region of the WPWP, pelagic sediments are mostly placed below the carbonate compensation depth (CCD; 4,000–5,000m depth in Pacific) and do not provide sediment accumulation rates to determine high-resolution climate variability (Figure 1-3). Thus acquisition of an appropriate sedimentary archive is crucial for the paleoceanographic studies of the margin of the WPWP including the central equatorial Pacific.

The atmospheric circulation, coupled to equatorial zonal SST gradient, has

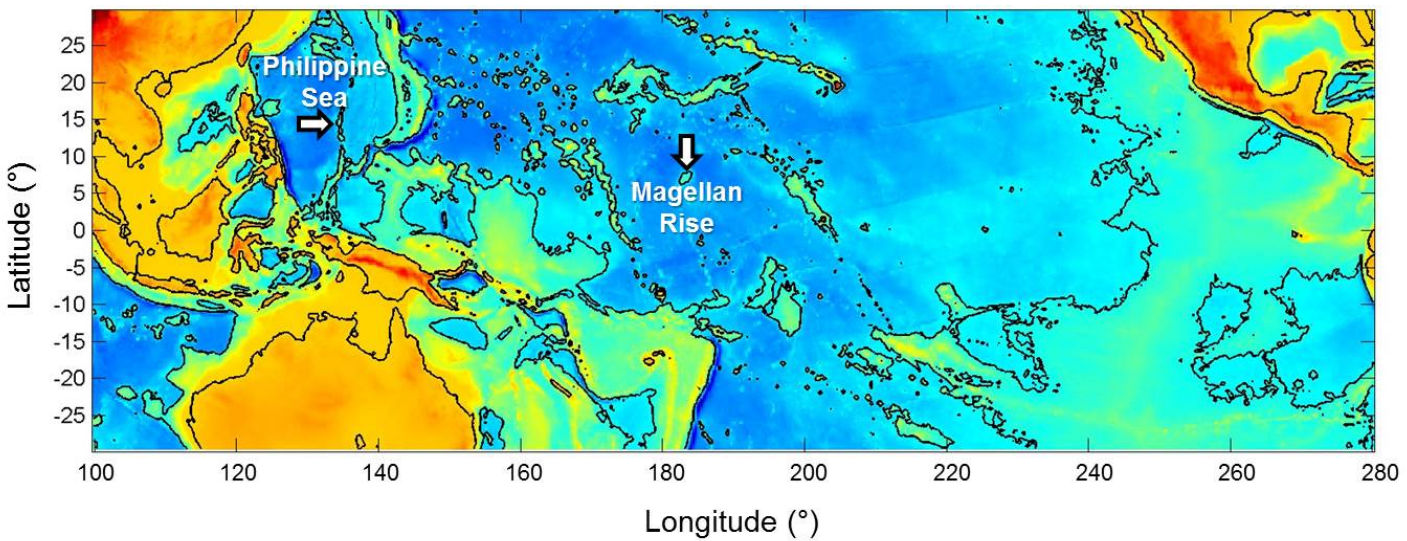

Figure 1-3. Bathymetry of tropical-subtropical Pacific. Black solid lines denote coastlines and 4000 m depth contour lines. Sampling locations are marked by arrows. Bathymetric data from *Ryan et al.* [2009]

been of interest as well in recent climate researches [*Held and Soden*, 2006; *Vecchi and Soden*, 2007; *Vecchi et al.*, 2006]. At present, the modes of prevailing winds in the tropical western Pacific vary by multiple meteorological factors; i.e., the migration of the inter-tropical convergence zone (ITCZ), Asian monsoon system, ENSO, etc. Therefore, the discussion dealing with the tropical climate and its variability should take into account not only the individual oceanographic and atmospheric variables, but also their interactions and feedbacks. The delineation of the source regions of wind-blown dust (i.e., airborne mineral particles) preserved in deep-sea sediments allows the reconstruction of changes in governing wind regimes over geologic timescales, which in turn aids in understanding the response of the atmospheric circulation system to forcing mechanisms. To date, most dust studies using deep-sea sediment archives from the Northwest Pacific, especially in the tropical-subtropical region, have focused on understanding the mass flux variation of Asian dust in terms of long-term climate variability [e.g., *Pettke et al.*, 2000; *Wan et al.*, 2012; *Xu et al.*, 2012], but have not considered specific transport pathways or specific dust source regions.

Provenance of wind-blown dust would give a valuable information of dust transport mechanisms and the past atmospheric circulation pattern, as exemplified in the studies to trace the paleo-position of the ITCZ [e.g., *Hyeong et al.*, 2014; *Xie and Marcantonio*, 2012]. In the geologic history, variation in ITCZ has been a major climatic response of tropical Pacific to high-latitude climate, through the change in atmospheric temperature gradient

resulting in the strength of southeast and northwest trade winds. The relative strength of trade winds, also a key driver of equatorial upwelling and the Walker Circulation, can be inferred from the ITCZ position. Therefore, the more integrated understanding of ocean-atmosphere coupling in the past can be achieved by reconstructing dust provenance and the oceanographic properties.

This study aims to describe and interpret climate evolution in the eastern boundary region of the WPWP during the Quaternary using various biogenic and lithogenic components and therein geochemical proxies. From the three deep-sea sediment cores acquired from the Palau-Kyushu Ridge and Magellan Rise (Figure 1-3), sedimentary records in relatively high-resolution could be obtained owing to the elevated topography (~2,000 m higher than nearby basins) of sampling sites. In addition, the ITCZ lies over the sampling sites where its seasonal latitudinal fluctuation is minimal; thus the mean position of the ITCZ and its possible connection to oceanographic variables can be assessed. This thesis consists of three main subjects; 1) Provenance and transport mechanism of dust in the subtropical northwest Pacific, 2) Change of atmospheric and surface ocean circulation in the central equatorial Pacific across the MPT, and 3) Climatic evolution of the central equatorial Pacific during the last deglacial period.

First, possible changes in atmospheric circulation pattern in the tropical Northwest Pacific (Palau-Kyushu Ridge in Philippine Sea, Figure 1-3) were examined as well with geochemical characterization of Asian deserts, the

most probable source regions for entire North Pacific. Based on the characteristics of mineral dust deposited in the North Pacific, the change in paleo-position of the ITCZ and the relevant oceanographic evolution across the Mid-Pleistocene Transition (MPT) at the Magellan Rise located in the eastern margin of WPWP. Finally, variations in SST and water column structure are investigated using oxygen isotopic compositions and Mg/Ca ratios of three planktic foraminifera species (*G. sacculifer*, *P. obliquiloculata*, and *G tumida*) that dwell in different water depth. This multi-species approach helps understand temperature gradients between the surface and the lower part of thermocline. This study provides high resolution proxy data in the central equatorial Pacific region for the first time, which allows better understanding on the changes in mean state of tropical Pacific across the MPT and for the last deglacial period by comparison with abundant proxy data available in the center of WPWP and EPCT.

CHAPTER 2. MATERIALS AND METHODS

2.1. Study Area

Three deep-sea sediment cores were obtained from the eastern and northern margins of the WPWP for the multi-proxy analyses (Figure 2-1). PC 631 was collected from the Palau-Kyushu Ridge in the Philippine Sea at the northern margin of the WPWP (12°30′N, 134°60′E, 3,728 m water depth). A multiple core, MC 931, and a piston core, PC 932, were acquired from the Magellan Rise, in the central equatorial Pacific at the eastern margin of the WPWP (6°40′N, 177°28′W, 3,365 m depth and 5°53′N, 177°26′W, 4,136 m depth, respectively).

The WPWP plays a leading role in driving a coupled ocean-atmospheric circulation. Solar heating and high precipitation maintain the warm water body buoyant with high SST and low sea surface salinity (SSS). The present-state WPWP was established about 4–3.6 Ma, resulted from the closure of the Indonesian and Central American seaways [*Chaisson and Ravelo*, 2000; *Li et al.*, 2006; *Sato et al.*, 2008]. Since its establishment, the role of warm pool, in the concept of the area of positive atmospheric heating (i.e. dynamic warm pool), is thought to be remained constant despite shifts in the background SST due to changes in climate states [*Hoyos and Webster*, 2012].

The Philippine Sea is a marginal sea on the western part of the North Pacific Ocean bordered by the Philippines and Taiwan to the west, Japan to the north, the Marianas to the east and Palau to the south (Figure 2-1). Surface water of the Philippine Sea is less saline due to the high precipitation caused by the influences of

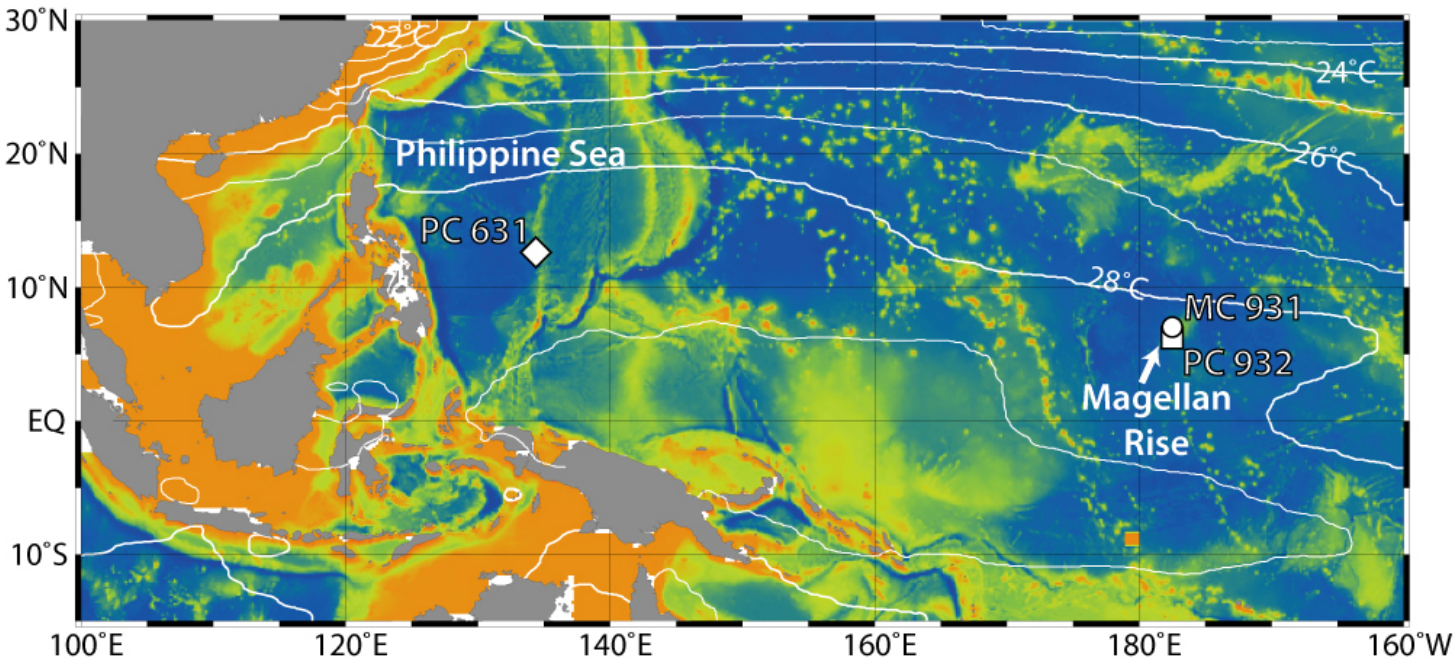

Figure 2-1. Locations of the sampling sites. The contours are for annual mean surface temperature (Data source: World Ocean Atlas 2013).

the ITCZ and upward component of the Walker cell [*Li and Wang*, 2012]. Since the Philippine Sea is one of the most oligotrophic regions in the world, biogenic components are not abundant in the sediment. Wind transport is thought to be the dominant depositional mechanism for the inorganic silicate component of sediments at the study site. Terrestrial sediments, transported by hemipelagic processes, are likely trapped in the marginal seas of China and the Philippine Basin due to the large distance between the site and surrounding coastlines and the elevated topography of the site (approximately 2000 m higher than the surrounding basin). The Kuroshio Current also prevents the long-distance transport of terrestrial sediments in suspension to the study area [*Huh et al.*, 1992; *Jiang et al.*, 2013; *Liu et al.*, 2007].

The Magellan Rise (Figure 1-3) is a large plateau located in the central equatorial Pacific, just north of the equator. The Pacific North Equatorial Countercurrent (NECC) transports surface warm water from the WPWP to the east over the Magellan Rise, while south bounding westward-flowing South Equatorial Current (SEC) at the equator induces equatorial divergence and recycling of nutrients. Owing to these two surface currents, the surface ocean at the Magellan Rise has SST similar to WPWP but higher biological productivity than WPWP center. The elevated topography (~3,000 m depth, about 2,000 m shallower than nearby basin) preserves carbonate-rich sediment with relatively high rates of accumulation with good preservation of microfossils. The input of lithogenic materials is considered being dominated by eolian process because of its isolated location from the continents.

2.2. Sample Information

A sediment core PC 631 is 240 cm long and composed of pelagic mud and calcareous-siliceous ooze. Based on the color of sediments, two lithological units are identified: foraminifera-rich, light brown mud (Unit A) and brown mud (Unit B) (Figure 2-2). The lithology of core is characterized by alternations of carbonate-rich mud and carbonate-poor mud. MC 931, a 32 cm-long multiple core, is composed of almost entirely calcareous ooze (Figure 2-2). PC 932 is 557 cm long, and composed of calcareous ooze and mud (Figure 2-3). Two lithological units are identified by sediment color: white carbonate ooze and pale brown carbonate ooze.

The cores were divided into 1 m-long sections and halved on board. The observation and sampling were performed on the working halves. The working sections were subsampled at 1 cm interval, freeze-dried and then stored in plastic bottles in a cool room. Every fourth sample was subjected to analyses in most cases. If necessary, additional samples were taken adjacent to these intervals. The main proxy systems used in this thesis are derived from the geochemical measurement of the calcite tests of the foraminifera, the isotopic and mineralogical composition of the airborne mineral particles and the relative contribution of various biological/detrital components. Three sediment cores used in this study were subjected to different multi-proxy analyses as summarized in Table 2-1.

2.3. Age Model

The conversion of depth to age in a sediment core is essential for data processing. In this study, various chronological approaches were taken depending on the

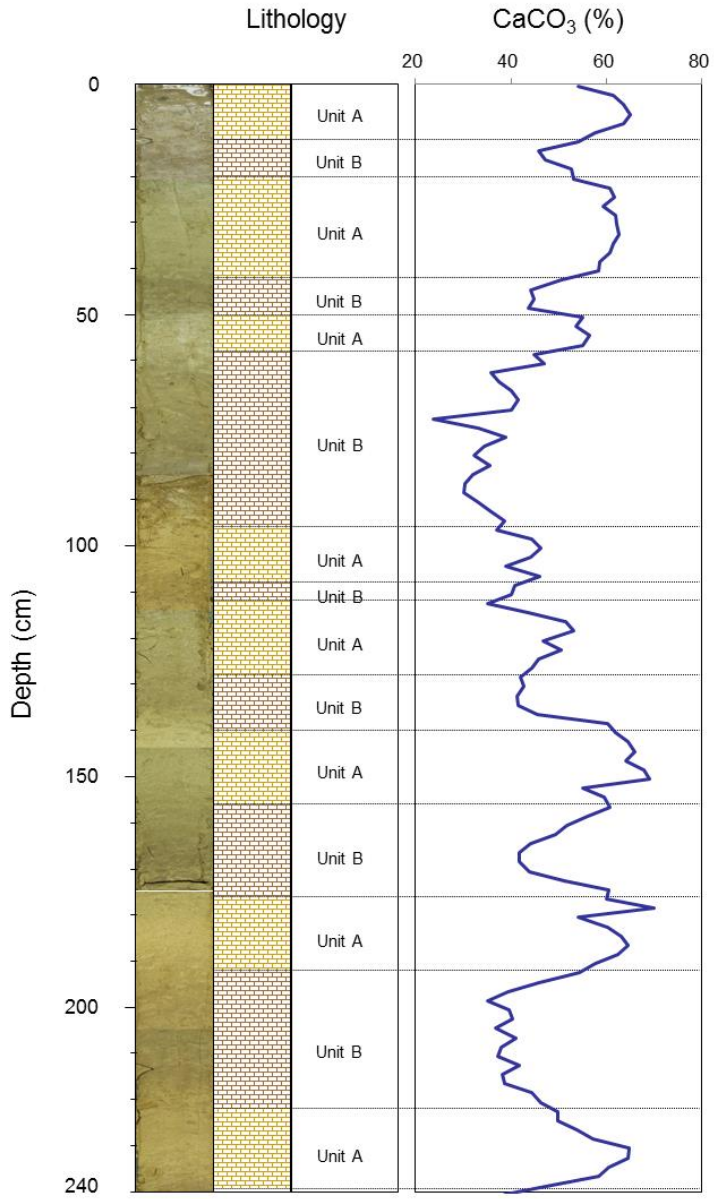

Figure 2-2. Slab photograph of PC 631 with its lithology and $CaCO_3$ content. Unit A: foraminifera-rich light brown mud, Unit b: brown mud.

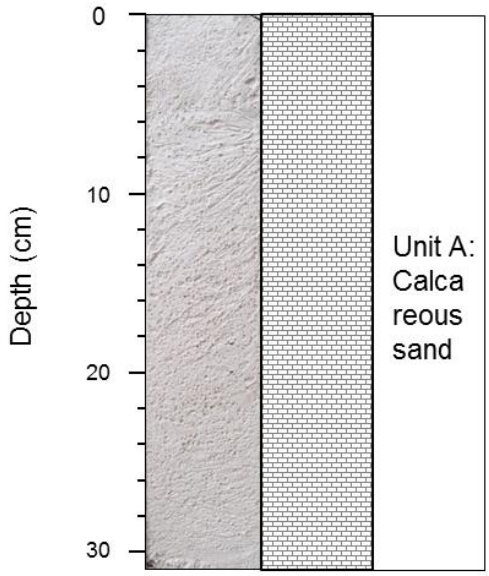

Figure 2-3. Slab photograph of MC 931 and its lithology.

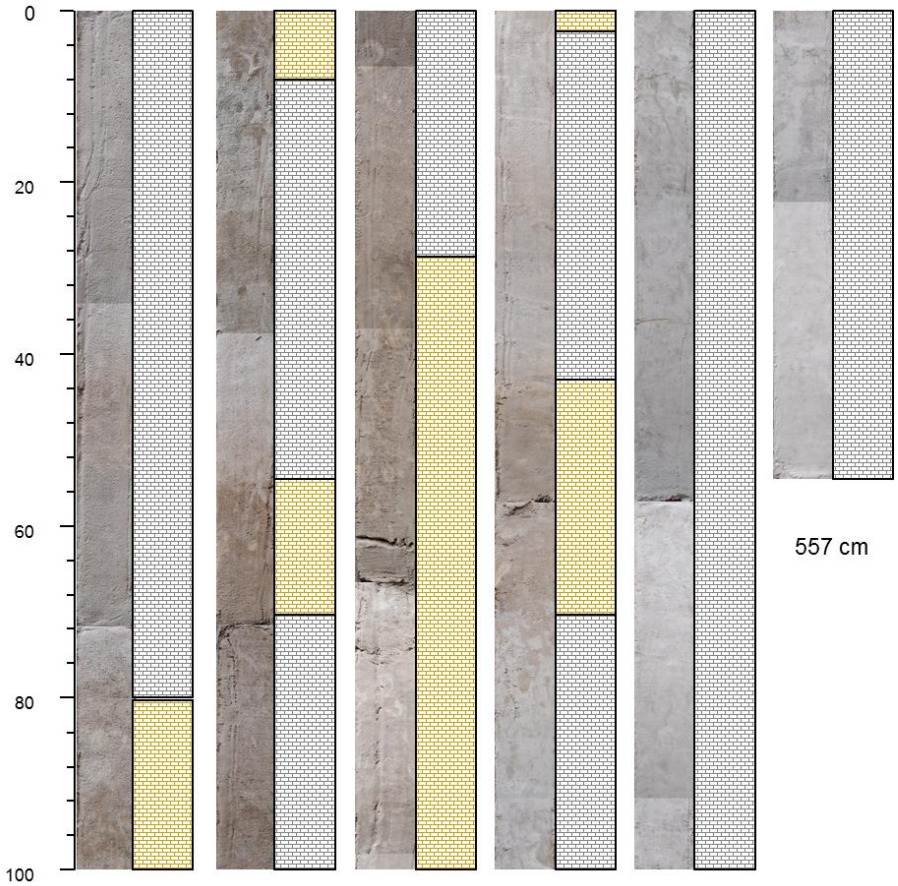

Figure 2-4. Slab photograph of PC 932 and its lithology.

Table 2-1. List of measured variables in this study

	Variable	PC 631	MC 931	PC 932
Age Model	Radiocarbon	√	√	
	Foraminifera $\delta^{18}O$	√	√	√
	Geomagnetic polarity			√
Biogenic components	Foraminifera Mg/Ca		√	
	Planktic foraminifera $\delta^{18}O$ and $\delta^{13}C$	√	√	√
	Benthic foraminifera $\delta^{18}O$ and $\delta^{13}C$	√		
	$CaCO_3$ content	√	√	√
	Biogenic silica content	√	√	√
Eolian components	Mass accumulation rate			√
	Radiogenic isotope composition ($^{87}Sr/^{86}Sr$, $^{143}Nd/^{144}Nd$)	√		√
	Clay mineral composition	√		

expected ages of samples and the temporal scope of the interpretation. For MC 931 and upper part of the PC 631, radiocarbon dating method was applied because these samples are expected to have ages younger than 50,000 yrs. On glacial-interglacial time scales, oxygen isotope composition ($\delta^{18}O$) of the planktic/benthic foraminifera in a marine sediment core is commonly used as a stratigraphic tool, based on the universality of the global seawater $\delta^{18}O$ fluctuation. For the lower part of the PC 631, oxygen isotope stratigraphy was successfully applied from the well-preserved foraminiferal record. The oxygen isotope composition of foraminifera in PC 932, however, gave an unreliable record, possibly indicating bioturbation by benthic organisms. Geomagnetic polarity reversals were therefore used to establish the age model of PC 932 although there are only three geomagnetic chrons over the last 1 Myr (i.e., Brunhes, Matuyama and Jaramillo).

2.4. Analyses of Biogenic Components

Biogenic components in deep-sea sediments provide a direct record of oceanographic condition in the past. The main carriers of paleoclimate information are the preserved organic and inorganic remains of microfossils: e.g., foraminifera, coccolithophores, diatoms as well as radiolarians and silicoflagellates. Among the various variables, SST and vertical water column structure are investigated using proxy records of foraminifera geochemistry. SST is a primary indicator of general climate state, providing information about oceanic heat and heat transport in the upper mixed layer. In addition, because proxy records can be easily calibrated into measurable environmental variable, proxy-derived SST can be the quantitative

verification of paleoclimate models.

2.4.1. Mg/Ca and stable oxygen isotope compositions of foraminiferal calcite

Foraminiferal Mg/Ca is one of the most successfully developed paleotemperature proxy. The exponential relationship observed between the amounts of Mg incorporated into foraminiferal calcite and the surrounding water temperature has been validated in many studies [*Anand et al.*, 2003; *Rosenthal et al.*, 1997; *Rosenthal and Lohmann*, 2002]. The relationship is empirically determined as a following equation:

$$Mg/Ca = b \times e^{aT},$$

where pre-exponential and exponential calibration constants are designated b and a, respectively, and T is calcification temperature. Recently, foraminiferal Mg/Ca in the Mediterranean Sea has varied significantly than cultured foraminifera in laboratory, and such variation was attributed to the large variation of seawater salinity [*Ferguson et al.*, 2008]. In this study, calibration constants with salinity component were adopted from *Sadekov et al.* [2009] that have been reported in the tropical western Pacific.

Besides of its use of chronological tool, stable oxygen isotope ($\delta^{18}O$) composition of foraminiferal calcite has been widely used as a proxy for seawater temperature and hydrographic properties. The $\delta^{18}O$ of foraminiferal calcite ($\delta^{18}O_c$) depends on the composition of seawater ($\delta^{18}O_{sw}$) and calcification temperature. $\delta^{18}O_{sw}$ is, for modern samples, locally defined as a function of salinity both been affected by evaporation and precipitation, among others hydrological effects. On

longer timescales (e.g., glacial-interglacial), $\delta^{18}O_{sw}$ also depends on global changes in ice volume. With a quantitative estimation of global ice volume and independent estimates of temperature, such as Mg/Ca of foraminifera, could help to constrain seawater salinity from $\delta^{18}O_c$.

In this study, three planktic foraminiferal species (*Globigerinoides sacculifer*, *Pulleniatina obliquiloculata*, *Globorotalia tumida*) are subjected to geochemical analyses. *G. sacculifer* lives in the upper 80 m of the water column, but its depth preferences varies depending on its growth stages and size classes [*Bijma and Hemleben*, 1994]. In its early stage of growth, *G. sacculifer* dwells in the upper photic zone (0–50 m depth) with small test size (<355 μm in diameter) [*Anand et al.*, 2003; *Bijma and Hemleben*, 1994; *Hemleben et al.*, 1987]. *P. obliquiloculata* dwells in the lower photic zone–upper thermocline (50–100 m depth), and its calcification temperature varies in a small temperature range [*Anand et al.*, 2003]. *G. tumida*, a thermocline-dwelling species, calcifies below the seasonal thermocline (100–250 m depth) [*Fairbanks and Wiebe*, 1980; *Farmer et al.*, 2007]. As *Sagawa et al.* [2012] verified the depth habitats of these three species in the WPWP region, calcification temperatures and seawater $\delta^{18}O$ of *G. sacculifer*, *P. obliquiloculata* and *G. tumida* are considered to represent those of mixed layer, upper thermocline and lower thermocline, respectively.

2.4.2. Calcium carbonate and biogenic silica contents

Marine biological processes responsible for changes in carbon cycle have been of interest in many researches because of their likely role in regulating atmospheric CO_2 level. In addition, information on marine paleoproductivity gives clue to

surface nutrient supply and utilization, and hence to ocean circulation in the past. Researches on the ocean surface productivity of the past have focused on the export flux of particulate organic carbon (POC) to the deep sea. However, because POC is easily regenerated in the water column before its burial, organic carbon content in the sediment does not represent the past export production properly. Instead, many parameters of deep-sea sediments have been suggested as a proxy for paleoproductivity although none of them is fully independent from diagenesis and dissolution that alter its property.

The quantitative methods relying on the flux of microfossils in the sediment are relatively simple approach to the estimation of surface production for the past. In this study, calcium carbonate and biogenic silica contents in sediments were measured from bulk sediments. Besides bulk sedimentation rate of biogenic components, the dominance of specific plankton group gives additional information about the oceanic condition favorable for the organism of interest. For instance, the relative concentration between nitrogen, phosphorous and silicate in the ocean dictates competitive dominance within phytoplankton communities [*Harrison*, 2000; *Yunev et al.*, 2007].

2.5. Analyses of Eolian Components

Because of the importance of mineral dust on the Earth's climate, in-depth understanding about the concentration, flux and transport pathways of mineral dust has been highlighted by many studies. One of the ways in which atmospheric dust has been studied is the use of model simulations, in which deflation, transport,

fallout and deposition are coupled, either on regional or worldwide scales [*Mahowald et al.*, 2007; *Tanaka and Chiba*, 2006]. For studies of dust for pre-historic time, mineral dust has been characterized with radiogenic isotope composition and clay mineralogy. Mineral aerosols from different sources are often indistinguishable in some cases when using a single geochemical or mineralogical attribute. Thus, the relative contribution of these potential sources requires investigation using multiple source indicators. For the delineation of dust sources, this study employs a multi-proxy approach using $^{87}Sr/^{86}Sr$, $^{143}Nd/^{144}Nd$ and clay mineral composition of dust fractions extracted from the acquired sediment samples.

2.5.1. Radiogenic Isotope Compositions ($^{143}Nd/^{144}Nd$ and $^{87}Sr/^{86}Sr$)

The radiogenic isotopic compositions of mineral aerosols reveal significant differences depending on geographic provinces. In the Pacific Ocean, the combination of Sr and Nd isotopic signatures, $^{87}Sr/^{86}Sr$ and $^{143}Nd/^{144}Nd$, has been proven to be an effective discriminator of dust source regions [*Asahara et al.*, 1995; *Hyeong et al.*, 2011; *Jones et al.*, 1994; *Nakai et al.*, 1993; *Stancin et al.*, 2006]. The major source regions of dust deposited in the Pacific Ocean are Central-Eastern Asian deserts, Central-South America and Australian deserts [*Hyeong et al.*, 2011; *Nakai et al.*, 1993; *Stancin et al.*, 2008; *Stancin et al.*, 2006]. Additionally, volcanic materials derived from the circum-Pacific arcs are clearly identified near the continents [*Asahara et al.*, 1995; *Nakai et al.*, 1993]. The analyzed Sr isotopes are usually given as their isotopic ratios, $^{87}Sr/^{86}Sr$, whereas the $^{143}Nd/^{144}Nd$ ratio is often expressed as a chondrite-normalized value $\varepsilon_{Nd}(0) = (((^{143}Nd/^{144}Nd/0.512638) - 1)\times10^4$ [*Jacobsen and Wasserburg*, 1980].

2.5.2. Clay Mineral Composition

Clay mineral assemblage in deep sea sediments has been used to define the provenance of detrital minerals. The mineralogy of the fine detrital fraction generally reflects the intensity of continental weathering in the source areas [*Biscaye*, 1965; *Griffin et al.*, 1968]. Clay mineral assemblage of deep sea sediments reflects relative input of various detrital sources supplied by hemipelagic and pelagic processes. Chemically stable clay minerals such as kaolinite and gibbsite are concentrated in the tropical-humid zone, whereas chlorite and illite are distributed at mid- to high-latitudes where intense chemical weathering is lacking [*Biscaye*, 1965; *Rateev et al.*, 1969]. The origin of marine smectite, or montmorillonite, is rather complicating because it can be derived from volcanism, hydrothermal activity or diagenetic processes [*Cole and Shaw*, 1983]. Without any evidences of such processes, smectite is often an indicator of mafic rock sources.

CHAPTER 3. PROVENANCE AND TRANSPORT MECHANISM OF DUST IN THE SUBTROPICAL NORTHWEST PACIFIC

Abstract

Dust transport to the tropical/subtropical northwestern Pacific over the past 600 kyr was investigated using radiogenic isotopes ($^{87}Sr/^{86}Sr$ and ε_{Nd}), together with the clay mineral composition, of eolian dust preserved in a sediment core obtained from the Philippine Sea (12°30′N, 134°60′E). These data revealed the influence of two prevailing dust sources, namely, the Asian deserts and nearby volcanic arcs (e.g., the Luzon Arc), with average contributions of around 70% and 30%, respectively, from each. The clay mineral composition of the core resembled dust from the central Asian deserts (CADs; e.g., the Taklimakan Desert) as in the North Central Pacific, but published aerosol data collected near the study site during winter/spring has the mineralogical signature of dust originating from the East Asian deserts (EADs). These data indicate that the relative contribution of EAD dust increases with the northeasterly surface winds associated with the East Asian Winter Monsoon (EAWM) during winter/spring, but the Prevailing Westerlies and Trade Winds that carry dust from the CADs is the dominant transport agent in the overall dust budget of the study site. The results of this study contradict the prevailing view that direct dust transport by the EAWM winds in spring dominates the annual flux of eolian dust in the northwest Pacific.

Chapter source: Seo, I., Y. I. Lee, C. M. Yoo, H. J. Kim, and K. Hyeong (2014), Sr-Nd isotope composition and clay mineral assemblages in eolian dust from the central Philippine Sea over the last 600 kyr: Implications for the transport mechanism of Asian dust, J. Geophys. Res. Atmos., 119, 11,492–11,504, doi:10.1002/2014JD022025.

3.1. Introduction

The delineation of the source regions of wind-blown dust (i.e., airborne mineral particles) preserved in deep-sea sediments allows the reconstruction of changes in governing wind regimes over geologic timescales, which in turn aids in understanding the response of the atmospheric circulation system to forcing mechanisms. Various geochemical attributes and clay mineral assemblages of eolian dust have been successfully used to identify source regions. For instance, dust carries the distinctive neodymium ($^{143}Nd/^{144}Nd$) and strontium ($^{87}Sr/^{86}Sr$) isotopic signatures of crustal evolution at the source region [*Asahara et al.,* 1995; *Biscaye and Dasch,* 1971; *Grousset et al.,* 1988; *Jones et al.,* 1994; *Nakai et al.,* 1993; *Stancin et al.,* 2006]. The clay mineral assemblages of dust preserved in deep-sea sediments also reflects the petrology of the parent rock and the weathering regime in the source regions [e.g., *Biscaye,* 1965; *Blank et al.,* 1985; *Griffin et al.,* 1968; *Petschick et al.,* 1996; *Wan et al.,* 2012].

The tropical/subtropical northwest Pacific is influenced by the seasonal reversal of prevailing surface winds due to the East Asian Monsoon system and the associated movement of the Intertropical Convergence Zone (Figure 3-1). As a result of this reversal, dust can be transported to the region from various sources; e.g., the central/east Asian deserts by either the East Asian Winter Monsoon (EAWM) or the zonal wind system (Prevailing Westerlies and Trade Winds) [*Merrill et al.,* 1989]; volcanic islands in the western Pacific; or the Australian deserts by the East Asian Summer Monsoon (Figure 3-1). It has also been suggested that North African dust, the largest dust source in the world, may reach the North

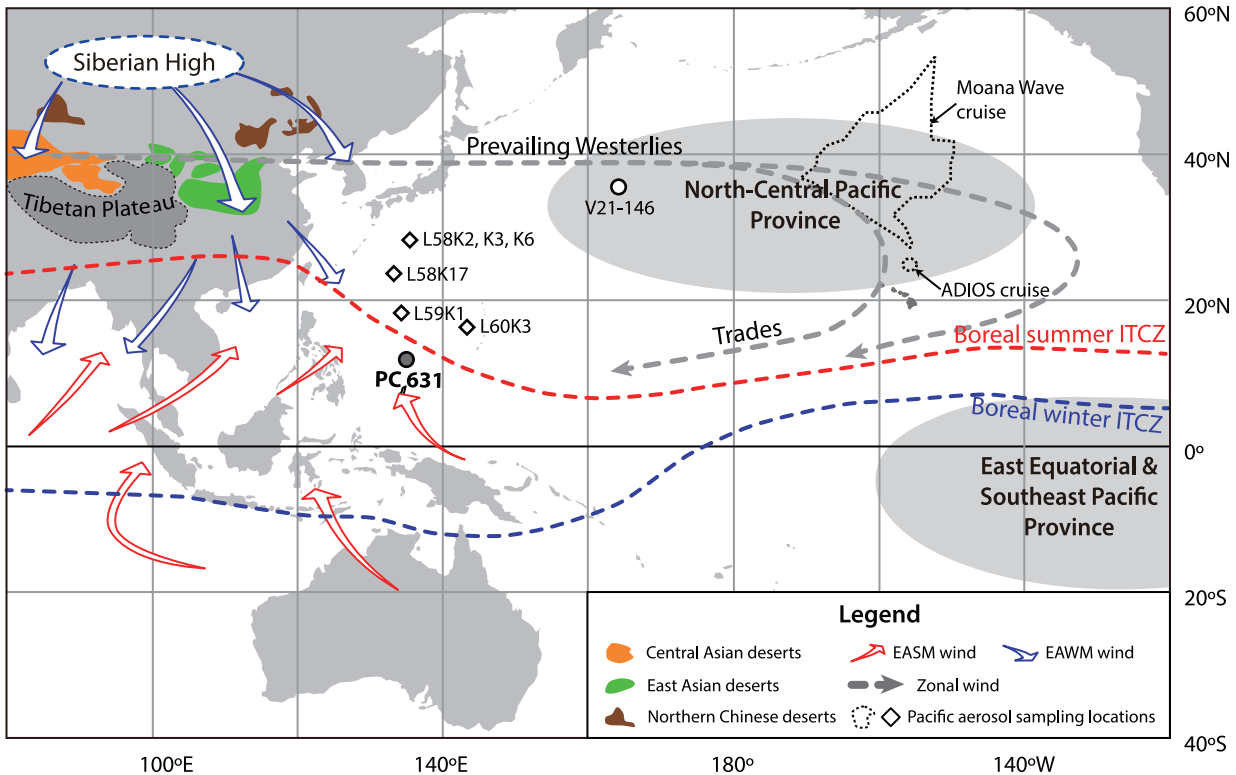

Figure 3-1. Location of core PC 631 (solid circle) and other aerosol (open diamonds) and sediment core (open circle) samples discussed in the text. Aerosol samples were collected during the Moana Wave cruise [*Arnold et al.*, 1998], ADIOS cruise [*Arnold et al.*, 1998], and in a series of DSDP cruises (L series samples) [*Leinen et al.*, 1994]. Location of core V21-146 from *Hovan et al.* [1991]. The winter and summer monsoon wind directions and trajectory of the prevailing westerlies are after *Merrill et al.* [1989], *Mohtadi et al.* [2011], *Nakagawa et al.* [2006], and *Zhang et al.* [1997]. The dust provinces north-central Pacific, and east equatorial and southeast Pacific, are from *Nakai et al.* [1993].

Pacific via long-range transport [*Hsu et al.*, 2012; *Lee et al.*, 2010; *Tanaka and Chiba*, 2006; *Tanaka et al.*, 2005].

The contribution of these potential sources to the global dust budget may be small, but the influence of each potential source could be significant at the regional scale [e.g., *Maher et al.*, 2010; *Tanaka and Chiba*, 2006]. These sources are not distinguishable in some cases when using a single geochemical or mineralogical attribute (e.g., $^{143}Nd/^{144}Nd$ and $^{87}Sr/^{86}Sr$ compositions of central and East Asian deserts, $^{87}Sr/^{86}Sr$ composition of Asian and Australian dust, and clay mineral composition of Australian and North African dust). Thus, the relative contribution of these potential sources requires further investigation using multiple source indicators [e.g., *Ferrat et al.*, 2011].

To date, most dust studies using deep-sea sediment archives from the North Pacific have focused on understanding the mass flux variation of Asian dust in terms of long-term climate variability [e.g., *Pettke et al.*, 2000; *Wan et al.*, 2012; *Xu et al.*, 2012], but have not considered specific transport pathways or dust source regions (e.g., central/East Asian deserts versus northern Chinese deserts). Dust is transported from Asia to the Pacific by two main air circulation systems; i.e., the Prevailing Westerlies and the near-surface northwesterly winds associated with the EAWM (Figure 3-1). Dust models and meteorological studies show that these two dust transport mechanisms follow different pathways and altitudes altitudes [*Shi and Liu*, 2011; *Yumimoto et al.*, 2009; *Zhang et al.*, 1997], and could transport dust from specific source region(s). However, dust transport mechanisms and source region relationships in the North Pacific have yet to be investigated using either aerosol or sediment studies.

This study examines the relative importance of these two dust-transport processes using geochemical indicators and clay mineral assemblage to differentiate between source regions. Additionally, as these two wind systems have varied in strength, direction, and pathway in the geologic past [*An*, 2000; *Ding et al.*, 1995; *Jiang and Lang*, 2010; *Liu and Ding*, 1993; *Nagashima et al.*, 2007; *Nagashima et al.*, 2011; *D Sun*, 2004; *Tian et al.*, 2005; *Zhang et al.*, 1999], it is possible that the contribution of potential dust sources and transport mechanisms has changed over longer timescales.

To characterize the provenance and transport pathways of eolian dust deposited in the western tropical/subtropical Pacific during the late Quaternary, we used the clay mineral composition, together with the $^{143}Nd/^{144}Nd$ and $^{87}Sr/^{86}Sr$ composition of the inorganic silicate fractions of a deep-sea sediment core retrieved from the Palau-Kyushu Ridge in the Philippine Sea (Figure 3-1). Using previously published data, we provide criteria to distinguish between dust from the major Asian dust source regions, which enabled us to identify prevailing transport pathways and the relative contribution of dust from specific sources to the dust budget of the study site. This study also provides a valuable dataset in an area with sparse isotopic and mineralogical data for furthering the understanding of dust sources and dust transport patterns in the northwest Pacific during the late Quaternary.

3.2. Materials and Methods

A 240-cm-long piston core, PC 631, was collected from the Palau-Kyushu Ridge in the Philippine Sea (12°30′N, 134°60′E, 3,728 m water depth; Figures 3-1 and -2).

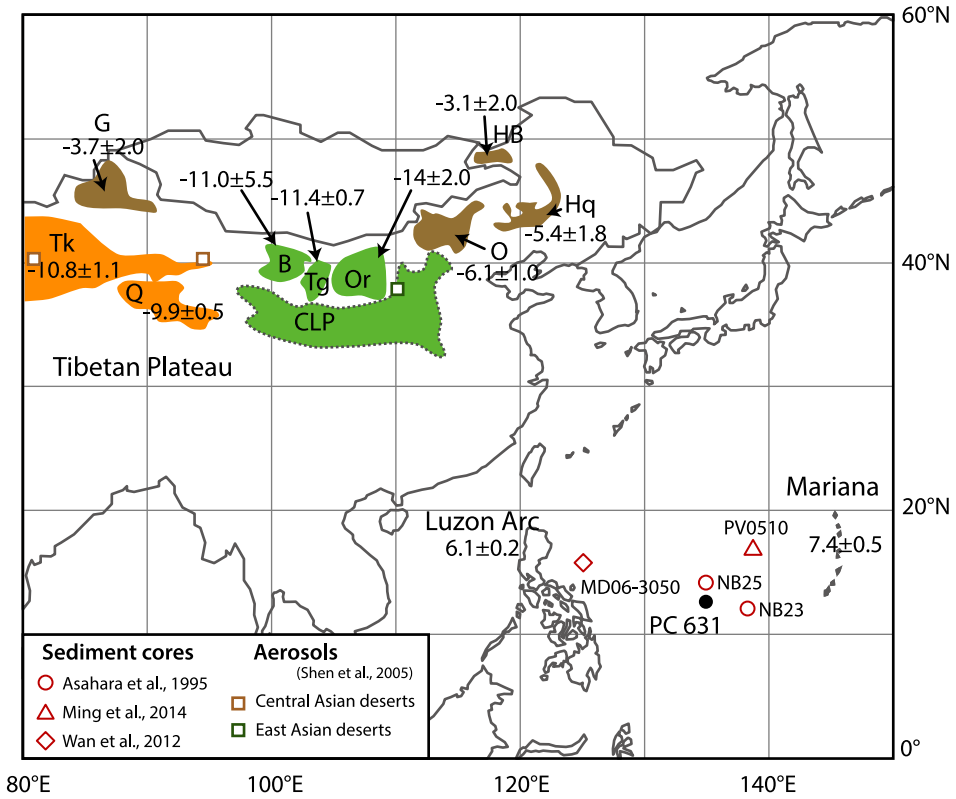

Figure 3-2. Locations of possible dust source regions (i.e., Chinese deserts, Luzon Island, and the Mariana Islands) and their reported ε_{Nd} compositions [*Chen et al.*, 2007; *Defant et al.*, 1990; *Dixon and Stern*, 1983; *Honda et al., 2004*; *Nakano et al.*, 2004; *Rao et al., 2008*; *Woodhead,* 1989]. The Asian deserts include the northern Chinese deserts (NCDs): the Gurbantunggut Desert (G), Onqin Daga Sandy Land (O), Hunlun Buir Sandy Land (HB), Horqin Sandy Land (HQ); the central Asian deserts (CADs): the Taklimakan Desert (Tk), Qaidam Desert (Q); and the East Asian deserts (EADs): the Badain Jaran Desert (B), Tengger Desert (TG), Ordos Desert (Or), and Chinese Loess Plateau (CLP).

Wind transport is thought to be the dominant depositional mechanism for the inorganic silicate component of sediments at the study site. Terrestrial sediments, transported by hemipelagic processes, are probably trapped in the marginal seas of China and/or the Philippine Basin due to the large distance between the site and surrounding coastlines, the elevated topography (ca. 2,000 m higher than the surrounding basin), and the Kuroshio Current, which also prevents the long-distance transport of terrestrial sediments in suspension to the study area [*Huh et al.*, 1992; *Jiang et al.*, 2013; *Liu et al.*, 2007].

The chronology of the core was determined by comparing the oxygen isotope record from the core derived from the benthic foraminifera, *Globocassidulina* sp., with the LR04 chronology [*Lisiecki and Raymo*, 2005]. Benthic foraminifera were picked at 2-cm intervals from the >125 μm size fraction. Isotopic analysis was carried out using a *Finnigan MAT 251* mass spectrometer at the University of Michigan at Ann Arbor, USA. The standard deviation of the repeat analyses of reference material NIST SRM-19 was less than 0.06% (n = 27).

The age model of the core was constructed using the Analyseries software [*Paillard et al.*, 1996] by graphical correlation of 34 tie points between the $\delta^{18}O$ record of PC 631 and the LR04 stack. Due to the disturbance of the top layer of the core during acquisition, additional ^{14}C ages from around 200 planktic foraminifera (*Globorotalia sacculifer*) were determined at 0–1 cm, 4–5 cm, and 14–15 cm intervals to avoid peak mismatching. ^{14}C was analyzed using a compact accelerator mass spectrometry system, *CAMS-500*, by Paleo Labo Co. Ltd., Japan. Age data were corrected for isotopic fractionation and calibrated to the calendar year before present (Cal ^{14}C age) using the Calib v. 7.0 software [*Stuiver and Reimer*, 1993].

This correction was based on the Marine13 dataset [*Reimer et al.*, 2013] and the local reservoir effect (ΔR) of 19 ± 50 years for Guam (13.5°N, 144.8°E) [*Southon et al.*, 2002].

The inorganic silicate fraction was extracted from 17 sediment samples following the method described by *Rea and Janecek* [1981]. The samples were treated with acetic acid buffered to pH 5 with sodium acetate to remove calcium carbonate. They were subsequently treated with a hot sodium citrate–sodium dithionite solution buffered with sodium bicarbonate to remove ferromanganese oxides and hydroxides. The solid residues were then sieved at 63 μm to remove coarse biogenic components, and finally treated with Na_2CO_3 solution to remove biogenic silica.

Grain size analysis of the inorganic silicate component was carried out for the 0.31–301 μm size interval using a *Master Sizer Micro* from Malvern Instrument Inc. Grain size data are reported as median grain size (in μm and ϕ_{50}) [*Folk*, 1974] with the amount of silty fraction (>16 μm), and the accuracy of the median diameter data is ± 2%.

$^{143}Nd/^{144}Nd$ and $^{87}Sr/^{86}Sr$ analyses, including chemical separation and multi-collector thermal ionization mass spectrometric (TIMS; *VG54-30*, *Isoprobe-T*) analyses, were performed at the Korea Basic Science Institute following *Cheong et al.* [2013]. Approximately 50 mg of the extracted powder samples were dissolved with an acid mixture of HF+$HClO_4$ (10:1) and HNO_3 for 24 hours in a tightly closed Teflon vials at 120°C. Sr was extracted by the conventional cation column chemistry (Dowex AG50W-X8, #200-400, H^+ form) using HCl media, and loaded on Ta filament with 1 M H_3PO_4. Major elements and rare earth element (REE) fractions were separated using conventional cation exchange column chemistry. Nd

was separated by the second step cation exchange column chemistry using 2-ethylhexyl phosphoric acid (HDEHP)-coated Teflon powder with HCl media, and loaded on Re filament with 0.1M H_3PO_4. $^{87}Sr/^{86}Sr$ and $^{143}Nd/^{144}Nd$ ratios were corrected for instrumental fractionation and spike contribution using $^{87}Sr/^{86}Sr$ = 0.1194, and $^{143}Nd/^{144}Nd$ = 0.7219, respectively. Replicate analysis of NIST SRM-987 and the La Jolla standard gave mean values of $^{87}Sr/^{86}Sr$ = 0.710246 ± 21 (n = 30, 2σ), and $^{143}Nd/^{144}Nd$ = 0.511832 ± 35 (n = 30, 2σ). Procedural blanks were less than 0.1 ng for Sr, and 0.04 ng for Nd. For convenience, $^{143}Nd/^{144}Nd$ ratios are expressed as ε_{Nd}; the deviation from the Chondritic Uniform Reservoir (CHUR) (ε_{Nd} = ($^{143}Nd/^{144}Nd/0.512638 - 1) \times 10^4$) [*Jacobsen and Wasserburg*, 1980].

Clay mineral assemblage was analyzed on bulk and oriented samples from the <4 μm size fraction of extracted inorganic silicates. This analysis was conducted on a *PANalytical X'pert Pro* X-ray diffractometer at the Korea Institute of Ocean Science and Technology, using CuKα radiation (40 kV, 30 mA) over the range of 3° to 30° at 0.02° steps. For the orientation of clay minerals, the supernatant <4 μm suspension was vacuum filtered onto a 0.45 μm membrane filter. The oriented samples were scanned after air-drying and ethylene glycol solvation. Semi-quantitative estimates of smectite (17 Å), illite (10 Å), kaolinite, and chlorite (7 Å) were made following the method of *Biscaye* [1965]. The relative amount of kaolinite and chlorite was determined by referring to the relative peak heights of 3.58 Å (kaolinite [002]) and 3.54 Å (chlorite [004]). For consistency, the clay mineral compositions of aerosol and sediments reported by *Arnold et al.* [1998], *Blank et al.* [1985], *Leinen et al.* [1994], and *Shen et al.* [2005] were converted using the weighting factors of *Biscaye* [1965].

3.3. Results

The median grain size of the silicate fraction varies in a very narrow range from 8.5 ϕ (2.8 μm) to 8.6 ϕ (2.6 μm), with an average of 8.6 ϕ (2.7 μm) (Table 3-1). The amount of silty components (>16 μm) is 2.2 ± 0.8 % (n=16, 1 σ). The graphical correlation between the $\delta^{18}O$ record of PC 631 and the LR04 stack [*Lisiecki and Raymo*, 2005] shows that the maximum age of the core sediments is approximately 600 kyr, which covers six glacial–interglacial cycles (Figure 3-3). The ages of the uppermost intervals, 0–1 cm, 4–5 cm, and 14–15 cm, were confirmed by ^{14}C ages (Table 3-1). The Cal ^{14}C ages of the 0–1 cm and 4–5 cm intervals are similar (10705 ± 58 and 11691 ± 106 yrs BP, 1σ, respectively), suggesting core-top disturbance during acquisition. The geochemical and clay mineral composition of the 4–5 cm interval is therefore not considered in the following discussion. The calendar age of the 14–15 cm interval (22019 ± 302 yrs BP, 1σ) is consistent with the estimated age from the $\delta^{18}O$ chronology (20.2 ka; Figure 3-3).

The $^{87}Sr/^{86}Sr$ and ε_{Nd} results are presented in Table 3-1 and Figure 3-3. ε_{Nd} and $^{87}Sr/^{86}Sr$ vary between −9.44 and −7.10, and 0.709627 and 0.711951, respectively. The $^{87}Sr/^{86}$ data are in good agreement with values of 0.7086 and 0.7103 reported by *Asahara et al.* [1995] at two nearby sites (NB23 and NB25; Figure 3-2). Neither ε_{Nd} nor $^{87}Sr/^{86}Sr$ showed any systematic down-core trend, but showed a moderate negative correlation ($r = -0.74$, $n = 16$). Clay mineral composition varied in a narrow range, and consisted mainly of illite (46 ± 4%, 1 σ) with subordinate amounts of smectite (25 ± 3%, 1σ), chlorite (19 ± 1%, 1σ), and

Table 3-1. Depositional age, $^{87}Sr/^{86}Sr$ and Nd isotopic compositions, clay mineral composition, and median grain size of the inorganic silicate fraction of the PC 631 sediments. Shaded intervals mark areas considered to have been disturbed during core acquisition (see text).

Depth (cm)	$\delta^{18}O$ Age (ka)	^{14}C age (yrs BP±1σ)	Cal ^{14}C age (yrs BP±1σ)	Isotope composition			Clay mineral composition (%)				Grain size (Φ50)	
				$^{87}Sr/^{86}Sr$ ±2σ	$^{143}Nd/^{144}Nd$ ±2σ	ε_{Nd}	Illite	Kaolinite	Chlorite	Smectite	(μm)	(ϕ)
0–1	0	11170 ±50	10705 ±58									
4–5	8.9	12208 ±57	11691 ±106	0.709247 ±11	0.512296 ±14	–6.67	45	14	18	24	3.2	8.3
14–15	20.2	20339 ±90	22019 ±302	0.709989 ±19	0.512247 ±13	–7.63	54	9	16	21	2.8	8.5
28–29	84.0			0.711077 ±13	0.512164 ±15	–9.25	53	9	18	20	2.7	8.5
44–45	106.4			0.710393 ±13	0.512196 ±15	–8.62	49	11	18	21	2.7	8.5
52–53	135.2			0.710474 ±13	0.512175 ±13	–9.03	49	10	19	22	2.7	8.5
71–72	208.4			0.709930 ±10	0.512242 ±14	–7.72	50	8	19	23	2.6	8.6
75–76	213.9			0.709792 ±11	0.512274 ±12	–7.10	47	8	19	26	2.7	8.5
84–85	226.5			0.709678 ±13	0.512250 ±14	–7.57	42	13	18	27	2.7	8.5
98–99	252.8			0.710151 ±11	0.512222 ±23	–8.11	46	9	20	25	2.7	8.5
108–109	278.3			0.710153 ±13	0.512233 ±13	–7.90	46	11	18	25	2.6	8.6

Table 3-1. (continued)

Depth (cm)	$\delta^{18}O$ Age (ka)	^{14}C age (yrs BP±1σ)	Cal ^{14}C age (yrs BP±1σ)	Isotope composition			Clay mineral composition (%)				Grain size (Φ50)	
				$^{87}Sr/^{86}Sr$ ±2σ	$^{143}Nd/^{144}Nd$ ±2σ	ε_{Nd}	Illite	Kaolinite	Chlorite	Smectite	(μm)	(ϕ)
114–115	291.4			0.709627 ±13	0.512270 ±11	–7.18	42	13	19	26	2.6	8.6
128–129	326.8			0.710710 ±14	0.512164 ±46	–9.25	39	11	19	31	2.6	8.6
146–147	352.5			0.710948 ±11	0.512231 ±13	–7.94	45	9	21	25	2.7	8.5
164–165	397.9			0.711139 ±14	0.512192 ±15	–8.70	45	10	20	25	2.6	8.6
184–185	434.3			0.711049 ±13	0.512244 ±12	–7.69	41	10	21	28	2.6	8.6
196–197	472.1			0.710859 ±15	0.512214 ±10	–8.27	41	10	18	31	2.6	8.6
228–229	573.7			0.711951 ±11	0.512154 ±15	–9.44	48	9	19	23	2.6	8.6
Average				0.710495	0.512217	–8.21	46	10	19	25	2.7	8.6

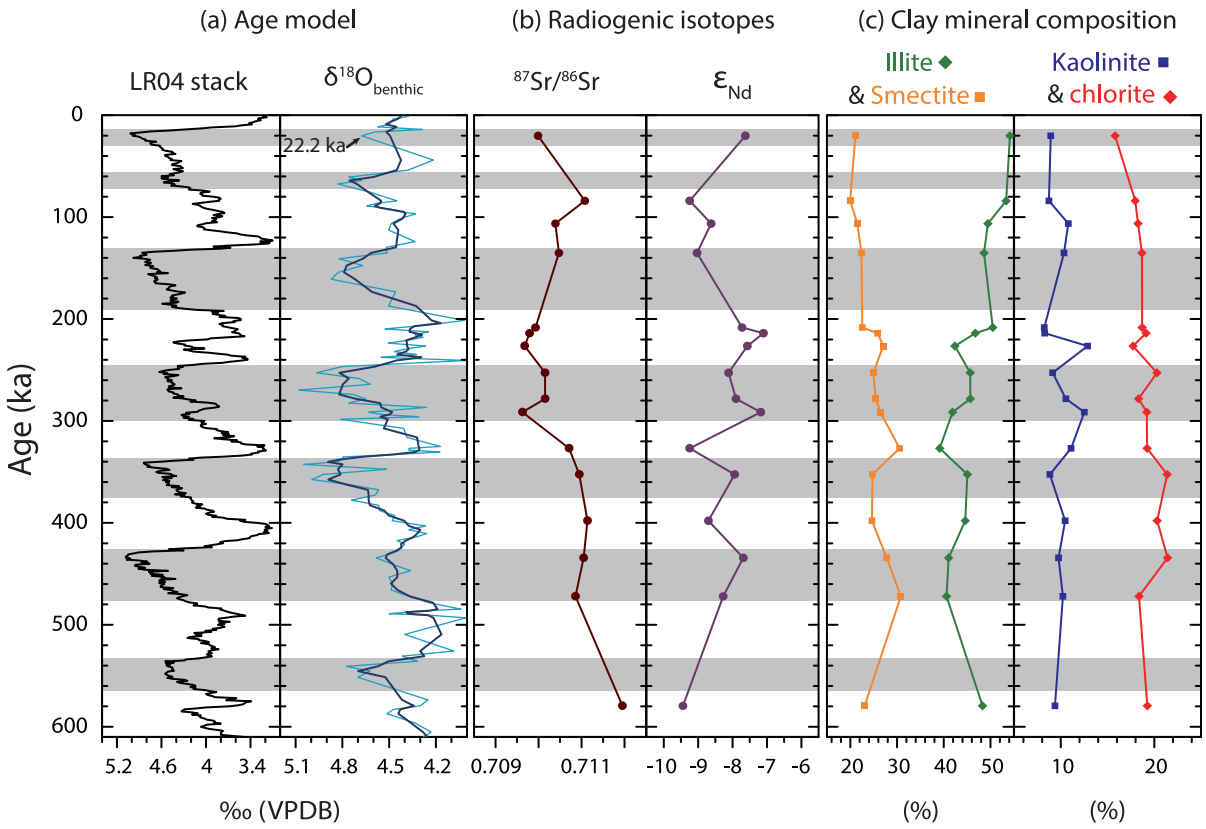

Figure 3-3. Down-core variations in: (a) stable oxygen isotope composition of benthic foraminifera in the LR04 stack and PC 631; (b) radiogenic isotopic compositions ($^{87}Sr/^{86}Sr$ and ε_{Nd}); and (c) clay mineral composition of the <4 μm fraction of eolian dust. The age model was constructed using the correlation between the benthic foraminiferal $\delta^{18}O$ records of PC 631 and the LR04 $\delta^{18}O$ stack [*Lisiecki and Raymo*, 2005] with AMS ^{14}C confirmation at the 14–15 cm interval (arrow). Shaded intervals indicate glacial periods.

kaolinite (10 ± 2%, 1σ; Figure 3-3).

3.4. Discussion

The median grain sizes of the abyssal sediments affected by hemipelagic processes are usually greater than 6.5 μm (<7.5 ϕ) because of the significant amount of silty components (>16 μm) supplied by hemipelagic processes [*Rea and Hovan*, 1995; *D Sun et al.*, 2002]. The winnowing process also concentrates coarser silty fractions at a depositional site as it removes fine fractions selectively. Thus, median grain size (2.7 ± 0.1 μm (8.6 ϕ)) and small amount (2.2 ± 0.8 % (n=16, 1 σ) of silty components (>16 μm) in the inorganic silicate fraction of PC 631 indicate negligible effect of hemipelagic and winnowing processes on sedimentation. In addition, the median grain size of inorganic silicate fraction of PC 631 is in good agreement with that (ca. 8.5 ϕ) of the north-central Pacific (NCP) where the hemipelagic processes are rare [*Rea*, 1994; *Rea and Hovan*, 1995]. These results indicate that the inorganic silicate fraction of this study is largely airborne mineral particles. For this reason, the inorganic silicate fraction is hereafter termed “eolian dust”, although it includes an unconstrained amount of volcanogenic and authigenic materials.

3.4.1. Sources of eolian dust in the PC 631 sediments

The NCP dust province (Figure 3-1) primarily receives dust from the central and East Asian deserts via the Prevailing Westerlies and Trade Winds, and has a distinctive isotopic (ε_{Nd}, $^{87}Sr/^{86}Sr$) and clay mineral composition [*Corliss and Hollister*, 1982; *Griffin et al.*, 1968; *Jones et al.*, 1994; *Nakai et al.*, 1993]. Our data

show slightly higher ε_{Nd} and lower $^{87}Sr/^{86}Sr$ than the NCP province sediments (Figure 3-4a), and are characterized by a slightly smectite-enriched composition compared to aerosols collected in the NCP (Figure 3-4b). Both Sr–Nd isotopes and clay mineral compositions plot along a mixing line between Asian dust, represented by NCP sediments, and the surrounding volcanic-arc components (Figure 3-4). This suggests that the study site has been influenced by the input of both Asian dust and volcanic arc material during its depositional history.

On a plot of ε_{Nd} versus $^{87}Sr/^{86}Sr$, the northwest Pacific and Mariana Basin sediments plot closer to the volcanic arc end-members than to samples from this study (Figure 3-4a), indicating that there is a higher contribution from arc materials in these areas. ε_{Nd} in samples from this study are also clearly distinguishable from south-central Pacific sediments, where eolian components are supplied from Australian deserts and New Zealand [*Stancin et al.*, 2008; *Xie and Marcantonio*, 2012] (Figure 3-4a). The clay mineral composition of samples from this study is also distinct from Australian and North African dust, which is enriched in kaolinite (Figure 3-4b). Consequently, all source indicators analyzed in this study; i.e., $^{87}Sr/^{86}Sr$, ε_{Nd}, and clay mineral composition, point to little or no contribution of Australian and Saharan dust to the study site.

The negligible input of Saharan dust to the western Pacific contradicts previous modeling results that predict the prevalence of Saharan dust in the region [e.g., *Luo et al.*, 2003; *Mahowald et al.*, 2007; *Tanaka and Chiba*, 2006]. As noted by *Tanaka and Chiba* [2006], the inconsistency between site-specific sediment data and modeling results may be due to the coarse resolution of the global dust models. The minimal contribution of Australian dust at the site may be a result of its small

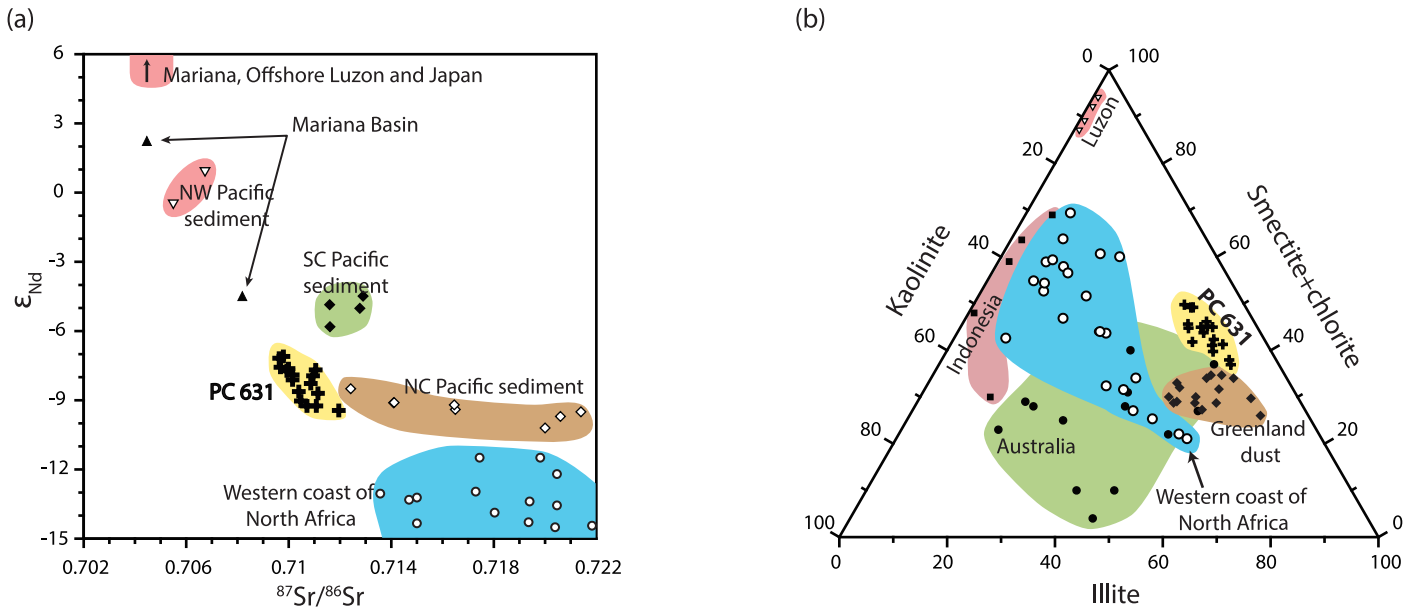

Figure 3-4. (a) ε_{Nd} versus $^{87}Sr/^{86}Sr$ cross plot, and (b) ternary diagram showing the clay mineral assemblage of eolian fractions of core PC 631 (samples from glacial intervals are shown as open crosses and those of interglacial intervals are solid crosses). $^{87}Sr/^{86}Sr$ and εNd are from *Grousset et al*. [1998], *Hyeong et al.* [2011], *Nakai et al.* [1993], *Pettke et al.* [2000], *Stancin et al.* [2008], and *Woodhead* [1989]. Clay mineral compositions are from *Arnold et al.* [1998], *Aston et al.* [1973], *Biscaye et al.* [1997], *Chester et al.* [1971; 1972], *Gingele et al.* [2001], *Gingele and De Deckker* [2004], *Glaccum and Prospero* [1980], *Leinen et al*. [1994], *Liu et al.* [2009], and *Shi et al.* [1997].

contribution to the global dust budget (ca. 6%; *Tanaka and Chiba* [2006]). Additionally, the air masses to the study site originate from Australia due to the prevailing boreal summer wind direction (Figure 3-1), but the long transport distance may limit the contribution of Australian dust to the record.

3.4.2. Relative contribution of volcanic arc and Asian dust components

To understand the relative contributions from Asian dust and volcanogenic components to the record, a simple two-component mixing model was constructed using $^{87}Sr/^{86}Sr–\varepsilon_{Nd}$ (Figure3-5a) and clay mineral compositions (Figure 3-5b). Asian dust source areas were classified into three regions in these models: the northern Chinese deserts (NCDs; the northernmost desert regions in China), the central Asian deserts (CADs; deserts on the northwestern margin of the Tibetan Plateau), and the East Asian deserts (EADs; the Chinese Loess Plateau (CLP) and nearby deserts; Figures 3-1 and -2). These three regions can be distinguished from each other using their ε_{Nd} values, $^{87}Sr/^{86}Sr$ ratios, and clay mineral compositions (Figures 3-5 and -6a). In addition, it is known that dust from the EADs is predominantly carried by northwesterly surface winds associated with the EAWM, while dust from the CADs is mainly transported via the Prevailing Westerlies in the mid- to high-level troposphere [*Shi and Liu*, 2011; *Sun et al.*, 2001]. Therefore, the identification of specific source regions helps to identify dust transport mechanisms to the study site.

For the $^{87}Sr/^{86}Sr$-ε_{Nd} mixing model, Asian dust data from the <5 μm size fraction were used to constrain the grain-size dependence of $^{87}Sr/^{86}Sr$ [*Asahara et al.*, 1995; *Chen et al.*, 2007; *Feng et al.*, 2009]. The <5 μm size fraction accounts for an average of 83% (± 1%, 1 σ, n=16) of the extracted dust components, which helps to

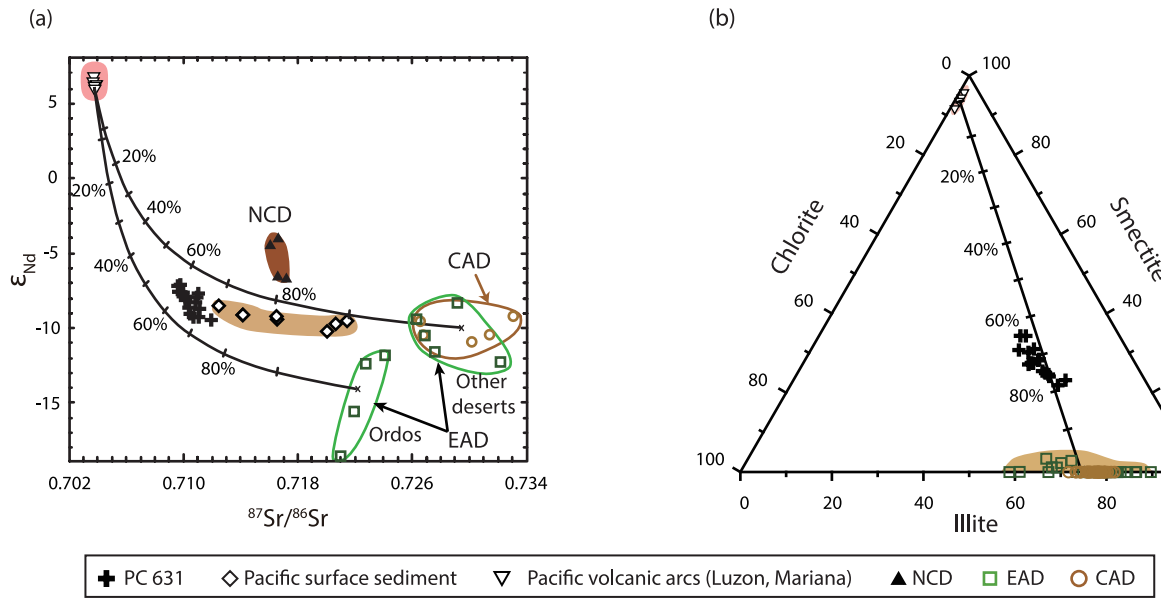

Figure 3-5. (a) ε_{Nd}–$^{87}Sr/^{86}Sr$ and (b) clay mineral composition of core PC 631 (crosses), north-central Pacific (NCP) surface sediment (diamonds), volcanic arcs in the western Pacific (inversed triangles), and soils in Chinese deserts grouped into three regions (see Figures 3-1 and 3-2). NCD, CAD, and EAD refer to the northern Chinese deserts, central Asian deserts, and East Asian deserts, respectively. Mixing lines are placed between the volcanic arc end-member, and the average composition of soils from the CADs and Ordos Desert in the ε_{Nd}–$^{87}Sr/^{86}Sr$ plot, and between volcanic arc end-members and the average composition of aerosols and soils from the EADs [*Biscaye et al.*, 1997; *Shen et al.*, 2005] and the CADs [*Shen et al.*, 2005] in the clay mineral composition plot. The known concentrations of Sr and Nd from Luzon Island (Sr = 440 ppm, Nd = 19 ppm) [*Defant et al.*, 1990] and the Chinese deserts (Sr = 111 ppm, Nd = 28.3 ppm) [*Kanayama et al.*, 2005] are used to develop mixing lines in the ε_{Nd}–$^{87}Sr/^{86}Sr$ plot. See Figure 3-4 for data sources.

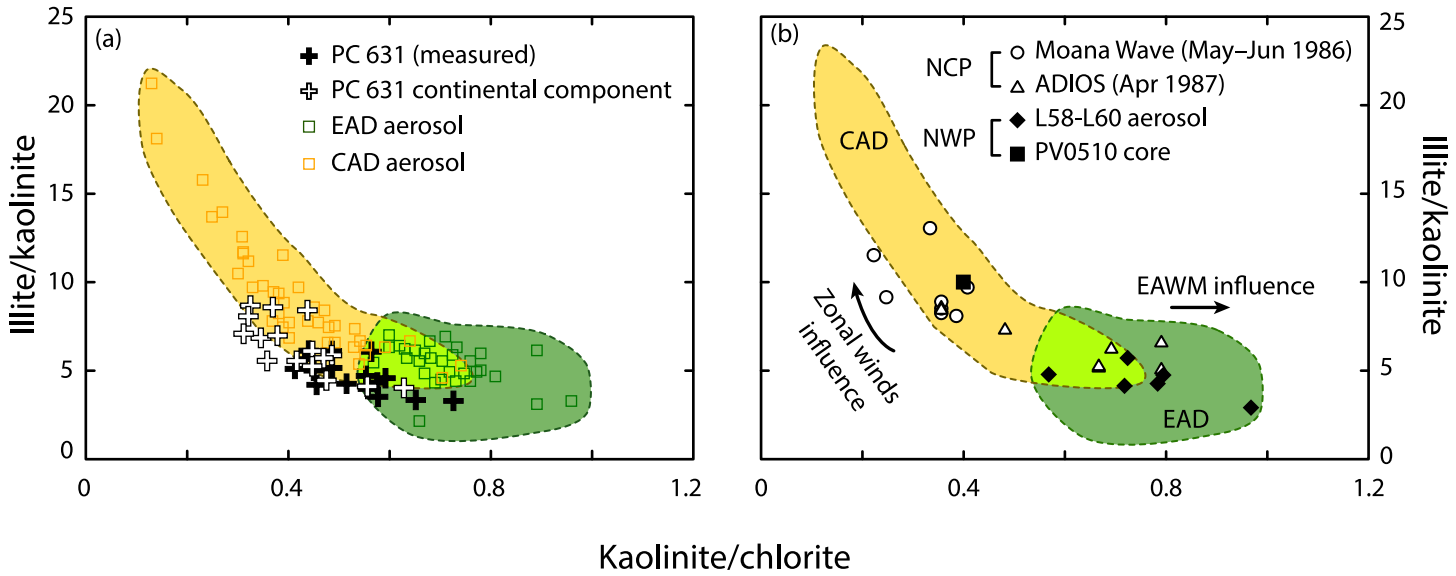

Figure 3-6. (a) Kaolinite/chlorite (K/C)–illite/kaolinite (I/K) diagram for core PC 631 and aerosol samples downwind of Asian dust source regions [*Shen et al.*, 2005]. The original composition (mixed dust from Asian deserts and the volcanic arc), and the estimated Asian dust end-member composition (see text for details) of PC 631 are marked as solid crosses and open crosses, respectively. (b) Kaolinite/chlorite (K/C)–illite/kaolinite (I/K) diagram of aerosols collected in the north-central Pacific (NCP) from the Moana Wave (open circles) and ADIOS (open triangles) cruises [*Arnold et al.*, 1998]. Aerosol (L58–L60) and sediment core (PV0510) data from the northwest Pacific are marked as solid diamonds and a solid square, respectively [*Leinen et al.*, 1994; *Ming et al.*, 2014]. The central Asian desert (CAD) and East Asian desert (EAD) domains are as Figure 3-6a.

minimize any errors related to differences in the grain size distributions between source and sample. For the clay mineral composition mixing-model, we used the composition of CLP sediments and aerosols collected downwind of the CADs and EADs as soil mineralogical data were unavailable.

In general, dust from the EADs and CADs possess a similar $^{87}Sr/^{86}Sr$–ε_{Nd} composition, except that the Ordos Desert has a distinctively low ε_{Nd} (Figure 3-5a). In the $^{87}Sr/^{86}Sr$–ε_{Nd} mixing model, samples plot between two mixing lines drawn between the average end-member compositions of volcanic arc–CAD sources (and EADs other than the Ordos Desert) and volcanic arc–Ordos Desert sources (Figure3- 5a), suggesting a supply of Asian dust from both CADs and EADs to the site. The mixing model also indicates that there is little contribution of dust from NCDs to the site, as its isotopic composition plots in an independent domain off the mixing lines (Figure 5a). Although the relative contribution of the CADs and EADs cannot be estimated uniquely, the mixing model suggests that Asian deserts contributed between 60% and 80% of the dust deposited at the study site, with the remainder originating from volcanic arcs (Figure 3-5a). This result is in agreement with the clay mineral composition mixing-model (Figure 3-5b).

3.4.3. Source regions and transport agents of Asian and volcanic arc dust

Dust storms frequently break out in the CADs (e.g., the Taklimakan Desert) throughout the year, and the entrainment of dust into high-level westerlies allows for the long-range transport of material to locations as distant as Greenland [*Bory et al.*, 2002, 2013; *Iwasaka et al.*, 2008; *Shi and Liu*, 2011]. In contrast, dust storms in the EADs primarily occur in spring, when the northwesterly winter monsoon

prevails. Dust from the EADs is therefore predominant downwind of mainland China and the northwest Pacific [*Shi and Liu,* 2011; *Sun et al.*, 2001; *Zhang et al.*, 1997] (Figure 3-1). The major transport agents of dust from the CADs and EADs are most likely the high-level westerlies and the low-level northwesterly winter monsoon, respectively.

Dust from the EADs and CADs have distinguishable illite/kaolinite (I/K) and kaolinite/chlorite (K/C) values (Figure 3-6) [*Shen et al.*, 2005], which enables an estimation of the relative contribution of these two major Asian dust source regions to the dust budget of the study site. Dust from the CADs is enriched in illite and chlorite, but is extremely poor in kaolinite (I/K = 9.2 ± 3.5, K/C = 0.4 ± 0.1, n = 40) due to the hyper-arid climate of the region (Figure 3-6a). In contrast, dust from the EADs is characterized by a moderate kaolinite content, and the resulting higher K/C (0.7 ± 0.1, n = 32) and lower I/K values (5.4 ± 1.1, n = 32) compared to CAD dust (Figure 3-6a) [*Shen et al.*, 2005; *Shi et al.*, 1997].

The I/K and K/C values of Pacific aerosols sampled at various zonal and meridional locations during winter and spring support the transport mechanisms and pathways of Chinese eolian dust discussed above (Figure 3-6b). Samples collected during the Moana Wave and ADIOS cruises in the NCP (Figure 3-1) are depleted in kaolinite [Arnold et al., 1998], and most have a clay mineral composition that corresponds to dust from the CADs (Figure 3-6b). This suggests that Asian dust, subjected to long-range transport by the Prevailing Westerlies, is dominantly sourced from the CADs rather than from the EADs. Aerosol samples collected in the month of April from the ADIOS cruise are kaolinite-rich compared to samples collected in May during the Moana Wave cruise (Figure 3-6b). This suggests that

increased entrainment of dust from the EADs into high-level westerlies contributes to the NCP dust budget in spring when the most intense and frequent dust storms occur in East Asia. In contrast to the NCP, aerosols collected during December–March in the northwest Pacific, when northwesterly winds associated with the EAWM prevail (L58K2, K3, K6, L59K1, and L60K3; Figure 3-1) [*Leinen et al.*, 1994], have clay mineral compositions that correspond to dust from the EADs (Figure 3-6b), confirming the dominance of this dust source in the region during winter and spring.

The eolian fraction of PC 631 sediments has I/K and K/C values (I/K = 4.6 ± 1, K/C = 0.53 ± 0.1, 1σ, n = 16; Figure 3-6a) in agreement with those of NCP aerosols, but plot in both the EAD and CAD fields (Figure 3-6). The clay mineral composition of samples corresponds to mixed dust from Asian deserts (60% to 80%) and volcanic arc sources (20% to 40%; see Section 4.2 for details). Thus, it is necessary to eliminate the components from volcanic sources to evaluate the relative importance of the CAD and EAD dust. To estimate the clay mineral composition of dust from Asian sources, we assumed an average 30% contribution from the volcanic component, with K/C and I/K values of 2 and 0, respectively, based on the average composition of Luzon soil [*Liu et al.*, 2009]. Exclusion of the volcanic components from the mineral composition mixing model results in a shift in the mineral composition of the observed data similar to those of NCP aerosol, suggesting the CADs as a likely dust source area (Figure 3-6). This suggests that, as in the NCP, the study site is dominated by CAD-sourced dust that travels via high-level westerlies. It is thought that dust from the CADs travels to the study site via the Prevailing Westerlies, and then via northeasterly Trade Winds, as depicted in the

dust transport trajectories in Figure 1 [*Merrill et al.*, 1989].

The results of this study are not in accordance with the reported clay mineral composition of dust from the EADs in the northwest Pacific from aerosol samples (L58-K2, -K3, -K6, -K17, L59K1, and L60K3; Figure 3-1) [*Leinen et al.*, 1994]. This discrepancy is most likely the result of differences in the timing of sample collection and the timescale of the two studies. As discussed earlier, collection of aerosol data from the northwest Pacific occurred in December–March, when dust from the EADs travels to the region primarily via northwesterly winds associated with the EAWM. In contrast, data from this study reflect the time-averaged composition of dust, and thus can be used to evaluate the relative importance of two dust transport mechanisms at the study site: the EAWM and the zonal wind system. Both datasets indicate that dust from EADs dominates during the EAWM season; however, dust from the CADs dominates the overall dust budget of the study site.

These results suggest that long-range transport via the Prevailing Westerlies and Trade Winds is the principal dust transport mechanism to the study site. The clay mineralogy of sediment core PV0510 (Figure 3-2), recovered in close proximity to our study site, was similar to that described here (I/K = ca. 10, K/C = ca. 0.4 on average of 2 myr interval; Figure 6b) [*Ming et al.*, 2014], which suggests the significant contribution of the CAD dusts in the northwest Pacific. The results of this study contradict the general perception that dust transport in spring by the EAWM dominates the annual flux of eolian dust to the northwest Pacific [e.g., *Ming et al.*, 2014; *Wan et al.*, 2012; *Xu et al.*, 2012], and highlights the importance of long-range transport by zonal winds to the dust budget of the northwest Pacific.

Data from volcanic arc materials collected near the study site have

similar $^{87}Sr/^{86}Sr$–ε_{Nd} values and clay mineral compositions (Figure 3-4). Consequently, the volcanic end-member sources cannot be evaluated using data from this study. However, $^{87}Sr/^{86}Sr$ and ε_{Nd} values, and clay mineral compositions, together with the proximity to the study site suggest that the Luzon Arc (represented by Luzon Island) is the most plausible source of volcanic end-member material. Volcanogenic particles and weathering products in the Luzon Arc may be transported to the study site when the summer monsoon prevails and westerly winds develop over the arc (Figure 3-1).

Despite its geographical proximity to the study site, the supply of volcanic materials from the Mariana arc is expected to be minor compared to that of the Luzon Arc because of its very small subaerially exposed area (ca. 1,000 km^2) compared to that of the Luzon Arc (ca. 300,000 km^2). Indonesia and Papua New Guinea are located in a tropical climate regime characterized by frequent storms and high precipitation, which results in weathering products dominated by kaolinite, as indicated in the mineral assemblages of Indonesian soil [*Gingele et al.*, 2001] (Figure 3-4b). These two sources do not explain the clay mineral composition of samples from this study, and they are thus excluded as potential volcanic end members. Mineral aerosols from Japanese arcs may be supplied to the study site, together with Asian dust, via surface winds associated with the EAWM. However, the transport of Japanese arc materials with the Prevailing Westerlies is limited to offshore areas proximal to the arc [*Asahara et al.*, 1995; *Jones et al.*, 1994; *Mahoney*, 2005; *Serno et al.*, 2014], probably due to the difficulty in entraining Japanese arc materials into high-level westerlies. As the study site is dominated by dust that travels via high-level westerlies, the contribution of Japanese arc materials

to the study site is considered negligible.

3.5. Conclusions

The ε_{Nd} values, $^{87}Sr/^{86}Sr$ ratios, and the clay mineral composition of eolian dust preserved in core PC 631 retrieved from the subtropical northwest Pacific indicate the mixed input of dust from the central and East Asian deserts (ca. 70%) and nearby volcanic islands (ca. 30%), likely the Luzon Arc, over the last 600 kyr. In contrast to the results obtained from previous global dust models, neither Australian nor North African dust contributed a detectable amount of dust to the study site, raising the possibility that the dust models underestimated the Asian dust contribution to budgets in the North Pacific. Further, the ε_{Nd} and $^{87}Sr/^{86}Sr$ composition of dust from the northern Chinese deserts, another major dust source in Asia, indicate that it was not a significant contributor at this site.

The clay mineral composition of the core resembles dust from the central Asian deserts (CADs; e.g., Taklimakan Desert), which is mainly transported to the north-central Pacific via the Prevailing Westerlies [*Iwasaka et al.*, 2008; *Shi and Liu*, 2011]. Thus, our results indicate that the zonal wind system is the dominant transport agent in the overall dust budget of the study site. Dust originating from the CADs most likely travels via the Prevailing Westerlies and then the northeasterly Trade Winds prior to deposition at the study site. In contrast, the clay mineral assemblages of aerosols trapped at the nearby site are similar to those of East Asian deserts (EADs) [*Leinen et al.*, 1994], indicating different transport pathways. As aerosol data reported by *Leinen et al.* [1994] were collected during the winter/spring

dust-storm season, this suggests that northwesterly surface winds associated with the East Asian Winter Monsoon act as the main dust transport agent during this period, but dust from the CADs dominates the overall dust budget. The results of this study do not agree with the general perception that transport by dust storms in spring dominates the annual flux of eolian dust in the northwest Pacific.

CHAPTER 4. CHANGE OF ATMOSPHERIC AND SURFACE OCEAN CIRCULATION IN THE CENTRAL EQUATORIAL PACIFIC ACROSS THE MID-PLEISTOCENE TRANSITION

Abstract

This paper investigates the causes of a brief, but prominent, cooling episode (1.1–0.8 Ma) that occurred in the equatorial upwelling region of the Atlantic and Pacific during the mid-Pleistocene Transition (MPT) using temporal changes in dust provenance, regional hydrology, and surface productivity recorded in a deep-sea sediment core from the central equatorial Pacific. The $^{87}Sr/^{86}Sr$ and ε_{Nd} values of the inorganic silicate fraction indicate deposition of dust from Australia and Central/South America before 0.8 Ma, but a gradual increase in Asian dust deposition after 0.8 Ma. The change in dust provenance was accompanied by an increased dust flux and a decrease in surface productivity and salinity. These changes can be explained by the southward movement of the Intertropical Convergence Zone (ITCZ) and North Equatorial Counter Current (NECC) and the direct influence of these features on the site after 0.8 Ma. Our results, together with previously published Atlantic data, suggest the northward position of the ITCZ between 1.1 and 0.9 Ma, and the southward position thereafter. The meridional movement of the ITCZ is in phase with the cooling and warming trend in upwelling regions in the equatorial Pacific and Atlantic, which suggests strengthening of

southeast trades relative to its northern counterpart between 1.1 and 0.9 Ma as a plausible cause of this brief cooling event. The southward movement of the ITCZ from 0.9 to 0.8 Ma indicates more significant cooling in the Northern Hemisphere (NH) than in the Southern Hemisphere, which is supportive of the interpretation that the NH ice sheet expanded significantly and stabilized after 0.9 Ma.

Chapter Source: Seo, I., Y. I. Lee, W. Kim, C. M. Yoo, and K. Hyeong (2015), Movement of the Intertropical Convergence Zone during the mid-pleistocene transition and the response of atmospheric and surface ocean circulations in the central equatorial Pacific, Geochem. Geophys. Geosyst., 16, 3973–3981, doi:10.1002/2015GC006077.

4.1. Introduction

The mid-Pleistocene transition (MPT) covers the period between 1.25 and 0.7 Ma during which the dominant glacial–interglacial periodicity changed from 41 kyr-cycles to 100 kyr-cycles [*Clark et al.,* 2006]. The appearance of strong 100-kyr periodicity at 0.9 Ma is often attributed to a significant increase in ice volume [*Elderfield et al.,* 2012; *McClymont et al.,* 2013]. Significant cooling of surface and deep water has been reported in polar/sub-polar regions prior to the emergence of the 100-kyr periodicity [*Lawrence et al.,* 2006; *Martínez-Garcia et al.,* 2010; *McClymont et al.,* 2008; *Sosdian and Rosenthal,* 2009], possibly preconditioning the development of major high-latitude glaciers and a change in the global ocean deep-water circulation [*Clark et al.,* 2006; *Head and Gibbard,* 2005; *McClymont et al.,* 2013].

One of aspects of this period that has received less attention is the pronounced cooling in the equatorial upwelling regions of the eastern equatorial Pacific/Atlantic between 1.1 and 0.8 Ma [*McClymont and Rosell-Melé,* 2005; *Schefuß et al.,* 2003] (Figure 4-1c and -1e), which is not evident in the global $\delta^{18}O$ stack and in the Western Pacific Warm Pool (WPWP) records [*Lisiecki and Raymo,* 2005; *McClymont and Rosell-Melé,* 2005] (Figure 4-1a and -1b). This cooling began at about 1.1 Ma and peaked at about 0.9 Ma. Sea surface temperature (SST) then rebounded rapidly and reached the background level around 0.8 Ma (Figure 4-1c and -1e). Although the lowest SSTs were recorded at the glacial maximum of Marine Isotope Stage 22, the SST drop during this period is particularly notable when compared with other glacial stages. As this cooling event was recorded both

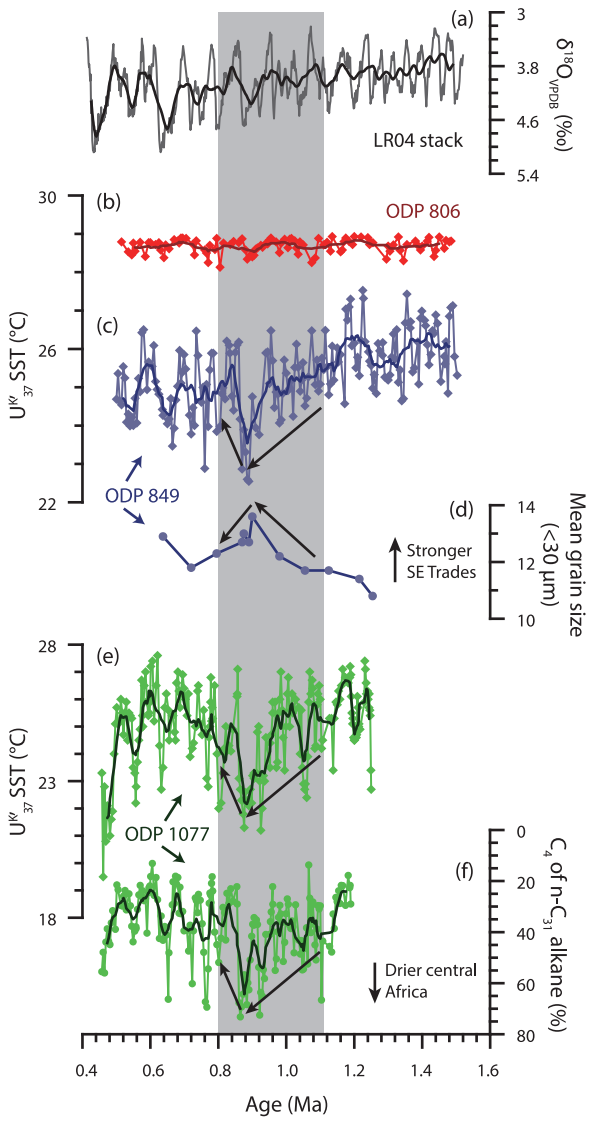

Figure 4-1. Long-term trends in paleoceanographic and paleoclimatic proxies during the middle to late Pleistocene. (a) LR04 benthic $\delta^{18}O$ stack [Lisiecki and Raymo, 2005], (b) $U^{K'}_{37}$ SST from Ocean Drilling Project (ODP) site 806 in the WPWP [McClymont and Rosell-Melé, 2005], (c) $U^{K'}_{37}$ SST, (d) mean grain size of fine sediment fraction (<30 μm), a proxy for trade winds strength, from ODP Site 849 in the central equatorial Pacific [McClymont and Rosell-Melé, 2005], (e) $U^{K'}_{37}$ SST, and (f) C_4 of n-C_{31} alkane (%) from ODP site 1077 in the eastern equatorial Atlantic [Schefuß et al., 2003].

in the equatorial Atlantic and Pacific, it can be seen as one of the major tropical responses to climate forcing during the MPT. As the MPT is regarded as the period during which more modern-like cold tongue and Walker Circulation first emerged [*de Garidel-Thoron et al.*, 2005; *Li et al.*, 2011], an explanation of the causes of this cooling event is required if we are to better understand the climatic evolution of the cold tongue region.

Latitudinal displacement of the Intertropical Convergence Zone (ITCZ), a belt of enhanced precipitation that results from the convergence of the northeast and southeast trade winds, has been highlighted as one of the key tropical responses to climate forcing over various timescales [*Broccoli et al.*, 2006; *Chao and Chen*, 2001; *Schneider et al.*, 2014]. In particular, shifts in the latitudinal position of the ITCZ are accompanied by changes in upwelling intensity and SST in the cold tongue region [*Koutavas and Lynch-Stieglitz*, 2003; *Timmermann et al.*, 2007; *Wang and Wang*, 1999]; consequently, tracing the ITCZ position during the MPT would assist our understanding of the mechanisms associated with the brief equatorial cooling event between 1.1 and 0.8 Ma.

This study aims to describe and interpret climate evolution over the equatorial Pacific during the MPT by investigating ITCZ movement and associated changes in regional hydrology and surface productivity. The study site is in the central equatorial Pacific near the international dateline, where the latitudinal range of the seasonal migration of the ITCZ is minimal (Figure 4-2), which helps us to trace its migration as the global climate changes. Our data also show the differential cooling history of each hemisphere over the MPT as the ITCZ shifts toward the hemisphere with reduced thermal gradient between equator and pole [e.g., *Broccoli et al.*, 2006;

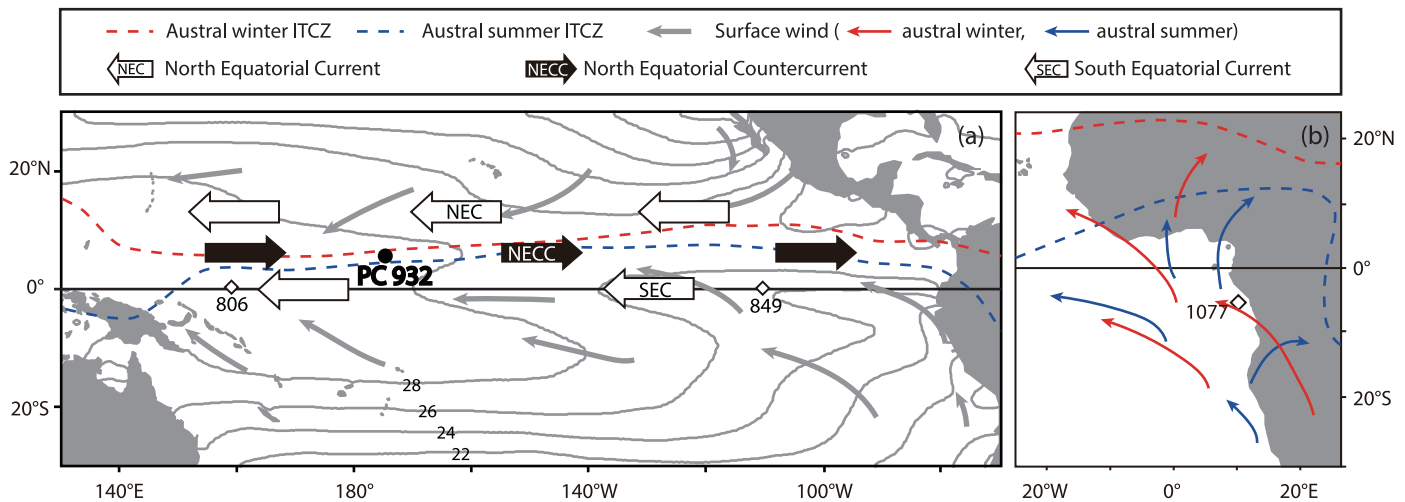

Figure 4-2. (a) Map of surface currents, surface winds and mean positions of the seasonal ITCZ over the tropical Pacific. The locations of the core analyzed in this study (PC 932), and ODP sites (806 and 849) are also marked. Annual mean SST data from the World Ocean Atlas 2013 are shown as gray contours [Boyer et al., 2013]. (b) General pattern of surface wind and ITCZ position over the east Atlantic with location of ODP site 1077 marked as open diamond.

Chiang and Friedman, 2012; *Flohn*, 1981; *McGee et al.*, 2014] .

4.2. Study Site and Analytical Methods

A 557-cm-long deep-sea sediment core, PC 932, was recovered from the Magellan Rise in the central equatorial Pacific (5°53′N, 177°26′W, 4,136 m water depth) during a cruise carried out by Korea Institute of Ocean Science and Technology (KIOST) in 2009 (Figure 4-2a). The core is composed mainly of calcareous ooze with minor contribution of pelagic mud and does not show any recognizable lithologic change with bare eyes. The North Equatorial Countercurrent (NECC), whose position is coupled with the ITCZ [*Donguy and Meyers*, 1996; *Masunaga and L'Ecuyer*, 2010], flows over the site and transports warm and low-nutrient surface water to the study site from the WPWP. To the south of the study site is the westward-flowing South Equatorial Current (SEC). Strong, upwelling favorable trade winds bring nutrients to the surface at the equator, resulting in higher primary production than in the WPWP and NECC regions [*Eldin and Rodier*, 2003; *Le Bouteiller et al.*, 2003].

The chronology of core PC 932 was established using magnetostratigraphic correlation. The core was sampled using u-channels of about 100 cm in length and a cross section of 4 cm^2 for paleomagnetic analysis. Magnetic remanence measurements of the u-channel samples were made at an interval of 1 cm using a 2G Enterprises pass-through superconducting magnetometer. The demagnetization data were processed using Puffinplot [*Lurcock and Wilson*, 2012].

To understand temporal changes in surface productivity, the total inorganic

carbon (TIC) and biogenic silica (Si_{bio}) contents were measured at a 4 cm interval. TIC was analyzed using a UIC CO_2 coulometer (CM5014) at the KIOST and then converted to $CaCO_3$ content by multiplying by 8.333 on the assumption that all inorganic carbon originated from $CaCO_3$. The analytical precision of the $CaCO_3$ content was ±1%. The Si_{bio} content was measured at KIOST using a UV spectrophotometer (UV-1601) and the wet alkaline extraction method adopted from *DeMaster* [1981] and *Müller and Schneider* [1993], with an analytical error of ±1%. The Si_{bio} was converted to opal content by multiplying by 2.4 [*Mortlock and Froelich*, 1989]. To semi-quantitatively assess the degree of carbonate dissolution, the size index (>63 μm $CaCO_3$/total $CaCO_3$ × 100%), proposed by *Broecker and Clark* [1999], was measured using the wet sieving method.

The radiogenic isotope composition of the eolian dust fraction in the studied samples was measured to investigate its source region. The inorganic silicate fraction (mostly eolian dust with very minor or trace amounts of volcanogenic and authigenic materials; hereafter termed eolian dust) was extracted from 12 sediment samples following the method described by *Hovan* [1995]. Referring to the "Pacific-style $CaCO_3$ cycles" [*Sexton and Barker*, 2012], the samples were collected at the horizons of maxima and minima over $CaCO_3$ cycles, which likely represent the glacial and interglacial periods, respectively. For the 12 samples, the eolian component was estimated from the following equation: weight of extracted inorganic silicate fraction/weight of bulk sediment × 2.5 × 100% [*Hovan*, 1995]. For other intervals, the fraction other than $CaCO_3$ and opal was approximated as an eolian component, and showed good agreement with the results of the other method (Figure. 4-3e). Analysis of the $^{143}Nd/^{144}Nd$ and $^{87}Sr/^{86}Sr$ ratios, including chemical

separation and multi-collector thermal ionization mass spectrometric (TIMS; *VG54-30, Isoprobe-T*) analysis, was performed at the Korea Basic Science Institute. Replicate analysis of NBS987 and JNdi-1 gave mean values of $^{87}Sr/^{86}Sr = 0.710246 \pm 0.000011$ (n = 10, 2σ), and $^{143}Nd/^{144}Nd = 0.512101 \pm 0.000015$ (n = 10, 2σ). For convenience, we express the $^{143}Nd/^{144}Nd$ ratios as ε_{Nd}; i.e., the deviation from a chondritic uniform reservoir ($\varepsilon_{Nd} = (^{143}Nd/^{144}Nd/0.512638 - 1) \times 10^4$) [*Jacobsen and Wasserburg*, 1980].

To understand temporal changes in local hydrology of the study site, stable oxygen isotope compositions ($\delta^{18}O$) of the planktic foraminifera *Globigerinoides sacculifer* (without final sac) in the 250–355 μm size fraction were determined using a Finnigan MAT 251 mass spectrometer at the University of Michigan at Ann Arbor, USA. The 1-sigma standard deviation of the repeat analyses of the reference material (NBS-19; National Bureau of Standards) was 0.09‰ (n = 24).

The relative content of each component to the bulk sediment was further converted to the mass accumulation rate (MAR) for the more accurate estimation of the influx of each component. The MAR is the product of the linear sedimentation rate (LSR) and the dry bulk density (DBD) of the sample. The latter was calculated from the determined porosity (P) and grain density of the sediments (ρ) using the relationship $DBD = (1 - P/100) \times \rho$ [*Rea and Janecek*, 1981]. Then, the MAR of each fraction (i.e., $CaCO_3$, opal, and eolian) was calculated by multiplying their weight percentage by the determined MAR.

4.3. Results

Sediment ages were determined at depths of 352 and 501 cm, which correspond to the boundaries of the geomagnetic chrons Brunhes–Matuyama (0.78 Ma) and Matuyama–Jaramillo (0.99 Ma), respectively (Figure 4-3a). The basal age of the core (557 cm) should be younger than the older boundary of the Jaramillo subchron (1.07 Ma) because the previous reversal subchron was not recovered in the core. Based on these magnetostratigraphic ages, the estimated LSRs were 0.45 cm/kyr and 0.70 cm/kyr for the 0–370 and 370–557 cm intervals, respectively.

$CaCO_3$, opal and eolian components account for, on average, 87.4% (78.3–92.2%), 7.9% (3.7–14.8%) and 4.7% (1.2–10.3%), respectively (Table 4-1). The relative contents of these three were converted to MARs and are presented in graphical form (Figure 4-3e). The size index, representing the >63μm fraction of the determined $CaCO_3$, accounts for 20.1 % on average (3.5–39.8%, Figure 4-3d). All four components show a significant up-core shift in content and MAR around 0.8 Ma (Figure 4-3d and -3e). The $\delta^{18}O$ of *G. sacculifer* ($\delta^{18}O_{Gsac}$) varies from −1.60 to −0.15‰ (−0.99‰ on average; Figure 4-3b). The glacial–interglacial variations are not clear enough for chronological correlation, and this is probably the result of the low sedimentation rate (ca. 0.5 cm/kyr) and bioturbation. However, the $\delta^{18}O_{Gsac}$ shows a marked up-core shift to lighter values from −0.72‰ to −1.14‰ on average around 0.8 Ma (Figure 4-3b). The gradual increase of $\delta^{18}O_{Gsac}$ until 0.9 Ma and subsequent decrease are apparent in the lower section younger than about 0.8 Ma. The measured ε_{Nd} and $^{87}Sr/^{86}Sr$ vary between −4.92 and −8.79, and 0.70949 and 0.71935, respectively (Figure 4-3d, Table 4-2), and show up-core trends towards gradually decreasing ε_{Nd} and increasing $^{87}Sr/^{86}Sr$ (Figure 4-3b). The compositional groupings between the upper (<0.8 Ma) and lower intervals (>0.8 Ma) are apparent

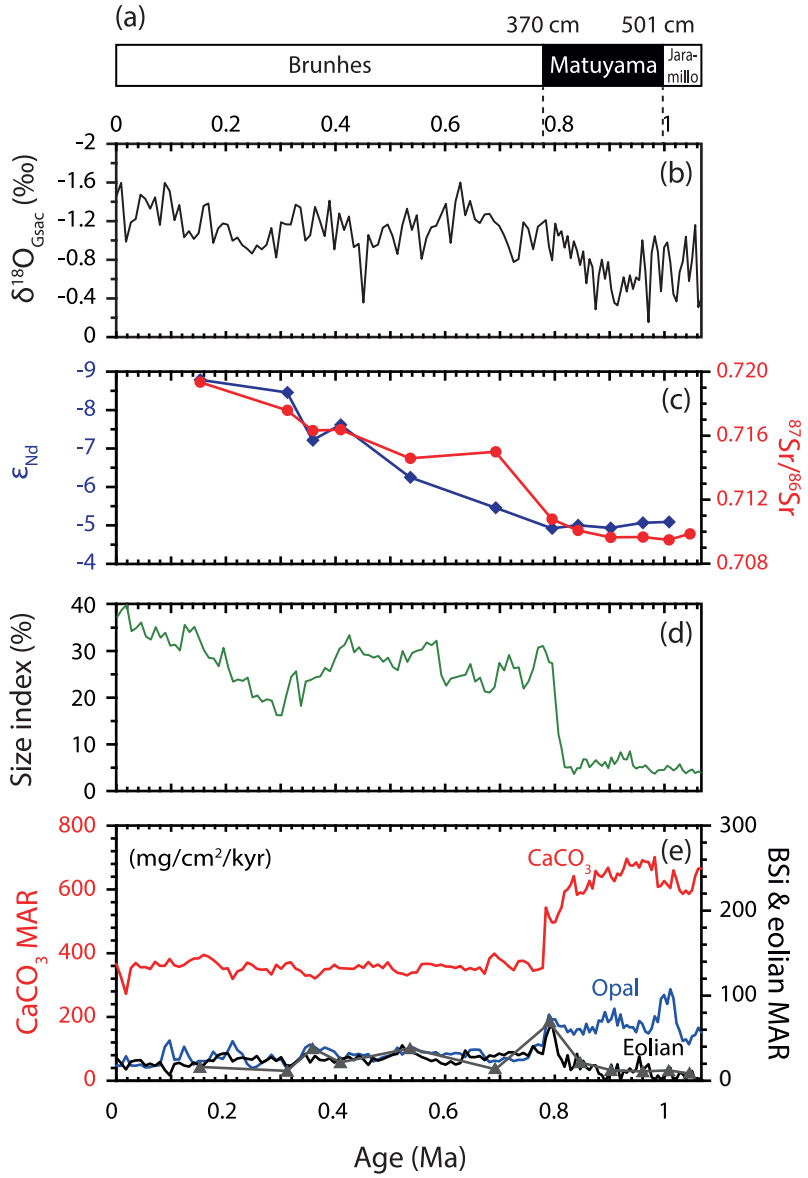

Figure 4-3. (a) Geomagnetic chrons used to define depositional age, (b) Stable oxygen isotope composition ($\delta^{18}O$) of planktic foraminifera *G. sacculifer*, (c) ε_{Nd} and $^{87}Sr/^{86}Sr$ values of the eolian component, (d) Proportion of coarse size fraction (CSF; >63 µm) in the $CaCO_3$ component, and (e) Mass accumulation rates (MARs) of $CaCO_3$ (in red), opalline silica (in blue), and eolian components (in black and gray) in core PC 932. Eolian MAR in black line represents the fractions other than $CaCO_3$ and opal, which show good agreement with eolian content measured using the chemical isolation method (gray triangles).

Table 4-1. Depositional ages and compositions of the studied core, PC 932 (5°53′N, 177°26′W, 4,136 m water depth).

Depth (cm)	Age (kyr)	$\delta^{18}O$ (‰)	Size index (>63 μm, %)	Amount of each composition (wt%)				MAR (mg/cm^2/kyr)				
				Opal	$CaCO_3$	Eolian[a]	Eolian[b]	Bulk	Opal	$CaCO_3$	Eolian[a]	Eolian[b]
0	0.0	-1.46	37.1	4.3	89.1		6.6	411	18	366		27
4	8.8	-1.60	38.8	4.9	89.4		5.7	362	18	324		21
8	17.7	-0.99	39.8	9.2	86.6		4.2	314	29	272		13
12	26.5	-1.19	34.1	4.6	89.8		5.7	393	18	353		22
16	35.4	-1.22	34.9	4.3	89.9		5.8	411	18	369		24
20	44.2	-1.47	36.0	4.8	89.1		6.1	399	19	356		24
24	53.0	-1.43	33.0	4.0	91.4		4.6	390	16	356		18
28	61.9	-1.33	32.3	4.1	90.7		5.2	386	16	350		20
32	70.7	-1.45	35.0	4.4	91.3		4.3	409	18	373		17
36	79.6	-1.16	32.8	4.5	89.9		5.5	401	18	361		22
40	88.4	-1.60	33.8	9.6	87.3		3.1	413	40	360		13
44	97.3	-1.51	31.0	10.8	87.7		1.5	436	47	382		6
48	106.1	-1.21	31.3	6.1	89.1		4.9	406	25	362		20
52	114.9	-1.37	30.0	6.2	88.5		5.2	404	25	357		21
56	123.8	-1.03	35.5	9.5	86.2		4.3	421	40	363		18
60	132.6	-1.10	33.9	6.7	89.3		4.0	420	28	375		17
64	141.5	-1.02	35.1	4.5	90.4		5.1	424	19	383		21
68	150.3	-1.08	32.6	5.5	90.2	3.7	4.3	426	23	384	16	18
72	159.1	-1.36	30.0	5.3	90.5		4.2	436	23	395		18
76	168.0	-1.38	28.4	5.4	89.1		5.6	437	23	389		24
80	176.8	-0.97	28.3	7.8	86.9		5.3	436	34	379		23
84	185.7	-1.12	26.6	6.5	86.4		7.1	423	27	366		30
88	194.5	-1.18	30.6	6.3	85.9		7.8	408	26	351		32
92	203.3	-1.16	26.4	8.3	84.0		7.7	420	35	353		32

Table 4-1. (continued)

Depth (cm)	Age (kyr)	$\delta^{18}O$ (‰)	Size index (>63 μm, %)	Amount of each composition (wt%)				MAR ($mg/cm^2/kyr$)				
				Opal	$CaCO_3$	Eolian[a]	Eolian[b]	Bulk	Opal	$CaCO_3$	Eolian[a]	Eolian[b]
96	212.2	-1.00	23.3	12.0	82.2		5.9	388	47	319		23
100	221.0	-1.03	23.8	8.9	84.7		6.5	405	36	343		26
104	229.9	-0.95	23.5	7.7	85.6		6.7	408	31	349		27
108	238.7	-0.91	24.2	4.8	89.0		6.2	416	20	370		26
112	247.5	-0.86	20.0	3.7	90.2		6.1	403	15	364		25
116	256.4	-0.95	20.4	4.2	88.5		7.3	397	17	351		29
120	265.2	-0.91	19.0	5.4	89.2		5.4	390	21	348		21
124	274.1	-0.96	19.6	6.0	87.9		6.1	398	24	350		24
128	282.9	-1.13	19.2	7.8	85.1		7.1	391	31	333		28
132	291.8	-0.82	16.2	5.9	88.5		5.7	411	24	364		23
136	300.6	-1.19	16.1	6.2	86.9		6.9	404	25	351		28
140	309.4	-1.17	20.4	4.0	91.5	2.7	4.5	402	16	368	11	18
144	318.3	-1.17	24.4	3.8	91.8		4.4	405	16	371		18
148	327.1	-1.37	25.6	5.6	89.0		5.4	395	22	352		22
152	336.0	-1.34	18.1	6.9	86.7		6.4	398	28	345		25
156	344.8	-1.00	23.4	9.8	82.4		7.9	400	39	330		32
160	353.6	-1.05	23.7	10.8	83.8		5.4	395	43	331		22
164	362.5	-1.35	24.2	10.1	82.4	9.6	7.5	389	39	321	38	29
168	371.3	-1.21	24.4	9.0	84.8		6.2	394	35	334		25
172	380.2	-1.04	26.3	9.5	84.7		5.8	413	39	350		24
176	389.0	-1.41	25.6	8.9	84.7		6.4	414	37	350		26
180	397.8	-0.91	28.2	8.1	86.8		5.1	419	34	364		21
184	406.7	-1.28	30.4	6.7	87.0	5.2	6.3	406	27	353	21	26
188	415.5	-1.11	31.2	6.2	87.3		6.5	404	25	353		26

Table 4-1. (continued)

Depth (cm)	Age (kyr)	$\delta^{18}O$ (‰)	Size index (>63 μm, %)	Amount of each composition (wt%)				MAR (mg/cm^2/kyr)				
				Opal	$CaCO_3$	Eolian[a]	Eolian[b]	Bulk	Opal	$CaCO_3$	Eolian[a]	Eolian[b]
192	424.4	-1.25	33.3	7.9	85.3		6.8	412	33	352		28
196	433.2	-0.93	29.6	7.5	86.6		6.0	405	30	351		24
200	442.0	-0.97	30.7	7.5	85.5		7.0	424	32	362		30
204	450.9	-0.36	29.2	7.3	86.6		6.1	409	30	354		25
208	459.7	-1.06	29.0	7.4	88.2		4.4	423	31	373		19
212	468.6	-0.93	28.5	5.6	87.9		6.6	407	23	357		27
216	477.4	-0.96	28.9	6.0	88.3		5.7	413	25	364		24
220	486.3	-1.13	27.6	6.8	86.9		6.3	407	28	354		25
224	495.1	-1.17	28.5	6.8	86.7		6.5	429	29	371		28
228	503.9	-1.05	26.5	7.4	85.1		7.4	411	31	350		31
232	512.8	-0.86	25.8	9.5	82.7		7.7	409	39	339		32
236	521.6	-1.15	29.9	7.5	82.3		10.2	408	31	336		42
240	530.5	-1.33	27.6	9.1	82.5	9.3	8.4	400	36	330	37	34
244	539.3	-1.11	29.5	9.6	82.3		8.1	412	40	339		34
248	548.1	-1.26	30.0	9.1	83.3		7.6	408	37	340		31
252	557.0	-0.81	30.2	7.9	85.6		6.5	427	34	366		28
256	565.8	-1.03	31.7	7.9	86.1		6.1	426	34	367		26
260	574.7	-1.14	31.2	7.7	86.8		5.5	422	32	366		23
264	583.5	-1.15	32.1	8.0	86.0		6.0	419	34	360		25
268	592.3	-1.26	24.7	7.0	88.0		5.0	414	29	364		21
272	601.2	-1.38	22.5	7.8	87.5		4.6	409	32	358		19
280	618.9	-1.40	24.3	8.0	87.3		4.7	405	33	354		19
284	627.7	-1.60	24.6	7.8	87.2		5.0	413	32	360		21
288	636.5	-1.26	24.8	6.8	84.5		8.7	410	28	346		36

Table 4-1. (continued)

Depth (cm)	Age (kyr)	$\delta^{18}O$ (‰)	Size index (>63 μm, %)	Amount of each composition (wt%)				MAR (mg/cm^2/kyr)				
				Opal	$CaCO_3$	Eolian[a]	Eolian[b]	Bulk	Opal	$CaCO_3$	Eolian[a]	Eolian[b]
292	645.4	-1.41	27.1	8.7	84.7		6.7	418	36	353		28
296	654.2	-1.22	23.3	8.9	84.4		6.7	412	37	348		28
300	663.1	-1.18	24.2	8.6	84.4		6.9	421	36	355		29
304	671.9	-1.27	21.2	7.3	86.5		6.2	388	28	336		24
308	680.8	-1.28	21.0	5.0	88.1		6.8	435	22	383		30
312	689.6	-1.19	22.1	5.2	88.4	2.9	6.3	451	24	399	13	29
316	698.4	-1.15	27.3	5.2	87.5		7.3	438	23	383		32
320	707.3	-1.06	25.7	6.2	86.8		7.0	429	27	373		30
324	716.1	-0.93	29.1	6.3	85.7		8.0	418	26	358		34
328	725.0	-0.78	26.2	5.7	86.0		8.2	403	23	347		33
332	733.8	-0.81	26.4	5.7	87.3		7.0	430	25	375		30
336	742.6	-1.19	21.9	5.6	86.8		7.6	433	24	376		33
340	751.5	-1.12	23.4	6.4	86.7		6.9	424	27	368		29
344	760.3	-0.91	26.1	9.4	81.1		9.6	425	40	345		41
348	769.2	-1.14	30.6	10.1	82.0		7.9	425	43	348		34
352	778.0	-1.09	31.0	9.6	83.0		7.4	426	41	354		31
356	783.7	-1.21	29.6	9.6	82.7		7.7	657	63	543		51
360	789.4	-0.94	27.5	11.9	78.8	10.3	9.3	654	78	515	68	61
364	795.0	-0.79	27.3	11.3	78.3		10.4	634	72	496		66
368	800.7	-1.18	19.6	11.7	80.4		7.9	618	72	497		49
372	806.4	-1.05	12.0	10.5	84.6		4.9	619	65	524		31
376	812.1	-1.10	9.0	10.1	85.9		4.0	632	64	543		25
380	817.7	-0.93	5.0	9.6	88.0		2.4	674	65	593		16
384	823.4	-1.05	4.9	8.3	87.3		4.4	687	57	600		30

Table 4-1. (continued)

Depth (cm)	Age (kyr)	$\delta^{18}O$ (‰)	Size index (>63 μm, %)	Amount of each composition (wt%)				MAR ($mg/cm^2/kyr$)				
				Opal	$CaCO_3$	Eolian[a]	Eolian[b]	Bulk	Opal	$CaCO_3$	Eolian[a]	Eolian[b]
388	829.1	-0.82	5.0	8.8	89.4		1.8	688	60	615		13
392	834.8	-0.99	3.5	7.6	90.1		2.3	713	54	642		17
396	840.4	-0.90	4.8	8.9	86.4		4.7	675	60	583		32
400	846.1	-0.75	4.8	9.1	88.8	3.2	2.0	665	61	590	21	14
404	851.8	-0.89	6.7	8.2	88.3		3.5	665	54	587		23
408	857.5	-0.56	6.6	9.8	87.9		2.3	684	67	601		16
412	863.1	-0.81	5.0	8.2	90.0		1.8	697	57	627		13
416	868.8	-0.72	5.7	9.2	88.1		2.6	684	63	603		18
420	874.5	-0.29	6.5	7.6	89.9		2.5	732	56	658		18
424	880.2	-0.64	5.8	9.8	89.0		1.2	724	71	644		9
428	885.8	-0.80	5.3	9.7	89.3		0.9	716	70	639		7
432	891.5	-0.60	6.1	11.1	89.3		0.1	730	81	652		1
436	897.2	-0.78	4.8	9.3	90.0		0.7	743	69	668		5
440	902.9	-0.50	7.1	9.9	87.5	1.6	2.6	730	73	639	12	19
444	908.5	-0.36	5.6	11.8	87.2		1.0	717	85	626		7
448	914.2	-0.33	6.6	8.9	88.5		2.6	734	65	650		19
452	919.9	-0.47	8.2	10.8	89.3		0.1	721	78	644		1
456	925.6	-0.62	6.7	8.4	90.0		1.6	739	62	665		12
460	931.2	-0.47	6.6	8.5	90.3		1.2	771	65	697		9
464	936.9	-0.64	8.4	8.3	89.8		1.9	753	63	676		14
468	942.6	-0.50	5.3	8.4	90.3		1.3	748	63	675		10
472	948.3	-0.62	4.7	7.5	90.7		1.7	755	57	685		13
476	953.9	-0.59	5.1	9.2	87.1		3.7	768	70	669		29
480	959.6	-1.00	5.0	8.7	89.9	1.4	1.4	770	67	692	10	11

Table 4-1. (continued)

Depth (cm)	Age (kyr)	$\delta^{18}O$ (‰)	Size index (>63 μm, %)	Amount of each composition (wt%)				MAR (mg/cm^2/kyr)				
				Opal	$CaCO_3$	Eolian[a]	Eolian[b]	Bulk	Opal	$CaCO_3$	Eolian[a]	Eolian[b]
484	965.3	-0.68	5.4	7.6	90.3		2.1	760	58	687		16
488	971.0	-0.15	4.7	7.3	90.1		2.5	761	56	686		19
492	976.6	-0.87	4.0	8.4	90.9		0.6	727	61	661		5
496	982.3	-1.05	3.6	9.8	90.5		0.1	775	76	701		1
500	988.0	-0.88	4.3	10.1	89.0		0.9	683	69	608		6
504	993.7	-0.47	4.4	13.6	86.3		0.1	709	96	612		1
508	999.4	-0.93	4.4	13.8	85.5		0.7	733	101	627		5
512	1005.0	-0.98	5.3	12.7	86.3	1.6	1.1	713	90	615	12	8
516	1010.7	-0.78	4.9	14.8	83.1		2.1	728	108	605		15
520	1016.4	-0.45	4.3	13.5	92.1		0.1	717	97	660		1
524	1022.1	-0.37	4.7	9.7	90.1		0.3	701	68	632		2
528	1027.7	-0.67	5.6	8.8	89.7		1.5	665	59	597		10
532	1033.4	-0.78	4.3	7.3	91.4		1.3	641	47	586		8
536	1039.1	-1.04	3.7	7.5	92.1		0.3	647	49	596		2
540	1044.8	-0.58	4.2	6.7	91.9	1.2	1.4	637	43	586	8	9
544	1050.4	-0.80	4.5	7.9	90.4		1.7	662	52	598		11
548	1056.1	-1.16	3.7	7.7	92.2		0.0	696	54	642		0
552	1061.8	-0.31	4.1	8.6	91.2		0.3	730	62	665		2
556	1067.5	-0.40	3.8	7.8	91.8		0.4	725	57	666		3

[a,b]Amounts and mass accumulation rates (MARs) of eolian component estimated from the extracted inorganic silicate fraction by following the method of Hovan [1995][a] and by subtracting $CaCO_3$ and opal fractions from 100%[b]. CSF: coarse-sized fraction in $CaCO_3$ (>63 μm, %), following Broecker and Clark [1999].

Table 4-2. $^{87}Sr/^{86}Sr$ and $^{143}Nd/^{144}Nd$ (ε_{Nd}) compositions of lithogenic components of PC 932.

Depth (cm)	Age (kyr)	$^{87}Sr/^{86}Sr$	±2σ SE	$^{143}Nd/^{144}Nd$	±2σ SE	ε_{Nd}
68	150.3	0.719349	0.000013	0.512188	0.000005	-8.79
140	309.4	0.717589	0.000005	0.512204	0.000004	-8.46
164	362.5	0.716321	0.000016	0.512268	0.000004	-7.21
184	406.7	0.716378	0.000021	0.512248	0.000005	-7.62
240	530.5	0.714586	0.000007	0.512318	0.000004	-6.25
312	689.6	0.714993	0.000006	0.512358	0.000003	-5.46
360	789.4	0.710784	0.000009	0.512386	0.000004	-4.92
400	846.1	0.710079	0.000016	0.512382	0.000003	-5.00
440	902.9	0.709643	0.000019	0.512385	0.000004	-4.93
480	959.6	0.709663	0.000015	0.512378	0.000005	-5.07
512	1005.0	0.709487	0.000015	0.512377	0.000009	-5.09
540	1044.8	0.709862	0.000018			

in a ε_{Nd} and $^{87}Sr/^{86}Sr$ crossplot (Figure 4-4).

4.4. Discussion

4.4.1. Cause of shifts in dust provenance, hydrology, and surface productivity

The MARs of the biogenic ($CaCO_3$ and opal) and eolian components of core PC 932 changed significantly across the boundary seen around 0.8 Ma. Furthermore, these changes are synchronous with the shifts in radiogenic isotope compositions (ε_{Nd} and $^{87}Sr/^{86}Sr$) of the eolian components and $\delta^{18}O_{Gsac}$. These findings indicate a fundamental change in the climate state of the central equatorial Pacific, including surface productivity, hydrology, and eolian dust transport pathways.

The ε_{Nd} and $^{87}Sr/^{86}Sr$ compositions of the eolian components show a compositional shift at the 0.8 Ma boundary (Figure 4-4). In the ε_{Nd} and $^{87}Sr/^{86}Sr$ crossplot, samples from the lower interval plot within the south–central Pacific domain and sediments from this region are clustered (Figure 4-4). In contrast, the samples from the upper interval follow a linear trend between the south–central and north–central Pacific domains. Since 0.8 Ma, the ε_{Nd}–$^{87}Sr/^{86}Sr$ composition has progressively evolved towards the north–central Pacific field in the crossplot (Figure 4-4).

The change in the radiogenic isotope composition of eolian dust at 0.8 Ma can be explained by the southward migration of the ITCZ towards the site and its effect on dust transport pathways. The ITCZ acts as a natural barrier to interhemispheric dust transport between the Southern and Northern Hemispheres (SH and NH,

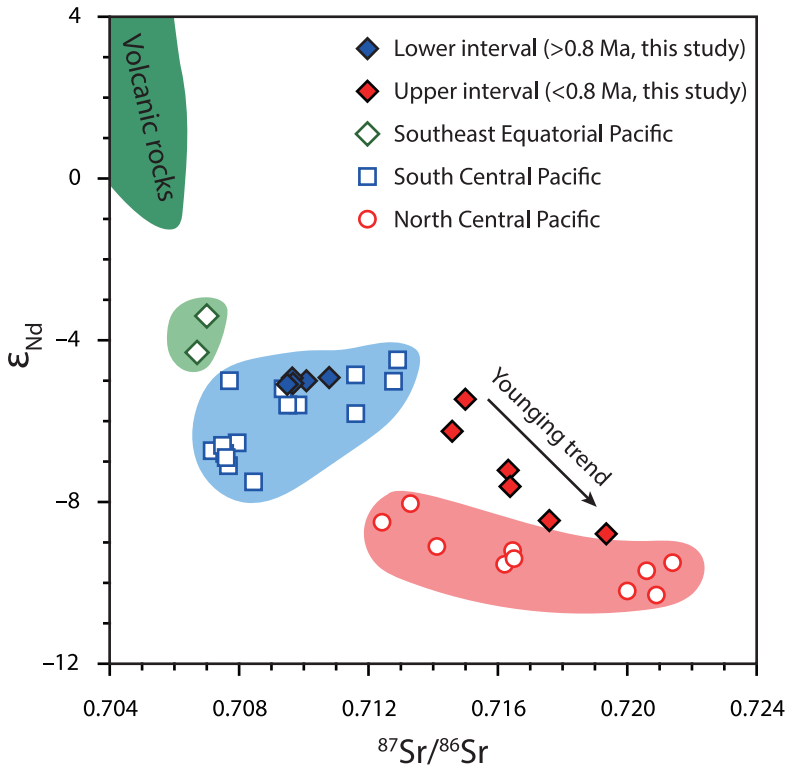

Figure 4-4. Crossplot of ε_{Nd} against $^{87}Sr/^{86}Sr$ from the eolian fraction of core PC 932 together with a compilation of reported values from the Pacific [data from Hyeong et al., 2011; Molina-Kescher et al., 2014; Nakai et al., 1993; Pettke et al., 2002; Stancin et al., 2006; Stancin et al., 2008].

respectively) [*Hovan*, 1995; *Hyeong et al.*, 2011; *Rea*, 1994; *Stancin et al.*, 2006]. As a result, in the central Pacific, dust from the Asian deserts dominates eolian deposition north of the ITCZ, while Australia and Central/South (C/S) America are the primary dust sources to the south of the ITCZ [*Molina-Kescher et al.*, 2014; *Nakai et al.*, 1993; *Rea*, 1994; *Stancin et al.*, 2006]. In regions that lie within the seasonal latitudinal range of the ITCZ, dust is delivered from both hemispheres and the isotopic composition shows a mixed value that tends to be closer to the dustier source region [*Xie and Marcantonio*, 2012].

In light of the dust depositional regime of the Pacific explained above, our data suggest that eolian dust originated from arid lands in the SH (i.e., Australia and C/S America) before 0.8 Ma, and then from both SH and NH (i.e., Asian) deserts after 0.8 Ma. The Asian dust input gradually increased from 0.8 Ma to the present (Figure 4-4), possibly because of the intensification of Asian drying that resulted from uplift of the Tibetan Plateau [e.g., *Cai et al.*, 2012; *Tian et al.*, 2015; *Wang et al.*, 2012]. The dominance of SH dust at the study site before 0.8 Ma indicates that the ITCZ was located to the north of the study site at this time. After 0.8 Ma, however, eolian dust deposited at the study site was supplied from both hemispheres, indicating that the study site might have been located within the seasonal latitudinal range of the ITCZ as it is today. Accordingly, the observed changes in the source signal can be best explained by the southward migration of the southern limit of the ITCZ to the study site at 0.8 Ma. This interpretation is consistent with the increased MAR of the eolian component after 0.8 Ma (Figure 4-3e). This was probably the result of the increased scavenging of dust particles by wet deposition in the ITCZ [e.g., *Hovan*, 1995] and increased supply of dust particles from Asia [*Rea*, 1994; *Tanaka and*

Chiba, 2006].

A southward shift of the ITCZ at 0.8 Ma is also supported by the synchronous shift of $\delta^{18}O_{Gsac}$ to more depleted values. This suggests an increase in the advection of warmer, less saline WPWP water transported by the NECC and increased precipitation at the study site after 0.8 Ma. The MARs of $CaCO_3$ and opal also decrease in the upper interval because of decreased surface production after 0.8 Ma. Based on the microscopic examination of degree of fragmentation of foraminifera tests and the size index, we excluded the possibility of increased $CaCO_3$ dissolution in the upper interval as an explanation because both would indicate more intense dissolution, if any, in the lower interval. Moreover, because of the opposite dissolution thermodynamics and resultant contrasts in preservation potential of these two components in the water column, the simultaneous decrease in MARs of opal and $CaCO_3$ cannot be explained by a change in water chemistry alone, as this would selectively increase the preservation of either opal or $CaCO_3$. The decrease in the MARs of the bulk and biogenic components after 0.8 Ma most probably resulted from a decrease in the supply of nutrients to the surface, which indicates a decrease in the surface production rate.

At the present time, the study site is characterized by oligotrophic open ocean conditions with low nitrate concentrations (<2 μmol/L) [*Le Bouteiller et al.*, 2003]. Advection of relatively nutrient-rich water from the equatorial upwelling region to the site is blocked by the NECC, which transports nutrient-poor WPWP surface water to the study site (Figure 4-2a). The ITCZ and NECC intensify water column stratification, which, together with the associated heavy rainfall, results in nutrient-poor conditions and low surface production. Our results indicate that the nutrient-

poor ocean environment has persisted at the study site since 0.8 Ma. Prior to 0.8 Ma, nutrient-rich water may have made the surface ocean environment relatively fertile as indicated by the biogenic components.

Such conditions could have been generated by a more northerly NECC and ITCZ due to changes in relative intensities of the trades [*Philander et al.*, 1987; *Wang and Wang*, 1999] and/or temperatures of thermocline water originated from the SH high-latitudes [*Dyez and Ravelo*, 2014]. The enhancement of equatorial upwelling would have been possible with a more northerly ITCZ because of the coupled behavior known as the ITCZ-cold tongue complex [*Wang and Wang*, 1999]. In addition, the NECC was probably located to the north of the study site before 0.8 Ma, as its location is coupled with that of the ITCZ [*Donguy and Meyers*, 1996; *Masunaga and L'Ecuyer*, 2010]. The off-equatorial positioning of the NECC and ITCZ before 0.8 Ma probably reduced the influence of nutrient-poor water from the WPWP and facilitated the supply of nutrient-enriched water from the equator to the study site. Thus, we conclude that the most likely cause of the changes in eolian dust provenance, warming and/or freshening of surface water, and decrease in surface productivity after 0.8 Ma was the strengthening of northeast trades relative to its southern counterpart and the resultant southward migration of the ITCZ/NECC.

4.4.2. Movement of ITCZ and the equatorial cooling event during the MPT

It is interesting to note that the southward migration of the ITCZ occurred at the end of the cooling event recorded in the equatorial upwelling regions of the Atlantic and Pacific between 1.1 and 0.8 Ma [*McClymont and Rosell-Melé*, 2005; *Schefuß et*

al., 2003] (Figure 4-1c and -1e). This cooling event is associated with the strengthening of the southeast trades, as indicated by the simultaneous increase in the size of dust particles [*McClymont and Rosell-Melé*, 2005] (Figure 4-1d). As zonal wind strength, ITCZ position, and equatorial upwelling are closely coupled [*Philander et al.*, 1987; *Wang and Wang*, 1999], this cooling event might be explained by increased upwelling and/or cooled thermocline water of tropical regions originated from the SH high-latitudes during the MPT. If the southward migration of the ITCZ recorded at our site at 0.8 Ma was connected to this cooling event peaked at 0.9 Ma (Figure 4-1c and -1d), it would have occurred as part of a continuous migration process occurring concurrently with the warming trend that began at 0.9 Ma and was recorded at 0.8 Ma at the study site. This reasoning further leads us to postulate that the ITCZ migrated northward between 1.1 and 0.9 Ma, and was at its northernmost position around 0.9 Ma, before it moved south. The southward migration of the ITCZ after 0.9 Ma is also supported by the contraction of the northern margin of the WPWP with relatively stable extent of its southern counterpart after around 0.9 Ma, which was attributed to the strengthening of northeast trades relative to southeast trades [*Russon et al.*, 2010]. This scenario is consistent with our $\delta^{18}O_{Gsac}$ data, which become heavier until 0.9 Ma but lighter from then on (Figure 4-3b), indicating that the coldest and/or most saline surface ocean conditions developed around 0.9 Ma; hence, the strongest influence of equatorial upwelling and/or cooling of thermocline water sunken in the SH high latitudes. We can also observe small peaks in the size index and MARs of opal and $CaCO_3$ around 0.9 Ma. The trends, however, are not apparent enough to indicate concomitant increase in productivity, which could have been resulted from the

position of NECC-SEC front being too far north for the site to record any critical change. This aspect requires further in-depth investigation with better defined stratigraphic age model and other productivity proxies such as foraminifera assemblages. Nevertheless of these uncertainties, similar ITCZ movement recorded at Ocean Drilling Project (ODP) site 1077 in the east equatorial Atlantic, off the coast of Africa (Figure 4-2b), discussed in the following paragraph, support our interpretation on northerly position of the ITCZ at ~0.9 Ma.

The east Atlantic upwelling region, where site 1077 is located, is also under the influence of the southeast trades and the ITCZ. The site recorded SST variation almost identical to that of the Pacific, showing a minimum SST at about 0.9 Ma (Figure 4-1e) [*Schefuß et al.*, 2003]. Interestingly, the supply of C_4 plant material mirrors that of SST (Figure 4-1f), indicating the drying of the nearby landmasses during the cooling episode. The drying of central Africa and expansion of C_4 plants, although previously attributed solely to the SST drop [*deMenocal*, 2004; *Schefuß et al.*, 2003], might have resulted from the displacement of the ITCZ to the north until 0.9 Ma and its subsequent southward migration afterward. Consequently, we suggest that the ITCZ migrated northwards until 0.9 Ma, accompanied by a strengthening of the southeast trades, and then moved south until 0.8 Ma. This change in atmospheric circulation could have then induced the cooling event and increase in surface productivity in the equatorial upwelling regions of the Pacific and Atlantic.

As the ITCZ shifts towards the hemisphere with a lowered thermal gradient between equator and pole [*Broccoli et al.*, 2006; *Chiang and Friedman*, 2012; *Flohn*, 1981; *McGee et al.*, 2014], the movement of the ITCZ provides information

on the cooling and warming of one hemisphere relative to the other. The northward migration of the ITCZ from 1.1 to 0.9 Ma suggests that the rate of increase of the pole-to-equator thermal gradient in the SH was greater than that in the NH during this time period, and the opposite movement of the ITCZ between 0.9 and 0.8 Ma suggests greater cooling in the NH than the SH. This proposed cooling history supports the suggestion that the NH ice sheet has expanded significantly and stabilized since 0.9 Ma [*Clark et al.*, 2006; *Clark and Pollard*, 1998; *Hernández-Almeida et al.*, 2012; *McClymont et al.*, 2008].

4.5. Conclusions

The $^{87}Sr/^{86}Sr$ and ε_{Nd} values of the inorganic silicate fraction in core PC 932 obtained from the central equatorial Pacific indicate deposition of dust from Australia and Central/South America before 0.8 Ma, and a gradual increase in Asian dust deposition toward the present after 0.8 Ma. This change in dust provenance was accompanied by increased dust flux and decreased surface productivity and salinity. These changes can be explained by the southward movement and direct influence of the ITCZ and NECC at the study site, which resulted in the input of Asian dust, weakening of equatorial upwelling, and the transport of the warm and less saline WPWP surface water to the site.

The previously published Atlantic data [i.e., *Schefuß et al.*, 2003] related to the drying of central Africa suggests the northward movement of the ITCZ between 1.1 and 0.9 Ma, and the southward movement from then on. The latter is consistent with the migration of the ITCZ recorded at 0.8 Ma at our study site. The ITCZ shifted its

position in-phase with the cooling and warming history recorded in the upwelling regions of the equatorial Pacific and Atlantic, which suggests a close relationship between ITCZ movement and the brief cooling event in the upwelling regions of the Atlantic and Pacific.

As the ITCZ moves towards the hemisphere with the reduced thermal gradient between the pole and equator, the southward movement of the ITCZ from 0.9 Ma indicates greater cooling of the NH than its counterpart. This might have contributed to expansion of the NH ice sheet, which supports the interpretation that the NH ice sheet has expanded significantly and stabilized since 0.9 Ma. The northward migration of the ITCZ from 1.1 to 0.9 Ma suggests that the rate of increase of the pole-to-equator thermal gradient in the SH was greater than that in the NH during this time periods.

CHAPTER 5. CLIMATIC EVOLUTION OF THE CENTRAL EQUATORIAL PACIFIC FOR THE LAST DEGLACIATION PERIOD

Abstract

Sea surface temperature and water column structure during the last deglaciation period were investigated in a central equatorial Pacific site (6°40′N, 177°28′W) using oxygen isotopic compositions ($\delta^{18}O$) and Mg/Ca ratios of three planktic foraminifera species: *G. sacculifer*, *P. obliquiloculata* and *G. tumida* that dwell in the mixed layer, upper thermocline and lower thermocline, respectively. Mg/Ca–derived temperatures for the mixed layer and lower thermocline water mass have varied in a narrow range since 18 ka. In contrast, those of upper thermocline was increased as high as 3°C during the last deglaciation period between 18 and 12 ka and has decreased to and maintained at the present level since 12 ka. Such a temporal variation was associated with simultaneous change of $\delta^{18}O$ in the upper thermocline: decrease between 18 and 12 ka and increase after 12 ka. This observation can be explained by enhanced mixing of the upper ocean and reduced depth separation of habitats between *P. obliquiloculata* and *G. sacculifer* during the 18–12 ka time interval. The time interval showing weak stratification includes two prominent Northern Hemisphere (NH) cooling events, Heinrich Stadial 1 (HS1) and Younger Dryas (YD), characterized by the southerly position of the Intertropical Convergence Zone (ITCZ) due to increased pole to equator temperature gradients in

the NH and resultant intensification of northeast trade winds. The faunal assemblage of planktic foraminifera during the deglaciation period at the study site agrees well with the present faunal assemblage of a subtropical central Pacific site (15°′N) that lies under the strong influence of northeast trade winds and North Equatorial Current (NEC). This suggests a possibility that the study site, now being under the control of ITCZ-North Equatorial Countercurrent, had been positioned north of the ITCZ and under the direct influence of northeast trade winds and NEC during the last deglaciation period.

5.1. Introduction

During the last deglaciation period (ca. 20–8 ka) from the last glacial maximum to the Holocene, global warming was punctuated by two abrupt Northern Hemisphere (NH) cooling events: Heinrich Stadial 1 (HS1; ca. 18–15 ka) and Younger Dryas (YD; 13–11.5 ka). These events are characterized by "bipolar see-saw" [*Broecker*, 1998]: warming in the Southern Hemisphere (SH) and cooling in the NH. The pronounced cooling and drying in NH high latitudes during these episodes had resulted in southward shift of the Intertropical Convergence Zone (ITCZ), a maximum precipitation belt resulted from the convergence of northeast and southeast trade winds [*Gibbons et al.*, 2014; *McGee et al.*, 2014].

Latitudinal displacement of the ITCZ has been suggested as one of the responses of the tropics to a climate forcing on various time scales [*Broccoli et al.*, 2006; *Chao and Chen*, 2001; *Schneider et al.*, 2014]. In particular, climatic anomalies reported in the tropical Pacific, such as reduced river runoffs and weaker Asian and stronger Australian summer monsoon systems, have been attributed to southward migration of the ITCZ during HS1 and YD events [*Gibbons et al.*, 2014; *Leduc et al.*, 2009; *Mohtadi et al.*, 2011; *Partin et al.*, 2007; *Wang et al.*, 2001]. However, these studies were carried out in the western boundary regions of the Pacific where regional precipitation pattern exhibits strong seasonal dependence. Thus, decoupling between consequences of migration of tropical rainfall belt, i.e., ITCZ, and monsoonal effects are often challenging in these regions. Up to date, observations documenting southward migration of the ITCZ during HS1 and YD are absent in remote tropical Pacific where influence of monsoon system is lacking.

This study aims to describe and interpret climate evolution in the eastern boundary region of the Western Pacific Warm Pool (WPWP) in the central equatorial Pacific for the last 23 kyrs in terms of influence of the ITCZ on the region. The central equatorial Pacific near the international dateline is characterized by the narrowest seasonal migration belt of the ITCZ at present. On the contrary, annually averaged position of the ITCZ shows the largest meridional displacement in response to a given change in inter-hemispheric thermal contrast in the modern ocean [*McGee et al.*, 2014]. Such characteristics are advantageous to track its migration over the global climate evolution history. A deep-sea sediment core was obtained from the Magellan Rise located in the central equatorial Pacific (6°40′N, 177°28′W; 3,365 m), where elevated topography above the carbonate compensation depth allows the preservation of relatively high-resolution sedimentary records (Figure 1-3). In this study, temporal variations in temperature and water column structure in the upper ocean are investigated using oxygen isotopic compositions (δ O) and Mg/Ca ratios of three planktonic foraminifera species, *Globigerinoides sacculifer*, *Pulleniatina obliquiloculata*, and *Globorotalia tumida*, each of which dwells in different depth range of water column. This multi-species approach helps understand temperature gradients between the surface and lower part of thermocline. This study reports high resolution proxy data for the last 23 kyrs in the central equatorial Pacific region for the first time and also addresses displacement of the ITCZ during the last deglaciation period and resultant response of the upper water column in the central equatorial Pacific.

5.2. Study Site and Analytical Methods

A 31 cm-long deep-sea sediment core, MC 931, was recovered using a multiple corer from the Magellan Rise in the central equatorial Pacific (6°40′N, 177°28′W; 3,365 m depth) during a cruise carried out by Korea Institute of Ocean Science and Technology (KIOST) in 2009 (Figure 5-1). Surface ocean environment in the study site shows small intra-annual variation. The elevated topography of the Magellan Rise, about 2,000 m shallower than the surrounding basin, prevents hemipelagic sedimentation and provides good preservation of microfossils in association with relatively high rates of accumulation. The core sediment is composed mainly of calcareous ooze containing approximately 90% carbonate, and does not show any recognizable lithologic change stratigraphically. The input of lithogenic materials is considered being dominated by eolian process because of its isolated location from the continents and elevated topography.

The North Equatorial Countercurrent (NECC), whose position is coupled with the ITCZ [*Donguy and Meyers*, 1996; *Masunaga and L'Ecuyer*, 2010], flows over the site and transports warm and low-nutrient surface water to the study site from the WPWP. South of the study site prevails the westward-flowing South Equatorial Current (SEC). Southeast trade winds induce upwelling and bring nutrients to the surface at the Equator, resulting in higher primary production than in the WPWP and NECC regions [*Eldin and Rodier*, 2003; *Le Bouteiller et al.*, 2003].

The chronology of core MC 931 was established with ^{14}C measurements of planktic foraminifera at 5–6, 13–14, 20–21 and 30–31 cm intervals. C was analyzed within an error range less than 60 years using an accelerator mass spectrometry (AMS) at Beta Analytic Radiocarbon Dating Laboratory, USA. Measured radiocarbon age data were corrected for isotopic fractionation and

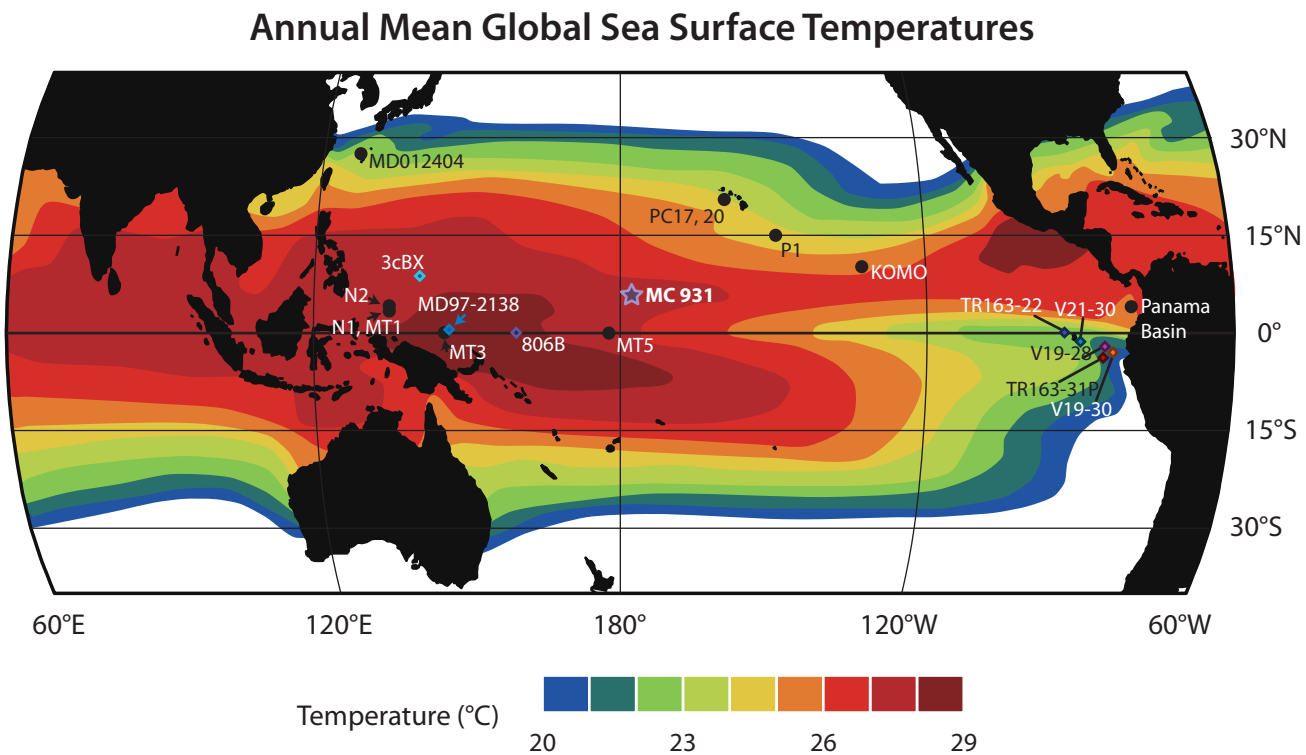

Figure 5-1. Locations of the study site (MC 931), cores with SST records (diamonds), and sites where planktic foraminifera species assemblages are available (solid circles) discussed in the text. Temperature and salinity data are from World Ocean Atlas 2013 [*Locarnini et al.*, 2013; *Zweng et al*., 2013]. Dotted line remarks the region where daily mean precipitation exceeds 7 mm day^{-1}.

calibrated to the calendar year before present (Cal ^{14}C age) using Calib v. 7.0 software [*Stuiver and Reimer*, 1993]. This correction was based on the Marine13 dataset [*Reimer et al.*, 2013] and the local reservoir effect (ΔR) of 9 ± 5 years [*Southon et al.*, 2002].

Three planktic foraminiferal species, *Globigerinoides sacculifer* (without the final sac, 250–355 μm), *Pulleniatina obliquiloculata* (355–425 μm), and *Globorotalia tumida* (355–425 μm), were analyzed for δ^{18}O and Mg/Ca ratios. *G. sacculifer* is known to inhabit in the upper 80 m of water column, but its depth preference varies depending on its growth stages and size classes [*Bijma and Hemleben*, 1994]. In early stage of growth, *G. sacculifer* dwells in the upper photic zone (0–50 m depth) because of small test size (<355 μm in diameter) [*Anand et al.*, 2003; *Bijma and Hemleben*, 1994; *Hemleben et al.*, 1987]. *P. obliquiloculata* dwells in the lower photic zone–upper thermocline (50–100 m depth), and its calcification temperature varies within a small temperature range [*Anand et al.*, 2003]. *G. tumida*, a thermocline-dwelling species, calcifies below the seasonal thermocline (100–250 m depth) [*Fairbanks and Wiebe*, 1980; *Farmer et al.*, 2007]. Following the depth habitats of these three species estimated in the WPWP region by *Sagawa et al.* [2012], calcification temperatures and seawater δ^{18}O of *G. sacculifer*, *P. obliquiloculata*, and *G. tumida* are considered to represent those of the mixed layer, upper thermocline and lower thermocline, respectively.

Stable oxygen isotope compositions (δ^{18}O) were determined using a Finnigan MAT 251 mass spectrometer at the University of Michigan at Ann Arbor, USA. The 1-sigma standard deviation of the repeat analyses of the reference material (NBS-19; National Bureau of Standards) was 0.09‰ (n = 24). Mg/Ca ratios were determined

using an inductively coupled plasma optical emission spectrophotometer (ICP-OES) (Perkin-Elmer Optima 3300 DV) at the Korea Institute of Ocean Science and Technology, Ansan, Korea. For Mg/Ca measurements, 20–30 monospecific tests were crushed and homogenized, and subsequently cleaned with methanol (clay removal), NaOH-buffered hydrogen peroxide (removal of organic matter) and a weak acid (removal of high-Mg calcite) following *Barker et al.* [2003]. Concentration of Ca and Mg were measured from the spectral lines at 407.776 and 279.553 nm, respectively. Instrumental drift was corrected according to *Schrag* [1999]. The analytical error of Mg/Ca, based on replicate measurements of ECRM 752-1 standard (Bureau of Analyzed Samples, Ltd) was 0.2 mmol/mol (1 s.d., n=61), which corresponds to temperature error of ~0.5°C.

5.3. Results

The age model of MC 931 core was established with ^{14}C measurement (Table 5-1). The core was deposited at a rate of 1.35 cm/kyr for approximately 23 kyrs, which covers the entire last deglaciation period.

Down-core $\delta^{18}O$ and Mg/Ca results of three species are shown in Table 5-2 and Figure 5-2a and -2b, respectively. $\delta^{18}O$ compositions of *G. sacculifer* (-1.36 ± 0.46‰; n=30, 1 σ), *P. obliquiloculata* (-0.73 ± 0.47‰; n=31, 1 σ), and *G. tumida* (0.48 ± 0.39‰; n=29, 1 σ) agree in general with those of the previously reported values in the WPWP center [*Sagawa et al.*, 2012] with minor offsets that likely reflect temperature and salinity differences between the two sites. The determined Mg/Ca ratios of *G. sacculifer* (3.93 ± 0.32; n=30, 1 σ) and *G. tumida* (1.72 ± 0.16;

Table 5-1. Radiocarbon ages of planktic foraminifera in MC 931.

Depth	AMS ^{14}C Ages (yr)	Error (yr)	Calendar Ages
5	6910	30	7420
13	11710	40	13190
20	15250	50	18040
30	19130	60	22560

Table 5-2. Stable oxygen isotope ($\delta^{18}O$) and Mg/Ca compositions of *G. sacculifer*, *P. obliquiloculata* and *G. tumida* and Mg/Ca-derived seawater temperature using equations provided by *Sadekov et al.* [2009].

Depth (cm)	Age (ka)	*G. sacculifer*			*P. obliquiloculata*			*G. tumida*		
		$\delta^{18}O$ (‰)	Mg/Ca (mmol/mol)	T (°C)	$\delta^{18}O$ (‰)	Mg/Ca (mmol/mol)	T (°C)	$\delta^{18}O$ (‰)	Mg/Ca (mmol/mol)	T (°C)
0.5	0.7	-1.9	4.04	26.3	-0.89	2.87	21.7	0.64	1.77	15.5
1.5	2.0	-0.9	4.05	26.3	-1.03	2.72	21.0	1.10	1.74	15.2
2.5	3.4	-1.7	4.11	26.5	-0.51	2.56	20.2	0.01	2.01	17.2
3.5	4.7	-1.8	4.38	27.4	-0.89	2.82	21.5	0.88	1.92	16.5
4.5	6.1	-2.0	4.15	26.6	-0.99	2.59	20.4	0.19	1.83	15.9
5.5	7.4	-1.3	3.88	25.7	-0.52	2.78	21.3	-0.23	1.50	13.3
6.5	8.1	-1.6	3.74	25.2	-1.09	2.60	20.4	0.36	1.81	15.7
7.5	8.9	-0.9	4.08	26.4	-0.76	3.04	22.5	0.04	1.90	16.4
8.5	9.6	-1.9	4.13	26.6	-1.27	2.54	20.1	-0.09	2.02	17.2
9.5	10.3	-1.6	4.21	26.8	-1.02	2.40	19.4	0.64	1.84	16.0
10.5	11.0	-1.4	4.09	26.4	-1.12	2.73	21.1	-0.17	1.66	14.6
11.5	11.7	-2.0	3.90	25.8	-0.96	2.66	20.7	1.03	1.70	14.9
12.5	12.5	-1.6	4.35	27.2	-1.32	2.87	21.7	0.81	1.56	13.7
13.5	13.2	-1.7	4.27	27.0	-1.65	2.51	20.0	0.25	1.80	15.7
14.5	13.9	-1.1	4.01	26.2	-0.98	3.21	23.3	0.51	1.79	15.6
15.5	14.6	-1.9	3.93	25.9	-1.06	3.25	23.4	0.48	1.54	13.6

Table 5-2. (continued)

Depth (cm)	Age (ka)	*G. sacculifer*			*P. obliquiloculata*			*G. tumida*		
		$\delta^{18}O$ (‰)	Mg/Ca (mmol/mol)	T (°C)	$\delta^{18}O$ (‰)	Mg/Ca (mmol/mol)	T (°C)	$\delta^{18}O$ (‰)	Mg/Ca (mmol/mol)	T (°C)
16.5	15.3	-0.8	4.15	26.6	-0.74	3.04	22.5	0.03	1.93	16.6
17.5	16.0	-2.2	3.99	26.1	-1.01	2.73	21.1	0.06	1.63	14.4
18.5	16.7	-1.1	4.24	26.9	-1.19	3.45	24.2	0.44	1.63	14.3
19.5	17.3	-1.5	3.65	24.9	-0.92	3.00	22.3	0.65	1.59	14.0
20.5	18.0	-1.1	4.17	26.7	-0.60	2.18	18.1	0.68	1.75	15.3
21.5	18.5	-0.5	3.76	25.3	-0.71	2.86	21.7	1.00	1.79	15.6
22.5	18.9	-0.9	3.80	25.5	-0.74	2.28	18.7	0.90	1.67	14.7
23.5	19.4	-1.5	3.91	25.8	-0.23	2.40	19.4	0.36	1.53	13.5
24.5	19.8	-1.3	4.01	26.2	0.20	2.75	21.2	0.66	2.00	17.1
25.5	20.3	-0.9	3.57	24.6	0.18	2.45	19.7	0.97	1.54	13.6
26.5	20.8	-1.3	3.41	24.0	-0.22	2.45	19.7	0.87	1.81	15.8
27.5	21.2	-0.7	3.00	22.3	-0.19	2.54	20.1	0.77	1.43	12.6
28.5	21.7	-1.4	3.57	24.6	-0.67	2.60	20.4	0.35	1.60	14.1
29.5	22.1	-0.6	3.42	24.0	-0.21	2.25	18.5	0.90	1.50	13.3
30.5	22.6	-0.8	3.26	23.4	0.37	2.35	19.1	0.48	1.71	15.0

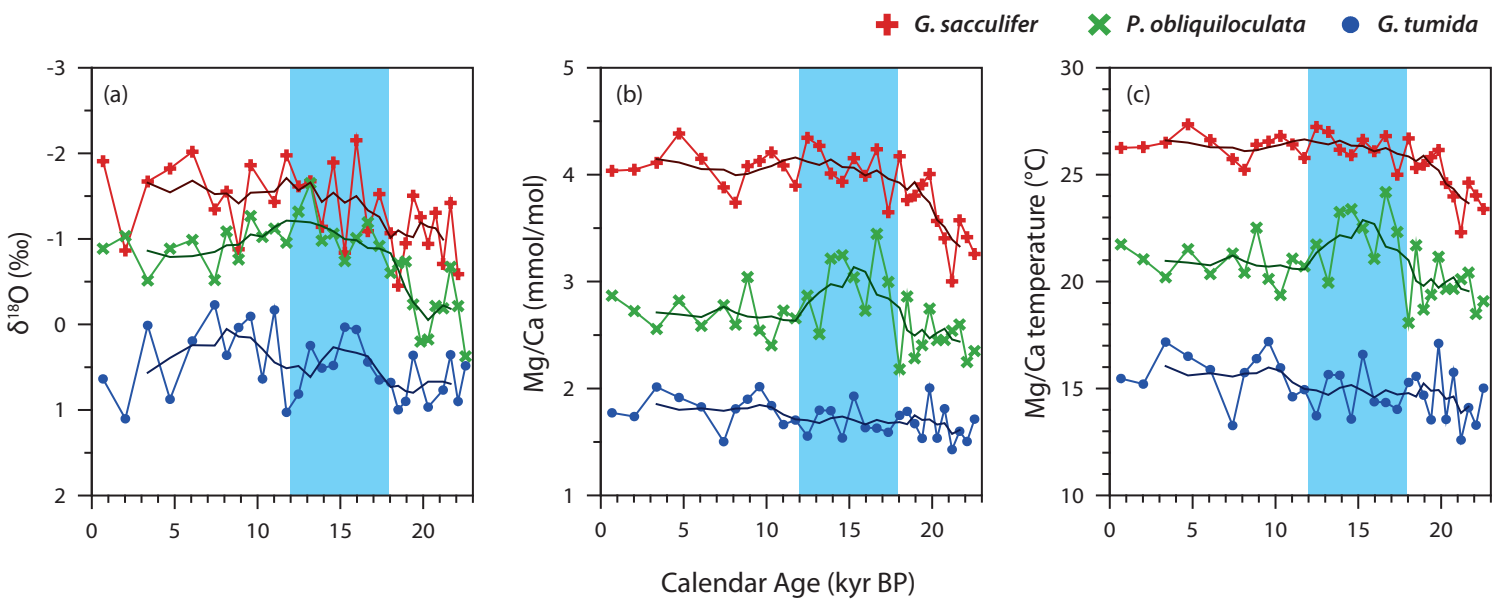

Figure 5-2. Analytical results of foraminiferal (a) $\delta^{18}O$ (a) and (b) Mg/Ca compositions of three species, and (c) Mg/Ca-derived calcification temperatures converted using equations provided in *Sadekov et al.* [2009]. Shades mark the time interval with reduced compositional gradient between species.

n=30, 1 σ) are similar to those (~ 3.8 and ~ 1.8, respectively, raw data not provided) of the WPWP center, but those of *P. obliquiloculata* (2.69 ± 0.30; n=31, 1 σ) are higher than those (~ 1.8, raw data not provided) of the WPWP center [*Sagawa et al.*, 2012].

5.4. Discussion

5.4.1. Estimation of calcification depth and temperature of three planktic foraminifer species

To estimate the calcification depth of planktic foraminifera species of interest, calcite $\delta^{18}O$–depth relationship was established at the study site using the theoretical equation between $\delta^{18}O$ of seawater and temperature [*Kim and O'Neil*, 1997], in which $\delta^{18}O$ of seawater was calculated from the salinity–$\delta^{18}O$ relationship of surface and subsurface water in the central tropical Pacific [*Conroy et al.*, 2014] and the optimum interpolation temperature and salinity were taken at 6.5°N, 177.5°W from World Ocean Atlas 2013 [*Locarnini et al.*, 2013; *Zweng et al.*, 2013] (Figure 5-3).

With the projection of an average late Holocene (<6 ka) $\delta^{18}O$ composition of each planktic foraminifera species to the established calcite $\delta^{18}O$ – depth relationship, calcification depth of each species was estimated to be 70-100 m for *G. sacculifer*, 120-140 m for *P. obliquiloculata*, and 160-200 m depth for *G. tumida* (Figure 5-3c). The predicted depths are slightly deeper than, but largely consistent with, previously reported depth habitats of three species estimated in the center of WPWP; 40-80 m for *G. sacculifer*, 100-130 m for *P. obliquiloculata*, and 140-180 m depth for *G.*

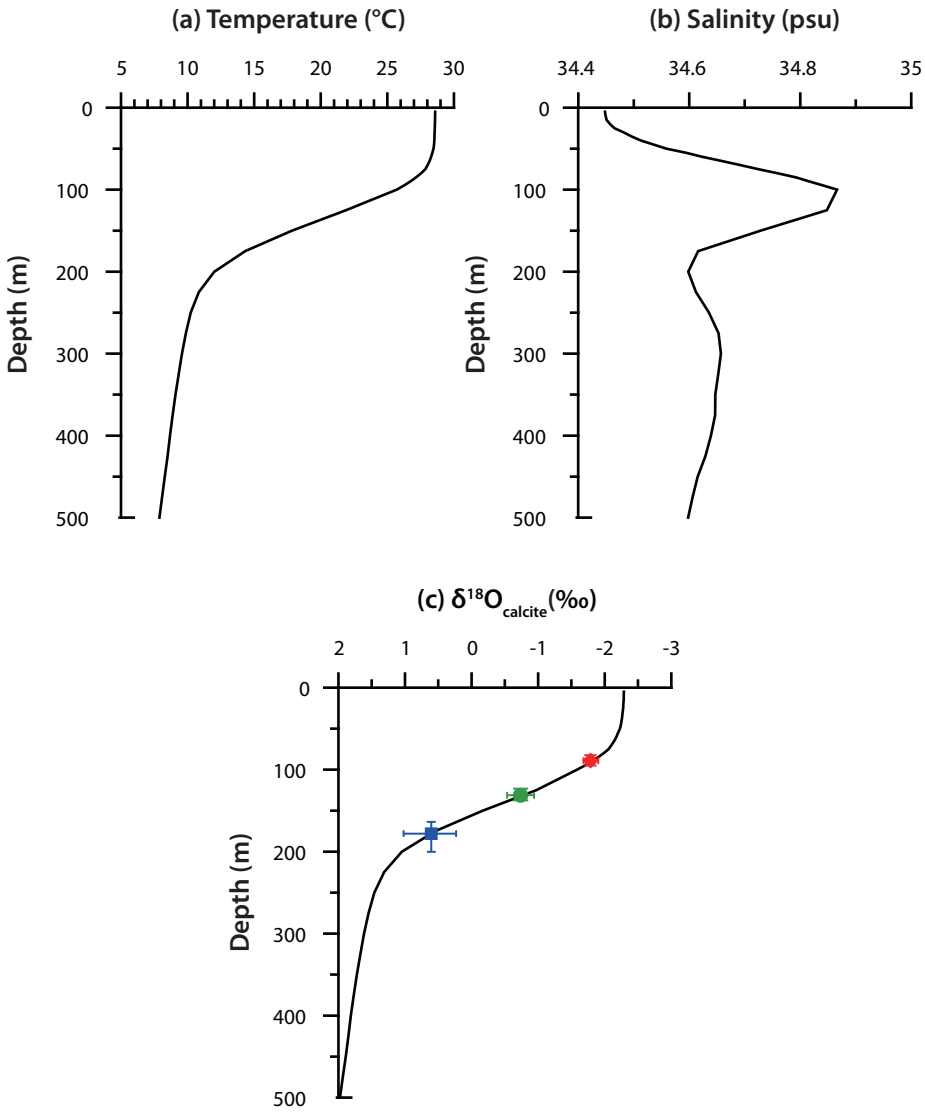

Figure 5-3. Depth profile of annual mean of optimum interpolated (OI) temperature (a) and salinity (b) records provided in World Ocean Atlas 2013 [*Locarnini et al.*, 2013; *Zweng et al.*, 2013]. (c) The estimated calcification depths of three species by comparison of an average $\delta^{18}O$ composition of late Holocene (<6 ka) planktic foraminifera species with the predicted calcite $\delta^{18}O$ (see text for details): *G. sacculifer* (red), *P. obliquiloculata* (green) and *G. tumida* (blue).

tumida [*Sagawa et al.*, 2012].

The calcification temperature (T) of planktic foraminifera is often expressed as Mg/Ca = b × exp(a × T), where a is an exponential constant and b is a pre-exponential constant [*Lea et al.*, 1999; *Nürnberg et al.*, 1996]. However, the effect of seawater salinity on foraminiferal calcite Mg/Ca has been argued as a cause for basin-dependent difference of calibration equation [*Anand et al.*, 2003; *Ferguson et al.*, 2008; *Nürnberg et al.*, 1996]. To avoid such complexity, a generalized equation that account for salinity variation was used to obtain calcification temperature in this study [*Sadekov et al.*, 2009]:

$$\text{Mg/Ca (mmol/mol)} = \exp[0.057(\pm0.012) \times S(\text{psu}) + 0.075(\pm0.006) \times T\ (°C) - 2.56(\pm0.46)],$$

where S and T are seawater salinity and temperature at habitat depth, respectively. The equation was established for *G. sacculifer* and *P. obliquiloculata* in the Western Pacific, but it was also applied to *G. tumida* as there has been no successful establishment of core-top calibration equation for *G. tumida* to date in the Pacific.

The Mg/Ca-derived calcification temperatures of three planktic foraminifera species for the late Holocene (<6 ka) were estimated to be 26.6°C (±0.4), 21.0°C (±0.7), and 16.0°C (±0.8) for *G. sacculifer*, *P. obliquiloculata*, and *G. tumida*, respectively at present. These temperatures are encountered at depths of 90 m, 130 m, and 160 m, respectively, at the study site; thus the Mg/Ca-derived temperature of each species represents that of the mixed layer, upper thermocline, and lower thermocline, respectively (Figure 5-3). These results are consistent with the

aforementioned calcification depths of three species derived from $\delta^{18}O$: 70-100 m for *G. sacculifer*, 120-140 m for *P. obliquiloculata*, and 160-200 m depth for *G. tumida*. Such consistent results indicate reliability of the estimated temperatures in this study.

5.4.2. Change in upper water column structure during the last deglaciation period

Mg/Ca–derived temperatures of the mixed layer and lower thermocline do not change much after 18 ka (Figure 5-2c). In contrast, upper thermocline temperatures were increased as high as 3°C during the last deglaciation period between 18 and 12 ka and were dropped and maintained to the present level since 12 ka (Figure 5-2c). It suggests that the vertical temperature gradient of dwelling depths between *P. obliquiloculata* and *G. sacculifer* was reduced during the 18–12 ka period, but that between *G. sacculifer* and *G. tumida* has not been changed in the same period. The observed trends during the last deglaciation period could have resulted from either increase of temperature at the dwelling depth and/or change in habitat depth of *P. obliquiloculata*.

The increase in deglacial subsurface water temperature could have been attained by the warming of thermocline water mass. Indeed, warming of intermediate water that upwells in the equatorial region is indicated by several observations during the last deglaciation period. Rapid increase of air temperatures was observed as early as 19 ka in the source region (Southern Hemisphere high latitudes) of equatorial intermediate water [*Bostock et al.*, 2013; *Calvo et al.*, 2007]. Concomitant increases of SSTs are also reported in the upwelling regions of East Equatorial Pacific (EEP)

[*Koutavas et al.*, 2002; *Martinez-Boti et al.*, 2015] (Figure 5-4). In addition, $\delta^{18}O$ of benthic foraminifera collected in the EEP at depths influenced by Subantarctic Mode Water and Antarctic Intermediate Water has decreased since 18 ka, simultaneously with rising temperatures in the Antarctica [*Bova et al*., 2015]. Such phenomenon was interpreted as a result of enhanced influence of warmer and less dense Antarctic Intermediate Water produced by melting of sea ice and poleward shift of the southern Westerly winds during the HS1 and YD [*Bova et al*., 2015]. All these observations support a possibility for warming of intermediate water that upwells in the equatorial region.

A hypothesis of sequential warming from deep thermostad water to thermocline water, however, cannot be applied to the study site. If it is the case, lower thermocline temperature, represented by Mg/Ca ratio of *G. tumida*, should have been increased simultaneously with that of the upper thermocline, but it had remained stable throughout the study period (Figure 5-2c). Despite the simultaneous increases of air temperatures [*Parrenin et al.*, 2013], surface ocean temperature [*Lamy et al.*, 2004; *Romero et al.*, 2006], and the intermediate water temperature [*Bova et al.*, 2015; *Pena et al.*, 2013] in the SH at this time, the well-developed thick mixed layer to the north of equator could have prevented the penetration of SH-sourced intermediate water to the upper ocean at the study site.

Interestingly, the difference between $\delta^{18}O$ compositions of *G. sacculifer* and *P. obliquiloculata* was decreased simultaneously with decrease in Mg/Ca temperature difference between them from 18 to 12 ka. It suggests that increase in calcification temperature of *P. obliquiloculata* had been accompanied by shallowing of the maximum population depth of *P. obliquiloculata* during this period. Although *P.*

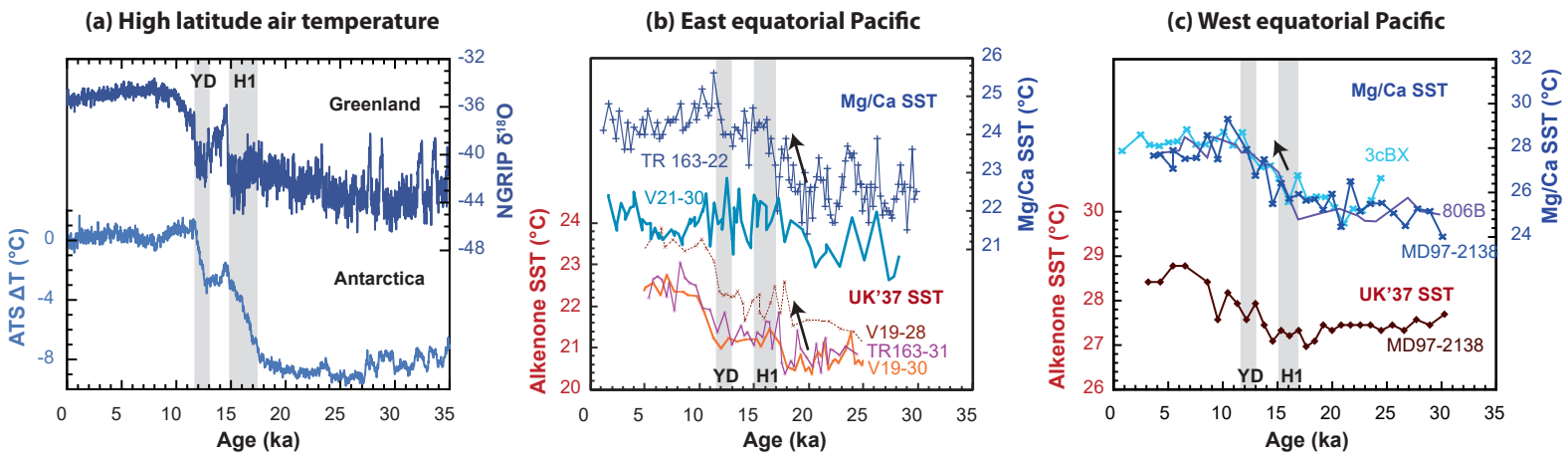

Figure 5-4. Compilation of published dataset showing deglacial warming. (a) Air temperatures from Greenland (NGRIP $\delta^{18}O$ on GICC05 × 1.0063 chronology [*North Greenland Ice Core Project members*, 2004]) and Antarctica ice cores (Antarctic Temperature Stack (ATS) [*Parrenin et al.*, 2013] in degrees Celsius relative to the present day on AICC12 × 1.0063 chronology [*Veres et al.*, 2013]). Foraminifera Mg/Ca and $U^{K'}_{37}$ SST (b) in the east equatorial Pacific [*Dubois et al.*, 2009; *Koutavas et al.*, 2002; *Koutavas and Sachs*, 2008; *Lea et al.*, 2006] and (c) in the west equatorial Pacific [*de Garidel-Thoron et al.*, 2007; *Sagawa et al.*, 2012; *Wara et al.*, 2003].

obliquiloculata occurs in tropical-subtropical subsurface water mainly at a depth range of 60–150 m [*Cléroux et al.*, 2008; *Erez and Honjo*, 1981; *Farmer et al.*, 2007], previous studies indicated wide variations in its habitat depth. In the tropical Pacific, for examples, the maximum population depth range of *P. obliquiloculata* was estimated at 100–140 m from its $\delta^{18}O$ composition in the western Pacific [*Patrick and Thunell*, 1997; *Sagawa et al.*, 2012; this study], but at 30–100 m in the eastern Pacific [*Rincón-Martínez et al.*, 2011]. Especially, depth habitats of *G. sacculifer* and *P. obliquiloculata* were reported being indistinguishable in the tropical eastern Pacific [*Rincón-Martínez et al.*, 2011].

Indistinguishable separation of depth habitats between these two foraminiferal species in the EEP is likely due to the weaker stratification of the upper water column. The density gradient in the EEP region gentler than its western counterpart makes water column structure and vertical zonation of planktic foraminifera unstable since the depth habitat of a foraminifera species primarily depends on density of water column. The separation of depth habitats between species can be lessened in a weakly stratified upper ocean condition [*Caromel et al.*, 2014; *Coxall et al.*, 2000; *Rashid and Boyle*, 2007]. Thus, the depth habitat of *P. obliquiloculata* at the study site could have overlapped with that of *G. sacculifer* under such conditions. This possibility is supported by other thermocline-dwelling species (*Globorotalia menardii* and *Neogloboquadrina dutetrei*) that show similar depth habitat variations across the tropical Pacific [*Patrick and Thunell*, 1997]. The lower thermocline inhabiting species, *G. tumida*, is known to dwell below the photic zone, mostly deeper than 100–150 m depth, and therefore does not show strong spatial variation in the habitat depth [*Rincón-Martínez et al.*, 2011; *Sagawa et al.*, 2012].

Therefore, during the time period between 18 and 12 ka, the increase of calcification temperature of *P. obliquiloculata*, which is unique among others, resulted most likely from shallowing of depth habitat, which suggests the weakly stratified upper water column structure at the study site during the time period between 18 and 12 ka.

5.4.4. Response of central equatorial Pacific to inter-hemispheric thermal asymmetry during the last deglaciation period

The weakening of upper ocean stratification from 18 to 12 ka without associated warming of deep thermocline water could have resulted from the enhanced wind-driven mixing. The study site today is positioned beneath the ITCZ, characterized by high precipitation, weak wind strength and buyout surface watermass. The meridional displacement of the ITCZ from its present position would have exposed the site under the influence of either northeast or southeast Trades, which likely brings about enhanced mixing of surface water column. It also aided to relax the strong water column stratification by placing the site out of intense precipitation zone.

Climate evolution history suggests the southward displacement of the ITCZ during the last deglaciation period. The early warming of SH high latitudes relative to NH counterpart [see *Denton et al.*, 2010 and references therein] resulted in a decreased pole-to-equator temperature gradient in SH. Especially, the interhemispheric thermal asymmetry between SH and NH became intensified significantly during the NH cooling events (i.e., HS1 and YD) [*Barker et al.*, 2009; *Denton et al.*, 2010; *McGee et al.*, 2014; *Stenni et al.*, 2011]. Such strong

asymmetric high latitude thermal forcing induced the southward displacement of the ITCZ through atmospheric teleconnection, which has been documented in many field observations [*Haug et al.*, 2001; *Mohtadi et al.*, 2011; *Montade et al.*, 2015; *Peterson et al.*, 2000] and model simulations (Figure 5-5) [*Gibbons et al.*, 2014; *McGee et al.*, 2014]. These studies documenting southward shift of the ITCZ and strengthening of northeast trade winds during the HS1 and YD strongly suggest the possibility that the ITCZ had been positioned south of the study site during these two episodes. As a result, the study site was likely under the influence of intensified northeast trade winds, which likely led to less stratified upper ocean structure by wind-driven mixing.

The temporal changes in faunal assemblages of planktic foraminifera in the studied core [*Lee*, 2015] supports this interpretation. The foraminifera in the study core are dominated by warm water species (e.g., *G. glutinata*, *G. ruber*, *G. sacculifer*, *P. obliquiloculata*, and *G. rubescens*) for the last 23 kyrs with increasing significance of warm oligotrophic WPWP species (*G. sacculifer* and *P. obliquloculata*) during the Holocene (Figure 5-6). It is noteworthy of the increase in abundance of *G. rubescens* during the last deglaciation period (ca. 18–12 ka) as it is rare in tropical Pacific at present and its high abundance was only reported in a sediment trap (Station P1, ~15°N) and core records (PC17 and PC20, ~21°N) from the subtropical Central Pacific near the Hawaii Islands (Figure 5-1) [*Lee et al.*, 2001; *Thunell and Honjo*, 1981]. The spatial occurrences of *G. rubescens* indicate its preference to more off-equatorial oligotrophic ocean condition. Interestingly, planktic foraminifera assemblages at these subtropical sites also show close resemblance to those at the study site during the last deglaciation period (Figure 5-

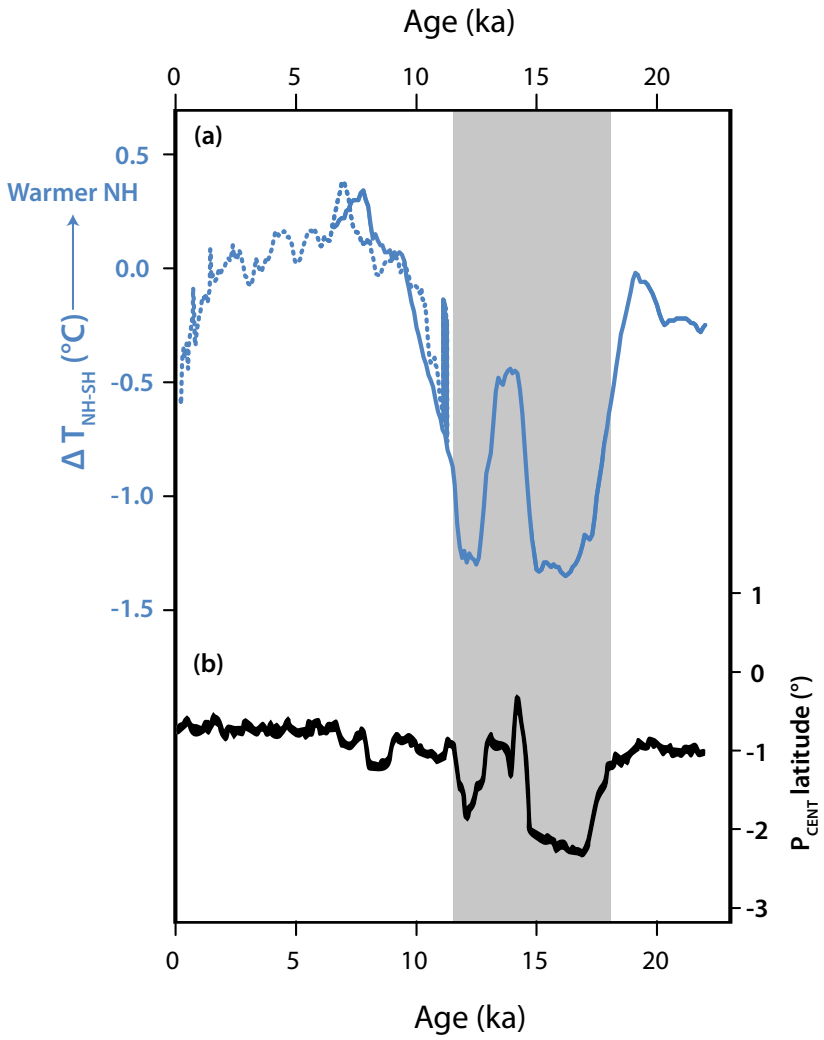

Figure 5-5. Relationship between interhemispheric temperature gradient and ITCZ position (adopted and modified from *McGee et al.* [2014]). (a) Reconstructed inter-hemisphere surface temperature gradients (area-weighted mean NH surface temperature minus area-weighted SH surface temperature), solid line: *Shakun et al.* [2012] and dashed line: *Marcott et al.* [2013]). (b) Changes in mean ITCZ position (P_{CENT}: latitude of maximum precipitation) in the TraCE-21 ka simulation by *McGee et al.* [2014].

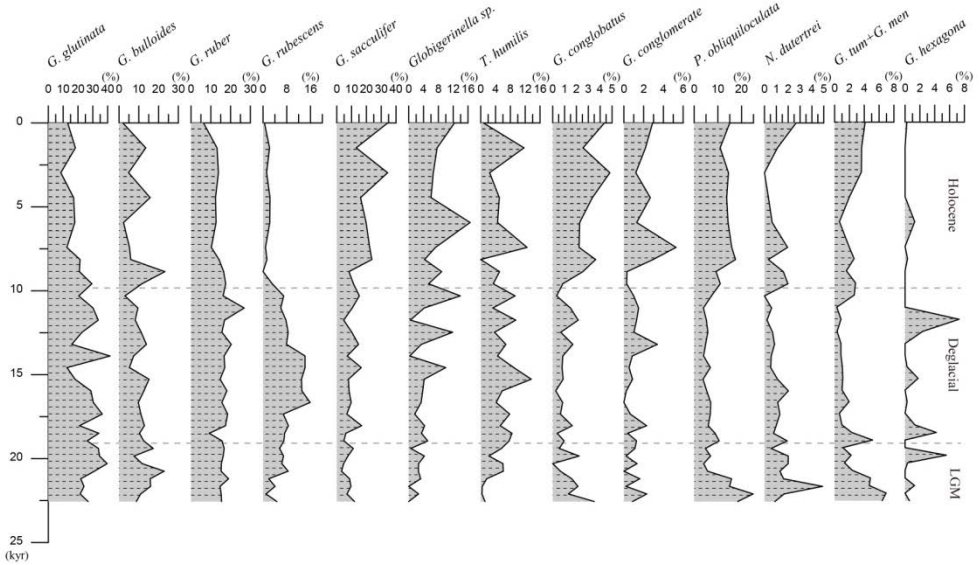

Figure 5-6. Faunal assemblage of planktic foraminifera in MC 931 sediment (modified from *Lee* [2015])

7): dominance of *G. glutinata* and *G. rubescens* with minor contribution of *G. sacculifer*. In contrast, faunal assemblages of the Holocene reveal closer affinity to those of the WPWP region (Figure 5-7). Thus, it can be postulated that the surface ocean condition at the study site during the last deglaciation period was similar to that in North Equatorial Current (NEC) region that is affected by strong northeast trade winds and characterized by weaker upper ocean stratification. To sum up, the surface ocean condition at the study site during the last deglaciation period was under the influence of northeast trade winds and NEC, which can be attributed to displacement of the ITCZ and NECC south to the study site.

The results of this study do not resolve the Bølling-Allerød episode of brief NH warming from HS1 and YD (Figure 5-2c); instead the record shows a broad high temperature bulge between 18 and 12 ka when these three events happened. This is likely due to the low temporal resolution (~1 ka) of the present data not enough to resolve such short term variability. After 12 ka, the upper ocean might have been stratified to the present level by the reduced interhemispheric thermal contrast than the preceding time interval and resultant migration of the ITCZ to its present position. Accordingly, it is interpreted that the present oceanographic and atmospheric conditions of the study site, influenced by the ITCZ and NECC, have been likely established at 12 ka with NH warming.

5.5. Conclusions

Changes in upper ocean temperature and water column structure in the central equatorial Pacific were investigated for the last deglaciation period using Mg/Ca

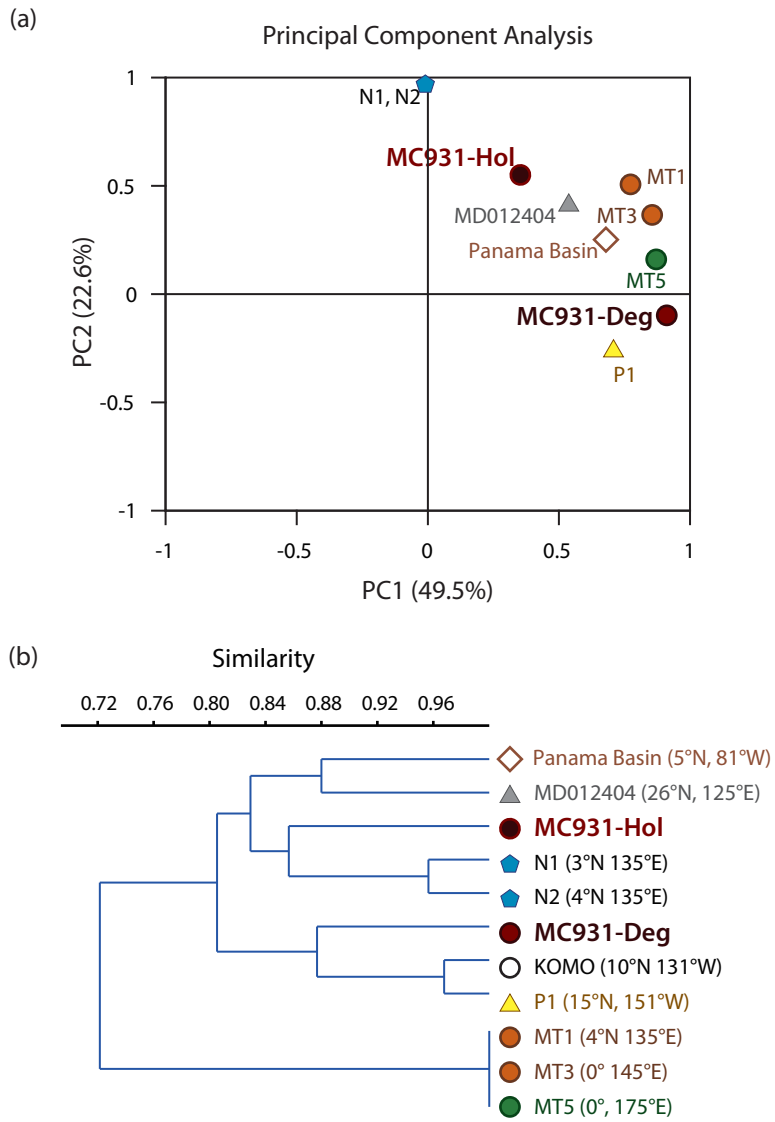

Figure 5-7. (a) Principal component and (b) cluster analyses on foraminifera assemblages determined for tropical and subtropical Pacific sediments. Data are from [*Chang et al.*, 2008; *Kawahata et al.*, 2002; *Lee et al.*, 2001; *Lee*, 2015; *Lee et al.*, 2014; *Thunell and Honjo*, 1981; *Thunell and Reynolds*, 1984; *Yamasaki et al.*, 2008]

and $\delta^{18}O$ compositions of three planktic foraminifera species. Comparison of the measured $\delta^{18}O$ with the predicted calcite $\delta^{18}O$ indicated the calcification depth of 70-100 m for *G. sacculifer*, 120-140 m for *P. obliquiloculata,* and 160-200 m depth for *G. tumida* during the late Holocene: thus Mg/Ca-derived temperatures of each species represents those of the mixed layer, upper thermocline, and lower thermocline, respectively.

Mg/Ca–derived temperatures for the mixed layer and lower thermocline do not change much after 18 ka. In contrast, upper thermocline temperatures had increased as high as 3°C during the last deglaciation period between 18 and 12 ka and has dropped and maintained to the present level since 12 ka. It suggests that the vertical temperature gradient between the dwelling depths of *P. obliquiloculata* and *G. sacculifer* was smaller during the last deglaciation period than before and after without changes in the lower thermocline temperatures. This phenomenon can be explained only with the poor separation of depth habitats between two species, resulted from weakening of water column stratification above the upper part of thermocline.

The observed weakening of stratification at the study site had occurred during the last deglaciation period that includes HS1 and YD, climatic aberrations characterized by NH cooling caused by NH ice sheet collapse and the subsequent weakening of the Atlantic Meridional Overturning Circulation. The NH cooling at these two events was associated with southerly location of the ITCZ due to increased pole to equator temperature gradients in the NH and resultant intensification of northeast trade winds. The faunal assemblage of planktic foraminifera at the study site during the last deglaciation period is similar to those

of North Equatorial Current region influenced by northeast trade winds. It suggests displacement of the ITCZ south to the study site during the deglaciation period. Influence of northeast trade winds and NEC at the site during the last deglaciation period likely had caused relaxed upper water stratification and lessened separation of depth habitats between foraminifera species due to wind-driven mixing. However, low temporal resolution (~1 ka) of the presented data does not allow resolving between the two cooling episodes (HS1 and YD) and a brief warming episode (Bølling-Allerød) in between. This interpretation leads to a conclusion that the ITCZ was positioned south of the study site during the last deglaciation and that the study site was under the influence of northeast trade winds that prevails north of the ITCZ.

CHAPTER 6. SUMMARY AND CONCLUSIONS

Despite the importance of the central equatorial Pacific in the global climate, understanding of ocean environment in the past is highly inadequate because of the paucity of sedimentary archives. By using the sediment cores acquired at the seamounts in the deep-sea basin, evolution of climate and its forcing mechanisms were investigated using various geochemical proxies in biogenic and lithogenic components across the mid-Pleistocene Transition (MPT, 1.2–0.8 Ma) and for the last 23 kyrs in the central equatorial Pacific. The acquisition of sedimentary archives for late Quaternary allows better understanding of changes in mean state of tropical Pacific by comparison with various proxy data available in the center of western Pacific Warm Pool (WPWP) and eastern Pacific Cold Tongue (EPCT).

For the last 600 kyr, eolian mineral dust deposited in the northwest Pacific, represented by a sediment core (12°30’N, 135°00’E) from the Philippine Sea, has been supplied predominantly from the central Asian deserts (e.g., Taklimakan desert). In contrast, eolian mineral dust deposited in a central equatorial Pacific site (5°53’N, 177°26’W) shows Australian/South American affinity before 0.8 Ma but gradually increasing Asian dust contribution after 0.8 Ma. Such change in dust provenance was accompanied by an increased dust flux and decrease in surface productivity and salinity. These changes can be best explained by the southward movement of the Intertropical Convergence Zone (ITCZ) and North Equatorial Counter Current (NECC) and the direct influence of these features on the site after 0.8 Ma. The southward movement of the ITCZ is in phase with the warming trend

observed in upwelling regions of the equatorial Pacific and Atlantic between 0.9 and 0.8 Ma. The southward movement of the ITCZ from 0.9 to 0.8 Ma indicates more significant cooling in the Northern Hemisphere (NH) than in the Southern Hemisphere, which is supportive of the interpretation that the NH ice sheet expanded significantly and stabilized after 0.9 Ma.

For the last deglacial period, water column structure and temperatures were investigated in the central equatorial Pacific (6°40′N, 177°28′W) from a multiple-core by using oxygen isotopic compositions and Mg/Ca ratios of three planktic foraminifer species (*G. sacculifer, P. obliquiloculata*, and *G tumida*) that dwell in mixed layer, upper thermocline, and lower thermocline, respectively.

Contrast to stable Mg/Ca–derived temperatures for mixed layer and lower thermocline since 18 ka, upper thermocline temperatures increased as high as 3°C during the last deglaciation between 18 and 12 ka, and has dropped to the present level of temperature since then. It can be explained by weakening of water column stratification in the upper part of thermocline and shallowing of *P. obliquiloculata* habitat at this time. Such change coincides the period of decreased pole to equator temperature gradients in the SH and following NH cooling events, the Heinrich Stadial 1 (HS1) and Younger Dryas (YD), resulting in intensification of northeast Trades and southward migration of the ITCZ. Intensified wind-driven mixing and reduced precipitation during the last deglacial period likely had caused relatively nutrient-rich surface water condition without a significant surface cooling and migration of *P. obliquiloculata* to shallower depth. This interpretation leads to a conclusion that the ITCZ was placed far south to the study site during the last deglaciation and the study site was influenced by northeast Trades that prevails

north of the ITCZ.

As exemplified by the evolution across the MPT, sea-air interaction (ITCZ movement–cooling/warming of intermediate water source region) forced from the high latitudes could result in the oceanographic change in the central equatorial Pacific. During the last deglaciation, especially during the HS 1 and YD, southward shift of the ITCZ due to NH high latitude thermal forcing exposed the northern part of central equatorial Pacific under the influence of the intensified northeast Trades and created less stratified surface water environments by wind-driven mixing. These results highlight the coupled behavior of ITCZ and surface oceanography in the central equatorial Pacific.

References

An, Z. (2000), The history and variability of the East Asian paleomonsoon climate, *Quaternary Science Reviews*, *19*(1–5), 171-187, doi:10.1016/S0277-3791(99)00060-8.

Anand, P., H. Elderfield, and M. H. Conte (2003), Calibration of Mg/Ca thermometry in planktonic foraminifera from a sediment trap time series, *Paleoceanography*, *18*(2), 1050, doi:10.1029/2002PA000846.

Arnold, E., J. Merrill, M. Leinen, and J. King (1998), The effect of source area and atmospheric transport on mineral aerosol collected over the North Pacific Ocean, *Global and Planetary Change*, *18*(3–4), 137-159, doi:10.1016/S0921-8181(98)00013-7.

Asahara, Y., T. Tanaka, H. Kamioka, and A. Nishimura (1995), Asian continental nature of $^{87}Sr/^{86}Sr$ ratios in north central Pacific sediments, *Earth and Planetary Science Letters*, *133*(1-2), 105-116.

Ashok, K., S. K. Behera, S. A. Rao, H. Weng, and T. Yamagata (2007), El Niño Modoki and its possible teleconnection, *Journal of Geophysical Research: Oceans*, *112*(C11), C11007, doi:10.1029/2006JC003798.

Aston, S. R., R. Chester, L. R. Johnson, and R. C. Padgham (1973), Eolian dust from the lower atmosphere of the eastern Atlantic and Indian Oceans, China Sea and Sea of Japan, *Marine Geology*, *14*(1), 15-28, doi:10.1016/0025-3227(73)90040-6.

Barker, S., P. Diz, M. J. Vautravers, J. Pike, G. Knorr, I. R. Hall, and W. S. Broecker (2009), Interhemispheric Atlantic seesaw response during the last deglaciation, *Nature*, *457*(7233), 1097-1102, doi:10.1038/nature07770.

Barker, S., M. Greaves, and H. Elderfield (2003), A study of cleaning procedures used for foraminiferal Mg/Ca paleothermometry, *Geochemistry, Geophysics, Geosystems*, *4*(9), 8407, doi:10.1029/2003GC000559.

Beaufort, L., T. de Garidel-Thoron, B. Linsley, D. Oppo, and N. Buchet (2003),

Biomass burning and oceanic primary production estimates in the Sulu Sea area over the last 380 kyr and the East Asian monsoon dynamics, *Marine Geology, 201*(1–3), 53-65, doi:10.1016/S0025-3227(03)00208-1.

Bian, Y., Z. Jian, C. Weng, W. Kuhnt, T. Bolliet, and A. Holbourn (2011), A palynological and palaeoclimatological record from the southern Philippines since the Last Glacial Maximum, *Chin. Sci. Bull., 56*(22), 2359-2365, doi:10.1007/s11434-011-4573-1.

Bijma, J., and C. Hemleben (1994), Population dynamics of the planktic foraminifer Globigerinoides sacculifer (Brady) from the central Red Sea, *Deep Sea Research Part I: Oceanographic Research Papers*, *41*(3), 485-510, doi:10.1016/0967-0637(94)90092-2.

Biscaye, P. E. (1965), Mineralogy and Sedimentation of Recent Deep-Sea Clay in the Atlantic Ocean and Adjacent Seas and Oceans, *Geological Society of America Bulletin*, *76*(7), 803-832, doi:10.1130/0016-7606.

Biscaye, P. E., and E. J. Dasch (1971), The rubidium, strontium, strontium-isotope system in deep-sea sediments: Argentine Basin, *Journal of Geophysical Research*, *76*(21), 5087-5096, doi:10.1029/JC076i021p05087.

Blank, M., M. Leinen, and J. M. Prospero (1985), Major Asian aeolian inputs indicated by the mineralogy of aerosols and sediments in the western North Pacific, *Nature*, *314*(6006), 84-86, doi:10.1038/314084a0.

Bory, A. J. M., W. Abouchami, S. J. G. Galer, A. Svensson, J. N. Christensen, and P. E. Biscaye (2013), A Chinese Imprint in Insoluble Pollutants Recently Deposited in Central Greenland As Indicated by Lead Isotopes, *Environmental Science & Technology*, *48*(3), 1451-1457, doi:10.1021/es4035655.

Bory, A. J. M., P. E. Biscaye, A. Svensson, and F. E. Grousset (2002), Seasonal variability in the origin of recent atmospheric mineral dust at NorthGRIP, Greenland, *Earth and Planetary Science Letters*, *196*(3–4), 123-134, doi:10.1016/S0012-821X(01)00609-4.

Bostock, H. C., et al. (2013), A review of the Australian–New Zealand sector of the

Southern Ocean over the last 30 ka (Aus-INTIMATE project), *Quaternary Science Reviews*, *74*, 35-57, doi:10.1016/j.quascirev.2012.07.018.

Bova, S. C., T. Herbert, Y. Rosenthal, J. Kalansky, M. Altabet, C. Chazen, A. Mojarro, and J. Zech (2015), Links between eastern equatorial Pacific stratification and atmospheric CO_2 rise during the last deglaciation, *Paleoceanography*, n/a-n/a, doi:10.1002/2015PA002816.

Boyer, T. P., et al. (2013), *World Ocean Database 2013*, 209 pp., Silver Spring, MD, doi:10.7289/V5NZ85MT.

Broccoli, A. J., K. A. Dahl, and R. J. Stouffer (2006), Response of the ITCZ to Northern Hemisphere cooling, *Geophysical Research Letters*, *33*(1), L01702, doi:10.1029/2005GL024546.

Broecker, W. S., and E. Clark (1999), CaCO3 size distribution: A paleocarbonate ion proxy?, *Paleoceanography*, *14*(5), 596-604, doi:10.1029/1999PA900016.

Cai, M., X. Fang, F. Wu, Y. Miao, and E. Appel (2012), Pliocene–Pleistocene stepwise drying of Central Asia: Evidence from paleomagnetism and sporopollen record of the deep borehole SG-3 in the western Qaidam Basin, NE Tibetan Plateau, *Global and Planetary Change*, *94–95*, 72-81, doi:10.1016/j.gloplacha.2012.07.002.

Calvo, E., C. Pelejero, P. De Deckker, and G. A. Logan (2007), Antarctic deglacial pattern in a 30 kyr record of sea surface temperature offshore South Australia, *Geophysical Research Letters*, *34*(13), L13707, doi:10.1029/2007GL029937.

Caromel, A. G. M., D. N. Schmidt, J. C. Phillips, and E. J. Rayfield (2014), Hydrodynamic constraints on the evolution and ecology of planktic foraminifera, *Marine Micropaleontology*, 106, 69-78, doi:10.1016/j.marmicro.2014.01.002.

Chaisson, W. P., and A. C. Ravelo (2000), Pliocene development of the east-west hydrographic gradient in the equatorial Pacific, *Paleoceanography*, *15*(5), 497-505, doi:10.1029/1999PA000442.

Chang, Y.-P., W.-L. Wang, Y. Yokoyama, H. Matsuzaki, H. Kawahata, and M.-T. Chen (2008), Millennial-Scale Planktic Foraminifer Faunal Variability in the East China Sea during the Past 40000 Years (IMAGES MD012404 from the Okinawa Trough), *Terrestrial, Atmospheric and Oceanic Sciences*, 19(4), 389-401.

Chao, W. C., and B. Chen (2001), The Origin of Monsoons, *Journal of the Atmospheric Sciences*, *58*(22), 3497-3507, doi:10.1175/1520-0469.

Chen, J., G. Li, J. Yang, W. Rao, H. Lu, W. Balsam, Y. Sun, and J. Ji (2007), Nd and Sr isotopic characteristics of Chinese deserts: Implications for the provenances of Asian dust, *Geochimica et Cosmochimica Acta*, *71*(15), 3904-3914, doi:10.1016/j.gca.2007.04.033.

Cheong, C.-s., J.-S. Ryu, and Y.-J. Jeong (2013), Simultaneous multiple collector-ICP-MS measurement of Nd isotopic composition and Sm/Nd ratio in geological reference materials by interference corrections and external calibration using matrix-matched standards, *Geoscience Journal*, *17*(4), 389-395, doi:10.1007/s12303-013-0056-5.

Chester, R., H. Elderfield, J. J. Griffin, L. R. Johnson, and R. C. Padgham (1972), Eolian dust along the eastern margins of the Atlantic Ocean, *Marine Geology*, *13*(2), 91-105, doi:10.1016/0025-3227(72)90048-5.

Chiang, J. C. H., and A. R. Friedman (2012), Extratropical Cooling, Interhemispheric Thermal Gradients, and Tropical Climate Change, *Annual Review of Earth and Planetary Sciences*, *40*(1), 383-412, doi:10.1146/annurev-earth-042711-105545.

Clark, P. U., D. Archer, D. Pollard, J. D. Blum, J. A. Rial, V. Brovkin, A. C. Mix, N. G. Pisias, and M. Roy (2006), The middle Pleistocene transition: characteristics, mechanisms, and implications for long-term changes in atmospheric pCO_2, *Quaternary Science Reviews*, *25*(23–24), 3150-3184, doi:10.1016/j.quascirev.2006.07.008.

Clark, P. U., and D. Pollard (1998), Origin of the Middle Pleistocene Transition by ice sheet erosion of regolith, *Paleoceanography*, *13*(1), 1-9,

doi:10.1029/97PA02660.

Cléroux, C., E. Cortijo, P. Anand, L. Labeyrie, F. Bassinot, N. Caillon, and J.-C. Duplessy (2008), Mg/Ca and Sr/Ca ratios in planktonic foraminifera: Proxies for upper water column temperature reconstruction, *Paleoceanography*, *23*(3), PA3214, doi:10.1029/2007PA001505.

Cole, T. G., and H. F. Shaw (1983), The nature and origin of authigenic smectites in some Recent marine sediments, *Clay Minerals*, *18*(3), 239-252, doi:10.1180/claymin.1983.018.3.02.

Conroy, J. L., K. M. Cobb, J. Lynch-Stieglitz, and P. J. Polissar (2014), Constraints on the salinity–oxygen isotope relationship in the central tropical Pacific Ocean, *Marine Chemistry*, *161*, 26-33, doi:10.1016/j.marchem.2014.02.001.

Corliss, B. H., and C. D. Hollister (1982), A paleoenvironmental model for Cenozoic sedimentation in the central North Pacific, in *The Ocean Floor-Bruce Heezen Commemorative Volume*, edited by R. A. Scrutton and M. Talwani, pp. 277-304, Wiley J., New York, U.S.A.

Coxall, H. K., P. N. Pearson, N. J. Shackleton, and M. A. Hall (2000), Hantkeninid depth adaptation: An evolving life strategy in a changing ocean, *Geology*, 28(1), 87-90, doi:10.1130/0091-7613(2000)28<87:hdaael>2.0.co;2.

Defant, M. J., R. Maury, J.-L. Joron, M. D. Feigenson, J. Leterrier, H. Bellon, D. Jacques, and M. Richard (1990), The geochemistry and tectonic setting of the northern section of the Luzon arc (The Philippines and Taiwan), *Tectonophysics, 183*(1–4), 187-205, doi:10.1016/0040-1951(90)90416-6.

de Garidel-Thoron, T., Y. Rosenthal, F. Bassinot, and L. Beaufort (2005), Stable sea surface temperatures in the western Pacific warm pool over the past 1.75 million years, *Nature, 433*(7023), 294-298, doi:10.1038/nature03189.

de Garidel-Thoron, T., Y. Rosenthal, L. Beaufort, E. Bard, C. Sonzogni, and A. C. Mix (2007), A multiproxy assessment of the western equatorial Pacific hydrography during the last 30 kyr, *Paleoceanography*, *22*(3), PA3204, doi:10.1029/2006PA001269.

DeMaster, D. J. (1981), The supply and accumulation of silica in the marine

environment, *Geochimica et Cosmochimica Acta*, *45*(10), 1715-1732, doi:10.1016/0016-7037(81)90006-5.

deMenocal, P. B. (2004), African climate change and faunal evolution during the Pliocene–Pleistocene, *Earth and Planetary Science Letters*, *220*(1–2), 3-24, doi:10.1016/S0012-821X(04)00003-2.

Denton, G. H., R. F. Anderson, J. R. Toggweiler, R. L. Edwards, J. M. Schaefer, and A. E. Putnam (2010), The Last Glacial Termination, *Science*, *328*(5986), 1652-1656, doi:10.1126/science.1184119.

DiNezio, P. N., and J. E. Tierney (2013), The effect of sea level on glacial Indo-Pacific climate, *Nature Geosci*, *6*(6), 485-491, doi:10.1038/ngeo1823.

Ding, Z., T. Liu, N. W. Rutter, Z. Yu, Z. Guo, and R. Zhu (1995), Ice-Volume Forcing of East Asian Winter Monsoon Variations in the Past 800,000 Years, *Quaternary Research*, *44*(2), 149-159, doi:10.1006/qres.1995.1059.

Dixon, T. H., and R. J. Stern (1983), Petrology, chemistry, and isotopic composition of submarine volcanoes in the southern Mariana arc, *Geological Society of America Bulletin*, *94*(10), 1159-1172, doi:10.1130/0016-7606.

Donguy, J.-R., and G. Meyers (1996), Mean annual variation of transport of major currents in the tropical Pacific Ocean, *Deep Sea Research Part I: Oceanographic Research Papers*, *43*(7), 1105-1122, doi:10.1016/0967-0637(96)00047-7.

Dubois, N., M. Kienast, C. Normandeau, and T. D. Herbert (2009), Eastern equatorial Pacific cold tongue during the Last Glacial Maximum as seen from alkenone paleothermometry, *Paleoceanography*, *24*(4), PA4207, doi:10.1029/2009PA001781.

Dyez, K. A., and A. C. Ravelo (2014), Dynamical changes in the tropical Pacific warm pool and zonal SST gradient during the Pleistocene, *Geophysical Research Letters*, *41*(21), 7626-7633, doi:10.1002/2014GL061639.

Elderfield, H., P. Ferretti, M. Greaves, S. Crowhurst, I. N. McCave, D. Hodell, and A. M. Piotrowski (2012), Evolution of Ocean Temperature and Ice Volume Through the Mid-Pleistocene Climate Transition, *Science*, *337*(6095), 704-

709, doi:10.1126/science.1221294.

Eldin, G., and M. Rodier (2003), Ocean physics and nutrient fields along 180° during an El Niño–Southern Oscillation cold phase, *Journal of Geophysical Research: Oceans*, *108*(C12), 8137, doi:10.1029/2000JC000746.

Erez, J., and S. Honjo (1981), Oxygen and Carbon Isotopes in Foraminifera Comparison of isotopic composition of planktonic foraminifera in plankton tows, sediment traps and sediments, *Palaeogeography, Palaeoclimatology, Palaeoecology*, *33*(1), 129-156, doi:10.1016/0031-0182(81)90035-3.

Fairbanks, R. G., and P. H. Wiebe (1980), Foraminifera and Chlorophyll Maximum: Vertical Distribution, Seasonal Succession, and Paleoceanographic Significance, *Science*, *209*(4464), 1524-1526, doi:10.1126/science.209.4464.1524.

Farmer, E. C., A. Kaplan, P. B. de Menocal, and J. Lynch-Stieglitz (2007), Corroborating ecological depth preferences of planktonic foraminifera in the tropical Atlantic with the stable oxygen isotope ratios of core top specimens, *Paleoceanography*, *22*(3), PA3205, doi:10.1029/2006PA001361.

Feldberg, M. J., and A. C. Mix (2002), Sea-surface temperature estimates in the Southeast Pacific based on planktonic foraminiferal species; modern calibration and Last Glacial Maximum, *Marine Micropaleontology*, *44*(1–2), 1-29, doi:10.1016/S0377-8398(01)00035-4.

Feng, J.-L., L.-P. Zhu, X.-L. Zhen, and Z.-G. Hu (2009), Grain size effect on Sr and Nd isotopic compositions in eolian dust: Implications for tracing dust provenance and Nd model age, *Geochemical Journal*, *43*(2), 123-131, doi:10.2343/geochemj.1.0007.

Ferguson, J. E., G. M. Henderson, M. Kucera, and R. E. M. Rickaby (2008), Systematic change of foraminiferal Mg/Ca ratios across a strong salinity gradient, *Earth and Planetary Science Letters*, *265*(1–2), 153-166, doi:10.1016/j.epsl.2007.10.011.

Ferrat, M., D. J. Weiss, S. Strekopytov, S. Dong, H. Chen, J. Najorka, Y. Sun, S. Gupta, R. Tada, and R. Sinha (2011), Improved provenance tracing of Asian

dust sources using rare earth elements and selected trace elements for palaeomonsoon studies on the eastern Tibetan Plateau, *Geochimica et Cosmochimica Acta*, *75*(21), 6374-6399, doi:10.1016/j.gca.2011.08.025.

Flohn, H. (1981), A hemispheric circulation asymmetry during Late Tertiar, *Geologische Rundschau*, *70*(2), 725-736, doi:10.1007/BF01822146.

Folk, R. L. (1974), *The Petrology of Sedimentary Rocks* Hemphill, Austin, TX.

Ford, H. L., A. C. Ravelo, and P. J. Polissar (2015), Reduced El Niño–Southern Oscillation during the Last Glacial Maximum, *Science*, *347*(6219), 255-258, doi:10.1126/science.1258437.

Gagan, M. K., E. J. Hendy, S. G. Haberle, and W. S. Hantoro (2004), Post-glacial evolution of the Indo-Pacific Warm Pool and El Niño-Southern oscillation, *Quaternary International*, *118–119*, 127-143, doi:10.1016/S1040-6182(03)00134-4.

Gibbons, F. T., D. W. Oppo, M. Mohtadi, Y. Rosenthal, J. Cheng, Z. Liu, and B. K. Linsley (2014), Deglacial $\delta^{18}O$ and hydrologic variability in the tropical Pacific and Indian Oceans, *Earth and Planetary Science Letters*, *387*, 240-251, doi:10.1016/j.epsl.2013.11.032.

Gill, A. E. (1983), An Estimation of Sea-Level and Surface-Current Anomalies during the 1972 El Niño and Consequent Thermal Effects, *Journal of Physical Oceanography*, *13*(4), 586-606, doi:10.1175/1520-0485.

Gingele, F. X., and P. De Deckker (2004), Fingerprinting Australia's rivers with clay minerals and the application for the marine record of climate change, *Australian Journal of Earth Sciences*, *51*(3), 339-348, doi:10.1111/j.1400-0952.2004.01061.x.

Gingele, F. X., P. De Deckker, and C.-D. Hillenbrand (2001), Clay mineral distribution in surface sediments between Indonesia and NW Australia — source and transport by ocean currents, *Marine Geology*, *179*(3–4), 135-146, doi:10.1016/S0025-3227(01)00194-3.

Glaccum, R. A., and J. M. Prospero (1980), Saharan aerosols over the tropical North Atlantic — Mineralogy, *Marine Geology*, *37*(3–4), 295-321,

doi:10.1016/0025-3227(80)90107-3.

Griffin, J. J., H. Windom, and E. D. Goldberg (1968), The distribution of clay minerals in the World Ocean, *Deep Sea Research and Oceanographic Abstracts*, *15*(4), 433-459.

Grousset, F. E., P. E. Biscaye, A. Zindler, J. Prospero, and R. Chester (1988), Neodymium isotopes as tracers in marine sediments and aerosols: North Atlantic, *Earth and Planetary Science Letters*, *87*(4), 367-378, doi:10.1016/0012-821X(88)90001-5.

Grousset, F. E., M. Parra, A. Bory, P. Martinez, P. Bertrand, G. Shimmield, and R. M. Ellam (1998), Saharan wind regimes traced by the Sr–Nd isotopic composition of subtropical Atlantic sediments: last glacial maximum vs. today, *Quaternary Science Reviews*, *17*(4–5), 395-409, doi:10.1016/S0277-3791(97)00048-6.

Harrison, K. G. (2000), Role of increased marine silica input on paleo-pCO_2 levels, *Paleoceanography*, *15*(3), 292-298, doi:10.1029/1999PA000427.

Haug, G. H., K. A. Hughen, D. M. Sigman, L. C. Peterson, and U. Röhl (2001), Southward Migration of the Intertropical Convergence Zone Through the Holocene, *Science*, *293*(5533), 1304-1308, doi:10.1126/science.1059725.

Head, M. J., and P. L. Gibbard (2005), Early-Middle Pleistocene Transitions: an overview and recommendation for the defining boundary, in *Early-Middle Pleistocene Transitions: The Land–Ocean Evidence*, edited by M. J. Head and P. L. Gibbard, pp. 1-18, The Geological Society of London, London, UK.

Held, I. M., and B. J. Soden (2006), Robust Responses of the Hydrological Cycle to Global Warming, *Journal of Climate*, *19*(21), 5686-5699, doi:10.1175/JCLI3990.1.

Hemleben, C., M. Spindler, I. Breitinger, and R. Ott (1987), Morphological and physiological responses of *Globigerinoides sacculifer* (Brady) under varying laboratory conditions, *Marine Micropaleontology*, *12*, 305-324, doi:10.1016/0377-8398(87)90025-9.

Hernández-Almeida, I., F. J. Sierro, I. Cacho, and J. A. Flores (2012), Impact of suborbital climate changes in the North Atlantic on ice sheet dynamics at the Mid-Pleistocene Transition, *Paleoceanography*, *27*(3), PA3214, doi:10.1029/2011PA002209.

Honda, M., S. Yabuki, and H. Shimizu (2004), Geochemical and isotopic studies of aeolian sediments in China, *Sedimentology*, *51*(2), 211-230, doi:10.1111/j.1365-3091.2004.00618.x.

Hovan, S. A., D. K. Rea, and N. G. Pisias (1991), Late Pleistocene Continental Climate and Oceanic Variability Recorded in Northwest Pacific Sediments, *Paleoceanography*, *6*(3), 349-370, doi:10.1029/91PA00559.

Hoyos, C., and P. Webster (2012), Evolution and modulation of tropical heating from the last glacial maximum through the twenty-first century, *Climate Dynamics*, *38*(7-8), 1501-1519, doi:10.1007/s00382-011-1181-3.

Hsu, S.-C., et al. (2012), Dust transport from non-East Asian sources to the North Pacific, *Geophysical Research Letters*, *39*(12), L12804, doi:10.1029/2012GL051962.

Huh, C.-A., J.-L. Peng, and J.-C. Chen (1992), Late Pleistocene pelagic sedimentation in the West Philippine Basin, *Journal of Southeast Asian Earth Sciences*, *7*(2–3), 159-164, doi:10.1016/0743-9547(92)90050-L.

Hyeong, K., J. Kim, T. Pettke, C. M. Yoo, and S.-d. Hur (2011), Lead, Nd and Sr isotope records of pelagic dust: Source indication versus the effects of dust extraction procedures and authigenic mineral growth, *Chemical Geology*, *286*(3-4), 240-251, doi:10.1016/j.chemgeo.2011.05.009.

Hyeong, K., J. Lee, I. Seo, M. J. Lee, C. M. Yoo, and B.-K. Khim (2014), Southward shift of the Intertropical Convergence Zone due to Northern Hemisphere cooling at the Oligocene-Miocene boundary, *Geology*, *42*(8), 667-670, doi:10.1130/g35664.1.

Iwasaka, Y., J. M. Li, G. Y. Shi, Y. S. Kim, A. Matsuki, D. Trochkine, M. Yamada, D. Zhang, Z. Shen, and C. S. Hong (2008), Mass Transport of Background Asian Dust Revealed by Balloon-Borne Measurement: Dust Particles

Transported during Calm Periods by Westerly from Taklamakan Desert, in *Advanced Environmental Monitoring*, edited by Y. Kim and U. Platt, pp. 121-135, Springer Netherlands, doi:10.1007/978-1-4020-6364-0_9.

Jacobsen, S. B., and G. J. Wasserburg (1980), Sm-Nd isotopic evolution of chondrites, *Earth and Planetary Science Letters*, *50*(1), 139-155, doi: 10.1016/0012-821X(80)90125-9.

Jiang, D., and X. Lang (2010), Last Glacial Maximum East Asian Monsoon: Results of PMIP Simulations, *Journal of Climate*, *23*(18), 5030-5038, doi:10.1175/2010JCLI3526.1.

Jiang, F., M. Frank, T. Li, T.-Y. Chen, Z. Xu, and A. Li (2013), Asian dust input in the western Philippine Sea: Evidence from radiogenic Sr and Nd isotopes, *Geochemistry, Geophysics, Geosystems*, *14*(5), 1538-1551, doi:10.1002/ggge.20116.

Jones, C. E., A. N. Halliday, D. K. Rea, and R. M. Owen (1994), Neodymium isotopic variations in North Pacific modern silicate sediment and the insignificance of detrital REE contributions to seawater, *Earth and Planetary Science Letters*, *127*(1-2), 55-66.

Kanayama, S., S. Yabuki, F. Zeng, M. Liu, Z. Shen, L. Liu, F. Yanagisawa, and O. Abe (2005), Size-Dependent Geochemical Characteristics of Asian Dust—Sr and Nd Isotope Compositions as Tracers for Source Identification—, *Journal of the Meteorological Society of Japan. Ser. II*, *83A*, 107–120, doi:10.2151/jmsj.83A.107.

Kao, H.-Y., and J.-Y. Yu (2009), Contrasting Eastern-Pacific and Central-Pacific Types of ENSO, *Journal of Climate*, *22*(3), 615-632, doi:10.1175/2008JCLI2309.1.

Kim, S.-T., and J. R. O'Neil (1997), Equilibrium and nonequilibrium oxygen isotope effects in synthetic carbonates, *Geochimica et Cosmochimica Acta*, *61*(16), 3461-3475, doi:10.1016/S0016-7037(97)00169-5.

Koutavas, A., J. Lynch-Stieglitz, T. M. Marchitto, and J. P. Sachs (2002), El Niño-Like Pattern in Ice Age Tropical Pacific Sea Surface Temperature, *Science*,

297(5579), 226-230, doi:10.1126/science.1072376.

Koutavas, A., and J. Lynch-Stieglitz (2003), Glacial-interglacial dynamics of the eastern equatorial Pacific cold tongue-Intertropical Convergence Zone system reconstructed from oxygen isotope records, *Paleoceanography*, *18*(4), 1089, doi:10.1029/2003pa000894.

Koutavas, A., and J. P. Sachs (2008), Northern timing of deglaciation in the eastern equatorial Pacific from alkenone paleothermometry, *Paleoceanography*, *23*(4), PA4205, doi:10.1029/2008PA001593.

Kug, J.-S., F.-F. Jin, and S.-I. An (2009), Two Types of El Niño Events: Cold Tongue El Niño and Warm Pool El Niño, *Journal of Climate*, *22*(6), 1499-1515, doi:10.1175/2008JCLI2624.1.

Lamy, F., J. Kaiser, U. Ninnemann, D. Hebbeln, H. W. Arz, and J. Stoner (2004), Antarctic Timing of Surface Water Changes off Chile and Patagonian Ice Sheet Response, *Science*, *304*(5679), 1959-1962, doi:10.1126/science.1097863.

Lawrence, K. T., Z. Liu, and T. D. Herbert (2006), Evolution of the Eastern Tropical Pacific Through Plio-Pleistocene Glaciation, *Science*, *312*(5770), 79-83, doi:10.1126/science.1120395.

Le Bouteiller, A., A. Leynaert, M. R. Landry, R. Le Borgne, J. Neveux, M. Rodier, J. Blanchot, and S. L. Brown (2003), Primary production, new production, and growth rate in the equatorial Pacific: Changes from mesotrophic to oligotrophic regime, *Journal of Geophysical Research: Oceans*, *108*(C12), 8141, doi:10.1029/2001JC000914.

Lea, D. W., D. K. Pak, C. L. Belanger, H. J. Spero, M. A. Hall, and N. J. Shackleton (2006), Paleoclimate history of Galápagos surface waters over the last 135,000 yr, *Quaternary Science Reviews*, *25*(11–12), 1152-1167, doi:10.1016/j.quascirev.2005.11.010.

Lee, K. E., N. C. Slowey, and T. D. Herbert (2001), Glacial sea surface temperatures in the subtropical North Pacific: A comparison of $U_{37}^{k'}$, $\delta^{18}O$, and foraminiferal assemblage temperature estimates, *Paleoceanography*, 16(3),

268-279, doi:10.1029/1999PA000493.

Lee, Y. (2015), Paleoenvironment reconstruction of Kuroshio Extension and Central Equatorial Pacific using planktic foraminifera assemblages since the last glacial maximum (LGM), MS thesis, 100 pp, Kyungpook National University, Daegu, Korea (in Korean).

Lee, Y., H. Asahi, H. J. Woo, H. J. Kim, S.-J. Lee, and B.-K. Khim (2014), Seasonal Variation of Planktonic Foraminifera Assemblage in response to Seasonal Shift of Inter-Tropical Convergence Zone in the Northeastern Equatorial Pacific, *Ocean and Polar Research*, 36(4), 437-445 (in Korean).

Lee, Y. C., X. Yang, and M. Wenig (2010), Transport of dusts from East Asian and non-East Asian sources to Hong Kong during dust storm related events 1996–2007, *Atmospheric Environment*, *44*(30), 3728-3738, doi:10.1016/j.atmosenv.2010.03.034.

Leinen, M., J. M. Prospero, E. Arnold, and M. Blank (1994), Mineralogy of aeolian dust reaching the North Pacific Ocean: 1. Sampling and analysis, *Journal of Geophysical Research: Atmospheres*, *99*(D10), 21017-21023, doi:10.1029/94JD01735.

Li, L., Q. Li, J. Tian, P. Wang, H. Wang, and Z. Liu (2011), A 4-Ma record of thermal evolution in the tropical western Pacific and its implications on climate change, *Earth and Planetary Science Letters*, *309*(1–2), 10-20, doi:10.1016/j.epsl.2011.04.016.

Li, Q., B. Li, G. Zhong, B. McGowran, Z. Zhou, J. Wang, and P. Wang (2006), Late Miocene development of the western Pacific warm pool: Planktonic foraminifer and oxygen isotopic evidence, *Palaeogeography, Palaeoclimatology, Palaeoecology*, *237*(2–4), 465-482, doi:10.1016/j.palaeo.2005.12.019.

Li, T., J. Zhao, Q. Nan, R. Sun, and X. Yu (2011), Palaeoproductivity evolution in the centre of the western Pacific warm pool during the last 250 ka, *Journal of Quaternary Science*, *26*(5), 478-484, doi:10.1002/jqs.1471.

Li, Y., and F. Wang (2012), Spreading and salinity change of North Pacific Tropical

Water in the Philippine Sea, *J Oceanogr*, *68*(3), 439-452, doi:10.1007/s10872-012-0110-3.

Lisiecki, L. E., and M. E. Raymo (2005), A Pliocene-Pleistocene stack of 57 globally distributed benthic $\delta^{18}O$ records, *Paleoceanography*, *20*(1), PA1003, doi:10.1029/2004PA001071.

Liu, J. P., K. H. Xu, A. C. Li, J. D. Milliman, D. M. Velozzi, S. B. Xiao, and Z. S. Yang (2007), Flux and fate of Yangtze River sediment delivered to the East China Sea, *Geomorphology*, *85*(3–4), 208-224, doi:10.1016/j.geomorph.2006.03.023.

Liu, T., and Z. Ding (1993), Stepwise coupling of monsoon circulations to global ice volume variations during the late Cenozoic, *Global and Planetary Change*, *7*(1–3), 119-130, doi:10.1016/0921-8181(93)90044-O.

Liu, Z., Y. Zhao, C. Colin, F. P. Siringan, and Q. Wu (2009), Chemical weathering in Luzon, Philippines from clay mineralogy and major-element geochemistry of river sediments, *Applied Geochemistry*, *24*(11), 2195-2205, doi:10.1016/j.apgeochem.2009.09.025.

Locarnini, R. A., et al. (2013), *World Ocean Atlas 2013, Volume 1: Temperature*, 40 pp.

Luo, C., N. M. Mahowald, and J. del Corral (2003), Sensitivity study of meteorological parameters on mineral aerosol mobilization, transport, and distribution, *Journal of Geophysical Research: Atmospheres*, *108*(D15), 4447, doi:10.1029/2003JD003483.

Lurcock, P. C., and G. S. Wilson (2012), PuffinPlot: A versatile, user-friendly program for paleomagnetic analysis, *Geochemistry, Geophysics, Geosystems*, *13*(6), Q06z45, doi:10.1029/2012GC004098.

Mackey, D. J., J. Parslow, H. W. Higgins, F. B. Griffiths, and J. E. O'Sullivan (1995), Plankton productivity and biomass in the western equatorial Pacific: Biological and physical controls, *Deep Sea Research Part II: Topical Studies in Oceanography*, *42*(2–3), 499-533, doi:10.1016/0967-0645(95)00038-R.

Maher, B. A., J. M. Prospero, D. Mackie, D. Gaiero, P. P. Hesse, and Y. Balkanski (2010), Global connections between aeolian dust, climate and ocean biogeochemistry at the present day and at the last glacial maximum, *Earth-Science Reviews*, *99*(1–2), 61-97, doi:10.1016/j.earscirev.2009.12.001.

Mahoney, J. B. (2005), Nd and Sr isotopic signatures of fine-grained clastic sediments: A case study of western Pacific marginal basins, *Sedimentary Geology*, *182*(1–4), 183-199, doi:10.1016/j.sedgeo.2005.07.009.

Mahowald, N. M., J. A. Ballantine, J. Feddema, and N. Ramankutty (2007), Global trends in visibility: implications for dust sources, *Atmospheric Chemistry and Physics*, *7*(12), 3309-3339, doi:10.5194/acp-7-3309-2007.

Marcott, S. A., J. D. Shakun, P. U. Clark, and A. C. Mix (2013), A Reconstruction of Regional and Global Temperature for the Past 11,300 Years, *Science*, *339*(6124), 1198-1201, doi:10.1126/science.1228026.

Martinez-Boti, M. A., G. Marino, G. L. Foster, P. Ziveri, M. J. Henehan, J. W. B. Rae, P. G. Mortyn, and D. Vance (2015), Boron isotope evidence for oceanic carbon dioxide leakage during the last deglaciation, *Nature*, *518*(7538), 219-222, doi:10.1038/nature14155.

Martínez-Garcia, A., A. Rosell-Melé, E. L. McClymont, R. Gersonde, and G. H. Haug (2010), Subpolar Link to the Emergence of the Modern Equatorial Pacific Cold Tongue, *Science*, *328*(5985), 1550-1553, doi:10.1126/science.1184480.

Martínez, I., L. Keigwin, T. T. Barrows, Y. Yokoyama, and J. Southon (2003), La Niña-like conditions in the eastern equatorial Pacific and a stronger Choco jet in the northern Andes during the last glaciation, *Paleoceanography*, *18*(2), 1033, doi:10.1029/2002PA000877.

Masunaga, H., and T. S. L'Ecuyer (2010), Equatorial Asymmetry of the East Pacific ITCZ: Observational Constraints on the Underlying Processes, *Journal of Climate*, *24*(6), 1784-1800, doi:10.1175/2010JCLI3854.1.

McClymont, E. L., and A. Rosell-Melé (2005), Links between the onset of modern Walker circulation and the mid-Pleistocene climate transition, *Geology*,

33(5), 389-392, doi:10.1130/g21292.1.

McClymont, E. L., A. Rosell-Melé, G. H. Haug, and J. M. Lloyd (2008), Expansion of subarctic water masses in the North Atlantic and Pacific oceans and implications for mid-Pleistocene ice sheet growth, *Paleoceanography*, *23*(4), PA4214, doi:10.1029/2008PA001622.

McClymont, E. L., S. M. Sosdian, A. Rosell-Melé, and Y. Rosenthal (2013), Pleistocene sea-surface temperature evolution: Early cooling, delayed glacial intensification, and implications for the mid-Pleistocene climate transition, *Earth-Science Reviews*, *123*, 173-193, doi:10.1016/j.earscirev.2013.04.006.

McGee, D., A. Donohoe, J. Marshall, and D. Ferreira (2014), Changes in ITCZ location and cross-equatorial heat transport at the Last Glacial Maximum, Heinrich Stadial 1, and the mid-Holocene, *Earth and Planetary Science Letters*, *390*, 69-79, doi:10.1016/j.epsl.2013.12.043.

McManus, J. F., R. Francois, J. M. Gherardi, L. D. Keigwin, and S. Brown-Leger (2004), Collapse and rapid resumption of Atlantic meridional circulation linked to deglacial climate changes, *Nature*, *428*(6985), 834-837, doi:10.1038/nature02494.

McPhaden, M. J., and J. Picaut (1990), El Niño-Southern Oscillation Displacements of the Western Equatorial Pacific Warm Pool, *Science*, *250*(4986), 1385-1388, doi:10.1126/science.250.4986.1385.

Merrill, J. T., M. Uematsu, and R. Bleck (1989), Meteorological analysis of long range transport of mineral aerosols over the North Pacific, *Journal of Geophysical Research: Atmospheres*, *94*(D6), 8584-8598, doi:10.1029/JD094iD06p08584.

Ming, J., A. Li, J. Huang, S. Wan, Q. Meng, F. Jiang, and W. Yan (2014), Assemblage characteristics of clay minerals and its implications to evolution of eolian dust input to the Parece Vela Basin since 1.95 Ma, *Chinese Journal of Oceanology and Limnology*, *32*(1), 174-186, doi:10.1007/s00343-014-3066-x.

Mohtadi, M., D. W. Oppo, S. Steinke, J.-B. W. Stuut, R. De Pol-Holz, D. Hebbeln, and A. Luckge (2011), Glacial to Holocene swings of the Australian-Indonesian monsoon, *Nature Geoscience*, *4*(8), 540-544, doi:10.1038/ngeo1209.

Molina-Kescher, M., M. Frank, and E. C. Hathorne (2014), Nd and Sr isotope compositions of different phases of surface sediments in the South Pacific: Extraction of seawater signatures, boundary exchange, and detrital/dust provenance, *Geochemistry, Geophysics, Geosystems*, *15*(9), 3502-3520, doi:10.1002/2014GC005443.

Montade, V., M. Kageyama, N. Combourieu-Nebout, M.-P. Ledru, E. Michel, G. Siani, and C. Kissel (2015), Teleconnection between the Intertropical Convergence Zone and southern westerly winds throughout the last deglaciation, *Geology*, *43*(8), 735-738, doi:10.1130/g36745.1.

Mortlock, R. A., and P. N. Froelich (1989), A simple method for the rapid determination of biogenic opal in pelagic marine sediments, *Deep Sea Research Part A. Oceanographic Research Papers*, *36*(9), 1415-1426, doi:10.1016/0198-0149(89)90092-7.

Mortyn, P. G., and C. D. Charles (2003), Planktonic foraminiferal depth habitat and $\delta^{18}O$ calibrations: Plankton tow results from the Atlantic sector of the Southern Ocean, *Paleoceanography*, *18*(2), n/a-n/a, doi:10.1029/2001PA000637.

Müller, P. J., and R. Schneider (1993), An automated leaching method for the determination of opal in sediments and particulate matter, *Deep Sea Research Part I: Oceanographic Research Papers*, *40*(3), 425-444, doi:10.1016/0967-0637(93)90140-X.

Nagashima, K., R. Tada, H. Matsui, T. Irino, A. Tani, and S. Toyoda (2007), Orbital- and millennial-scale variations in Asian dust transport path to the Japan Sea, *Palaeogeography, Palaeoclimatology, Palaeoecology*, *247*(1–2), 144-161, doi:10.1016/j.palaeo.2006.11.027.

Nagashima, K., R. Tada, A. Tani, Y. Sun, Y. Isozaki, S. Toyoda, and H. Hasegawa

(2011), Millennial-scale oscillations of the westerly jet path during the last glacial period, *Journal of Asian Earth Sciences*, *40*(6), 1214-1220, doi:10.1016/j.jseaes.2010.08.010.

Nakagawa, T., P. E. Tarasov, H. Kitagawa, Y. Yasuda, and K. Gotanda (2006), Seasonally specific responses of the East Asian monsoon to deglacial climate changes, *Geology*, *34*(7), 521-524, doi:10.1130/g21764.1.

Nakai, S. i., A. N. Halliday, and D. K. Rea (1993), Provenance of dust in the Pacific Ocean, *Earth and Planetary Science Letters*, *119*(1-2), 143-157.

Nakano, T., Y. Yokoo, M. Nishikawa, and H. Koyanagi (2004), Regional Sr–Nd isotopic ratios of soil minerals in northern China as Asian dust fingerprints, *Atmospheric Environment*, *38*(19), 3061-3067, doi:10.1016/j.atmosenv.2004.02.016.

North Greenland Ice Core Project members (2004), High-resolution record of Northern Hemisphere climate extending into the last interglacial period, *Nature*, 431(7005), 147-151, doi:10.1038/nature02805.

Nürnberg, D., J. Bijma, and C. Hemleben (1996), Assessing the reliability of magnesium in foraminiferal calcite as a proxy for water mass temperatures, *Geochimica et Cosmochimica Acta*, *60*(5), 803-814, doi:10.1016/0016-7037(95)00446-7.

Paillard, D., L. Labeyrie, and P. Yiou (1996), Macintosh Program performs time-series analysis, *Eos, Transactions American Geophysical Union*, *77*(39), 379-379, doi:10.1029/96EO00259.

Parrenin, F., V. Masson-Delmotte, P. Köhler, D. Raynaud, D. Paillard, J. Schwander, C. Barbante, A. Landais, A. Wegner, and J. Jouzel (2013), Synchronous Change of Atmospheric CO_2 and Antarctic Temperature During the Last Deglacial Warming, *Science*, 339(6123), 1060-1063, doi:10.1126/science.1226368.

Partin, J. W., K. M. Cobb, J. F. Adkins, B. Clark, and D. P. Fernandez (2007), Millennial-scale trends in west Pacific warm pool hydrology since the Last Glacial Maximum, *Nature*, 449(7161), 452-455, doi:10.1038/nature06164.

Patrick, A., and R. C. Thunell (1997), Tropical Pacific sea surface temperatures and upper water column thermal structure during the Last Glacial Maximum, *Paleoceanography*, *12*(5), 649-657, doi:10.1029/97PA01553.

Pena, L. D., S. L. Goldstein, S. R. Hemming, K. M. Jones, E. Calvo, C. Pelejero, and I. Cacho (2013), Rapid changes in meridional advection of Southern Ocean intermediate waters to the tropical Pacific during the last 30 kyr, *Earth and Planetary Science Letters*, *368*, 20-32, doi:10.1016/j.epsl.2013.02.028.

Peterson, L. C., G. H. Haug, K. A. Hughen, and U. Röhl (2000), Rapid Changes in the Hydrologic Cycle of the Tropical Atlantic During the Last Glacial, *Science*, *290*(5498), 1947-1951, doi:10.1126/science.290.5498.1947.

Petschick, R., G. Kuhn, and F. Gingele (1996), Clay mineral distribution in surface sediments of the South Atlantic: sources, transport, and relation to oceanography, *Marine Geology*, *130*(3–4), 203-229, doi:10.1016/0025-3227(95)00148-4.

Pettke, T., A. N. Halliday, C. M. Hall, and D. K. Rea (2000), Dust production and deposition in Asia and the north Pacific Ocean over the past 12 Myr, *Earth and Planetary Science Letters*, *178*(3-4), 397-413.

Pettke, T., A. N. Halliday, and D. K. Rea (2002), Cenozoic evolution of Asian climate and sources of Pacific seawater Pb and Nd derived from eolian dust of sediment core LL44-GPC3, *Paleoceanography*, *17*, 1031, doi:10.1029/2001PA000673.

Philander, S. G., W. J. Hurlin, and A. D. Seigel (1987), Simulation of the Seasonal Cycle of the Tropical Pacific Ocean, *Journal of Physical Oceanography*, *17*(11), 1986-2002, doi:10.1175/1520-0485.

Picaut, J., M. Ioualalen, C. Menkes, T. Delcroix, and M. J. McPhaden (1996), Mechanism of the Zonal Displacements of the Pacific Warm Pool: Implications for ENSO, *Science*, *274*(5292), 1486-1489, doi:10.1126/science.274.5292.1486.

Picaut, J., F. Masia, and Y. du Penhoat (1997), An Advective-Reflective Conceptual

Model for the Oscillatory Nature of the ENSO, *Science*, *277*(5326), 663-666, doi:10.1126/science.277.5326.663.

Pichat, S., W. Abouchami, and S. J. G. Galer (2014), Lead isotopes in the Eastern Equatorial Pacific record Quaternary migration of the South Westerlies, *Earth and Planetary Science Letters*, *388*, 293-305, doi:10.1016/j.epsl.2013.11.035.

Qiu, X., T. Li, F. Chang, Q. Nan, Z. Xiong, and H. Sun (2014), Sea surface temperature and salinity reconstruction based on stable isotopes and Mg/Ca of planktonic foraminifera in the western Pacific Warm Pool during the last 155 ka, *Chinese Journal of Oceanology and Limnology*, *32*(1), 187-200, doi:10.1007/s00343-014-3073-y.

Radenac, M.-H., and M. Rodier (1996), Nitrate and chlorophyll distributions in relation to thermohaline and current structures in the western tropical Pacific during 1985–1989, *Deep Sea Research Part II: Topical Studies in Oceanography*, *43*(4–6), 725-752, doi:10.1016/0967-0645(96)00025-2.

Rao, W., J. U. N. Chen, J. Yang, J. Ji, G. Li, and H. Tan (2008), Sr-Nd isotopic characteristics of eolian deposits in the Erdos Desert and Chinese Loess Plateau: Implications for their provenances, *Geochemical Journal*, *42*(3), 273-282, doi:10.2343/geochemj.42.273.

Rashid, H., and E. A. Boyle (2007), Mixed-Layer Deepening During Heinrich Events: A Multi-Planktonic Foraminiferal $\delta^{18}O$ Approach, *Science*, 318(5849), 439-441, doi:10.1126/science.1146138.

Rasmusson, E. M., and J. M. Wallace (1983), Meteorological Aspects of the El Niño/Southern Oscillation, *Science*, *222*(4629), 1195-1202, doi:10.1126/science.222.4629.1195.

Rateev, M. A., Z. N. Gorbunova, A. P. Lisitzyn, and G. L. Nosov (1969), The distribution of clay minerals in the oceans, *Sedimentology*, *13*(1-2), 21-43, doi:10.1111/j.1365-3091.1969.tb01119.x.

Rea, D. K. (1994), The paleoclimatic record provided by eolian deposition in the deep sea: The geologic history of wind, *Reviews of Geophysics*, *32*(2), 159-

195, doi:10.1029/93RG03257.

Rea, D. K., and S. A. Hovan (1995), Grain size distribution and depositional processes of the mineral component of abyssal sediments: Lessons from the North Pacific, *Paleoceanography*, *10*(2), 251-258, doi:10.1029/94PA03355.

Rea, D. K., and T. R. Janecek (1981), Late cretaceous history of eolian deposition in the mid-pacific mountains, central North Pacific Ocean, *Palaeogeography, Palaeoclimatology, Palaeoecology*, *36*(1–2), 55-67, doi:10.1016/0031-0182(81)90048-1.

Reimer, P. J., et al. (2013), IntCal13 and Marine13 Radiocarbon Age Calibration Curves 0–50,000 Years cal BP, *Radiocarbon*, *55*(4), 1869-1887, doi:10.2458/azu_js_rc.55.16947.

Rincón-Martínez, D., S. Steph, F. Lamy, A. Mix, and R. Tiedemann (2011), Tracking the equatorial front in the eastern equatorial Pacific Ocean by the isotopic and faunal composition of planktonic foraminifera, *Marine Micropaleontology*, *79*(1–2), 24-40, doi:10.1016/j.marmicro.2011.01.001.

Romero, O. E., J.-H. Kim, and D. Hebbeln (2006), Paleoproductivity evolution off central Chile from the Last Glacial Maximum to the Early Holocene, *Quaternary Research*, *65*(3), 519-525, doi:10.1016/j.yqres.2005.07.003.

Rosenthal, Y., E. A. Boyle, and N. Slowey (1997), Temperature control on the incorporation of magnesium, strontium, fluorine, and cadmium into benthic foraminiferal shells from Little Bahama Bank: Prospects for thermocline paleoceanography, *Geochimica et Cosmochimica Acta*, *61*(17), 3633-3643, doi:10.1016/S0016-7037(97)00181-6.

Rosenthal, Y., and G. P. Lohmann (2002), Accurate estimation of sea surface temperatures using dissolution-corrected calibrations for Mg/Ca paleothermometry, *Paleoceanography*, *17*(3), 1044, doi:10.1029/2001PA000749.

Russon, T., M. Elliot, A. Sadekov, G. Cabioch, T. Corrège, and P. De Deckker (2010), Inter-hemispheric asymmetry in the early Pleistocene Pacific warm pool, *Geophysical Research Letters*, *37*(11), L11601,

doi:10.1029/2010GL043191.

Ryan, W. B. F., et al. (2009), Global Multi-Resolution Topography synthesis, *Geochemistry, Geophysics, Geosystems*, *10*(3), Q03014, doi:10.1029/2008GC002332.

Sadekov, A., S. M. Eggins, P. De Deckker, U. Ninnemann, W. Kuhnt, and F. Bassinot (2009), Surface and subsurface seawater temperature reconstruction using Mg/Ca microanalysis of planktonic foraminifera *Globigerinoides ruber*, *Globigerinoides sacculifer*, and *Pulleniatina obliquiloculata*, *Paleoceanography*, *24*(3), PA3201, doi:10.1029/2008PA001664.

Sagawa, T., Y. Yokoyama, M. Ikehara, and M. Kuwae (2012), Shoaling of the western equatorial Pacific thermocline during the last glacial maximum inferred from multispecies temperature reconstruction of planktonic foraminifera, *Palaeogeography, Palaeoclimatology, Palaeoecology*, *346–347*, 120-129, doi:10.1016/j.palaeo.2012.06.002.

Sarnthein, M., and K. Winn (1990), Reconstruction of Low and Middle Latitude Export Productivity, 30,000 Years BP to Present: Implications for Global Carbon Reservoirs, in *Climate-Ocean Interaction*, edited by M. E. Schlesinger, pp. 319-342, Springer Netherlands, doi:10.1007/978-94-009-2093-4_16.

Sato, K., M. Oda, S. Chiyonobu, K. Kimoto, H. Domitsu, and J. C. Ingle Jr (2008), Establishment of the western Pacific warm pool during the Pliocene: Evidence from planktic foraminifera, oxygen isotopes, and Mg/Ca ratios, *Palaeogeography, Palaeoclimatology, Palaeoecology*, *265*(1–2), 140-147, doi:10.1016/j.palaeo.2008.05.003.

Schefuß, E., S. Schouten, J. H. F. Jansen, and J. S. Sinninghe Damste (2003), African vegetation controlled by tropical sea surface temperatures in the mid-Pleistocene period, *Nature*, *422*(6930), 418-421, doi:10.1038/nature01500.

Schneider, T., T. Bischoff, and G. H. Haug (2014), Migrations and dynamics of the

intertropical convergence zone, *Nature*, *513*(7516), 45-53, doi:10.1038/nature13636.

Schubert, S. D., M. J. Suarez, P. J. Pegion, R. D. Koster, and J. T. Bacmeister (2004), On the Cause of the 1930s Dust Bowl, *Science*, *303*(5665), 1855-1859, doi:10.1126/science.1095048.

Seo, I., Y. I. Lee, W. Kim, C. M. Yoo, and K. Hyeong (2015), Movement of the Intertropical Convergence Zone during the mid-pleistocene transition and the response of atmospheric and surface ocean circulations in the central equatorial Pacific, *Geochemistry, Geophysics, Geosystems*, 16, 3973–3981, doi:10.1002/2015GC006077.

Seo, I., Y. I. Lee, C. M. Yoo, H. J. Kim, and K. Hyeong (2014), Sr-Nd isotope composition and clay mineral assemblages in eolian dust from the central Philippine Sea over the last 600 kyr: Implications for the transport mechanism of Asian dust, *Journal of Geophysical Research: Atmospheres*, *119*(19), 11,492-411,504, doi:10.1002/2014JD022025.

Serno, S., G. Winckler, R. F. Anderson, C. T. Hayes, D. McGee, B. Machalett, H. Ren, S. M. Straub, R. Gersonde, and G. H. Haug (2014), Eolian dust input to the Subarctic North Pacific, *Earth and Planetary Science Letters*, *387*, 252-263, doi:10.1016/j.epsl.2013.11.008.

Sexton, P. F., and S. Barker (2012), Onset of 'Pacific-style' deep-sea sedimentary carbonate cycles at the mid-Pleistocene transition, *Earth and Planetary Science Letters*, *321–322*, 81-94, doi:10.1016/j.epsl.2011.12.043.

Shakun, J. D., P. U. Clark, F. He, S. A. Marcott, A. C. Mix, Z. Liu, B. Otto-Bliesner, A. Schmittner, and E. Bard (2012), Global warming preceded by increasing carbon dioxide concentrations during the last deglaciation, *Nature*, *484*(7392), 49-54, doi:10.1038/nature10915.

Shen, Z., X. Li, J. Cao, S. Caquineau, Y. Wang, and X. Zhang (2005), Characteristics of clay minerals in asian dust and their environmental significance, *China Particuology*, *3*(5), 260-264, doi:10.1016/S1672-2515(07)60198-5.

Shi, Y., X. Dai, J. Li, and J. Wang (1997), Origin and significance of clay minerals in the last interglacial loess in Lanzhou area, North-central China, *Marine Geology and Quaternary Geology*, *17*(1), 87-94.

Shi, Z., and X. Liu (2011), Distinguishing the provenance of fine-grained eolian dust over the Chinese Loess Plateau from a modelling perspective, *Tellus B*, *63*(5), 959-970, doi:10.1111/j.1600-0889.2011.00561.x.

Skonieczny, C., et al. (2011), The 7–13 March 2006 major Saharan outbreak: Multiproxy characterization of mineral dust deposited on the West African margin, *Journal of Geophysical Research: Atmospheres*, *116*(D18), D18210, doi:10.1029/2011JD016173.

Sosdian, S., and Y. Rosenthal (2009), Deep-Sea Temperature and Ice Volume Changes Across the Pliocene-Pleistocene Climate Transitions, *Science*, *325*(5938), 306-310, doi:10.1126/science.1169938.

Southon, J., M. Kashgarian, M. Fontugne, B. Metivier, and W. W. S. Yim (2002), Marine reservoir corrections for the Indian Ocean and Southeast Asia, *Radiocarbon*, *44*(1), 167-180.

Siegert, F., G. Ruecker, A. Hinrichs, and A. A. Hoffmann (2001), Increased damage from fires in logged forests during droughts caused by El Nino, *Nature*, *414*(6862), 437-440, doi:10.1038/35106547.

Stancin, A. M., J. D. Gleason, S. A. Hovan, D. K. Rea, R. M. Owen, T. C. Moore Jr, C. M. Hall, and J. D. Blum (2008), Miocene to recent eolian dust record from the Southwest Pacific Ocean at 40°S latitude, *Palaeogeography, Palaeoclimatology, Palaeoecology*, *261*(3–4), 218-233, doi:10.1016/j.palaeo.2007.12.015.

Stancin, A. M., J. D. Gleason, D. K. Rea, R. M. Owen, T. C. Moore Jr, J. D. Blum, and S. A. Hovan (2006), Radiogenic isotopic mapping of late Cenozoic eolian and hemipelagic sediment distribution in the east-central Pacific, *Earth and Planetary Science Letters*, *248*(3–4), 840-850, doi:10.1016/j.epsl.2006.06.038.

Stenni, B., et al. (2011), Expression of the bipolar see-saw in Antarctic climate

records during the last deglaciation, *Nature Geoscience*, *4*(1), 46-49, doi:10.1038/ngeo1026.

Stuiver, M., and P. J. Reimer (1993), Extended ^{14}C data base and revised CALIB 3.0 ^{14}C age calibration program, *Radiocarbon*, *35*, 215-230.

Sun, D. (2004), Monsoon and westerly circulation changes recorded in the late Cenozoic aeolian sequences of Northern China, *Global and Planetary Change*, *41*(1), 63-80, doi:10.1016/j.gloplacha.2003.11.001.

Sun, D., J. Bloemendal, D. K. Rea, J. Vandenberghe, F. Jiang, Z. An, and R. Su (2002), Grain-size distribution function of polymodal sediments in hydraulic and aeolian environments, and numerical partitioning of the sedimentary components, *Sedimentary Geology*, *152*(3–4), 263-277, doi:10.1016/S0037-0738(02)00082-9.

Sun, J., M. Zhang, and T. Liu (2001), Spatial and temporal characteristics of dust storms in China and its surrounding regions, 1960–1999: Relations to source area and climate, *Journal of Geophysical Research: Atmospheres*, *106*(D10), 10325-10333, doi:10.1029/2000JD900665.

Tanaka, T. Y., and M. Chiba (2006), A numerical study of the contributions of dust source regions to the global dust budget, *Global and Planetary Change*, *52*(1-4), 88-104, doi:10.1016/j.gloplacha.2006.02.002.

Tanaka, T. Y., Y. Kurosaki, M. Chiba, T. Matsumura, T. Nagai, A. Yamazaki, A. Uchiyama, N. Tsunematsu, and K. Kai (2005), Possible transcontinental dust transport from North Africa and the Middle East to East Asia, *Atmospheric Environment*, *39*(21), 3901-3909, doi:10.1016/j.atmosenv.2005.03.034.

Tang, Z., T. Li, F. Chang, Q. Nan, and Q. Li (2013), Paleoproductivity evolution in the West Philippine Sea during the last 700 ka, *Chinese Journal of Oceanology and Limnology*, *31*(2), 435-444, doi:10.1007/s00343-013-2117-z.

Thunell, R. C., and S. Honjo (1981), Planktonic foraminiferal flux to the deep ocean: Sediment trap results from the tropical Atlantic and the central Pacific,

Marine Geology, 40(3), 237-253, doi:10.1016/0025-3227(81)90142-0.

Thunell, R. C., and L. A. Reynolds (1984), Sedimentation of Planktonic Foraminifera: Seasonal Changes in Species Flux in the Panama Basin, *Micropaleontology*, 30(3), 243-262, doi:10.2307/1485688.

Tian, J., P. Wang, R. Chen, and X. Cheng (2005), Quaternary upper ocean thermal gradient variations in the South China Sea: Implications for east Asian monsoon climate, *Paleoceanography*, *20*(4), PA4007, doi:10.1029/2004PA001115.

Tian, Y., B. P. Kohn, S. Hu, and A. J. W. Gleadow (2015), Synchronous fluvial response to surface uplift in the eastern Tibetan Plateau: Implications for crustal dynamics, *Geophysical Research Letters*, *42*(1), 29-35, doi:10.1002/2014GL062383.

Timmermann, A., S. J. Lorenz, S. I. An, A. Clement, and S. P. Xie (2007), The Effect of Orbital Forcing on the Mean Climate and Variability of the Tropical Pacific, *Journal of Climate*, *20*(16), 4147-4159, doi:10.1175/JCLI4240.1.

Vecchi, G. A., A. Clement, and B. J. Soden (2008), Examining the Tropical Pacific's Response to Global Warming, *Eos, Transactions American Geophysical Union*, *89*(9), 81-83, doi:10.1029/2008EO090002.

Vecchi, G. A., and B. J. Soden (2007), Global Warming and the Weakening of the Tropical Circulation, *Journal of Climate*, *20*(17), 4316-4340, doi:10.1175/JCLI4258.1.

Vecchi, G. A., B. J. Soden, A. T. Wittenberg, I. M. Held, A. Leetmaa, and M. J. Harrison (2006), Weakening of tropical Pacific atmospheric circulation due to anthropogenic forcing, *Nature*, *441*(7089), 73-76, doi:10.1038/nature04744.

Veres, D., et al. (2013), The Antarctic ice core chronology (AICC2012): an optimized multi-parameter and multi-site dating approach for the last 120 thousand years, *Climate of the Past*, 9(4), 1733-1748, doi:10.5194/cp-9-1733-2013.

Wan, S., Z. Yu, P. D. Clift, H. Sun, A. Li, and T. Li (2012), History of Asian eolian input to the West Philippine Sea over the last one million years, *Palaeogeography, Palaeoclimatology, Palaeoecology, 326–328*, 152-159, doi:10.1016/j.palaeo.2012.02.015.

Wang, B., R. Wu, and K. M. Lau (2001), Interannual Variability of the Asian Summer Monsoon: Contrasts between the Indian and the Western North Pacific–East Asian Monsoons*, *Journal of Climate*, *14*(20), 4073-4090, doi:10.1175/1520-0442.

Wang, B., and Y. Wang (1999), Dynamics of the ITCZ–Equatorial Cold Tongue Complex and Causes of the Latitudinal Climate Asymmetry, *Journal of Climate*, *12*(6), 1830-1847, doi:10.1175/1520-0442(1999)012<1830:DOTIEC>2.0.CO;2.

Wang, J., X. Fang, E. Appel, and C. Song (2012), Pliocene–Pleistocene Climate Change At the NE Tibetan Plateau Deduced From Lithofacies Variation In the Drill Core SG-1, Western Qaidam Basin, China, *Journal of Sedimentary Research*, *82*(12), 933-952, doi:10.2110/jsr.2012.76.

Wang, Y. J., H. Cheng, R. L. Edwards, Z. S. An, J. Y. Wu, C.-C. Shen, and J. A. Dorale (2001), A High-Resolution Absolute-Dated Late Pleistocene Monsoon Record from Hulu Cave, China, *Science*, 294(5550), 2345-2348, doi:10.1126/science.1064618.

Wara, M. W., M. L. Delaney, T. D. Bullen, and A. C. Ravelo (2003), Possible roles of pH, temperature, and partial dissolution in determining boron concentration and isotopic composition in planktonic foraminifera, *Paleoceanography*, *18*(4), 1100, doi:10.1029/2002PA000797.

Wara, M. W., A. C. Ravelo, and M. L. Delaney (2005), Permanent El Niño-Like Conditions During the Pliocene Warm Period, *Science*, *309*(5735), 758-761, doi:10.1126/science.1112596.

Watkins, J. M., A. C. Mix, and J. Wilson (1998), Living planktic foraminifera in the central tropical Pacific Ocean: articulating the equatorial ‘cold tongue’ during La Niña, 1992, *Marine Micropaleontology*, *33*(3–4), 157-174,

doi:10.1016/S0377-8398(97)00036-4.

Webster, P. J. (1994), The role of hydrological processes in ocean-atmosphere interactions, *Reviews of Geophysics*, *32*(4), 427-476, doi:10.1029/94RG01873.

Woodhead, J. D. (1989), Geochemistry of the Mariana arc (western Pacific): Source composition and processes, *Chemical Geology*, *76*(1–2), 1-24, doi:10.1016/0009-2541(89)90124-1.

Wurster, C. M., M. I. Bird, I. D. Bull, F. Creed, C. Bryant, J. A. J. Dungait, and V. Paz (2010), Forest contraction in north equatorial Southeast Asia during the Last Glacial Period, *Proceedings of the National Academy of Sciences*, *107*(35), 15508-15511, doi:10.1073/pnas.1005507107.

Xie, R. C., and F. Marcantonio (2012), Deglacial dust provenance changes in the Eastern Equatorial Pacific and implications for ITCZ movement, *Earth and Planetary Science Letters*, *317–318*, 386-395, doi:10.1016/j.epsl.2011.11.014.

Xu, Z., T. Li, S. Wan, Q. Nan, A. Li, F. Chang, F. Jiang, and Z. Tang (2012), Evolution of East Asian monsoon: Clay mineral evidence in the western Philippine Sea over the past 700 kyr, *Journal of Asian Earth Sciences*, *60*, 188-196, doi:10.1016/j.jseaes.2012.08.018.

Yeh, S.-W., J.-S. Kug, B. Dewitte, M.-H. Kwon, B. P. Kirtman, and F.-F. Jin (2009), El Nino in a changing climate, *Nature*, *461*(7263), 511-514, doi:10.1038/nature08316.

Yumimoto, K., K. Eguchi, I. Uno, T. Takemura, Z. Liu, A. Shimizu, and N. Sugimoto (2009), An elevated large-scale dust veil from the Taklimakan Desert: Intercontinental transport and three-dimensional structure as captured by CALIPSO and regional and global models, *Atmospheric Chemistry and Physics*, *9*(21), 8545-8558, doi:10.5194/acp-9-8545-2009.

Yunev, O. A., J. Carstensen, S. Moncheva, A. Khaliulin, G. Ærtebjerg, and S. Nixon (2007), Nutrient and phytoplankton trends on the western Black Sea shelf in response to cultural eutrophication and climate changes, *Estuarine, Coastal*

and Shelf Science, *74*(1–2), 63-76, doi:10.1016/j.ecss.2007.03.030.

Zhang, J., P. Wang, Q. Li, X. Cheng, H. Jin, and S. Zhang (2007), Western equatorial Pacific productivity and carbonate dissolution over the last 550 kyr: Foraminiferal and nannofossil evidence from ODP Hole 807A, *Marine Micropaleontology*, *64*(3–4), 121-140, doi:10.1016/j.marmicro.2007.03.003.

Zhang, X. Y., R. Arimoto, and Z. S. An (1997), Dust emission from Chinese desert sources linked to variations in atmospheric circulation, *Journal of Geophysical Research: Atmospheres*, *102*(D23), 28041-28047, doi:10.1029/97JD02300.

Zhang, X. Y., R. Arimoto, and Z. S. An (1999), Glacial and interglacial patterns for Asian dust transport, *Quaternary Science Reviews*, *18*(6), 811-819, doi:10.1016/S0277-3791(98)00028-6.

Zweng, M. M., et al. (2013), *World Ocean Atlas 2013, Volume 2: Salinity*, 39 pp.

국문초록

신생대 제 4기 동안의 서태평양 난수역의 해양학적 특성과 대기순환 복원

중앙태평양 적도 해역은 서태평양 난수역과 동태평양 용승대의 경계부에 해당하여 적도태평양의 해양학적 환경을 이해하는 데 매우 중요한 위치에 있음에도 불구하고 퇴적물 기록의 부재로 과거 기후에 대해 알려진 바가 거의 없다. 본 연구에서는 신생대 제 4기 동안 서태평양 난수역의 동쪽 경계부에서의 고해양학적 환경 변화와 그 기작을 살펴보기 위하여 북서태평양 및 중앙태평양 적도해역에서 퇴적물 기록을 획득하였다. 대기와 표층 해양의 상호작용을 파악하기 위하여, 풍성 기원 입자의 기원지와 생물 기원 퇴적물의 구성 성분을 함께 분석하였다.

북서태평양 필리핀 해(12° 30’ N, 135° 00’ E)의 퇴적물 기록에 따르면, 중앙 아시아의 사막 지대 (예: 타클라마칸 사막)에서 기원한 광물 입자가 지난 60만 년 동안 공급된 것으로 판단된다. 필리핀 해가 계절풍의 영향이 강한 지역임에도 불구하고 동아시아가 아닌 중앙아시아의 영향이 나타나는 것은 탁월풍이 가장 중요한 황사 운반 기작이며 중앙아시아 기원 광물 입자의 조성이 북태평양 전역에 나타날 것임을 시사한다. 이러한 결과는 현재 중앙태평양 적도해역(5° 53’ N, 177° 26’ W)에 퇴적된 풍성기원 입자 조성과도 일치하나, 0.8 Ma 이전에 적도 해역에 퇴적된 광물입자는 호주와

남아메리카 기원과 유사한 조성을 나타냈다. 0.8 Ma에 풍성기원입자의 주된 기원지가 남반구에서 북반구로 변화함과 동시에, 해양에서는 표층 염도와 생산성이 급격히 감소하고 풍성기원입자의 유입량이 증가하였다. 이러한 대기-해양의 변화는 적도수렴대와 북적도반류가 연구해역으로 남하하면서 발생한 결과로 해석되며, 북동무역풍이 남동무역풍에 비해 강화되었음을 시사한다. 북동무역풍의 상대적 강화는 북반구의 적도-극지역의 열적 구배가 증가한 결과로, 중기플라이스토세 전환기 (Mid-Pleistocene Transition) 동안 북반구의 빙하가 상대적으로 크게 발달하였을 가능성을 지지한다.

마지막 해빙기 동안 중앙태평양 적도해역(6° 40′ N, 177° 28′ W)의 수층구조 변화를 알아보기 위해 혼합층, 상부수온약층, 하부수온약층에 각각 서식하는 부유성 유공충 *G. sacculifer*, *P. obliquiloculata*, *G. tumida*의 안정산소동위원소 조성과 Mg/Ca 조성을 분석하였다. 표층과 하부수온약층의 수온은 18 ka 이후 안정적으로 유지된 반면, 해빙기의 18-12 ka 기간에 상부수온약층의 수온이 상승하였고 이후 다시 하강하여 현재와 비슷한 조성이 유지되었다. 이는 해당 시기 표층 바람의 세기가 증가하여 성층 구조가 약화되어 유공충 종들 간 서식 깊이가 혼합되어 나타난 결과로 보인다. 이러한 변화는 해빙기에 남반구의 온난화가 빨리 진행되고 북반구의 차별적 냉각 사건들이 발생하면서 북동무역풍이 강화되고 적도수렴대가 연구해역보다 남쪽에 위치하게 되면서 발생하였을 것으로 여겨진다. 중기플라이스토세 전환기와 지난 해빙기의 기록으로 볼 때,

중앙태평양 적도 해역의 해양학적 변화는 남북반구의 열적 변화에 의한 대기순환 변화에 크게 영향을 받음을 알 수 있다.

주요어 : 고해양학, 홍적세, 적도수렴대, 적도태평양, 기후변화
학 번 : 2011-30917

이학박사학위논문

Reconstruction of oceanographic properties and atmospheric circulation at the marginal regions of the Western Pacific Warm Pool during the late Quaternary

신생대 제 4기 동안의 서태평양 난수역의 해양학적 특성과 대기순환 복원

2016 년 2 월

서울대학교 대학원

지구환경과학부

서 인 아

Reconstruction of oceanographic properties and atmospheric circulation at the marginal regions of the Western Pacific Warm Pool during the late Quaternary

신생대 제 4기 동안의 서태평양 난수역의 해양학적 특성과 대기순환 복원

지도교수 이 용 일

이 논문을 이학박사 학위논문으로 제출함
2016 년 2 월

서울대학교 대학원
지구환경과학부
서 인 아

서인아의 이학박사 학위논문을 인준함
2016 년 2 월

위 원 장 최 영 숙 (인)
부위원장 이 용 일 (인)
위 원 안 진 호 (인)
위 원 최 기 성 (인)
위 원 정 대 교 (인)

Abstract

Reconstruction of oceanographic properties and atmospheric circulation at the marginal regions of the Western Pacific Warm Pool during the late Quaternary

Inah Seo

School or Earth and Environmental Sciences

The Graduate School

Seoul National University

Evolution of surface ocean environment in the eastern margin of the Western Pacific Warm Pool and its forcing mechanisms during the late Quaternary were investigated using various biogenic and lithogenic components in the northwestern and central equatorial Pacific where paleoclimatic records are rare due to paucity of sedimentary archives. To better understand the coupled behavior and interactions between the atmosphere and surface ocean dynamics, the provenance of eolian mineral dust and the composition of biogenic microfossils were investigated together.

For the last 600 kyr, eolian mineral dust deposited in the northwest Pacific, represented by a sediment core (12°30’N, 135°00’E) from the Philippine Sea, has

been supplied predominantly from the central Asian deserts (e.g., Taklimakan desert). It highlights that the prevailing wind system, rather than seasonal monsoon, has been the main transporting agent of eolian dust from Asian inland to the North Pacific. In contrast, eolian mineral dust deposited in a central equatorial Pacific site (5°53'N, 177°26'W) reveals Australian/South American dust affinity before 0.8 Ma but gradually increasing Asian dust signal after 0.8 Ma. The change in dust provenance was accompanied by an increased dust flux and a decrease in surface productivity and salinity. These changes can be explained by the southward movement of the Intertropical Convergence Zone (ITCZ) and North Equatorial Counter Current (NECC) and the direct influence of these features on the site after 0.8 Ma. The southward movement of the ITCZ is in phase with the warming trend observed in upwelling regions of the equatorial Pacific and Atlantic between 0.9 and 0.8 Ma. The southward movement of the ITCZ from 0.9 to 0.8 Ma indicates more significant cooling in the Northern Hemisphere (NH) than in the Southern Hemisphere across the Mid-Pleistocene Transition, which is supportive of the interpretation that the NH ice sheet expanded significantly and stabilized after 0.9 Ma.

For the last deglacial period, water column structure and temperatures were investigated in the central equatorial Pacific (6°40′N, 177°28′W) from a multiple-core by using oxygen isotopic compositions and Mg/Ca ratios of three planktplankticonic foraminifer species (*G. sacculifer*, *P. obliquiloculata*, and *G. tumida*) that dwell in mixed layer, upper thermocline, and lower thermocline, respectively. Only the upper thermocline temperatures have risen as high as 3°C during the last deglaciation between 18 and 12 ka, and then decreased to the present level since then. It can be explained by weakening of water column

stratification in the upper part of thermocline and shallowing of *P. obliquiloculata* habitat at this time. Such change coincides the period of decreased pole to equator temperature gradients in the SH and following NH cooling events, the Heinrich Stadial 1 (HS1) and Younger Dryas (YD), resulting in intensification of northeast Trades and southward migration of the ITCZ. Intensified wind-driven mixing and reduced precipitation during the last deglacial period likely had caused relatively nutrient-rich surface water condition without a significant surface cooling and migration of *P. obliquiloculata* to shallower depth. This interpretation leads to a conclusion that the ITCZ was placed far south to the study site during the last deglaciation and the study site was influenced by northeast Trades that prevails north of the ITCZ. This thesis emphasizes the strong control of atmospheric processes on the surface oceanography at the study site, i.e., north central equatorial Pacific, on the long-term global climate change.

Keywords : paleoceanography, late Pleistocene, inter-tropical convergence zone, equatorial Pacific, climate change

Student Number : 2011-30917

TABLE OF CONTENTS

LIST OF FIGURES

LIST OF TABLES

CHAPTER 1. INTRODUCTION

The buoyant warm water body with mean annual temperature exceeding 28°C and relatively low salinity (<35 psu) occupies approximately 11% of the Earth's surface ocean [*Gagan et al.*, 2004; *Webster*, 1994]. The largest expanse of this warm water, so called Western Pacific Warm Pool (WPWP), is located in the western equatorial Pacific (Figure 1-1). Easterly trade winds over the equator accumulate warm water to the west and induce equatorial upwelling off Peru and Ecuador, which maintains the zonal heat contrast between the eastern equatorial Pacific and WPWP. A subtle change, a fraction of a degree Celsius, in the zonal gradient of sea surface temperature (SST) across the equatorial Pacific causes a range of anomalous weather phenomena such as tropical storm activities, global patterns of flood and drought, and oceanic biological activity [e.g., *Rasmusson and Wallace*, 1983; *Schubert et al.*, 2004; *Siegert et al.*, 2001]. Because of its importance in the global climate system, the equatorial Pacific zonal SST gradient has been of great interest for past and future climate researches.

In the modern climate system, the fluctuation in the equatorial zonal SST gradient is manifested by two extremes: El Niño and La Niña (Figure 1-2). Therefore, a weakening of the zonal SST gradient and atmospheric circulation in the past and future climate research has been termed "El Niño-like," referring to modern analogy and a strengthening thereof has been termed ''La

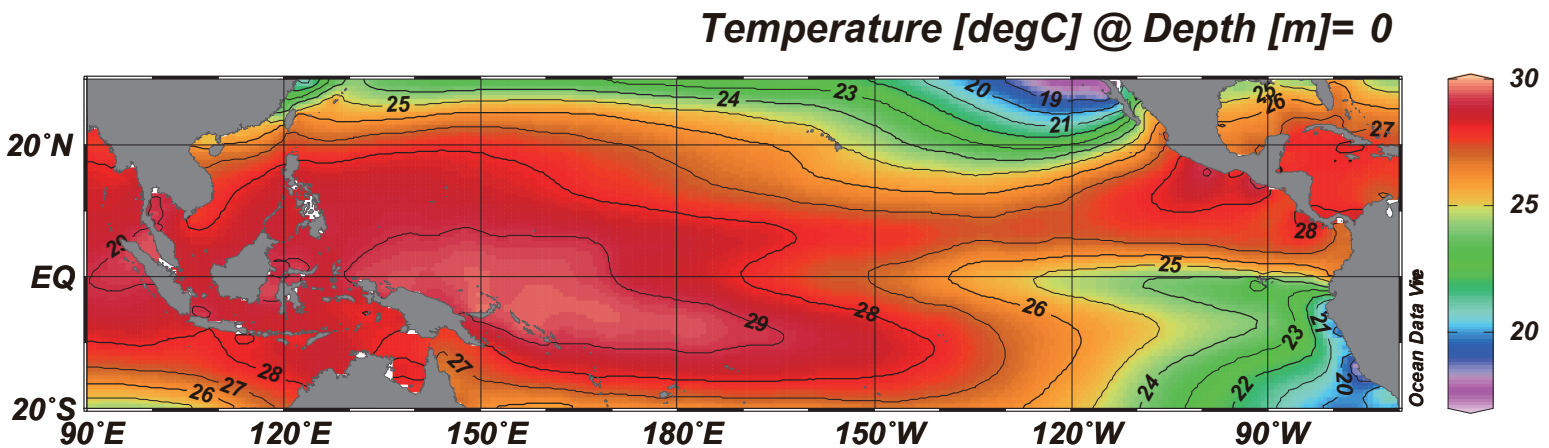

Figure 1-1. Annual mean surface temperature of the tropical-subtropical Pacific ocean (data source: World Ocean Atlas 2013).

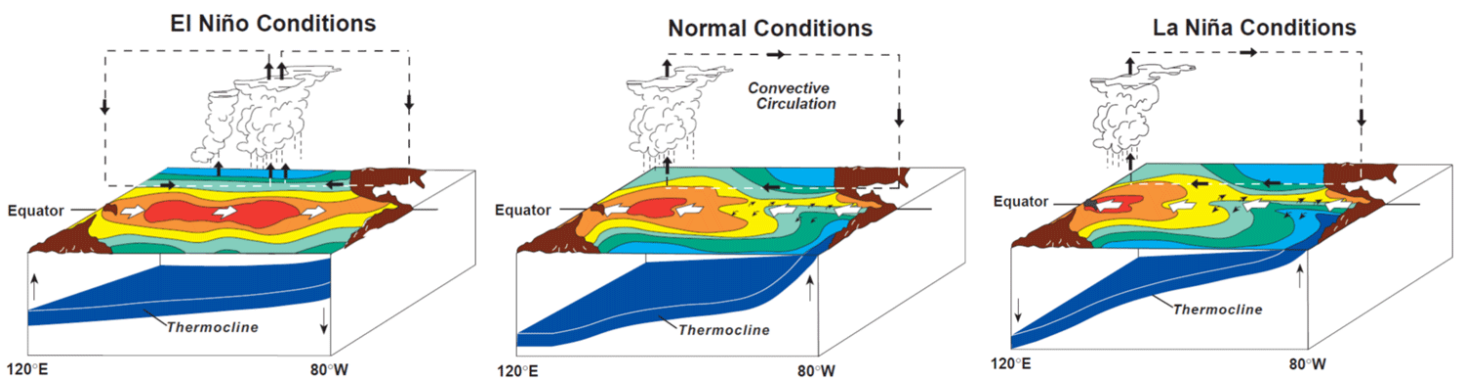

Figure 1-2. A schematic diagram showing an inter-annual variation of SST and water column structure in the tropical Pacific. Source: NOAA/PMEL/TAO Project Office, Dr. Michael J. McPhaden, Director

Niña-like'' in past and future climate studies [e.g., *Koutavas et al.*, 2002; *Vecchi et al.*, 2008; *Wara et al.*, 2005]. However, "El Niño-like" and "La Niña-like" conditions are defined solely based on the SST difference between the center of WPWP and East Pacific Cold Tongue (EPCT). Such simplified characterization of oceanographic and atmospheric states does not fully depict the mean state of tropical Pacific because forcing and feedback mechanisms in geologic past were likely different from those of the present. For example, oceanographic states of the Last Glacial Maximum (LGM) reveal the characteristics of both El Niño and La Niña of the modern climate system. In specific, the mean state of tropical Pacific during the LGM is often described as "El Niño-like" because of the decreased zonal SST difference between the centers of WPWP and EPCT regions [*Ford et al.*, 2015; *Koutavas et al.*, 2002], but also reveals faunal characteristics of the modern La Niña in the upwelling intensity in the EPCT region under the modern La Niña condition [*Feldberg and Mix*, 2002; *Martínez et al.*, 2003]. Thus, it is necessary to be supplemented with SST and water column structure data from multiple locations across the equator, in addition to two key locations (center of WPWP and EPCT), in order to better understand mean states of tropical Pacific in the geologic past.

The equatorial central Pacific near the date line is a critical location to monitor the climate state of tropical Pacific. For instance, weakened easterly winds under the El Niño condition induce the eastward expansion and/or migration of the WPWP, which causes cooling and shoaling in the western

Pacific and warming and deepening of thermocline in the central Pacific (Figure 1-2). In contrast, intensified easterly winds during La Niña shift the WPWP farther west and bring cold water to the central Pacific (Figure 1-2). For this reason, the zonal extent of WPWP has also been successfully used to describe the mean state of tropical Pacific during ENSO events [*Gill*, 1983; *McPhaden and Picaut*, 1990; *Picaut et al.*, 1996; *Picaut et al.*, 1997]. In addition, Central Pacific-type El Niño (El Niño "Modoki") and La Niña (La Niña "Modoki"), nontraditional ENSO variation, involve temperature anomalies arisen in the central Pacific [*Ashok et al.*, 2007; *Kao and Yu*, 2009; *Kug et al.*, 2009; *Yeh et al.*, 2009]. Thus, the central Pacific is one of the most plausible locations to understand the mean state of tropical Pacific in addition to the center of WPWP and EPCT.

Despite such climatic importance, paleo-extent and paleo-location of the eastern margin of WPWP and paleo-SST of the central equatorial Pacific have not been investigated so far partly because of the deficiency in sedimentary archives in this region. In the boundary region of the WPWP, pelagic sediments are mostly placed below the carbonate compensation depth (CCD; 4,000–5,000m depth in Pacific) and do not provide sediment accumulation rates to determine high-resolution climate variability (Figure 1-3). Thus acquisition of an appropriate sedimentary archive is crucial for the paleoceanographic studies of the margin of the WPWP including the central equatorial Pacific.

The atmospheric circulation, coupled to equatorial zonal SST gradient, has

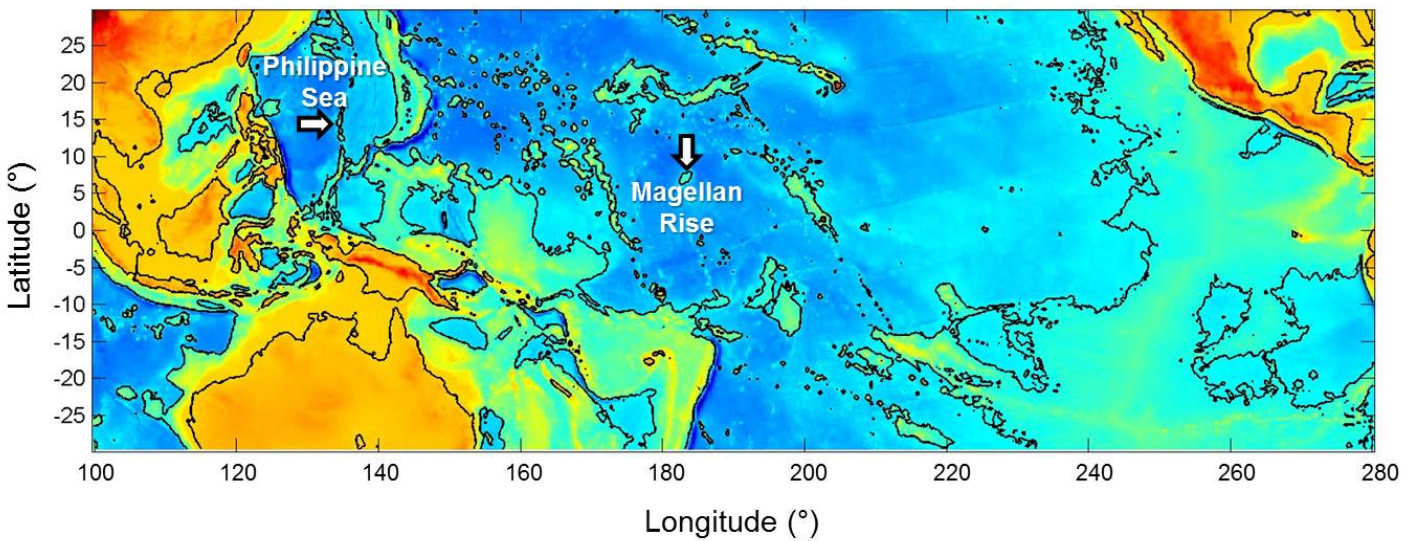

Figure 1-3. Bathymetry of tropical-subtropical Pacific. Black solid lines denote coastlines and 4000 m depth contour lines. Sampling locations are marked by arrows. Bathymetric data from *Ryan et al.* [2009]

been of interest as well in recent climate researches [*Held and Soden*, 2006; *Vecchi and Soden*, 2007; *Vecchi et al.*, 2006]. At present, the modes of prevailing winds in the tropical western Pacific vary by multiple meteorological factors; i.e., the migration of the inter-tropical convergence zone (ITCZ), Asian monsoon system, ENSO, etc. Therefore, the discussion dealing with the tropical climate and its variability should take into account not only the individual oceanographic and atmospheric variables, but also their interactions and feedbacks. The delineation of the source regions of wind-blown dust (i.e., airborne mineral particles) preserved in deep-sea sediments allows the reconstruction of changes in governing wind regimes over geologic timescales, which in turn aids in understanding the response of the atmospheric circulation system to forcing mechanisms. To date, most dust studies using deep-sea sediment archives from the Northwest Pacific, especially in the tropical-subtropical region, have focused on understanding the mass flux variation of Asian dust in terms of long-term climate variability [e.g., *Pettke et al.*, 2000; *Wan et al.*, 2012; *Xu et al.*, 2012], but have not considered specific transport pathways or specific dust source regions.

Provenance of wind-blown dust would give a valuable information of dust transport mechanisms and the past atmospheric circulation pattern, as exemplified in the studies to trace the paleo-position of the ITCZ [e.g., *Hyeong et al.*, 2014; *Xie and Marcantonio*, 2012]. In the geologic history, variation in ITCZ has been a major climatic response of tropical Pacific to high-latitude climate, through the change in atmospheric temperature gradient

resulting in the strength of southeast and northwest trade winds. The relative strength of trade winds, also a key driver of equatorial upwelling and the Walker Circulation, can be inferred from the ITCZ position. Therefore, the more integrated understanding of ocean-atmosphere coupling in the past can be achieved by reconstructing dust provenance and the oceanographic properties.

This study aims to describe and interpret climate evolution in the eastern boundary region of the WPWP during the Quaternary using various biogenic and lithogenic components and therein geochemical proxies. From the three deep-sea sediment cores acquired from the Palau-Kyushu Ridge and Magellan Rise (Figure 1-3), sedimentary records in relatively high-resolution could be obtained owing to the elevated topography (~2,000 m higher than nearby basins) of sampling sites. In addition, the ITCZ lies over the sampling sites where its seasonal latitudinal fluctuation is minimal; thus the mean position of the ITCZ and its possible connection to oceanographic variables can be assessed. This thesis consists of three main subjects; 1) Provenance and transport mechanism of dust in the subtropical northwest Pacific, 2) Change of atmospheric and surface ocean circulation in the central equatorial Pacific across the MPT, and 3) Climatic evolution of the central equatorial Pacific during the last deglacial period.

First, possible changes in atmospheric circulation pattern in the tropical Northwest Pacific (Palau-Kyushu Ridge in Philippine Sea, Figure 1-3) were examined as well with geochemical characterization of Asian deserts, the

most probable source regions for entire North Pacific. Based on the characteristics of mineral dust deposited in the North Pacific, the change in paleo-position of the ITCZ and the relevant oceanographic evolution across the Mid-Pleistocene Transition (MPT) at the Magellan Rise located in the eastern margin of WPWP. Finally, variations in SST and water column structure are investigated using oxygen isotopic compositions and Mg/Ca ratios of three planktic foraminifera species (*G. sacculifer*, *P. obliquiloculata*, and *G tumida*) that dwell in different water depth. This multi-species approach helps understand temperature gradients between the surface and the lower part of thermocline. This study provides high resolution proxy data in the central equatorial Pacific region for the first time, which allows better understanding on the changes in mean state of tropical Pacific across the MPT and for the last deglacial period by comparison with abundant proxy data available in the center of WPWP and EPCT.

CHAPTER 2. MATERIALS AND METHODS

2.1. Study Area

Three deep-sea sediment cores were obtained from the eastern and northern margins of the WPWP for the multi-proxy analyses (Figure 2-1). PC 631 was collected from the Palau-Kyushu Ridge in the Philippine Sea at the northern margin of the WPWP (12°30′N, 134°60′E, 3,728 m water depth). A multiple core, MC 931, and a piston core, PC 932, were acquired from the Magellan Rise, in the central equatorial Pacific at the eastern margin of the WPWP (6°40′N, 177°28′W, 3,365 m depth and 5°53′N, 177°26′W, 4,136 m depth, respectively).

The WPWP plays a leading role in driving a coupled ocean-atmospheric circulation. Solar heating and high precipitation maintain the warm water body buoyant with high SST and low sea surface salinity (SSS). The present-state WPWP was established about 4–3.6 Ma, resulted from the closure of the Indonesian and Central American seaways [*Chaisson and Ravelo*, 2000; *Li et al.*, 2006; *Sato et al.*, 2008]. Since its establishment, the role of warm pool, in the concept of the area of positive atmospheric heating (i.e. dynamic warm pool), is thought to be remained constant despite shifts in the background SST due to changes in climate states [*Hoyos and Webster*, 2012].

The Philippine Sea is a marginal sea on the western part of the North Pacific Ocean bordered by the Philippines and Taiwan to the west, Japan to the north, the Marianas to the east and Palau to the south (Figure 2-1). Surface water of the Philippine Sea is less saline due to the high precipitation caused by the influences of

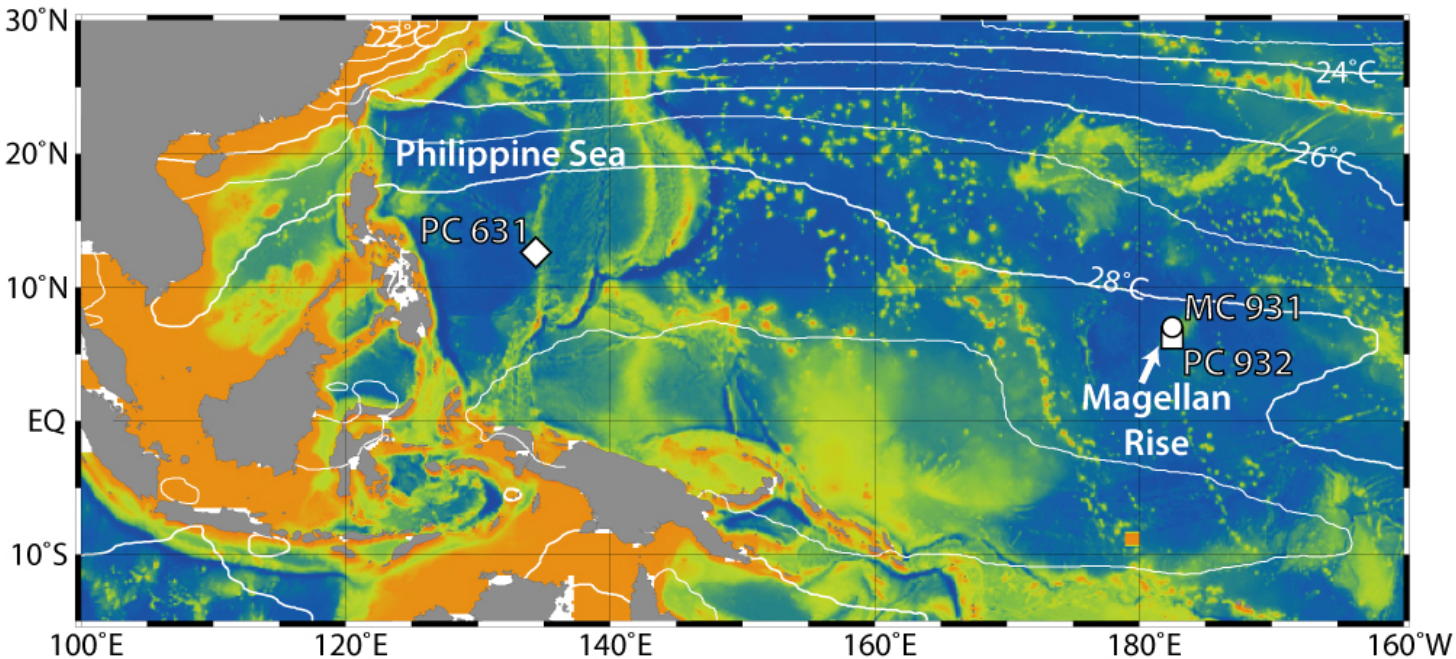

Figure 2-1. Locations of the sampling sites. The contours are for annual mean surface temperature (Data source: World Ocean Atlas 2013).

the ITCZ and upward component of the Walker cell [*Li and Wang*, 2012]. Since the Philippine Sea is one of the most oligotrophic regions in the world, biogenic components are not abundant in the sediment. Wind transport is thought to be the dominant depositional mechanism for the inorganic silicate component of sediments at the study site. Terrestrial sediments, transported by hemipelagic processes, are likely trapped in the marginal seas of China and the Philippine Basin due to the large distance between the site and surrounding coastlines and the elevated topography of the site (approximately 2000 m higher than the surrounding basin). The Kuroshio Current also prevents the long-distance transport of terrestrial sediments in suspension to the study area [*Huh et al.*, 1992; *Jiang et al.*, 2013; *Liu et al.*, 2007].

The Magellan Rise (Figure 1-3) is a large plateau located in the central equatorial Pacific, just north of the equator. The Pacific North Equatorial Countercurrent (NECC) transports surface warm water from the WPWP to the east over the Magellan Rise, while south bounding westward-flowing South Equatorial Current (SEC) at the equator induces equatorial divergence and recycling of nutrients. Owing to these two surface currents, the surface ocean at the Magellan Rise has SST similar to WPWP but higher biological productivity than WPWP center. The elevated topography (~3,000 m depth, about 2,000 m shallower than nearby basin) preserves carbonate-rich sediment with relatively high rates of accumulation with good preservation of microfossils. The input of lithogenic materials is considered being dominated by eolian process because of its isolated location from the continents.

2.2. Sample Information

A sediment core PC 631 is 240 cm long and composed of pelagic mud and calcareous-siliceous ooze. Based on the color of sediments, two lithological units are identified: foraminifera-rich, light brown mud (Unit A) and brown mud (Unit B) (Figure 2-2). The lithology of core is characterized by alternations of carbonate-rich mud and carbonate-poor mud. MC 931, a 32 cm-long multiple core, is composed of almost entirely calcareous ooze (Figure 2-2). PC 932 is 557 cm long, and composed of calcareous ooze and mud (Figure 2-3). Two lithological units are identified by sediment color: white carbonate ooze and pale brown carbonate ooze.

The cores were divided into 1 m-long sections and halved on board. The observation and sampling were performed on the working halves. The working sections were subsampled at 1 cm interval, freeze-dried and then stored in plastic bottles in a cool room. Every fourth sample was subjected to analyses in most cases. If necessary, additional samples were taken adjacent to these intervals. The main proxy systems used in this thesis are derived from the geochemical measurement of the calcite tests of the foraminifera, the isotopic and mineralogical composition of the airborne mineral particles and the relative contribution of various biological/detrital components. Three sediment cores used in this study were subjected to different multi-proxy analyses as summarized in Table 2-1.

2.3. Age Model

The conversion of depth to age in a sediment core is essential for data processing. In this study, various chronological approaches were taken depending on the

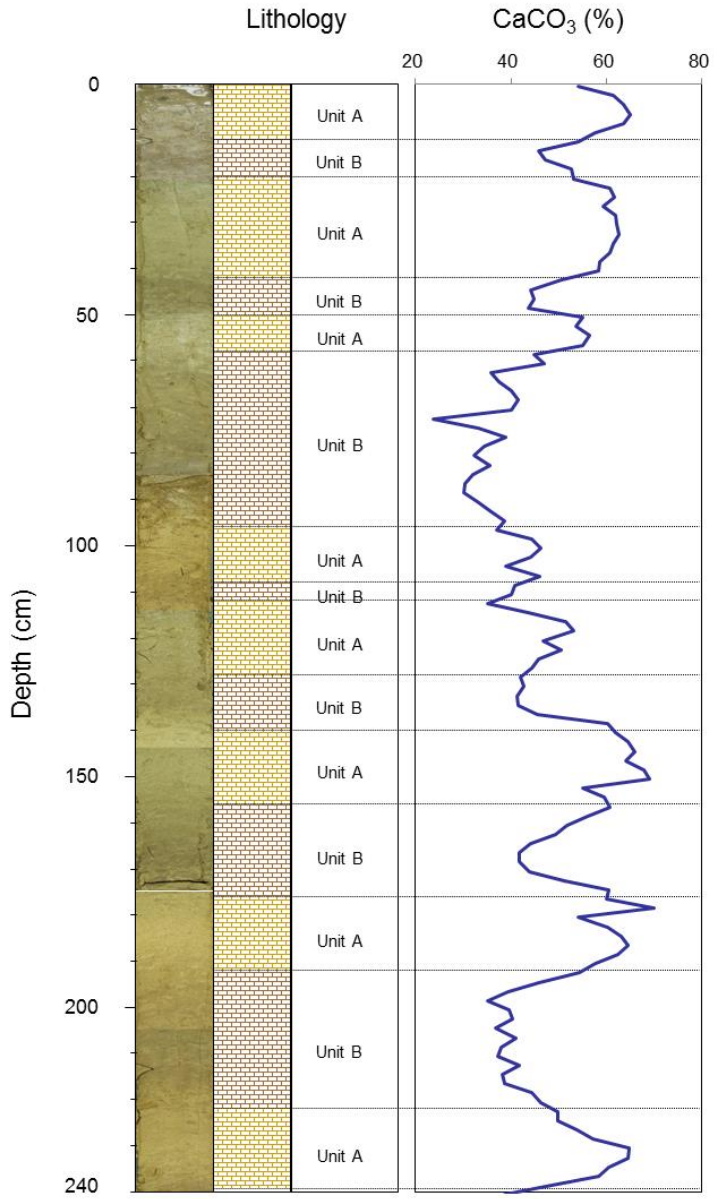

Figure 2-2. Slab photograph of PC 631 with its lithology and $CaCO_3$ content. Unit A: foraminifera-rich light brown mud, Unit b: brown mud.

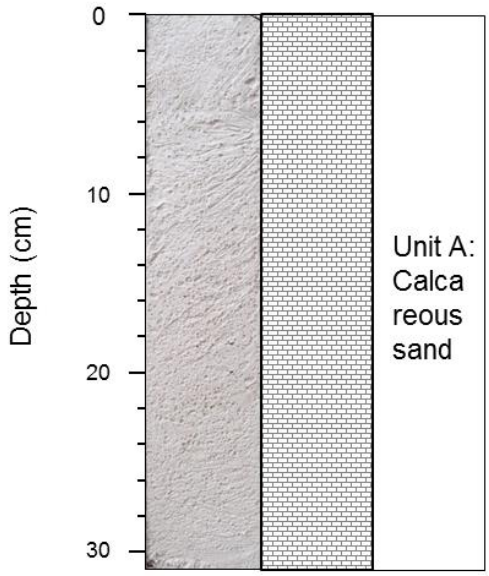

Figure 2-3. Slab photograph of MC 931 and its lithology.

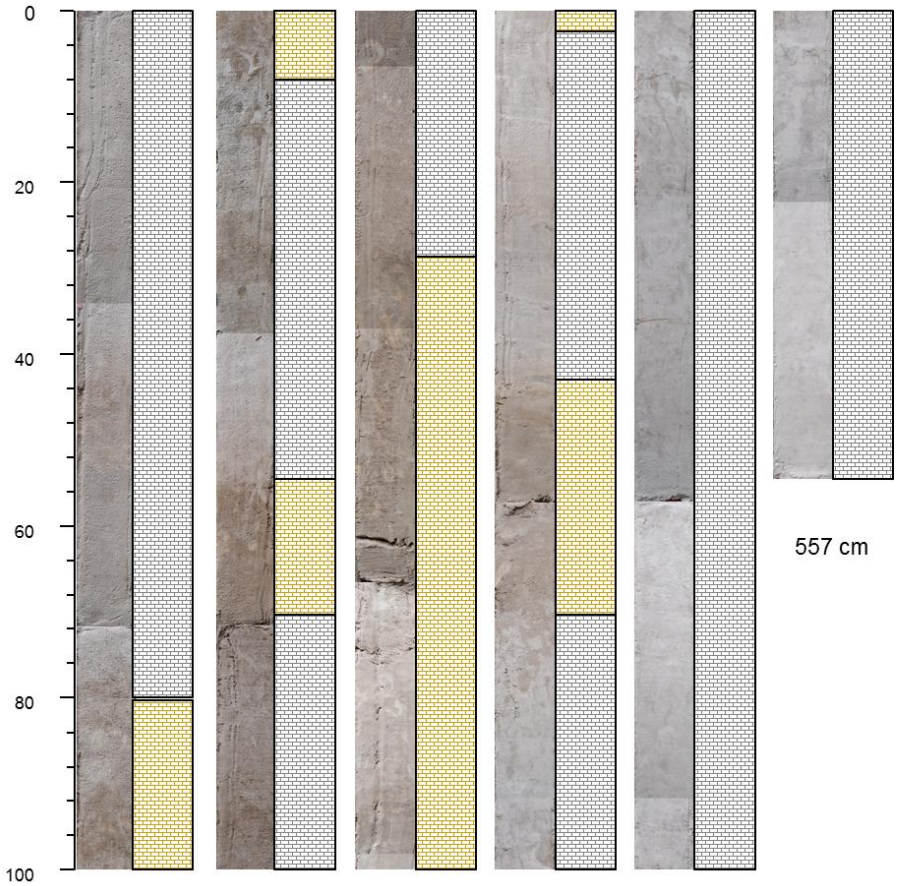

Figure 2-4. Slab photograph of PC 932 and its lithology.

Table 2-1. List of measured variables in this study

	Variable	PC 631	MC 931	PC 932
Age Model	Radiocarbon	√	√	
	Foraminifera $\delta^{18}O$	√	√	√
	Geomagnetic polarity			√
Biogenic components	Foraminifera Mg/Ca		√	
	Planktic foraminifera $\delta^{18}O$ and $\delta^{13}C$	√	√	√
	Benthic foraminifera $\delta^{18}O$ and $\delta^{13}C$	√		
	$CaCO_3$ content	√	√	√
	Biogenic silica content	√	√	√
Eolian components	Mass accumulation rate			√
	Radiogenic isotope composition ($^{87}Sr/^{86}Sr$, $^{143}Nd/^{144}Nd$)	√		√
	Clay mineral composition	√		

expected ages of samples and the temporal scope of the interpretation. For MC 931 and upper part of the PC 631, radiocarbon dating method was applied because these samples are expected to have ages younger than 50,000 yrs. On glacial-interglacial time scales, oxygen isotope composition ($\delta^{18}O$) of the planktic/benthic foraminifera in a marine sediment core is commonly used as a stratigraphic tool, based on the universality of the global seawater $\delta^{18}O$ fluctuation. For the lower part of the PC 631, oxygen isotope stratigraphy was successfully applied from the well-preserved foraminiferal record. The oxygen isotope composition of foraminifera in PC 932, however, gave an unreliable record, possibly indicating bioturbation by benthic organisms. Geomagnetic polarity reversals were therefore used to establish the age model of PC 932 although there are only three geomagnetic chrons over the last 1 Myr (i.e., Brunhes, Matuyama and Jaramillo).

2.4. Analyses of Biogenic Components

Biogenic components in deep-sea sediments provide a direct record of oceanographic condition in the past. The main carriers of paleoclimate information are the preserved organic and inorganic remains of microfossils: e.g., foraminifera, coccolithophores, diatoms as well as radiolarians and silicoflagellates. Among the various variables, SST and vertical water column structure are investigated using proxy records of foraminifera geochemistry. SST is a primary indicator of general climate state, providing information about oceanic heat and heat transport in the upper mixed layer. In addition, because proxy records can be easily calibrated into measurable environmental variable, proxy-derived SST can be the quantitative

verification of paleoclimate models.

2.4.1. Mg/Ca and stable oxygen isotope compositions of foraminiferal calcite

Foraminiferal Mg/Ca is one of the most successfully developed paleotemperature proxy. The exponential relationship observed between the amounts of Mg incorporated into foraminiferal calcite and the surrounding water temperature has been validated in many studies [*Anand et al.*, 2003; *Rosenthal et al.*, 1997; *Rosenthal and Lohmann*, 2002]. The relationship is empirically determined as a following equation:

$$Mg/Ca = b \times e^{aT},$$

where pre-exponential and exponential calibration constants are designated b and a, respectively, and T is calcification temperature. Recently, foraminiferal Mg/Ca in the Mediterranean Sea has varied significantly than cultured foraminifera in laboratory, and such variation was attributed to the large variation of seawater salinity [*Ferguson et al.*, 2008]. In this study, calibration constants with salinity component were adopted from *Sadekov et al.* [2009] that have been reported in the tropical western Pacific.

Besides of its use of chronological tool, stable oxygen isotope ($\delta^{18}O$) composition of foraminiferal calcite has been widely used as a proxy for seawater temperature and hydrographic properties. The $\delta^{18}O$ of foraminiferal calcite ($\delta^{18}O_c$) depends on the composition of seawater ($\delta^{18}O_{sw}$) and calcification temperature. $\delta^{18}O_{sw}$ is, for modern samples, locally defined as a function of salinity both been affected by evaporation and precipitation, among others hydrological effects. On

longer timescales (e.g., glacial-interglacial), $\delta^{18}O_{sw}$ also depends on global changes in ice volume. With a quantitative estimation of global ice volume and independent estimates of temperature, such as Mg/Ca of foraminifera, could help to constrain seawater salinity from $\delta^{18}O_c$.

In this study, three planktic foraminiferal species (*Globigerinoides sacculifer*, *Pulleniatina obliquiloculata*, *Globorotalia tumida*) are subjected to geochemical analyses. *G. sacculifer* lives in the upper 80 m of the water column, but its depth preferences varies depending on its growth stages and size classes [*Bijma and Hemleben*, 1994]. In its early stage of growth, *G. sacculifer* dwells in the upper photic zone (0–50 m depth) with small test size (<355 μm in diameter) [*Anand et al.*, 2003; *Bijma and Hemleben*, 1994; *Hemleben et al.*, 1987]. *P. obliquiloculata* dwells in the lower photic zone–upper thermocline (50–100 m depth), and its calcification temperature varies in a small temperature range [*Anand et al.*, 2003]. *G. tumida*, a thermocline-dwelling species, calcifies below the seasonal thermocline (100–250 m depth) [*Fairbanks and Wiebe*, 1980; *Farmer et al.*, 2007]. As *Sagawa et al.* [2012] verified the depth habitats of these three species in the WPWP region, calcification temperatures and seawater $\delta^{18}O$ of *G. sacculifer*, *P. obliquiloculata* and *G. tumida* are considered to represent those of mixed layer, upper thermocline and lower thermocline, respectively.

2.4.2. Calcium carbonate and biogenic silica contents

Marine biological processes responsible for changes in carbon cycle have been of interest in many researches because of their likely role in regulating atmospheric CO_2 level. In addition, information on marine paleoproductivity gives clue to

surface nutrient supply and utilization, and hence to ocean circulation in the past. Researches on the ocean surface productivity of the past have focused on the export flux of particulate organic carbon (POC) to the deep sea. However, because POC is easily regenerated in the water column before its burial, organic carbon content in the sediment does not represent the past export production properly. Instead, many parameters of deep-sea sediments have been suggested as a proxy for paleoproductivity although none of them is fully independent from diagenesis and dissolution that alter its property.

The quantitative methods relying on the flux of microfossils in the sediment are relatively simple approach to the estimation of surface production for the past. In this study, calcium carbonate and biogenic silica contents in sediments were measured from bulk sediments. Besides bulk sedimentation rate of biogenic components, the dominance of specific plankton group gives additional information about the oceanic condition favorable for the organism of interest. For instance, the relative concentration between nitrogen, phosphorous and silicate in the ocean dictates competitive dominance within phytoplankton communities [*Harrison*, 2000; *Yunev et al.*, 2007].

2.5. Analyses of Eolian Components

Because of the importance of mineral dust on the Earth's climate, in-depth understanding about the concentration, flux and transport pathways of mineral dust has been highlighted by many studies. One of the ways in which atmospheric dust has been studied is the use of model simulations, in which deflation, transport,

fallout and deposition are coupled, either on regional or worldwide scales [*Mahowald et al.*, 2007; *Tanaka and Chiba*, 2006]. For studies of dust for pre-historic time, mineral dust has been characterized with radiogenic isotope composition and clay mineralogy. Mineral aerosols from different sources are often indistinguishable in some cases when using a single geochemical or mineralogical attribute. Thus, the relative contribution of these potential sources requires investigation using multiple source indicators. For the delineation of dust sources, this study employs a multi-proxy approach using $^{87}Sr/^{86}Sr$, $^{143}Nd/^{144}Nd$ and clay mineral composition of dust fractions extracted from the acquired sediment samples.

2.5.1. Radiogenic Isotope Compositions ($^{143}Nd/^{144}Nd$ and $^{87}Sr/^{86}Sr$)

The radiogenic isotopic compositions of mineral aerosols reveal significant differences depending on geographic provinces. In the Pacific Ocean, the combination of Sr and Nd isotopic signatures, $^{87}Sr/^{86}Sr$ and $^{143}Nd/^{144}Nd$, has been proven to be an effective discriminator of dust source regions [*Asahara et al.*, 1995; *Hyeong et al.*, 2011; *Jones et al.*, 1994; *Nakai et al.*, 1993; *Stancin et al.*, 2006]. The major source regions of dust deposited in the Pacific Ocean are Central-Eastern Asian deserts, Central-South America and Australian deserts [*Hyeong et al.*, 2011; *Nakai et al.*, 1993; *Stancin et al.*, 2008; *Stancin et al.*, 2006]. Additionally, volcanic materials derived from the circum-Pacific arcs are clearly identified near the continents [*Asahara et al.*, 1995; *Nakai et al.*, 1993]. The analyzed Sr isotopes are usually given as their isotopic ratios, $^{87}Sr/^{86}Sr$, whereas the $^{143}Nd/^{144}Nd$ ratio is often expressed as a chondrite-normalized value $\varepsilon_{Nd}(0) = (((^{143}Nd/^{144}Nd/0.512638) - 1)\times10^4$ [*Jacobsen and Wasserburg*, 1980].

2.5.2. Clay Mineral Composition

Clay mineral assemblage in deep sea sediments has been used to define the provenance of detrital minerals. The mineralogy of the fine detrital fraction generally reflects the intensity of continental weathering in the source areas [*Biscaye*, 1965; *Griffin et al.*, 1968]. Clay mineral assemblage of deep sea sediments reflects relative input of various detrital sources supplied by hemipelagic and pelagic processes. Chemically stable clay minerals such as kaolinite and gibbsite are concentrated in the tropical-humid zone, whereas chlorite and illite are distributed at mid- to high-latitudes where intense chemical weathering is lacking [*Biscaye*, 1965; *Rateev et al.*, 1969]. The origin of marine smectite, or montmorillonite, is rather complicating because it can be derived from volcanism, hydrothermal activity or diagenetic processes [*Cole and Shaw*, 1983]. Without any evidences of such processes, smectite is often an indicator of mafic rock sources.

CHAPTER 3. PROVENANCE AND TRANSPORT MECHANISM OF DUST IN THE SUBTROPICAL NORTHWEST PACIFIC

Abstract

Dust transport to the tropical/subtropical northwestern Pacific over the past 600 kyr was investigated using radiogenic isotopes ($^{87}Sr/^{86}Sr$ and ε_{Nd}), together with the clay mineral composition, of eolian dust preserved in a sediment core obtained from the Philippine Sea (12°30′N, 134°60′E). These data revealed the influence of two prevailing dust sources, namely, the Asian deserts and nearby volcanic arcs (e.g., the Luzon Arc), with average contributions of around 70% and 30%, respectively, from each. The clay mineral composition of the core resembled dust from the central Asian deserts (CADs; e.g., the Taklimakan Desert) as in the North Central Pacific, but published aerosol data collected near the study site during winter/spring has the mineralogical signature of dust originating from the East Asian deserts (EADs). These data indicate that the relative contribution of EAD dust increases with the northeasterly surface winds associated with the East Asian Winter Monsoon (EAWM) during winter/spring, but the Prevailing Westerlies and Trade Winds that carry dust from the CADs is the dominant transport agent in the overall dust budget of the study site. The results of this study contradict the prevailing view that direct dust transport by the EAWM winds in spring dominates the annual flux of eolian dust in the northwest Pacific.

Chapter source: Seo, I., Y. I. Lee, C. M. Yoo, H. J. Kim, and K. Hyeong (2014), Sr-Nd isotope composition and clay mineral assemblages in eolian dust from the central Philippine Sea over the last 600 kyr: Implications for the transport mechanism of Asian dust, J. Geophys. Res. Atmos., 119, 11,492–11,504, doi:10.1002/2014JD022025.

3.1. Introduction

The delineation of the source regions of wind-blown dust (i.e., airborne mineral particles) preserved in deep-sea sediments allows the reconstruction of changes in governing wind regimes over geologic timescales, which in turn aids in understanding the response of the atmospheric circulation system to forcing mechanisms. Various geochemical attributes and clay mineral assemblages of eolian dust have been successfully used to identify source regions. For instance, dust carries the distinctive neodymium ($^{143}Nd/^{144}Nd$) and strontium ($^{87}Sr/^{86}Sr$) isotopic signatures of crustal evolution at the source region [*Asahara et al.,* 1995; *Biscaye and Dasch,* 1971; *Grousset et al.,* 1988; *Jones et al.,* 1994; *Nakai et al.,* 1993; *Stancin et al.,* 2006]. The clay mineral assemblages of dust preserved in deep-sea sediments also reflects the petrology of the parent rock and the weathering regime in the source regions [e.g., *Biscaye,* 1965; *Blank et al.,* 1985; *Griffin et al.,* 1968; *Petschick et al.,* 1996; *Wan et al.,* 2012].

The tropical/subtropical northwest Pacific is influenced by the seasonal reversal of prevailing surface winds due to the East Asian Monsoon system and the associated movement of the Intertropical Convergence Zone (Figure 3-1). As a result of this reversal, dust can be transported to the region from various sources; e.g., the central/east Asian deserts by either the East Asian Winter Monsoon (EAWM) or the zonal wind system (Prevailing Westerlies and Trade Winds) [*Merrill et al.,* 1989]; volcanic islands in the western Pacific; or the Australian deserts by the East Asian Summer Monsoon (Figure 3-1). It has also been suggested that North African dust, the largest dust source in the world, may reach the North

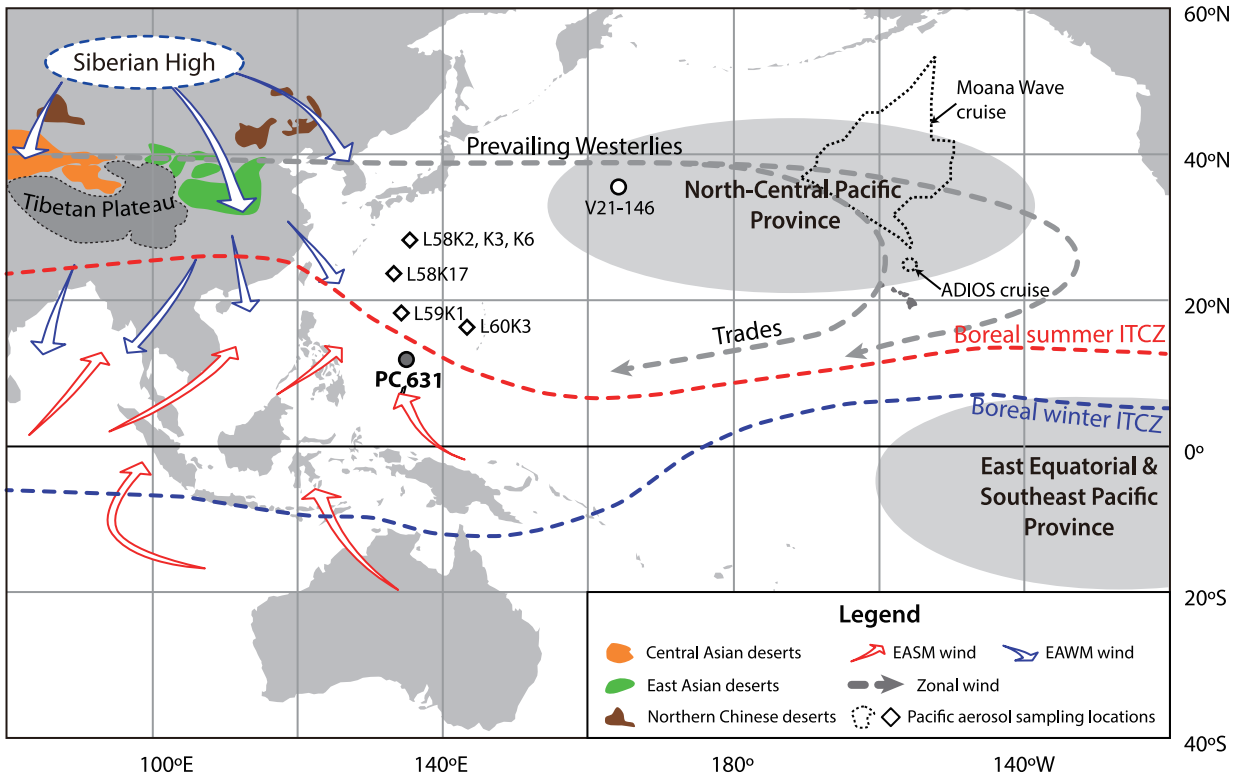

Figure 3-1. Location of core PC 631 (solid circle) and other aerosol (open diamonds) and sediment core (open circle) samples discussed in the text. Aerosol samples were collected during the Moana Wave cruise [*Arnold et al.*, 1998], ADIOS cruise [*Arnold et al.*, 1998], and in a series of DSDP cruises (L series samples) [*Leinen et al.*, 1994]. Location of core V21-146 from *Hovan et al.* [1991]. The winter and summer monsoon wind directions and trajectory of the prevailing westerlies are after *Merrill et al.* [1989], *Mohtadi et al.* [2011], *Nakagawa et al.* [2006], and *Zhang et al.* [1997]. The dust provinces north-central Pacific, and east equatorial and southeast Pacific, are from *Nakai et al.* [1993].

Pacific via long-range transport [*Hsu et al.*, 2012; *Lee et al.*, 2010; *Tanaka and Chiba*, 2006; *Tanaka et al.*, 2005].

The contribution of these potential sources to the global dust budget may be small, but the influence of each potential source could be significant at the regional scale [e.g., *Maher et al.*, 2010; *Tanaka and Chiba*, 2006]. These sources are not distinguishable in some cases when using a single geochemical or mineralogical attribute (e.g., $^{143}Nd/^{144}Nd$ and $^{87}Sr/^{86}Sr$ compositions of central and East Asian deserts, $^{87}Sr/^{86}Sr$ composition of Asian and Australian dust, and clay mineral composition of Australian and North African dust). Thus, the relative contribution of these potential sources requires further investigation using multiple source indicators [e.g., *Ferrat et al.*, 2011].

To date, most dust studies using deep-sea sediment archives from the North Pacific have focused on understanding the mass flux variation of Asian dust in terms of long-term climate variability [e.g., *Pettke et al.*, 2000; *Wan et al.*, 2012; *Xu et al.*, 2012], but have not considered specific transport pathways or dust source regions (e.g., central/East Asian deserts versus northern Chinese deserts). Dust is transported from Asia to the Pacific by two main air circulation systems; i.e., the Prevailing Westerlies and the near-surface northwesterly winds associated with the EAWM (Figure 3-1). Dust models and meteorological studies show that these two dust transport mechanisms follow different pathways and altitudes altitudes [*Shi and Liu*, 2011; *Yumimoto et al.*, 2009; *Zhang et al.*, 1997], and could transport dust from specific source region(s). However, dust transport mechanisms and source region relationships in the North Pacific have yet to be investigated using either aerosol or sediment studies.

This study examines the relative importance of these two dust-transport processes using geochemical indicators and clay mineral assemblage to differentiate between source regions. Additionally, as these two wind systems have varied in strength, direction, and pathway in the geologic past [*An*, 2000; *Ding et al.*, 1995; *Jiang and Lang*, 2010; *Liu and Ding*, 1993; *Nagashima et al.*, 2007; *Nagashima et al.*, 2011; *D Sun*, 2004; *Tian et al.*, 2005; *Zhang et al.*, 1999], it is possible that the contribution of potential dust sources and transport mechanisms has changed over longer timescales.

To characterize the provenance and transport pathways of eolian dust deposited in the western tropical/subtropical Pacific during the late Quaternary, we used the clay mineral composition, together with the $^{143}Nd/^{144}Nd$ and $^{87}Sr/^{86}Sr$ composition of the inorganic silicate fractions of a deep-sea sediment core retrieved from the Palau-Kyushu Ridge in the Philippine Sea (Figure 3-1). Using previously published data, we provide criteria to distinguish between dust from the major Asian dust source regions, which enabled us to identify prevailing transport pathways and the relative contribution of dust from specific sources to the dust budget of the study site. This study also provides a valuable dataset in an area with sparse isotopic and mineralogical data for furthering the understanding of dust sources and dust transport patterns in the northwest Pacific during the late Quaternary.

3.2. Materials and Methods

A 240-cm-long piston core, PC 631, was collected from the Palau-Kyushu Ridge in the Philippine Sea (12°30′N, 134°60′E, 3,728 m water depth; Figures 3-1 and -2).

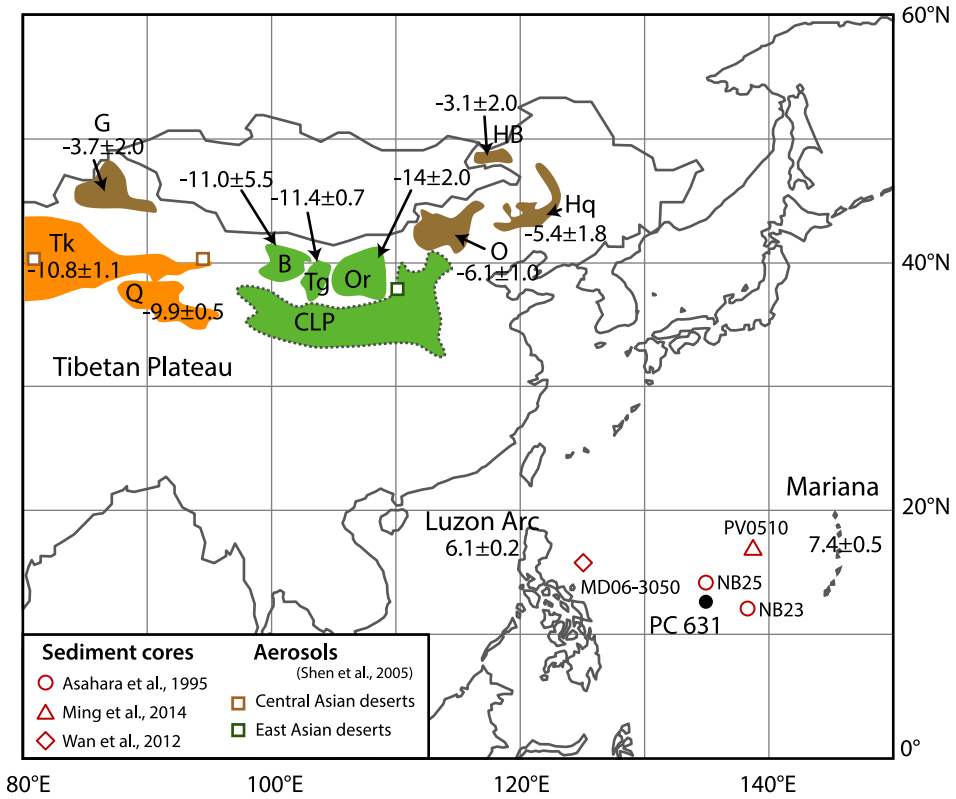

Figure 3-2. Locations of possible dust source regions (i.e., Chinese deserts, Luzon Island, and the Mariana Islands) and their reported ε_{Nd} compositions [*Chen et al.*, 2007; *Defant et al.*, 1990; *Dixon and Stern*, 1983; *Honda et al., 2004*; *Nakano et al.*, 2004; *Rao et al., 2008*; *Woodhead,* 1989]. The Asian deserts include the northern Chinese deserts (NCDs): the Gurbantunggut Desert (G), Onqin Daga Sandy Land (O), Hunlun Buir Sandy Land (HB), Horqin Sandy Land (HQ); the central Asian deserts (CADs): the Taklimakan Desert (Tk), Qaidam Desert (Q); and the East Asian deserts (EADs): the Badain Jaran Desert (B), Tengger Desert (TG), Ordos Desert (Or), and Chinese Loess Plateau (CLP).

Wind transport is thought to be the dominant depositional mechanism for the inorganic silicate component of sediments at the study site. Terrestrial sediments, transported by hemipelagic processes, are probably trapped in the marginal seas of China and/or the Philippine Basin due to the large distance between the site and surrounding coastlines, the elevated topography (ca. 2,000 m higher than the surrounding basin), and the Kuroshio Current, which also prevents the long-distance transport of terrestrial sediments in suspension to the study area [*Huh et al.*, 1992; *Jiang et al.*, 2013; *Liu et al.*, 2007].

The chronology of the core was determined by comparing the oxygen isotope record from the core derived from the benthic foraminifera, *Globocassidulina* sp., with the LR04 chronology [*Lisiecki and Raymo*, 2005]. Benthic foraminifera were picked at 2-cm intervals from the >125 μm size fraction. Isotopic analysis was carried out using a *Finnigan MAT 251* mass spectrometer at the University of Michigan at Ann Arbor, USA. The standard deviation of the repeat analyses of reference material NIST SRM-19 was less than 0.06% (n = 27).

The age model of the core was constructed using the Analyseries software [*Paillard et al.*, 1996] by graphical correlation of 34 tie points between the $\delta^{18}O$ record of PC 631 and the LR04 stack. Due to the disturbance of the top layer of the core during acquisition, additional ^{14}C ages from around 200 planktic foraminifera (*Globorotalia sacculifer*) were determined at 0–1 cm, 4–5 cm, and 14–15 cm intervals to avoid peak mismatching. ^{14}C was analyzed using a compact accelerator mass spectrometry system, *CAMS-500*, by Paleo Labo Co. Ltd., Japan. Age data were corrected for isotopic fractionation and calibrated to the calendar year before present (Cal ^{14}C age) using the Calib v. 7.0 software [*Stuiver and Reimer*, 1993].

This correction was based on the Marine13 dataset [*Reimer et al.*, 2013] and the local reservoir effect (ΔR) of 19 ± 50 years for Guam (13.5°N, 144.8°E) [*Southon et al.*, 2002].

The inorganic silicate fraction was extracted from 17 sediment samples following the method described by *Rea and Janecek* [1981]. The samples were treated with acetic acid buffered to pH 5 with sodium acetate to remove calcium carbonate. They were subsequently treated with a hot sodium citrate–sodium dithionite solution buffered with sodium bicarbonate to remove ferromanganese oxides and hydroxides. The solid residues were then sieved at 63 μm to remove coarse biogenic components, and finally treated with Na_2CO_3 solution to remove biogenic silica.

Grain size analysis of the inorganic silicate component was carried out for the 0.31–301 μm size interval using a *Master Sizer Micro* from Malvern Instrument Inc. Grain size data are reported as median grain size (in μm and ϕ_{50}) [*Folk*, 1974] with the amount of silty fraction (>16 μm), and the accuracy of the median diameter data is ± 2%.

$^{143}Nd/^{144}Nd$ and $^{87}Sr/^{86}Sr$ analyses, including chemical separation and multi-collector thermal ionization mass spectrometric (TIMS; *VG54-30*, *Isoprobe-T*) analyses, were performed at the Korea Basic Science Institute following *Cheong et al.* [2013]. Approximately 50 mg of the extracted powder samples were dissolved with an acid mixture of HF+$HClO_4$ (10:1) and HNO_3 for 24 hours in a tightly closed Teflon vials at 120°C. Sr was extracted by the conventional cation column chemistry (Dowex AG50W-X8, #200-400, H^+ form) using HCl media, and loaded on Ta filament with 1 M H_3PO_4. Major elements and rare earth element (REE) fractions were separated using conventional cation exchange column chemistry. Nd

was separated by the second step cation exchange column chemistry using 2-ethylhexyl phosphoric acid (HDEHP)-coated Teflon powder with HCl media, and loaded on Re filament with 0.1M H_3PO_4. $^{87}Sr/^{86}Sr$ and $^{143}Nd/^{144}Nd$ ratios were corrected for instrumental fractionation and spike contribution using $^{87}Sr/^{86}Sr$ = 0.1194, and $^{143}Nd/^{144}Nd$ = 0.7219, respectively. Replicate analysis of NIST SRM-987 and the La Jolla standard gave mean values of $^{87}Sr/^{86}Sr$ = 0.710246 ± 21 (n = 30, 2σ), and $^{143}Nd/^{144}Nd$ = 0.511832 ± 35 (n = 30, 2σ). Procedural blanks were less than 0.1 ng for Sr, and 0.04 ng for Nd. For convenience, $^{143}Nd/^{144}Nd$ ratios are expressed as ε_{Nd}; the deviation from the Chondritic Uniform Reservoir (CHUR) (ε_{Nd} = ($^{143}Nd/^{144}Nd/0.512638 - 1) \times 10^4$) [*Jacobsen and Wasserburg*, 1980].

Clay mineral assemblage was analyzed on bulk and oriented samples from the <4 μm size fraction of extracted inorganic silicates. This analysis was conducted on a *PANalytical X'pert Pro* X-ray diffractometer at the Korea Institute of Ocean Science and Technology, using CuKα radiation (40 kV, 30 mA) over the range of 3° to 30° at 0.02° steps. For the orientation of clay minerals, the supernatant <4 μm suspension was vacuum filtered onto a 0.45 μm membrane filter. The oriented samples were scanned after air-drying and ethylene glycol solvation. Semi-quantitative estimates of smectite (17 Å), illite (10 Å), kaolinite, and chlorite (7 Å) were made following the method of *Biscaye* [1965]. The relative amount of kaolinite and chlorite was determined by referring to the relative peak heights of 3.58 Å (kaolinite [002]) and 3.54 Å (chlorite [004]). For consistency, the clay mineral compositions of aerosol and sediments reported by *Arnold et al.* [1998], *Blank et al.* [1985], *Leinen et al.* [1994], and *Shen et al.* [2005] were converted using the weighting factors of *Biscaye* [1965].

3.3. Results

The median grain size of the silicate fraction varies in a very narrow range from 8.5 ϕ (2.8 μm) to 8.6 ϕ (2.6 μm), with an average of 8.6 ϕ (2.7 μm) (Table 3-1). The amount of silty components (>16 μm) is 2.2 ± 0.8 % (n=16, 1 σ). The graphical correlation between the $\delta^{18}O$ record of PC 631 and the LR04 stack [*Lisiecki and Raymo*, 2005] shows that the maximum age of the core sediments is approximately 600 kyr, which covers six glacial–interglacial cycles (Figure 3-3). The ages of the uppermost intervals, 0–1 cm, 4–5 cm, and 14–15 cm, were confirmed by ^{14}C ages (Table 3-1). The Cal ^{14}C ages of the 0–1 cm and 4–5 cm intervals are similar (10705 ± 58 and 11691 ± 106 yrs BP, 1σ, respectively), suggesting core-top disturbance during acquisition. The geochemical and clay mineral composition of the 4–5 cm interval is therefore not considered in the following discussion. The calendar age of the 14–15 cm interval (22019 ± 302 yrs BP, 1σ) is consistent with the estimated age from the $\delta^{18}O$ chronology (20.2 ka; Figure 3-3).

The $^{87}Sr/^{86}Sr$ and ε_{Nd} results are presented in Table 3-1 and Figure 3-3. ε_{Nd} and $^{87}Sr/^{86}Sr$ vary between −9.44 and −7.10, and 0.709627 and 0.711951, respectively. The $^{87}Sr/^{86}$ data are in good agreement with values of 0.7086 and 0.7103 reported by *Asahara et al.* [1995] at two nearby sites (NB23 and NB25; Figure 3-2). Neither ε_{Nd} nor $^{87}Sr/^{86}Sr$ showed any systematic down-core trend, but showed a moderate negative correlation ($r = -0.74$, $n = 16$). Clay mineral composition varied in a narrow range, and consisted mainly of illite (46 ± 4%, 1 σ) with subordinate amounts of smectite (25 ± 3%, 1σ), chlorite (19 ± 1%, 1σ), and

Table 3-1. Depositional age, $^{87}Sr/^{86}Sr$ and Nd isotopic compositions, clay mineral composition, and median grain size of the inorganic silicate fraction of the PC 631 sediments. Shaded intervals mark areas considered to have been disturbed during core acquisition (see text).

Depth (cm)	$\delta^{18}O$ Age (ka)	^{14}C age (yrs BP±1σ)	Cal ^{14}C age (yrs BP±1σ)	Isotope composition			Clay mineral composition (%)				Grain size (Φ50)	
				$^{87}Sr/^{86}Sr$ ±2σ	$^{143}Nd/^{144}Nd$ ±2σ	ε_{Nd}	Illite	Kaolinite	Chlorite	Smectite	(μm)	(ϕ)
0–1	0	11170 ±50	10705 ±58									
4–5	8.9	12208 ±57	11691 ±106	0.709247 ±11	0.512296 ±14	–6.67	45	14	18	24	3.2	8.3
14–15	20.2	20339 ±90	22019 ±302	0.709989 ±19	0.512247 ±13	–7.63	54	9	16	21	2.8	8.5
28–29	84.0			0.711077 ±13	0.512164 ±15	–9.25	53	9	18	20	2.7	8.5
44–45	106.4			0.710393 ±13	0.512196 ±15	–8.62	49	11	18	21	2.7	8.5
52–53	135.2			0.710474 ±13	0.512175 ±13	–9.03	49	10	19	22	2.7	8.5
71–72	208.4			0.709930 ±10	0.512242 ±14	–7.72	50	8	19	23	2.6	8.6
75–76	213.9			0.709792 ±11	0.512274 ±12	–7.10	47	8	19	26	2.7	8.5
84–85	226.5			0.709678 ±13	0.512250 ±14	–7.57	42	13	18	27	2.7	8.5
98–99	252.8			0.710151 ±11	0.512222 ±23	–8.11	46	9	20	25	2.7	8.5
108–109	278.3			0.710153 ±13	0.512233 ±13	–7.90	46	11	18	25	2.6	8.6

Table 3-1. (continued)

Depth (cm)	$\delta^{18}O$ Age (ka)	^{14}C age (yrs BP±1σ)	Cal ^{14}C age (yrs BP±1σ)	Isotope composition			Clay mineral composition (%)				Grain size (Φ50)	
				$^{87}Sr/^{86}Sr$ ±2σ	$^{143}Nd/^{144}Nd$ ±2σ	ε_{Nd}	Illite	Kaolinite	Chlorite	Smectite	(μm)	(ϕ)
114–115	291.4			0.709627 ±13	0.512270 ±11	–7.18	42	13	19	26	2.6	8.6
128–129	326.8			0.710710 ±14	0.512164 ±46	–9.25	39	11	19	31	2.6	8.6
146–147	352.5			0.710948 ±11	0.512231 ±13	–7.94	45	9	21	25	2.7	8.5
164–165	397.9			0.711139 ±14	0.512192 ±15	–8.70	45	10	20	25	2.6	8.6
184–185	434.3			0.711049 ±13	0.512244 ±12	–7.69	41	10	21	28	2.6	8.6
196–197	472.1			0.710859 ±15	0.512214 ±10	–8.27	41	10	18	31	2.6	8.6
228–229	573.7			0.711951 ±11	0.512154 ±15	–9.44	48	9	19	23	2.6	8.6
Average				0.710495	0.512217	–8.21	46	10	19	25	2.7	8.6

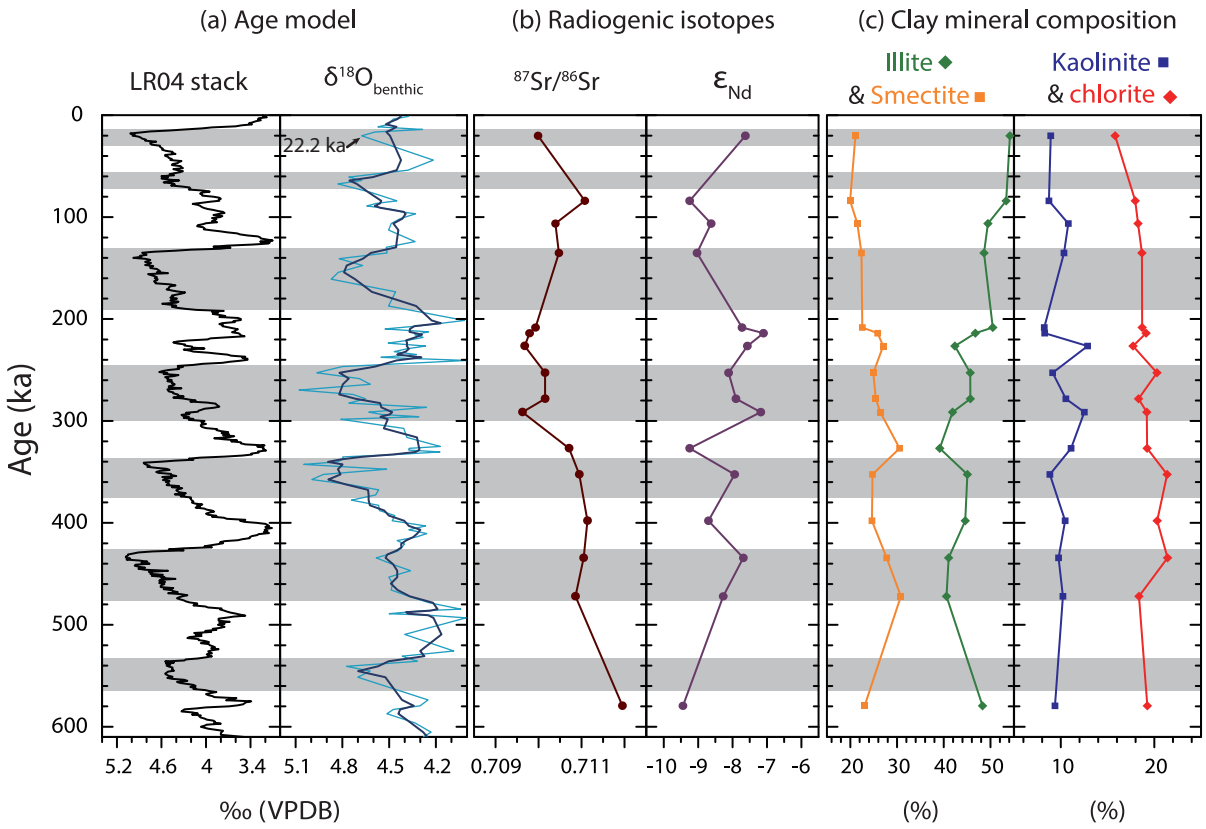

Figure 3-3. Down-core variations in: (a) stable oxygen isotope composition of benthic foraminifera in the LR04 stack and PC 631; (b) radiogenic isotopic compositions ($^{87}Sr/^{86}Sr$ and ε_{Nd}); and (c) clay mineral composition of the <4 μm fraction of eolian dust. The age model was constructed using the correlation between the benthic foraminiferal $\delta^{18}O$ records of PC 631 and the LR04 $\delta^{18}O$ stack [*Lisiecki and Raymo*, 2005] with AMS ^{14}C confirmation at the 14–15 cm interval (arrow). Shaded intervals indicate glacial periods.

kaolinite (10 ± 2%, 1σ; Figure 3-3).

3.4. Discussion

The median grain sizes of the abyssal sediments affected by hemipelagic processes are usually greater than 6.5 μm (<7.5 ϕ) because of the significant amount of silty components (>16 μm) supplied by hemipelagic processes [*Rea and Hovan*, 1995; *D Sun et al.*, 2002]. The winnowing process also concentrates coarser silty fractions at a depositional site as it removes fine fractions selectively. Thus, median grain size (2.7 ± 0.1 μm (8.6 ϕ)) and small amount (2.2 ± 0.8 % (n=16, 1 σ) of silty components (>16 μm) in the inorganic silicate fraction of PC 631 indicate negligible effect of hemipelagic and winnowing processes on sedimentation. In addition, the median grain size of inorganic silicate fraction of PC 631 is in good agreement with that (ca. 8.5 ϕ) of the north-central Pacific (NCP) where the hemipelagic processes are rare [*Rea*, 1994; *Rea and Hovan*, 1995]. These results indicate that the inorganic silicate fraction of this study is largely airborne mineral particles. For this reason, the inorganic silicate fraction is hereafter termed “eolian dust”, although it includes an unconstrained amount of volcanogenic and authigenic materials.

3.4.1. Sources of eolian dust in the PC 631 sediments

The NCP dust province (Figure 3-1) primarily receives dust from the central and East Asian deserts via the Prevailing Westerlies and Trade Winds, and has a distinctive isotopic (ε_{Nd}, $^{87}Sr/^{86}Sr$) and clay mineral composition [*Corliss and Hollister*, 1982; *Griffin et al.*, 1968; *Jones et al.*, 1994; *Nakai et al.*, 1993]. Our data

show slightly higher ε_{Nd} and lower $^{87}Sr/^{86}Sr$ than the NCP province sediments (Figure 3-4a), and are characterized by a slightly smectite-enriched composition compared to aerosols collected in the NCP (Figure 3-4b). Both Sr–Nd isotopes and clay mineral compositions plot along a mixing line between Asian dust, represented by NCP sediments, and the surrounding volcanic-arc components (Figure 3-4). This suggests that the study site has been influenced by the input of both Asian dust and volcanic arc material during its depositional history.

On a plot of ε_{Nd} versus $^{87}Sr/^{86}Sr$, the northwest Pacific and Mariana Basin sediments plot closer to the volcanic arc end-members than to samples from this study (Figure 3-4a), indicating that there is a higher contribution from arc materials in these areas. ε_{Nd} in samples from this study are also clearly distinguishable from south-central Pacific sediments, where eolian components are supplied from Australian deserts and New Zealand [*Stancin et al.*, 2008; *Xie and Marcantonio*, 2012] (Figure 3-4a). The clay mineral composition of samples from this study is also distinct from Australian and North African dust, which is enriched in kaolinite (Figure 3-4b). Consequently, all source indicators analyzed in this study; i.e., $^{87}Sr/^{86}Sr$, ε_{Nd}, and clay mineral composition, point to little or no contribution of Australian and Saharan dust to the study site.

The negligible input of Saharan dust to the western Pacific contradicts previous modeling results that predict the prevalence of Saharan dust in the region [e.g., *Luo et al.*, 2003; *Mahowald et al.*, 2007; *Tanaka and Chiba*, 2006]. As noted by *Tanaka and Chiba* [2006], the inconsistency between site-specific sediment data and modeling results may be due to the coarse resolution of the global dust models. The minimal contribution of Australian dust at the site may be a result of its small

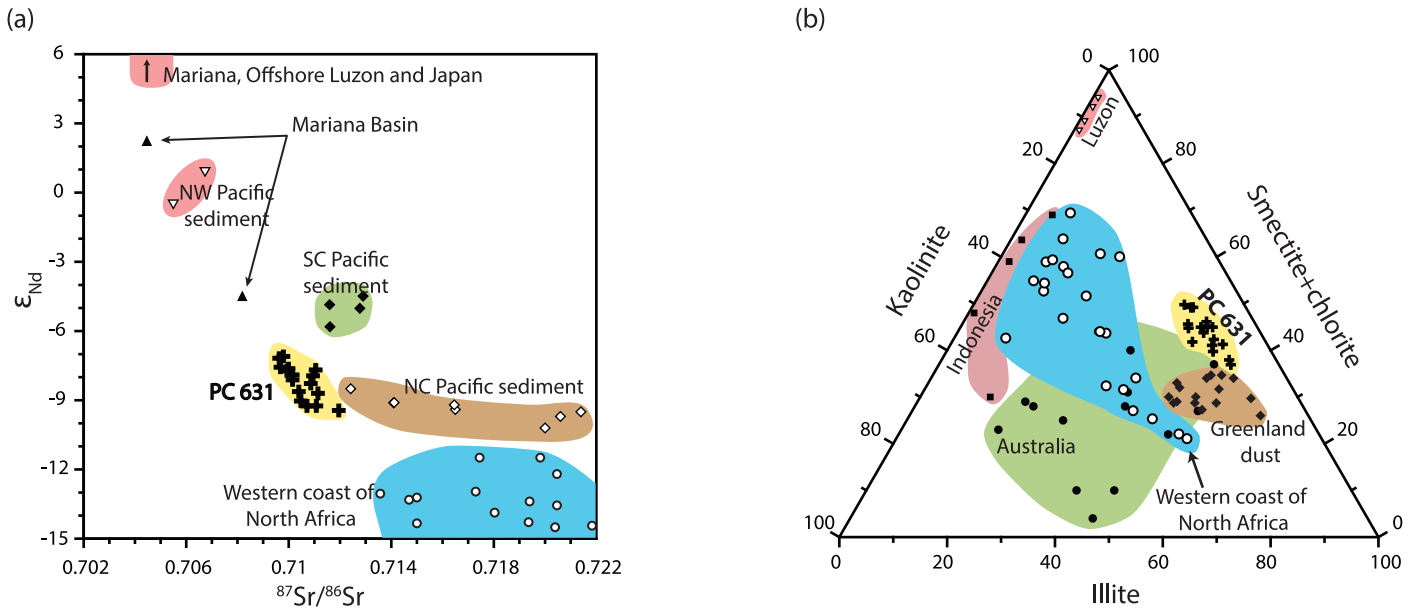

Figure 3-4. (a) ε_{Nd} versus $^{87}Sr/^{86}Sr$ cross plot, and (b) ternary diagram showing the clay mineral assemblage of eolian fractions of core PC 631 (samples from glacial intervals are shown as open crosses and those of interglacial intervals are solid crosses). $^{87}Sr/^{86}Sr$ and εNd are from *Grousset et al*. [1998], *Hyeong et al.* [2011], *Nakai et al.* [1993], *Pettke et al.* [2000], *Stancin et al.* [2008], and *Woodhead* [1989]. Clay mineral compositions are from *Arnold et al.* [1998], *Aston et al.* [1973], *Biscaye et al.* [1997], *Chester et al.* [1971; 1972], *Gingele et al.* [2001], *Gingele and De Deckker* [2004], *Glaccum and Prospero* [1980], *Leinen et al*. [1994], *Liu et al.* [2009], and *Shi et al.* [1997].

contribution to the global dust budget (ca. 6%; *Tanaka and Chiba* [2006]). Additionally, the air masses to the study site originate from Australia due to the prevailing boreal summer wind direction (Figure 3-1), but the long transport distance may limit the contribution of Australian dust to the record.

3.4.2. Relative contribution of volcanic arc and Asian dust components

To understand the relative contributions from Asian dust and volcanogenic components to the record, a simple two-component mixing model was constructed using $^{87}Sr/^{86}Sr–\varepsilon_{Nd}$ (Figure3-5a) and clay mineral compositions (Figure 3-5b). Asian dust source areas were classified into three regions in these models: the northern Chinese deserts (NCDs; the northernmost desert regions in China), the central Asian deserts (CADs; deserts on the northwestern margin of the Tibetan Plateau), and the East Asian deserts (EADs; the Chinese Loess Plateau (CLP) and nearby deserts; Figures 3-1 and -2). These three regions can be distinguished from each other using their ε_{Nd} values, $^{87}Sr/^{86}Sr$ ratios, and clay mineral compositions (Figures 3-5 and -6a). In addition, it is known that dust from the EADs is predominantly carried by northwesterly surface winds associated with the EAWM, while dust from the CADs is mainly transported via the Prevailing Westerlies in the mid- to high-level troposphere [*Shi and Liu*, 2011; *Sun et al.*, 2001]. Therefore, the identification of specific source regions helps to identify dust transport mechanisms to the study site.

For the $^{87}Sr/^{86}Sr$-ε_{Nd} mixing model, Asian dust data from the <5 μm size fraction were used to constrain the grain-size dependence of $^{87}Sr/^{86}Sr$ [*Asahara et al.*, 1995; *Chen et al.*, 2007; *Feng et al.*, 2009]. The <5 μm size fraction accounts for an average of 83% (± 1%, 1 σ, n=16) of the extracted dust components, which helps to

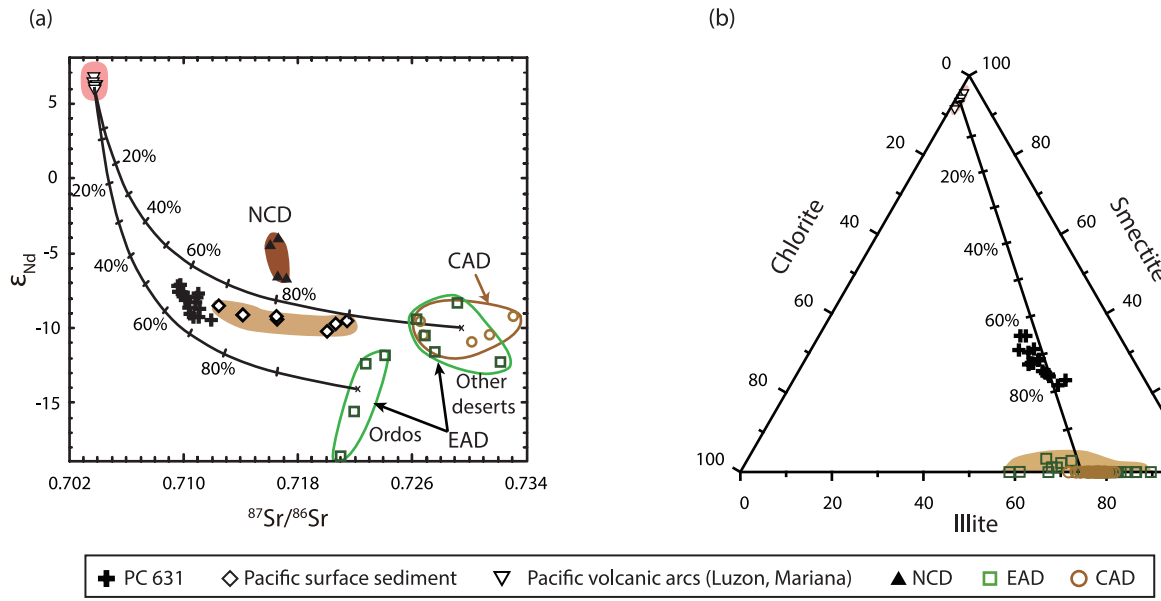

Figure 3-5. (a) ε_{Nd}–$^{87}Sr/^{86}Sr$ and (b) clay mineral composition of core PC 631 (crosses), north-central Pacific (NCP) surface sediment (diamonds), volcanic arcs in the western Pacific (inversed triangles), and soils in Chinese deserts grouped into three regions (see Figures 3-1 and 3-2). NCD, CAD, and EAD refer to the northern Chinese deserts, central Asian deserts, and East Asian deserts, respectively. Mixing lines are placed between the volcanic arc end-member, and the average composition of soils from the CADs and Ordos Desert in the ε_{Nd}–$^{87}Sr/^{86}Sr$ plot, and between volcanic arc end-members and the average composition of aerosols and soils from the EADs [*Biscaye et al.*, 1997; *Shen et al.*, 2005] and the CADs [*Shen et al.*, 2005] in the clay mineral composition plot. The known concentrations of Sr and Nd from Luzon Island (Sr = 440 ppm, Nd = 19 ppm) [*Defant et al.*, 1990] and the Chinese deserts (Sr = 111 ppm, Nd = 28.3 ppm) [*Kanayama et al.*, 2005] are used to develop mixing lines in the ε_{Nd}–$^{87}Sr/^{86}Sr$ plot. See Figure 3-4 for data sources.

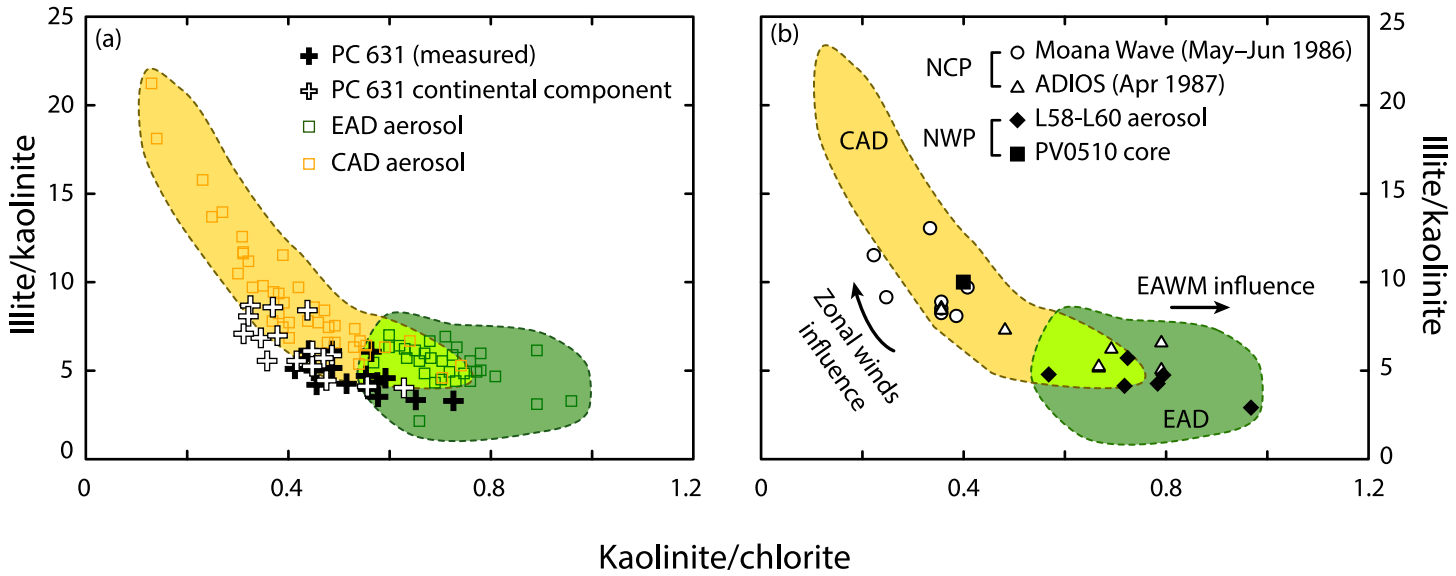

Figure 3-6. (a) Kaolinite/chlorite (K/C)–illite/kaolinite (I/K) diagram for core PC 631 and aerosol samples downwind of Asian dust source regions [*Shen et al.*, 2005]. The original composition (mixed dust from Asian deserts and the volcanic arc), and the estimated Asian dust end-member composition (see text for details) of PC 631 are marked as solid crosses and open crosses, respectively. (b) Kaolinite/chlorite (K/C)–illite/kaolinite (I/K) diagram of aerosols collected in the north-central Pacific (NCP) from the Moana Wave (open circles) and ADIOS (open triangles) cruises [*Arnold et al.*, 1998]. Aerosol (L58–L60) and sediment core (PV0510) data from the northwest Pacific are marked as solid diamonds and a solid square, respectively [*Leinen et al.*, 1994; *Ming et al.*, 2014]. The central Asian desert (CAD) and East Asian desert (EAD) domains are as Figure 3-6a.

minimize any errors related to differences in the grain size distributions between source and sample. For the clay mineral composition mixing-model, we used the composition of CLP sediments and aerosols collected downwind of the CADs and EADs as soil mineralogical data were unavailable.

In general, dust from the EADs and CADs possess a similar $^{87}Sr/^{86}Sr$–ε_{Nd} composition, except that the Ordos Desert has a distinctively low ε_{Nd} (Figure 3-5a). In the $^{87}Sr/^{86}Sr$–ε_{Nd} mixing model, samples plot between two mixing lines drawn between the average end-member compositions of volcanic arc–CAD sources (and EADs other than the Ordos Desert) and volcanic arc–Ordos Desert sources (Figure3- 5a), suggesting a supply of Asian dust from both CADs and EADs to the site. The mixing model also indicates that there is little contribution of dust from NCDs to the site, as its isotopic composition plots in an independent domain off the mixing lines (Figure 5a). Although the relative contribution of the CADs and EADs cannot be estimated uniquely, the mixing model suggests that Asian deserts contributed between 60% and 80% of the dust deposited at the study site, with the remainder originating from volcanic arcs (Figure 3-5a). This result is in agreement with the clay mineral composition mixing-model (Figure 3-5b).

3.4.3. Source regions and transport agents of Asian and volcanic arc dust

Dust storms frequently break out in the CADs (e.g., the Taklimakan Desert) throughout the year, and the entrainment of dust into high-level westerlies allows for the long-range transport of material to locations as distant as Greenland [*Bory et al.*, 2002, 2013; *Iwasaka et al.*, 2008; *Shi and Liu*, 2011]. In contrast, dust storms in the EADs primarily occur in spring, when the northwesterly winter monsoon

prevails. Dust from the EADs is therefore predominant downwind of mainland China and the northwest Pacific [*Shi and Liu,* 2011; *Sun et al.*, 2001; *Zhang et al.*, 1997] (Figure 3-1). The major transport agents of dust from the CADs and EADs are most likely the high-level westerlies and the low-level northwesterly winter monsoon, respectively.

Dust from the EADs and CADs have distinguishable illite/kaolinite (I/K) and kaolinite/chlorite (K/C) values (Figure 3-6) [*Shen et al.*, 2005], which enables an estimation of the relative contribution of these two major Asian dust source regions to the dust budget of the study site. Dust from the CADs is enriched in illite and chlorite, but is extremely poor in kaolinite (I/K = 9.2 ± 3.5, K/C = 0.4 ± 0.1, n = 40) due to the hyper-arid climate of the region (Figure 3-6a). In contrast, dust from the EADs is characterized by a moderate kaolinite content, and the resulting higher K/C (0.7 ± 0.1, n = 32) and lower I/K values (5.4 ± 1.1, n = 32) compared to CAD dust (Figure 3-6a) [*Shen et al.*, 2005; *Shi et al.*, 1997].

The I/K and K/C values of Pacific aerosols sampled at various zonal and meridional locations during winter and spring support the transport mechanisms and pathways of Chinese eolian dust discussed above (Figure 3-6b). Samples collected during the Moana Wave and ADIOS cruises in the NCP (Figure 3-1) are depleted in kaolinite [Arnold et al., 1998], and most have a clay mineral composition that corresponds to dust from the CADs (Figure 3-6b). This suggests that Asian dust, subjected to long-range transport by the Prevailing Westerlies, is dominantly sourced from the CADs rather than from the EADs. Aerosol samples collected in the month of April from the ADIOS cruise are kaolinite-rich compared to samples collected in May during the Moana Wave cruise (Figure 3-6b). This suggests that

increased entrainment of dust from the EADs into high-level westerlies contributes to the NCP dust budget in spring when the most intense and frequent dust storms occur in East Asia. In contrast to the NCP, aerosols collected during December–March in the northwest Pacific, when northwesterly winds associated with the EAWM prevail (L58K2, K3, K6, L59K1, and L60K3; Figure 3-1) [*Leinen et al.*, 1994], have clay mineral compositions that correspond to dust from the EADs (Figure 3-6b), confirming the dominance of this dust source in the region during winter and spring.

The eolian fraction of PC 631 sediments has I/K and K/C values (I/K = 4.6 ± 1, K/C = 0.53 ± 0.1, 1σ, n = 16; Figure 3-6a) in agreement with those of NCP aerosols, but plot in both the EAD and CAD fields (Figure 3-6). The clay mineral composition of samples corresponds to mixed dust from Asian deserts (60% to 80%) and volcanic arc sources (20% to 40%; see Section 4.2 for details). Thus, it is necessary to eliminate the components from volcanic sources to evaluate the relative importance of the CAD and EAD dust. To estimate the clay mineral composition of dust from Asian sources, we assumed an average 30% contribution from the volcanic component, with K/C and I/K values of 2 and 0, respectively, based on the average composition of Luzon soil [*Liu et al.*, 2009]. Exclusion of the volcanic components from the mineral composition mixing model results in a shift in the mineral composition of the observed data similar to those of NCP aerosol, suggesting the CADs as a likely dust source area (Figure 3-6). This suggests that, as in the NCP, the study site is dominated by CAD-sourced dust that travels via high-level westerlies. It is thought that dust from the CADs travels to the study site via the Prevailing Westerlies, and then via northeasterly Trade Winds, as depicted in the

dust transport trajectories in Figure 1 [*Merrill et al.*, 1989].

The results of this study are not in accordance with the reported clay mineral composition of dust from the EADs in the northwest Pacific from aerosol samples (L58-K2, -K3, -K6, -K17, L59K1, and L60K3; Figure 3-1) [*Leinen et al.*, 1994]. This discrepancy is most likely the result of differences in the timing of sample collection and the timescale of the two studies. As discussed earlier, collection of aerosol data from the northwest Pacific occurred in December–March, when dust from the EADs travels to the region primarily via northwesterly winds associated with the EAWM. In contrast, data from this study reflect the time-averaged composition of dust, and thus can be used to evaluate the relative importance of two dust transport mechanisms at the study site: the EAWM and the zonal wind system. Both datasets indicate that dust from EADs dominates during the EAWM season; however, dust from the CADs dominates the overall dust budget of the study site.

These results suggest that long-range transport via the Prevailing Westerlies and Trade Winds is the principal dust transport mechanism to the study site. The clay mineralogy of sediment core PV0510 (Figure 3-2), recovered in close proximity to our study site, was similar to that described here (I/K = ca. 10, K/C = ca. 0.4 on average of 2 myr interval; Figure 6b) [*Ming et al.*, 2014], which suggests the significant contribution of the CAD dusts in the northwest Pacific. The results of this study contradict the general perception that dust transport in spring by the EAWM dominates the annual flux of eolian dust to the northwest Pacific [e.g., *Ming et al.*, 2014; *Wan et al.*, 2012; *Xu et al.*, 2012], and highlights the importance of long-range transport by zonal winds to the dust budget of the northwest Pacific.

Data from volcanic arc materials collected near the study site have

similar $^{87}Sr/^{86}Sr$–ε_{Nd} values and clay mineral compositions (Figure 3-4). Consequently, the volcanic end-member sources cannot be evaluated using data from this study. However, $^{87}Sr/^{86}Sr$ and ε_{Nd} values, and clay mineral compositions, together with the proximity to the study site suggest that the Luzon Arc (represented by Luzon Island) is the most plausible source of volcanic end-member material. Volcanogenic particles and weathering products in the Luzon Arc may be transported to the study site when the summer monsoon prevails and westerly winds develop over the arc (Figure 3-1).

Despite its geographical proximity to the study site, the supply of volcanic materials from the Mariana arc is expected to be minor compared to that of the Luzon Arc because of its very small subaerially exposed area (ca. 1,000 km^2) compared to that of the Luzon Arc (ca. 300,000 km^2). Indonesia and Papua New Guinea are located in a tropical climate regime characterized by frequent storms and high precipitation, which results in weathering products dominated by kaolinite, as indicated in the mineral assemblages of Indonesian soil [*Gingele et al.*, 2001] (Figure 3-4b). These two sources do not explain the clay mineral composition of samples from this study, and they are thus excluded as potential volcanic end members. Mineral aerosols from Japanese arcs may be supplied to the study site, together with Asian dust, via surface winds associated with the EAWM. However, the transport of Japanese arc materials with the Prevailing Westerlies is limited to offshore areas proximal to the arc [*Asahara et al.*, 1995; *Jones et al.*, 1994; *Mahoney*, 2005; *Serno et al.*, 2014], probably due to the difficulty in entraining Japanese arc materials into high-level westerlies. As the study site is dominated by dust that travels via high-level westerlies, the contribution of Japanese arc materials

to the study site is considered negligible.

3.5. Conclusions

The ε_{Nd} values, $^{87}Sr/^{86}Sr$ ratios, and the clay mineral composition of eolian dust preserved in core PC 631 retrieved from the subtropical northwest Pacific indicate the mixed input of dust from the central and East Asian deserts (ca. 70%) and nearby volcanic islands (ca. 30%), likely the Luzon Arc, over the last 600 kyr. In contrast to the results obtained from previous global dust models, neither Australian nor North African dust contributed a detectable amount of dust to the study site, raising the possibility that the dust models underestimated the Asian dust contribution to budgets in the North Pacific. Further, the ε_{Nd} and $^{87}Sr/^{86}Sr$ composition of dust from the northern Chinese deserts, another major dust source in Asia, indicate that it was not a significant contributor at this site.

The clay mineral composition of the core resembles dust from the central Asian deserts (CADs; e.g., Taklimakan Desert), which is mainly transported to the north-central Pacific via the Prevailing Westerlies [*Iwasaka et al.*, 2008; *Shi and Liu*, 2011]. Thus, our results indicate that the zonal wind system is the dominant transport agent in the overall dust budget of the study site. Dust originating from the CADs most likely travels via the Prevailing Westerlies and then the northeasterly Trade Winds prior to deposition at the study site. In contrast, the clay mineral assemblages of aerosols trapped at the nearby site are similar to those of East Asian deserts (EADs) [*Leinen et al.*, 1994], indicating different transport pathways. As aerosol data reported by *Leinen et al.* [1994] were collected during the winter/spring

dust-storm season, this suggests that northwesterly surface winds associated with the East Asian Winter Monsoon act as the main dust transport agent during this period, but dust from the CADs dominates the overall dust budget. The results of this study do not agree with the general perception that transport by dust storms in spring dominates the annual flux of eolian dust in the northwest Pacific.

CHAPTER 4. CHANGE OF ATMOSPHERIC AND SURFACE OCEAN CIRCULATION IN THE CENTRAL EQUATORIAL PACIFIC ACROSS THE MID-PLEISTOCENE TRANSITION

Abstract

This paper investigates the causes of a brief, but prominent, cooling episode (1.1–0.8 Ma) that occurred in the equatorial upwelling region of the Atlantic and Pacific during the mid-Pleistocene Transition (MPT) using temporal changes in dust provenance, regional hydrology, and surface productivity recorded in a deep-sea sediment core from the central equatorial Pacific. The $^{87}Sr/^{86}Sr$ and ε_{Nd} values of the inorganic silicate fraction indicate deposition of dust from Australia and Central/South America before 0.8 Ma, but a gradual increase in Asian dust deposition after 0.8 Ma. The change in dust provenance was accompanied by an increased dust flux and a decrease in surface productivity and salinity. These changes can be explained by the southward movement of the Intertropical Convergence Zone (ITCZ) and North Equatorial Counter Current (NECC) and the direct influence of these features on the site after 0.8 Ma. Our results, together with previously published Atlantic data, suggest the northward position of the ITCZ between 1.1 and 0.9 Ma, and the southward position thereafter. The meridional movement of the ITCZ is in phase with the cooling and warming trend in upwelling regions in the equatorial Pacific and Atlantic, which suggests strengthening of

southeast trades relative to its northern counterpart between 1.1 and 0.9 Ma as a plausible cause of this brief cooling event. The southward movement of the ITCZ from 0.9 to 0.8 Ma indicates more significant cooling in the Northern Hemisphere (NH) than in the Southern Hemisphere, which is supportive of the interpretation that the NH ice sheet expanded significantly and stabilized after 0.9 Ma.

Chapter Source: Seo, I., Y. I. Lee, W. Kim, C. M. Yoo, and K. Hyeong (2015), Movement of the Intertropical Convergence Zone during the mid-pleistocene transition and the response of atmospheric and surface ocean circulations in the central equatorial Pacific, Geochem. Geophys. Geosyst., 16, 3973–3981, doi:10.1002/2015GC006077.

4.1. Introduction

The mid-Pleistocene transition (MPT) covers the period between 1.25 and 0.7 Ma during which the dominant glacial–interglacial periodicity changed from 41 kyr-cycles to 100 kyr-cycles [*Clark et al.,* 2006]. The appearance of strong 100-kyr periodicity at 0.9 Ma is often attributed to a significant increase in ice volume [*Elderfield et al.,* 2012; *McClymont et al.,* 2013]. Significant cooling of surface and deep water has been reported in polar/sub-polar regions prior to the emergence of the 100-kyr periodicity [*Lawrence et al.,* 2006; *Martínez-Garcia et al.,* 2010; *McClymont et al.,* 2008; *Sosdian and Rosenthal,* 2009], possibly preconditioning the development of major high-latitude glaciers and a change in the global ocean deep-water circulation [*Clark et al.,* 2006; *Head and Gibbard,* 2005; *McClymont et al.,* 2013].

One of aspects of this period that has received less attention is the pronounced cooling in the equatorial upwelling regions of the eastern equatorial Pacific/Atlantic between 1.1 and 0.8 Ma [*McClymont and Rosell-Melé,* 2005; *Schefuß et al.,* 2003] (Figure 4-1c and -1e), which is not evident in the global $\delta^{18}O$ stack and in the Western Pacific Warm Pool (WPWP) records [*Lisiecki and Raymo,* 2005; *McClymont and Rosell-Melé,* 2005] (Figure 4-1a and -1b). This cooling began at about 1.1 Ma and peaked at about 0.9 Ma. Sea surface temperature (SST) then rebounded rapidly and reached the background level around 0.8 Ma (Figure 4-1c and -1e). Although the lowest SSTs were recorded at the glacial maximum of Marine Isotope Stage 22, the SST drop during this period is particularly notable when compared with other glacial stages. As this cooling event was recorded both

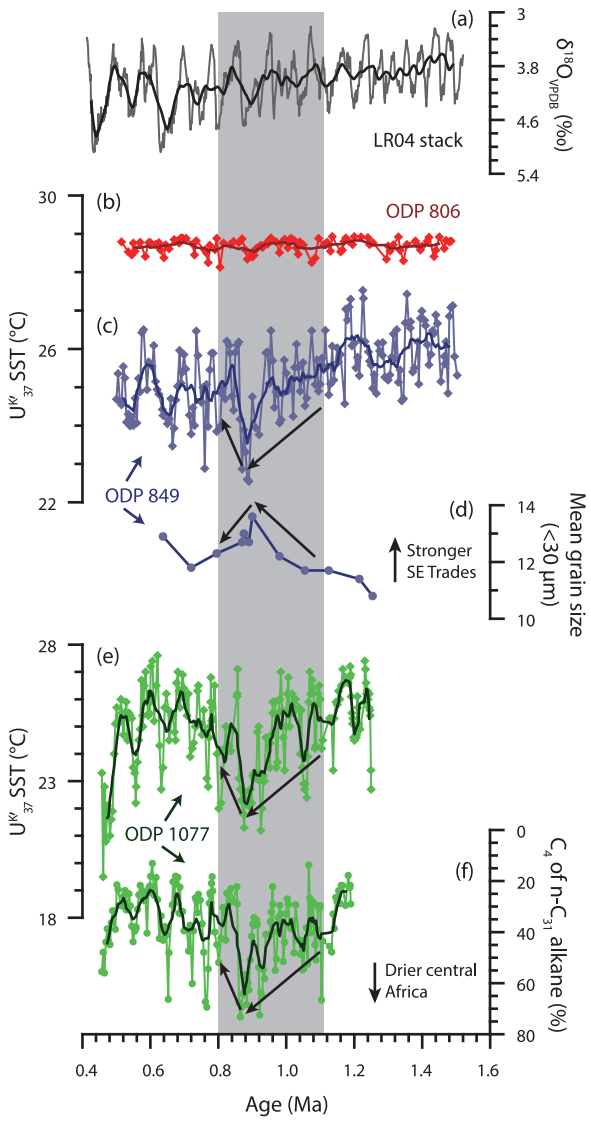

Figure 4-1. Long-term trends in paleoceanographic and paleoclimatic proxies during the middle to late Pleistocene. (a) LR04 benthic $\delta^{18}O$ stack [Lisiecki and Raymo, 2005], (b) $U^{K'}_{37}$ SST from Ocean Drilling Project (ODP) site 806 in the WPWP [McClymont and Rosell-Melé, 2005], (c) $U^{K'}_{37}$ SST, (d) mean grain size of fine sediment fraction (<30 μm), a proxy for trade winds strength, from ODP Site 849 in the central equatorial Pacific [McClymont and Rosell-Melé, 2005], (e) $U^{K'}_{37}$ SST, and (f) C_4 of n-C_{31} alkane (%) from ODP site 1077 in the eastern equatorial Atlantic [Schefuß et al., 2003].

in the equatorial Atlantic and Pacific, it can be seen as one of the major tropical responses to climate forcing during the MPT. As the MPT is regarded as the period during which more modern-like cold tongue and Walker Circulation first emerged [*de Garidel-Thoron et al.*, 2005; *Li et al.*, 2011], an explanation of the causes of this cooling event is required if we are to better understand the climatic evolution of the cold tongue region.

Latitudinal displacement of the Intertropical Convergence Zone (ITCZ), a belt of enhanced precipitation that results from the convergence of the northeast and southeast trade winds, has been highlighted as one of the key tropical responses to climate forcing over various timescales [*Broccoli et al.*, 2006; *Chao and Chen*, 2001; *Schneider et al.*, 2014]. In particular, shifts in the latitudinal position of the ITCZ are accompanied by changes in upwelling intensity and SST in the cold tongue region [*Koutavas and Lynch-Stieglitz*, 2003; *Timmermann et al.*, 2007; *Wang and Wang*, 1999]; consequently, tracing the ITCZ position during the MPT would assist our understanding of the mechanisms associated with the brief equatorial cooling event between 1.1 and 0.8 Ma.

This study aims to describe and interpret climate evolution over the equatorial Pacific during the MPT by investigating ITCZ movement and associated changes in regional hydrology and surface productivity. The study site is in the central equatorial Pacific near the international dateline, where the latitudinal range of the seasonal migration of the ITCZ is minimal (Figure 4-2), which helps us to trace its migration as the global climate changes. Our data also show the differential cooling history of each hemisphere over the MPT as the ITCZ shifts toward the hemisphere with reduced thermal gradient between equator and pole [e.g., *Broccoli et al.*, 2006;

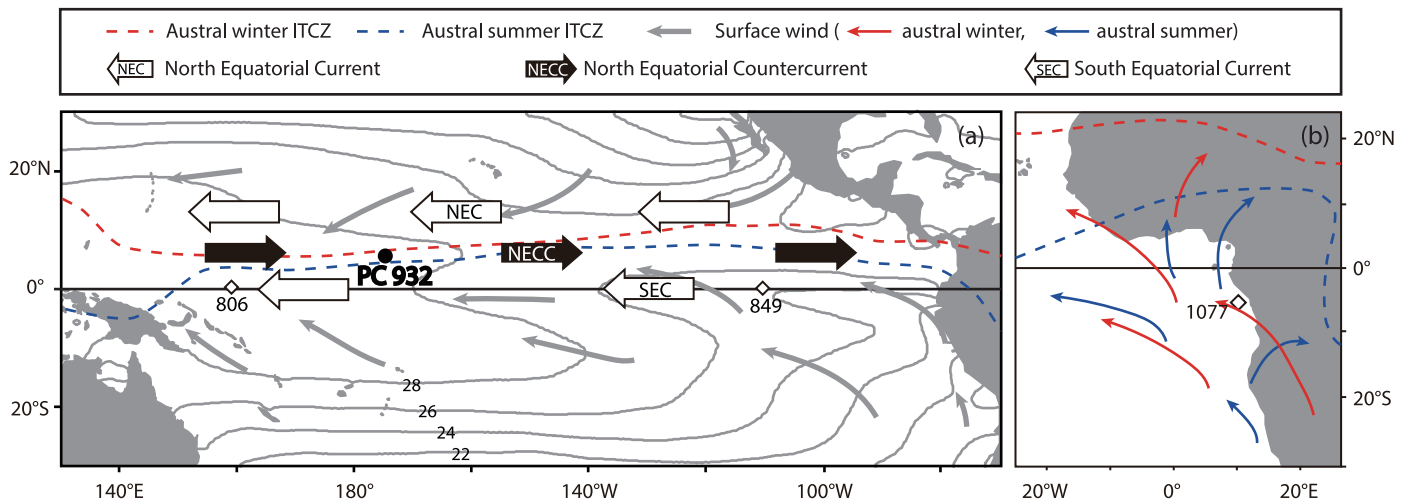

Figure 4-2. (a) Map of surface currents, surface winds and mean positions of the seasonal ITCZ over the tropical Pacific. The locations of the core analyzed in this study (PC 932), and ODP sites (806 and 849) are also marked. Annual mean SST data from the World Ocean Atlas 2013 are shown as gray contours [Boyer et al., 2013]. (b) General pattern of surface wind and ITCZ position over the east Atlantic with location of ODP site 1077 marked as open diamond.

Chiang and Friedman, 2012; *Flohn*, 1981; *McGee et al.*, 2014] .

4.2. Study Site and Analytical Methods

A 557-cm-long deep-sea sediment core, PC 932, was recovered from the Magellan Rise in the central equatorial Pacific (5°53′N, 177°26′W, 4,136 m water depth) during a cruise carried out by Korea Institute of Ocean Science and Technology (KIOST) in 2009 (Figure 4-2a). The core is composed mainly of calcareous ooze with minor contribution of pelagic mud and does not show any recognizable lithologic change with bare eyes. The North Equatorial Countercurrent (NECC), whose position is coupled with the ITCZ [*Donguy and Meyers*, 1996; *Masunaga and L'Ecuyer*, 2010], flows over the site and transports warm and low-nutrient surface water to the study site from the WPWP. To the south of the study site is the westward-flowing South Equatorial Current (SEC). Strong, upwelling favorable trade winds bring nutrients to the surface at the equator, resulting in higher primary production than in the WPWP and NECC regions [*Eldin and Rodier*, 2003; *Le Bouteiller et al.*, 2003].

The chronology of core PC 932 was established using magnetostratigraphic correlation. The core was sampled using u-channels of about 100 cm in length and a cross section of 4 cm^2 for paleomagnetic analysis. Magnetic remanence measurements of the u-channel samples were made at an interval of 1 cm using a 2G Enterprises pass-through superconducting magnetometer. The demagnetization data were processed using Puffinplot [*Lurcock and Wilson*, 2012].

To understand temporal changes in surface productivity, the total inorganic

carbon (TIC) and biogenic silica (Si_{bio}) contents were measured at a 4 cm interval. TIC was analyzed using a UIC CO_2 coulometer (CM5014) at the KIOST and then converted to $CaCO_3$ content by multiplying by 8.333 on the assumption that all inorganic carbon originated from $CaCO_3$. The analytical precision of the $CaCO_3$ content was ±1%. The Si_{bio} content was measured at KIOST using a UV spectrophotometer (UV-1601) and the wet alkaline extraction method adopted from *DeMaster* [1981] and *Müller and Schneider* [1993], with an analytical error of ±1%. The Si_{bio} was converted to opal content by multiplying by 2.4 [*Mortlock and Froelich*, 1989]. To semi-quantitatively assess the degree of carbonate dissolution, the size index (>63 μm $CaCO_3$/total $CaCO_3$ × 100%), proposed by *Broecker and Clark* [1999], was measured using the wet sieving method.

The radiogenic isotope composition of the eolian dust fraction in the studied samples was measured to investigate its source region. The inorganic silicate fraction (mostly eolian dust with very minor or trace amounts of volcanogenic and authigenic materials; hereafter termed eolian dust) was extracted from 12 sediment samples following the method described by *Hovan* [1995]. Referring to the "Pacific-style $CaCO_3$ cycles" [*Sexton and Barker*, 2012], the samples were collected at the horizons of maxima and minima over $CaCO_3$ cycles, which likely represent the glacial and interglacial periods, respectively. For the 12 samples, the eolian component was estimated from the following equation: weight of extracted inorganic silicate fraction/weight of bulk sediment × 2.5 × 100% [*Hovan*, 1995]. For other intervals, the fraction other than $CaCO_3$ and opal was approximated as an eolian component, and showed good agreement with the results of the other method (Figure. 4-3e). Analysis of the $^{143}Nd/^{144}Nd$ and $^{87}Sr/^{86}Sr$ ratios, including chemical

separation and multi-collector thermal ionization mass spectrometric (TIMS; *VG54-30, Isoprobe-T*) analysis, was performed at the Korea Basic Science Institute. Replicate analysis of NBS987 and JNdi-1 gave mean values of $^{87}Sr/^{86}Sr = 0.710246 \pm 0.000011$ (n = 10, 2σ), and $^{143}Nd/^{144}Nd = 0.512101 \pm 0.000015$ (n = 10, 2σ). For convenience, we express the $^{143}Nd/^{144}Nd$ ratios as ε_{Nd}; i.e., the deviation from a chondritic uniform reservoir ($\varepsilon_{Nd} = (^{143}Nd/^{144}Nd/0.512638 - 1) \times 10^4$) [*Jacobsen and Wasserburg*, 1980].

To understand temporal changes in local hydrology of the study site, stable oxygen isotope compositions ($\delta^{18}O$) of the planktic foraminifera *Globigerinoides sacculifer* (without final sac) in the 250–355 μm size fraction were determined using a Finnigan MAT 251 mass spectrometer at the University of Michigan at Ann Arbor, USA. The 1-sigma standard deviation of the repeat analyses of the reference material (NBS-19; National Bureau of Standards) was 0.09‰ (n = 24).

The relative content of each component to the bulk sediment was further converted to the mass accumulation rate (MAR) for the more accurate estimation of the influx of each component. The MAR is the product of the linear sedimentation rate (LSR) and the dry bulk density (DBD) of the sample. The latter was calculated from the determined porosity (P) and grain density of the sediments (ρ) using the relationship $DBD = (1 - P/100) \times \rho$ [*Rea and Janecek*, 1981]. Then, the MAR of each fraction (i.e., $CaCO_3$, opal, and eolian) was calculated by multiplying their weight percentage by the determined MAR.

4.3. Results

Sediment ages were determined at depths of 352 and 501 cm, which correspond to the boundaries of the geomagnetic chrons Brunhes–Matuyama (0.78 Ma) and Matuyama–Jaramillo (0.99 Ma), respectively (Figure 4-3a). The basal age of the core (557 cm) should be younger than the older boundary of the Jaramillo subchron (1.07 Ma) because the previous reversal subchron was not recovered in the core. Based on these magnetostratigraphic ages, the estimated LSRs were 0.45 cm/kyr and 0.70 cm/kyr for the 0–370 and 370–557 cm intervals, respectively.

$CaCO_3$, opal and eolian components account for, on average, 87.4% (78.3–92.2%), 7.9% (3.7–14.8%) and 4.7% (1.2–10.3%), respectively (Table 4-1). The relative contents of these three were converted to MARs and are presented in graphical form (Figure 4-3e). The size index, representing the >63μm fraction of the determined $CaCO_3$, accounts for 20.1 % on average (3.5–39.8%, Figure 4-3d). All four components show a significant up-core shift in content and MAR around 0.8 Ma (Figure 4-3d and -3e). The $\delta^{18}O$ of *G. sacculifer* ($\delta^{18}O_{Gsac}$) varies from −1.60 to −0.15‰ (−0.99‰ on average; Figure 4-3b). The glacial–interglacial variations are not clear enough for chronological correlation, and this is probably the result of the low sedimentation rate (ca. 0.5 cm/kyr) and bioturbation. However, the $\delta^{18}O_{Gsac}$ shows a marked up-core shift to lighter values from −0.72‰ to −1.14‰ on average around 0.8 Ma (Figure 4-3b). The gradual increase of $\delta^{18}O_{Gsac}$ until 0.9 Ma and subsequent decrease are apparent in the lower section younger than about 0.8 Ma. The measured ε_{Nd} and $^{87}Sr/^{86}Sr$ vary between −4.92 and −8.79, and 0.70949 and 0.71935, respectively (Figure 4-3d, Table 4-2), and show up-core trends towards gradually decreasing ε_{Nd} and increasing $^{87}Sr/^{86}Sr$ (Figure 4-3b). The compositional groupings between the upper (<0.8 Ma) and lower intervals (>0.8 Ma) are apparent

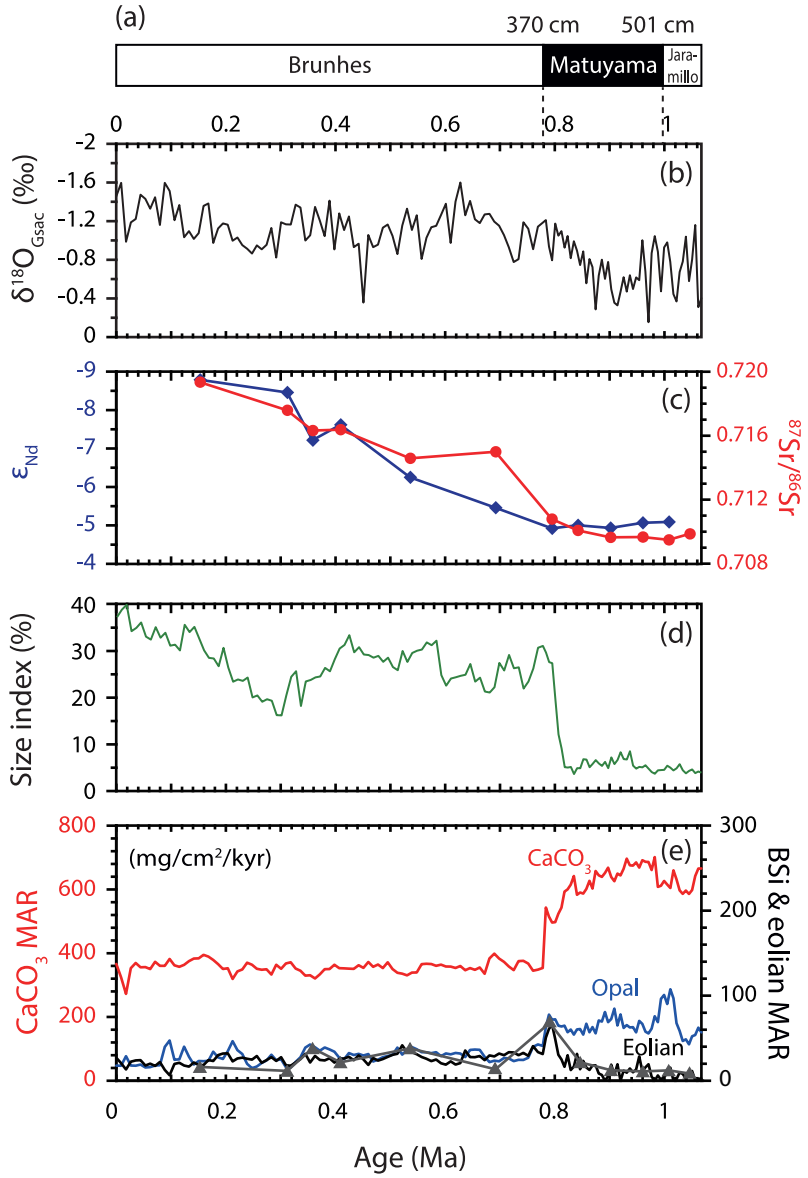

Figure 4-3. (a) Geomagnetic chrons used to define depositional age, (b) Stable oxygen isotope composition ($\delta^{18}O$) of planktic foraminifera *G. sacculifer*, (c) ε_{Nd} and $^{87}Sr/^{86}Sr$ values of the eolian component, (d) Proportion of coarse size fraction (CSF; >63 µm) in the $CaCO_3$ component, and (e) Mass accumulation rates (MARs) of $CaCO_3$ (in red), opalline silica (in blue), and eolian components (in black and gray) in core PC 932. Eolian MAR in black line represents the fractions other than $CaCO_3$ and opal, which show good agreement with eolian content measured using the chemical isolation method (gray triangles).

Table 4-1. Depositional ages and compositions of the studied core, PC 932 (5°53′N, 177°26′W, 4,136 m water depth).

Depth (cm)	Age (kyr)	$\delta^{18}O$ (‰)	Size index (>63 μm, %)	Amount of each composition (wt%)				MAR (mg/cm^2/kyr)				
				Opal	$CaCO_3$	Eolian[a]	Eolian[b]	Bulk	Opal	$CaCO_3$	Eolian[a]	Eolian[b]
0	0.0	-1.46	37.1	4.3	89.1		6.6	411	18	366		27
4	8.8	-1.60	38.8	4.9	89.4		5.7	362	18	324		21
8	17.7	-0.99	39.8	9.2	86.6		4.2	314	29	272		13
12	26.5	-1.19	34.1	4.6	89.8		5.7	393	18	353		22
16	35.4	-1.22	34.9	4.3	89.9		5.8	411	18	369		24
20	44.2	-1.47	36.0	4.8	89.1		6.1	399	19	356		24
24	53.0	-1.43	33.0	4.0	91.4		4.6	390	16	356		18
28	61.9	-1.33	32.3	4.1	90.7		5.2	386	16	350		20
32	70.7	-1.45	35.0	4.4	91.3		4.3	409	18	373		17
36	79.6	-1.16	32.8	4.5	89.9		5.5	401	18	361		22
40	88.4	-1.60	33.8	9.6	87.3		3.1	413	40	360		13
44	97.3	-1.51	31.0	10.8	87.7		1.5	436	47	382		6
48	106.1	-1.21	31.3	6.1	89.1		4.9	406	25	362		20
52	114.9	-1.37	30.0	6.2	88.5		5.2	404	25	357		21
56	123.8	-1.03	35.5	9.5	86.2		4.3	421	40	363		18
60	132.6	-1.10	33.9	6.7	89.3		4.0	420	28	375		17
64	141.5	-1.02	35.1	4.5	90.4		5.1	424	19	383		21
68	150.3	-1.08	32.6	5.5	90.2	3.7	4.3	426	23	384	16	18
72	159.1	-1.36	30.0	5.3	90.5		4.2	436	23	395		18
76	168.0	-1.38	28.4	5.4	89.1		5.6	437	23	389		24
80	176.8	-0.97	28.3	7.8	86.9		5.3	436	34	379		23
84	185.7	-1.12	26.6	6.5	86.4		7.1	423	27	366		30
88	194.5	-1.18	30.6	6.3	85.9		7.8	408	26	351		32
92	203.3	-1.16	26.4	8.3	84.0		7.7	420	35	353		32

Table 4-1. (continued)

Depth (cm)	Age (kyr)	$\delta^{18}O$ (‰)	Size index (>63 μm, %)	Amount of each composition (wt%)				MAR ($mg/cm^2/kyr$)				
				Opal	$CaCO_3$	Eolian[a]	Eolian[b]	Bulk	Opal	$CaCO_3$	Eolian[a]	Eolian[b]
96	212.2	-1.00	23.3	12.0	82.2		5.9	388	47	319		23
100	221.0	-1.03	23.8	8.9	84.7		6.5	405	36	343		26
104	229.9	-0.95	23.5	7.7	85.6		6.7	408	31	349		27
108	238.7	-0.91	24.2	4.8	89.0		6.2	416	20	370		26
112	247.5	-0.86	20.0	3.7	90.2		6.1	403	15	364		25
116	256.4	-0.95	20.4	4.2	88.5		7.3	397	17	351		29
120	265.2	-0.91	19.0	5.4	89.2		5.4	390	21	348		21
124	274.1	-0.96	19.6	6.0	87.9		6.1	398	24	350		24
128	282.9	-1.13	19.2	7.8	85.1		7.1	391	31	333		28
132	291.8	-0.82	16.2	5.9	88.5		5.7	411	24	364		23
136	300.6	-1.19	16.1	6.2	86.9		6.9	404	25	351		28
140	309.4	-1.17	20.4	4.0	91.5	2.7	4.5	402	16	368	11	18
144	318.3	-1.17	24.4	3.8	91.8		4.4	405	16	371		18
148	327.1	-1.37	25.6	5.6	89.0		5.4	395	22	352		22
152	336.0	-1.34	18.1	6.9	86.7		6.4	398	28	345		25
156	344.8	-1.00	23.4	9.8	82.4		7.9	400	39	330		32
160	353.6	-1.05	23.7	10.8	83.8		5.4	395	43	331		22
164	362.5	-1.35	24.2	10.1	82.4	9.6	7.5	389	39	321	38	29
168	371.3	-1.21	24.4	9.0	84.8		6.2	394	35	334		25
172	380.2	-1.04	26.3	9.5	84.7		5.8	413	39	350		24
176	389.0	-1.41	25.6	8.9	84.7		6.4	414	37	350		26
180	397.8	-0.91	28.2	8.1	86.8		5.1	419	34	364		21
184	406.7	-1.28	30.4	6.7	87.0	5.2	6.3	406	27	353	21	26
188	415.5	-1.11	31.2	6.2	87.3		6.5	404	25	353		26

Table 4-1. (continued)

Depth (cm)	Age (kyr)	$\delta^{18}O$ (‰)	Size index (>63 μm, %)	Amount of each composition (wt%)				MAR (mg/cm^2/kyr)				
				Opal	$CaCO_3$	Eolian[a]	Eolian[b]	Bulk	Opal	$CaCO_3$	Eolian[a]	Eolian[b]
192	424.4	-1.25	33.3	7.9	85.3		6.8	412	33	352		28
196	433.2	-0.93	29.6	7.5	86.6		6.0	405	30	351		24
200	442.0	-0.97	30.7	7.5	85.5		7.0	424	32	362		30
204	450.9	-0.36	29.2	7.3	86.6		6.1	409	30	354		25
208	459.7	-1.06	29.0	7.4	88.2		4.4	423	31	373		19
212	468.6	-0.93	28.5	5.6	87.9		6.6	407	23	357		27
216	477.4	-0.96	28.9	6.0	88.3		5.7	413	25	364		24
220	486.3	-1.13	27.6	6.8	86.9		6.3	407	28	354		25
224	495.1	-1.17	28.5	6.8	86.7		6.5	429	29	371		28
228	503.9	-1.05	26.5	7.4	85.1		7.4	411	31	350		31
232	512.8	-0.86	25.8	9.5	82.7		7.7	409	39	339		32
236	521.6	-1.15	29.9	7.5	82.3		10.2	408	31	336		42
240	530.5	-1.33	27.6	9.1	82.5	9.3	8.4	400	36	330	37	34
244	539.3	-1.11	29.5	9.6	82.3		8.1	412	40	339		34
248	548.1	-1.26	30.0	9.1	83.3		7.6	408	37	340		31
252	557.0	-0.81	30.2	7.9	85.6		6.5	427	34	366		28
256	565.8	-1.03	31.7	7.9	86.1		6.1	426	34	367		26
260	574.7	-1.14	31.2	7.7	86.8		5.5	422	32	366		23
264	583.5	-1.15	32.1	8.0	86.0		6.0	419	34	360		25
268	592.3	-1.26	24.7	7.0	88.0		5.0	414	29	364		21
272	601.2	-1.38	22.5	7.8	87.5		4.6	409	32	358		19
280	618.9	-1.40	24.3	8.0	87.3		4.7	405	33	354		19
284	627.7	-1.60	24.6	7.8	87.2		5.0	413	32	360		21
288	636.5	-1.26	24.8	6.8	84.5		8.7	410	28	346		36

Table 4-1. (continued)

Depth (cm)	Age (kyr)	$\delta^{18}O$ (‰)	Size index (>63 μm, %)	Amount of each composition (wt%)				MAR (mg/cm^2/kyr)				
				Opal	$CaCO_3$	Eolian[a]	Eolian[b]	Bulk	Opal	$CaCO_3$	Eolian[a]	Eolian[b]
292	645.4	-1.41	27.1	8.7	84.7		6.7	418	36	353		28
296	654.2	-1.22	23.3	8.9	84.4		6.7	412	37	348		28
300	663.1	-1.18	24.2	8.6	84.4		6.9	421	36	355		29
304	671.9	-1.27	21.2	7.3	86.5		6.2	388	28	336		24
308	680.8	-1.28	21.0	5.0	88.1		6.8	435	22	383		30
312	689.6	-1.19	22.1	5.2	88.4	2.9	6.3	451	24	399	13	29
316	698.4	-1.15	27.3	5.2	87.5		7.3	438	23	383		32
320	707.3	-1.06	25.7	6.2	86.8		7.0	429	27	373		30
324	716.1	-0.93	29.1	6.3	85.7		8.0	418	26	358		34
328	725.0	-0.78	26.2	5.7	86.0		8.2	403	23	347		33
332	733.8	-0.81	26.4	5.7	87.3		7.0	430	25	375		30
336	742.6	-1.19	21.9	5.6	86.8		7.6	433	24	376		33
340	751.5	-1.12	23.4	6.4	86.7		6.9	424	27	368		29
344	760.3	-0.91	26.1	9.4	81.1		9.6	425	40	345		41
348	769.2	-1.14	30.6	10.1	82.0		7.9	425	43	348		34
352	778.0	-1.09	31.0	9.6	83.0		7.4	426	41	354		31
356	783.7	-1.21	29.6	9.6	82.7		7.7	657	63	543		51
360	789.4	-0.94	27.5	11.9	78.8	10.3	9.3	654	78	515	68	61
364	795.0	-0.79	27.3	11.3	78.3		10.4	634	72	496		66
368	800.7	-1.18	19.6	11.7	80.4		7.9	618	72	497		49
372	806.4	-1.05	12.0	10.5	84.6		4.9	619	65	524		31
376	812.1	-1.10	9.0	10.1	85.9		4.0	632	64	543		25
380	817.7	-0.93	5.0	9.6	88.0		2.4	674	65	593		16
384	823.4	-1.05	4.9	8.3	87.3		4.4	687	57	600		30

Table 4-1. (continued)

Depth (cm)	Age (kyr)	$\delta^{18}O$ (‰)	Size index (>63 μm, %)	Amount of each composition (wt%)				MAR ($mg/cm^2/kyr$)				
				Opal	$CaCO_3$	Eolian[a]	Eolian[b]	Bulk	Opal	$CaCO_3$	Eolian[a]	Eolian[b]
388	829.1	-0.82	5.0	8.8	89.4		1.8	688	60	615		13
392	834.8	-0.99	3.5	7.6	90.1		2.3	713	54	642		17
396	840.4	-0.90	4.8	8.9	86.4		4.7	675	60	583		32
400	846.1	-0.75	4.8	9.1	88.8	3.2	2.0	665	61	590	21	14
404	851.8	-0.89	6.7	8.2	88.3		3.5	665	54	587		23
408	857.5	-0.56	6.6	9.8	87.9		2.3	684	67	601		16
412	863.1	-0.81	5.0	8.2	90.0		1.8	697	57	627		13
416	868.8	-0.72	5.7	9.2	88.1		2.6	684	63	603		18
420	874.5	-0.29	6.5	7.6	89.9		2.5	732	56	658		18
424	880.2	-0.64	5.8	9.8	89.0		1.2	724	71	644		9
428	885.8	-0.80	5.3	9.7	89.3		0.9	716	70	639		7
432	891.5	-0.60	6.1	11.1	89.3		0.1	730	81	652		1
436	897.2	-0.78	4.8	9.3	90.0		0.7	743	69	668		5
440	902.9	-0.50	7.1	9.9	87.5	1.6	2.6	730	73	639	12	19
444	908.5	-0.36	5.6	11.8	87.2		1.0	717	85	626		7
448	914.2	-0.33	6.6	8.9	88.5		2.6	734	65	650		19
452	919.9	-0.47	8.2	10.8	89.3		0.1	721	78	644		1
456	925.6	-0.62	6.7	8.4	90.0		1.6	739	62	665		12
460	931.2	-0.47	6.6	8.5	90.3		1.2	771	65	697		9
464	936.9	-0.64	8.4	8.3	89.8		1.9	753	63	676		14
468	942.6	-0.50	5.3	8.4	90.3		1.3	748	63	675		10
472	948.3	-0.62	4.7	7.5	90.7		1.7	755	57	685		13
476	953.9	-0.59	5.1	9.2	87.1		3.7	768	70	669		29
480	959.6	-1.00	5.0	8.7	89.9	1.4	1.4	770	67	692	10	11

Table 4-1. (continued)

Depth (cm)	Age (kyr)	$\delta^{18}O$ (‰)	Size index (>63 μm, %)	Amount of each composition (wt%)				MAR (mg/cm^2/kyr)				
				Opal	$CaCO_3$	Eolian[a]	Eolian[b]	Bulk	Opal	$CaCO_3$	Eolian[a]	Eolian[b]
484	965.3	-0.68	5.4	7.6	90.3		2.1	760	58	687		16
488	971.0	-0.15	4.7	7.3	90.1		2.5	761	56	686		19
492	976.6	-0.87	4.0	8.4	90.9		0.6	727	61	661		5
496	982.3	-1.05	3.6	9.8	90.5		0.1	775	76	701		1
500	988.0	-0.88	4.3	10.1	89.0		0.9	683	69	608		6
504	993.7	-0.47	4.4	13.6	86.3		0.1	709	96	612		1
508	999.4	-0.93	4.4	13.8	85.5		0.7	733	101	627		5
512	1005.0	-0.98	5.3	12.7	86.3	1.6	1.1	713	90	615	12	8
516	1010.7	-0.78	4.9	14.8	83.1		2.1	728	108	605		15
520	1016.4	-0.45	4.3	13.5	92.1		0.1	717	97	660		1
524	1022.1	-0.37	4.7	9.7	90.1		0.3	701	68	632		2
528	1027.7	-0.67	5.6	8.8	89.7		1.5	665	59	597		10
532	1033.4	-0.78	4.3	7.3	91.4		1.3	641	47	586		8
536	1039.1	-1.04	3.7	7.5	92.1		0.3	647	49	596		2
540	1044.8	-0.58	4.2	6.7	91.9	1.2	1.4	637	43	586	8	9
544	1050.4	-0.80	4.5	7.9	90.4		1.7	662	52	598		11
548	1056.1	-1.16	3.7	7.7	92.2		0.0	696	54	642		0
552	1061.8	-0.31	4.1	8.6	91.2		0.3	730	62	665		2
556	1067.5	-0.40	3.8	7.8	91.8		0.4	725	57	666		3

[a,b]Amounts and mass accumulation rates (MARs) of eolian component estimated from the extracted inorganic silicate fraction by following the method of Hovan [1995][a] and by subtracting $CaCO_3$ and opal fractions from 100%[b]. CSF: coarse-sized fraction in $CaCO_3$ (>63 μm, %), following Broecker and Clark [1999].

Table 4-2. $^{87}Sr/^{86}Sr$ and $^{143}Nd/^{144}Nd$ (ε_{Nd}) compositions of lithogenic components of PC 932.

Depth (cm)	Age (kyr)	$^{87}Sr/^{86}Sr$	±2σ SE	$^{143}Nd/^{144}Nd$	±2σ SE	ε_{Nd}
68	150.3	0.719349	0.000013	0.512188	0.000005	-8.79
140	309.4	0.717589	0.000005	0.512204	0.000004	-8.46
164	362.5	0.716321	0.000016	0.512268	0.000004	-7.21
184	406.7	0.716378	0.000021	0.512248	0.000005	-7.62
240	530.5	0.714586	0.000007	0.512318	0.000004	-6.25
312	689.6	0.714993	0.000006	0.512358	0.000003	-5.46
360	789.4	0.710784	0.000009	0.512386	0.000004	-4.92
400	846.1	0.710079	0.000016	0.512382	0.000003	-5.00
440	902.9	0.709643	0.000019	0.512385	0.000004	-4.93
480	959.6	0.709663	0.000015	0.512378	0.000005	-5.07
512	1005.0	0.709487	0.000015	0.512377	0.000009	-5.09
540	1044.8	0.709862	0.000018			

in a ε_{Nd} and $^{87}Sr/^{86}Sr$ crossplot (Figure 4-4).

4.4. Discussion

4.4.1. Cause of shifts in dust provenance, hydrology, and surface productivity

The MARs of the biogenic ($CaCO_3$ and opal) and eolian components of core PC 932 changed significantly across the boundary seen around 0.8 Ma. Furthermore, these changes are synchronous with the shifts in radiogenic isotope compositions (ε_{Nd} and $^{87}Sr/^{86}Sr$) of the eolian components and $\delta^{18}O_{Gsac}$. These findings indicate a fundamental change in the climate state of the central equatorial Pacific, including surface productivity, hydrology, and eolian dust transport pathways.

The ε_{Nd} and $^{87}Sr/^{86}Sr$ compositions of the eolian components show a compositional shift at the 0.8 Ma boundary (Figure 4-4). In the ε_{Nd} and $^{87}Sr/^{86}Sr$ crossplot, samples from the lower interval plot within the south–central Pacific domain and sediments from this region are clustered (Figure 4-4). In contrast, the samples from the upper interval follow a linear trend between the south–central and north–central Pacific domains. Since 0.8 Ma, the ε_{Nd}–$^{87}Sr/^{86}Sr$ composition has progressively evolved towards the north–central Pacific field in the crossplot (Figure 4-4).

The change in the radiogenic isotope composition of eolian dust at 0.8 Ma can be explained by the southward migration of the ITCZ towards the site and its effect on dust transport pathways. The ITCZ acts as a natural barrier to interhemispheric dust transport between the Southern and Northern Hemispheres (SH and NH,

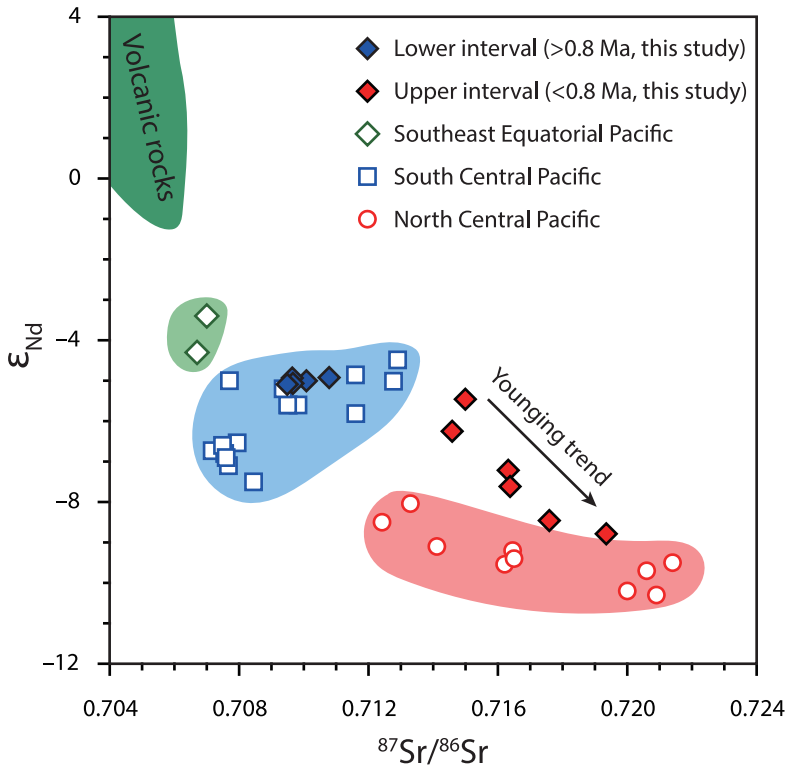

Figure 4-4. Crossplot of ε_{Nd} against $^{87}Sr/^{86}Sr$ from the eolian fraction of core PC 932 together with a compilation of reported values from the Pacific [data from Hyeong et al., 2011; Molina-Kescher et al., 2014; Nakai et al., 1993; Pettke et al., 2002; Stancin et al., 2006; Stancin et al., 2008].

respectively) [*Hovan*, 1995; *Hyeong et al.*, 2011; *Rea*, 1994; *Stancin et al.*, 2006]. As a result, in the central Pacific, dust from the Asian deserts dominates eolian deposition north of the ITCZ, while Australia and Central/South (C/S) America are the primary dust sources to the south of the ITCZ [*Molina-Kescher et al.*, 2014; *Nakai et al.*, 1993; *Rea*, 1994; *Stancin et al.*, 2006]. In regions that lie within the seasonal latitudinal range of the ITCZ, dust is delivered from both hemispheres and the isotopic composition shows a mixed value that tends to be closer to the dustier source region [*Xie and Marcantonio*, 2012].

In light of the dust depositional regime of the Pacific explained above, our data suggest that eolian dust originated from arid lands in the SH (i.e., Australia and C/S America) before 0.8 Ma, and then from both SH and NH (i.e., Asian) deserts after 0.8 Ma. The Asian dust input gradually increased from 0.8 Ma to the present (Figure 4-4), possibly because of the intensification of Asian drying that resulted from uplift of the Tibetan Plateau [e.g., *Cai et al.*, 2012; *Tian et al.*, 2015; *Wang et al.*, 2012]. The dominance of SH dust at the study site before 0.8 Ma indicates that the ITCZ was located to the north of the study site at this time. After 0.8 Ma, however, eolian dust deposited at the study site was supplied from both hemispheres, indicating that the study site might have been located within the seasonal latitudinal range of the ITCZ as it is today. Accordingly, the observed changes in the source signal can be best explained by the southward migration of the southern limit of the ITCZ to the study site at 0.8 Ma. This interpretation is consistent with the increased MAR of the eolian component after 0.8 Ma (Figure 4-3e). This was probably the result of the increased scavenging of dust particles by wet deposition in the ITCZ [e.g., *Hovan*, 1995] and increased supply of dust particles from Asia [*Rea*, 1994; *Tanaka and*

Chiba, 2006].

A southward shift of the ITCZ at 0.8 Ma is also supported by the synchronous shift of $\delta^{18}O_{Gsac}$ to more depleted values. This suggests an increase in the advection of warmer, less saline WPWP water transported by the NECC and increased precipitation at the study site after 0.8 Ma. The MARs of $CaCO_3$ and opal also decrease in the upper interval because of decreased surface production after 0.8 Ma. Based on the microscopic examination of degree of fragmentation of foraminifera tests and the size index, we excluded the possibility of increased $CaCO_3$ dissolution in the upper interval as an explanation because both would indicate more intense dissolution, if any, in the lower interval. Moreover, because of the opposite dissolution thermodynamics and resultant contrasts in preservation potential of these two components in the water column, the simultaneous decrease in MARs of opal and $CaCO_3$ cannot be explained by a change in water chemistry alone, as this would selectively increase the preservation of either opal or $CaCO_3$. The decrease in the MARs of the bulk and biogenic components after 0.8 Ma most probably resulted from a decrease in the supply of nutrients to the surface, which indicates a decrease in the surface production rate.

At the present time, the study site is characterized by oligotrophic open ocean conditions with low nitrate concentrations (<2 μmol/L) [*Le Bouteiller et al.*, 2003]. Advection of relatively nutrient-rich water from the equatorial upwelling region to the site is blocked by the NECC, which transports nutrient-poor WPWP surface water to the study site (Figure 4-2a). The ITCZ and NECC intensify water column stratification, which, together with the associated heavy rainfall, results in nutrient-poor conditions and low surface production. Our results indicate that the nutrient-

poor ocean environment has persisted at the study site since 0.8 Ma. Prior to 0.8 Ma, nutrient-rich water may have made the surface ocean environment relatively fertile as indicated by the biogenic components.

Such conditions could have been generated by a more northerly NECC and ITCZ due to changes in relative intensities of the trades [*Philander et al.*, 1987; *Wang and Wang*, 1999] and/or temperatures of thermocline water originated from the SH high-latitudes [*Dyez and Ravelo*, 2014]. The enhancement of equatorial upwelling would have been possible with a more northerly ITCZ because of the coupled behavior known as the ITCZ-cold tongue complex [*Wang and Wang*, 1999]. In addition, the NECC was probably located to the north of the study site before 0.8 Ma, as its location is coupled with that of the ITCZ [*Donguy and Meyers*, 1996; *Masunaga and L'Ecuyer*, 2010]. The off-equatorial positioning of the NECC and ITCZ before 0.8 Ma probably reduced the influence of nutrient-poor water from the WPWP and facilitated the supply of nutrient-enriched water from the equator to the study site. Thus, we conclude that the most likely cause of the changes in eolian dust provenance, warming and/or freshening of surface water, and decrease in surface productivity after 0.8 Ma was the strengthening of northeast trades relative to its southern counterpart and the resultant southward migration of the ITCZ/NECC.

4.4.2. Movement of ITCZ and the equatorial cooling event during the MPT

It is interesting to note that the southward migration of the ITCZ occurred at the end of the cooling event recorded in the equatorial upwelling regions of the Atlantic and Pacific between 1.1 and 0.8 Ma [*McClymont and Rosell-Melé*, 2005; *Schefuß et*

al., 2003] (Figure 4-1c and -1e). This cooling event is associated with the strengthening of the southeast trades, as indicated by the simultaneous increase in the size of dust particles [*McClymont and Rosell-Melé*, 2005] (Figure 4-1d). As zonal wind strength, ITCZ position, and equatorial upwelling are closely coupled [*Philander et al.*, 1987; *Wang and Wang*, 1999], this cooling event might be explained by increased upwelling and/or cooled thermocline water of tropical regions originated from the SH high-latitudes during the MPT. If the southward migration of the ITCZ recorded at our site at 0.8 Ma was connected to this cooling event peaked at 0.9 Ma (Figure 4-1c and -1d), it would have occurred as part of a continuous migration process occurring concurrently with the warming trend that began at 0.9 Ma and was recorded at 0.8 Ma at the study site. This reasoning further leads us to postulate that the ITCZ migrated northward between 1.1 and 0.9 Ma, and was at its northernmost position around 0.9 Ma, before it moved south. The southward migration of the ITCZ after 0.9 Ma is also supported by the contraction of the northern margin of the WPWP with relatively stable extent of its southern counterpart after around 0.9 Ma, which was attributed to the strengthening of northeast trades relative to southeast trades [*Russon et al.*, 2010]. This scenario is consistent with our $\delta^{18}O_{Gsac}$ data, which become heavier until 0.9 Ma but lighter from then on (Figure 4-3b), indicating that the coldest and/or most saline surface ocean conditions developed around 0.9 Ma; hence, the strongest influence of equatorial upwelling and/or cooling of thermocline water sunken in the SH high latitudes. We can also observe small peaks in the size index and MARs of opal and $CaCO_3$ around 0.9 Ma. The trends, however, are not apparent enough to indicate concomitant increase in productivity, which could have been resulted from the

position of NECC-SEC front being too far north for the site to record any critical change. This aspect requires further in-depth investigation with better defined stratigraphic age model and other productivity proxies such as foraminifera assemblages. Nevertheless of these uncertainties, similar ITCZ movement recorded at Ocean Drilling Project (ODP) site 1077 in the east equatorial Atlantic, off the coast of Africa (Figure 4-2b), discussed in the following paragraph, support our interpretation on northerly position of the ITCZ at ~0.9 Ma.

The east Atlantic upwelling region, where site 1077 is located, is also under the influence of the southeast trades and the ITCZ. The site recorded SST variation almost identical to that of the Pacific, showing a minimum SST at about 0.9 Ma (Figure 4-1e) [*Schefuß et al.*, 2003]. Interestingly, the supply of C_4 plant material mirrors that of SST (Figure 4-1f), indicating the drying of the nearby landmasses during the cooling episode. The drying of central Africa and expansion of C_4 plants, although previously attributed solely to the SST drop [*deMenocal*, 2004; *Schefuß et al.*, 2003], might have resulted from the displacement of the ITCZ to the north until 0.9 Ma and its subsequent southward migration afterward. Consequently, we suggest that the ITCZ migrated northwards until 0.9 Ma, accompanied by a strengthening of the southeast trades, and then moved south until 0.8 Ma. This change in atmospheric circulation could have then induced the cooling event and increase in surface productivity in the equatorial upwelling regions of the Pacific and Atlantic.

As the ITCZ shifts towards the hemisphere with a lowered thermal gradient between equator and pole [*Broccoli et al.*, 2006; *Chiang and Friedman*, 2012; *Flohn*, 1981; *McGee et al.*, 2014], the movement of the ITCZ provides information

on the cooling and warming of one hemisphere relative to the other. The northward migration of the ITCZ from 1.1 to 0.9 Ma suggests that the rate of increase of the pole-to-equator thermal gradient in the SH was greater than that in the NH during this time period, and the opposite movement of the ITCZ between 0.9 and 0.8 Ma suggests greater cooling in the NH than the SH. This proposed cooling history supports the suggestion that the NH ice sheet has expanded significantly and stabilized since 0.9 Ma [*Clark et al.*, 2006; *Clark and Pollard*, 1998; *Hernández-Almeida et al.*, 2012; *McClymont et al.*, 2008].

4.5. Conclusions

The $^{87}Sr/^{86}Sr$ and ε_{Nd} values of the inorganic silicate fraction in core PC 932 obtained from the central equatorial Pacific indicate deposition of dust from Australia and Central/South America before 0.8 Ma, and a gradual increase in Asian dust deposition toward the present after 0.8 Ma. This change in dust provenance was accompanied by increased dust flux and decreased surface productivity and salinity. These changes can be explained by the southward movement and direct influence of the ITCZ and NECC at the study site, which resulted in the input of Asian dust, weakening of equatorial upwelling, and the transport of the warm and less saline WPWP surface water to the site.

The previously published Atlantic data [i.e., *Schefuß et al.*, 2003] related to the drying of central Africa suggests the northward movement of the ITCZ between 1.1 and 0.9 Ma, and the southward movement from then on. The latter is consistent with the migration of the ITCZ recorded at 0.8 Ma at our study site. The ITCZ shifted its

position in-phase with the cooling and warming history recorded in the upwelling regions of the equatorial Pacific and Atlantic, which suggests a close relationship between ITCZ movement and the brief cooling event in the upwelling regions of the Atlantic and Pacific.

As the ITCZ moves towards the hemisphere with the reduced thermal gradient between the pole and equator, the southward movement of the ITCZ from 0.9 Ma indicates greater cooling of the NH than its counterpart. This might have contributed to expansion of the NH ice sheet, which supports the interpretation that the NH ice sheet has expanded significantly and stabilized since 0.9 Ma. The northward migration of the ITCZ from 1.1 to 0.9 Ma suggests that the rate of increase of the pole-to-equator thermal gradient in the SH was greater than that in the NH during this time periods.

CHAPTER 5. CLIMATIC EVOLUTION OF THE CENTRAL EQUATORIAL PACIFIC FOR THE LAST DEGLACIATION PERIOD

Abstract

Sea surface temperature and water column structure during the last deglaciation period were investigated in a central equatorial Pacific site (6°40′N, 177°28′W) using oxygen isotopic compositions ($\delta^{18}O$) and Mg/Ca ratios of three planktic foraminifera species: *G. sacculifer*, *P. obliquiloculata* and *G. tumida* that dwell in the mixed layer, upper thermocline and lower thermocline, respectively. Mg/Ca–derived temperatures for the mixed layer and lower thermocline water mass have varied in a narrow range since 18 ka. In contrast, those of upper thermocline was increased as high as 3°C during the last deglaciation period between 18 and 12 ka and has decreased to and maintained at the present level since 12 ka. Such a temporal variation was associated with simultaneous change of $\delta^{18}O$ in the upper thermocline: decrease between 18 and 12 ka and increase after 12 ka. This observation can be explained by enhanced mixing of the upper ocean and reduced depth separation of habitats between *P. obliquiloculata* and *G. sacculifer* during the 18–12 ka time interval. The time interval showing weak stratification includes two prominent Northern Hemisphere (NH) cooling events, Heinrich Stadial 1 (HS1) and Younger Dryas (YD), characterized by the southerly position of the Intertropical Convergence Zone (ITCZ) due to increased pole to equator temperature gradients in

the NH and resultant intensification of northeast trade winds. The faunal assemblage of planktic foraminifera during the deglaciation period at the study site agrees well with the present faunal assemblage of a subtropical central Pacific site (15°′N) that lies under the strong influence of northeast trade winds and North Equatorial Current (NEC). This suggests a possibility that the study site, now being under the control of ITCZ-North Equatorial Countercurrent, had been positioned north of the ITCZ and under the direct influence of northeast trade winds and NEC during the last deglaciation period.

5.1. Introduction

During the last deglaciation period (ca. 20–8 ka) from the last glacial maximum to the Holocene, global warming was punctuated by two abrupt Northern Hemisphere (NH) cooling events: Heinrich Stadial 1 (HS1; ca. 18–15 ka) and Younger Dryas (YD; 13–11.5 ka). These events are characterized by "bipolar see-saw" [*Broecker*, 1998]: warming in the Southern Hemisphere (SH) and cooling in the NH. The pronounced cooling and drying in NH high latitudes during these episodes had resulted in southward shift of the Intertropical Convergence Zone (ITCZ), a maximum precipitation belt resulted from the convergence of northeast and southeast trade winds [*Gibbons et al.*, 2014; *McGee et al.*, 2014].

Latitudinal displacement of the ITCZ has been suggested as one of the responses of the tropics to a climate forcing on various time scales [*Broccoli et al.*, 2006; *Chao and Chen*, 2001; *Schneider et al.*, 2014]. In particular, climatic anomalies reported in the tropical Pacific, such as reduced river runoffs and weaker Asian and stronger Australian summer monsoon systems, have been attributed to southward migration of the ITCZ during HS1 and YD events [*Gibbons et al.*, 2014; *Leduc et al.*, 2009; *Mohtadi et al.*, 2011; *Partin et al.*, 2007; *Wang et al.*, 2001]. However, these studies were carried out in the western boundary regions of the Pacific where regional precipitation pattern exhibits strong seasonal dependence. Thus, decoupling between consequences of migration of tropical rainfall belt, i.e., ITCZ, and monsoonal effects are often challenging in these regions. Up to date, observations documenting southward migration of the ITCZ during HS1 and YD are absent in remote tropical Pacific where influence of monsoon system is lacking.

This study aims to describe and interpret climate evolution in the eastern boundary region of the Western Pacific Warm Pool (WPWP) in the central equatorial Pacific for the last 23 kyrs in terms of influence of the ITCZ on the region. The central equatorial Pacific near the international dateline is characterized by the narrowest seasonal migration belt of the ITCZ at present. On the contrary, annually averaged position of the ITCZ shows the largest meridional displacement in response to a given change in inter-hemispheric thermal contrast in the modern ocean [*McGee et al.*, 2014]. Such characteristics are advantageous to track its migration over the global climate evolution history. A deep-sea sediment core was obtained from the Magellan Rise located in the central equatorial Pacific (6°40′N, 177°28′W; 3,365 m), where elevated topography above the carbonate compensation depth allows the preservation of relatively high-resolution sedimentary records (Figure 1-3). In this study, temporal variations in temperature and water column structure in the upper ocean are investigated using oxygen isotopic compositions (δ O) and Mg/Ca ratios of three planktonic foraminifera species, *Globigerinoides sacculifer*, *Pulleniatina obliquiloculata*, and *Globorotalia tumida*, each of which dwells in different depth range of water column. This multi-species approach helps understand temperature gradients between the surface and lower part of thermocline. This study reports high resolution proxy data for the last 23 kyrs in the central equatorial Pacific region for the first time and also addresses displacement of the ITCZ during the last deglaciation period and resultant response of the upper water column in the central equatorial Pacific.

5.2. Study Site and Analytical Methods

A 31 cm-long deep-sea sediment core, MC 931, was recovered using a multiple corer from the Magellan Rise in the central equatorial Pacific (6°40′N, 177°28′W; 3,365 m depth) during a cruise carried out by Korea Institute of Ocean Science and Technology (KIOST) in 2009 (Figure 5-1). Surface ocean environment in the study site shows small intra-annual variation. The elevated topography of the Magellan Rise, about 2,000 m shallower than the surrounding basin, prevents hemipelagic sedimentation and provides good preservation of microfossils in association with relatively high rates of accumulation. The core sediment is composed mainly of calcareous ooze containing approximately 90% carbonate, and does not show any recognizable lithologic change stratigraphically. The input of lithogenic materials is considered being dominated by eolian process because of its isolated location from the continents and elevated topography.

The North Equatorial Countercurrent (NECC), whose position is coupled with the ITCZ [*Donguy and Meyers*, 1996; *Masunaga and L'Ecuyer*, 2010], flows over the site and transports warm and low-nutrient surface water to the study site from the WPWP. South of the study site prevails the westward-flowing South Equatorial Current (SEC). Southeast trade winds induce upwelling and bring nutrients to the surface at the Equator, resulting in higher primary production than in the WPWP and NECC regions [*Eldin and Rodier*, 2003; *Le Bouteiller et al.*, 2003].

The chronology of core MC 931 was established with ^{14}C measurements of planktic foraminifera at 5–6, 13–14, 20–21 and 30–31 cm intervals. C was analyzed within an error range less than 60 years using an accelerator mass spectrometry (AMS) at Beta Analytic Radiocarbon Dating Laboratory, USA. Measured radiocarbon age data were corrected for isotopic fractionation and

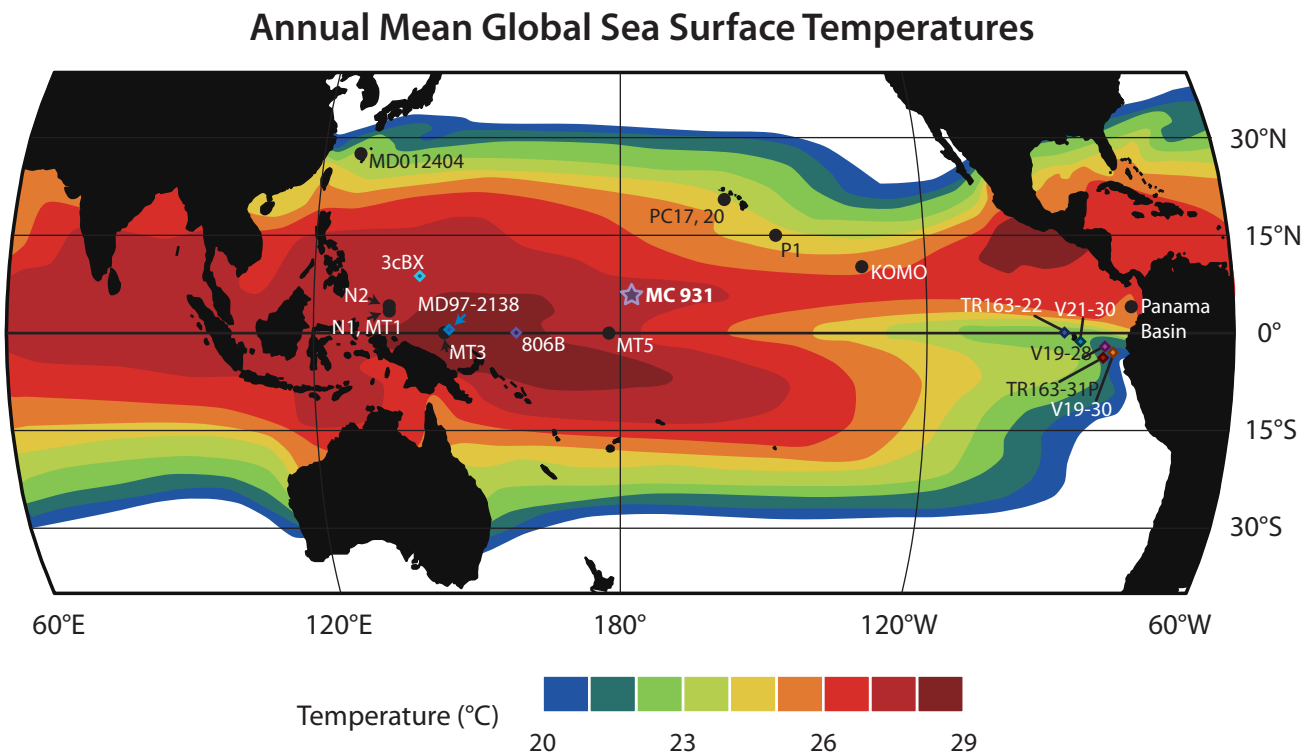

Figure 5-1. Locations of the study site (MC 931), cores with SST records (diamonds), and sites where planktic foraminifera species assemblages are available (solid circles) discussed in the text. Temperature and salinity data are from World Ocean Atlas 2013 [*Locarnini et al.*, 2013; *Zweng et al*., 2013]. Dotted line remarks the region where daily mean precipitation exceeds 7 mm day^{-1}.

calibrated to the calendar year before present (Cal ^{14}C age) using Calib v. 7.0 software [*Stuiver and Reimer*, 1993]. This correction was based on the Marine13 dataset [*Reimer et al.*, 2013] and the local reservoir effect (ΔR) of 9 ± 5 years [*Southon et al.*, 2002].

Three planktic foraminiferal species, *Globigerinoides sacculifer* (without the final sac, 250–355 μm), *Pulleniatina obliquiloculata* (355–425 μm), and *Globorotalia tumida* (355–425 μm), were analyzed for δ^{18}O and Mg/Ca ratios. *G. sacculifer* is known to inhabit in the upper 80 m of water column, but its depth preference varies depending on its growth stages and size classes [*Bijma and Hemleben*, 1994]. In early stage of growth, *G. sacculifer* dwells in the upper photic zone (0–50 m depth) because of small test size (<355 μm in diameter) [*Anand et al.*, 2003; *Bijma and Hemleben*, 1994; *Hemleben et al.*, 1987]. *P. obliquiloculata* dwells in the lower photic zone–upper thermocline (50–100 m depth), and its calcification temperature varies within a small temperature range [*Anand et al.*, 2003]. *G. tumida*, a thermocline-dwelling species, calcifies below the seasonal thermocline (100–250 m depth) [*Fairbanks and Wiebe*, 1980; *Farmer et al.*, 2007]. Following the depth habitats of these three species estimated in the WPWP region by *Sagawa et al.* [2012], calcification temperatures and seawater δ^{18}O of *G. sacculifer*, *P. obliquiloculata*, and *G. tumida* are considered to represent those of the mixed layer, upper thermocline and lower thermocline, respectively.

Stable oxygen isotope compositions (δ^{18}O) were determined using a Finnigan MAT 251 mass spectrometer at the University of Michigan at Ann Arbor, USA. The 1-sigma standard deviation of the repeat analyses of the reference material (NBS-19; National Bureau of Standards) was 0.09‰ (n = 24). Mg/Ca ratios were determined

using an inductively coupled plasma optical emission spectrophotometer (ICP-OES) (Perkin-Elmer Optima 3300 DV) at the Korea Institute of Ocean Science and Technology, Ansan, Korea. For Mg/Ca measurements, 20–30 monospecific tests were crushed and homogenized, and subsequently cleaned with methanol (clay removal), NaOH-buffered hydrogen peroxide (removal of organic matter) and a weak acid (removal of high-Mg calcite) following *Barker et al.* [2003]. Concentration of Ca and Mg were measured from the spectral lines at 407.776 and 279.553 nm, respectively. Instrumental drift was corrected according to *Schrag* [1999]. The analytical error of Mg/Ca, based on replicate measurements of ECRM 752-1 standard (Bureau of Analyzed Samples, Ltd) was 0.2 mmol/mol (1 s.d., n=61), which corresponds to temperature error of ~0.5°C.

5.3. Results

The age model of MC 931 core was established with ^{14}C measurement (Table 5-1). The core was deposited at a rate of 1.35 cm/kyr for approximately 23 kyrs, which covers the entire last deglaciation period.

Down-core $\delta^{18}O$ and Mg/Ca results of three species are shown in Table 5-2 and Figure 5-2a and -2b, respectively. $\delta^{18}O$ compositions of *G. sacculifer* (-1.36 ± 0.46‰; n=30, 1 σ), *P. obliquiloculata* (-0.73 ± 0.47‰; n=31, 1 σ), and *G. tumida* (0.48 ± 0.39‰; n=29, 1 σ) agree in general with those of the previously reported values in the WPWP center [*Sagawa et al.*, 2012] with minor offsets that likely reflect temperature and salinity differences between the two sites. The determined Mg/Ca ratios of *G. sacculifer* (3.93 ± 0.32; n=30, 1 σ) and *G. tumida* (1.72 ± 0.16;

Table 5-1. Radiocarbon ages of planktic foraminifera in MC 931.

Depth	AMS ^{14}C Ages (yr)	Error (yr)	Calendar Ages
5	6910	30	7420
13	11710	40	13190
20	15250	50	18040
30	19130	60	22560

Table 5-2. Stable oxygen isotope ($\delta^{18}O$) and Mg/Ca compositions of *G. sacculifer*, *P. obliquiloculata* and *G. tumida* and Mg/Ca-derived seawater temperature using equations provided by *Sadekov et al.* [2009].

Depth (cm)	Age (ka)	*G. sacculifer*			*P. obliquiloculata*			*G. tumida*		
		$\delta^{18}O$ (‰)	Mg/Ca (mmol/mol)	T (°C)	$\delta^{18}O$ (‰)	Mg/Ca (mmol/mol)	T (°C)	$\delta^{18}O$ (‰)	Mg/Ca (mmol/mol)	T (°C)
0.5	0.7	-1.9	4.04	26.3	-0.89	2.87	21.7	0.64	1.77	15.5
1.5	2.0	-0.9	4.05	26.3	-1.03	2.72	21.0	1.10	1.74	15.2
2.5	3.4	-1.7	4.11	26.5	-0.51	2.56	20.2	0.01	2.01	17.2
3.5	4.7	-1.8	4.38	27.4	-0.89	2.82	21.5	0.88	1.92	16.5
4.5	6.1	-2.0	4.15	26.6	-0.99	2.59	20.4	0.19	1.83	15.9
5.5	7.4	-1.3	3.88	25.7	-0.52	2.78	21.3	-0.23	1.50	13.3
6.5	8.1	-1.6	3.74	25.2	-1.09	2.60	20.4	0.36	1.81	15.7
7.5	8.9	-0.9	4.08	26.4	-0.76	3.04	22.5	0.04	1.90	16.4
8.5	9.6	-1.9	4.13	26.6	-1.27	2.54	20.1	-0.09	2.02	17.2
9.5	10.3	-1.6	4.21	26.8	-1.02	2.40	19.4	0.64	1.84	16.0
10.5	11.0	-1.4	4.09	26.4	-1.12	2.73	21.1	-0.17	1.66	14.6
11.5	11.7	-2.0	3.90	25.8	-0.96	2.66	20.7	1.03	1.70	14.9
12.5	12.5	-1.6	4.35	27.2	-1.32	2.87	21.7	0.81	1.56	13.7
13.5	13.2	-1.7	4.27	27.0	-1.65	2.51	20.0	0.25	1.80	15.7
14.5	13.9	-1.1	4.01	26.2	-0.98	3.21	23.3	0.51	1.79	15.6
15.5	14.6	-1.9	3.93	25.9	-1.06	3.25	23.4	0.48	1.54	13.6

Table 5-2. (continued)

Depth (cm)	Age (ka)	*G. sacculifer*			*P. obliquiloculata*			*G. tumida*		
		$\delta^{18}O$ (‰)	Mg/Ca (mmol/mol)	T (°C)	$\delta^{18}O$ (‰)	Mg/Ca (mmol/mol)	T (°C)	$\delta^{18}O$ (‰)	Mg/Ca (mmol/mol)	T (°C)
16.5	15.3	-0.8	4.15	26.6	-0.74	3.04	22.5	0.03	1.93	16.6
17.5	16.0	-2.2	3.99	26.1	-1.01	2.73	21.1	0.06	1.63	14.4
18.5	16.7	-1.1	4.24	26.9	-1.19	3.45	24.2	0.44	1.63	14.3
19.5	17.3	-1.5	3.65	24.9	-0.92	3.00	22.3	0.65	1.59	14.0
20.5	18.0	-1.1	4.17	26.7	-0.60	2.18	18.1	0.68	1.75	15.3
21.5	18.5	-0.5	3.76	25.3	-0.71	2.86	21.7	1.00	1.79	15.6
22.5	18.9	-0.9	3.80	25.5	-0.74	2.28	18.7	0.90	1.67	14.7
23.5	19.4	-1.5	3.91	25.8	-0.23	2.40	19.4	0.36	1.53	13.5
24.5	19.8	-1.3	4.01	26.2	0.20	2.75	21.2	0.66	2.00	17.1
25.5	20.3	-0.9	3.57	24.6	0.18	2.45	19.7	0.97	1.54	13.6
26.5	20.8	-1.3	3.41	24.0	-0.22	2.45	19.7	0.87	1.81	15.8
27.5	21.2	-0.7	3.00	22.3	-0.19	2.54	20.1	0.77	1.43	12.6
28.5	21.7	-1.4	3.57	24.6	-0.67	2.60	20.4	0.35	1.60	14.1
29.5	22.1	-0.6	3.42	24.0	-0.21	2.25	18.5	0.90	1.50	13.3
30.5	22.6	-0.8	3.26	23.4	0.37	2.35	19.1	0.48	1.71	15.0

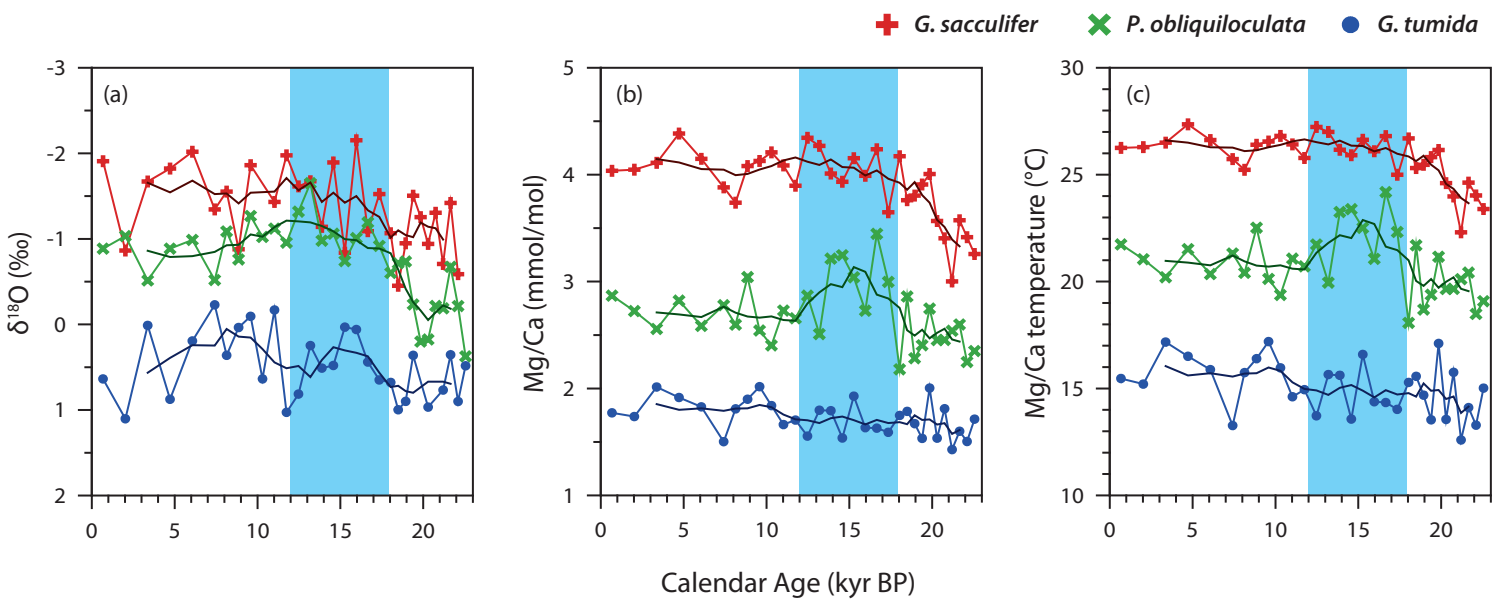

Figure 5-2. Analytical results of foraminiferal (a) $\delta^{18}O$ (a) and (b) Mg/Ca compositions of three species, and (c) Mg/Ca-derived calcification temperatures converted using equations provided in *Sadekov et al.* [2009]. Shades mark the time interval with reduced compositional gradient between species.

n=30, 1 σ) are similar to those (~ 3.8 and ~ 1.8, respectively, raw data not provided) of the WPWP center, but those of *P. obliquiloculata* (2.69 ± 0.30; n=31, 1 σ) are higher than those (~ 1.8, raw data not provided) of the WPWP center [*Sagawa et al.*, 2012].

5.4. Discussion

5.4.1. Estimation of calcification depth and temperature of three planktic foraminifer species

To estimate the calcification depth of planktic foraminifera species of interest, calcite $\delta^{18}O$–depth relationship was established at the study site using the theoretical equation between $\delta^{18}O$ of seawater and temperature [*Kim and O'Neil*, 1997], in which $\delta^{18}O$ of seawater was calculated from the salinity–$\delta^{18}O$ relationship of surface and subsurface water in the central tropical Pacific [*Conroy et al.*, 2014] and the optimum interpolation temperature and salinity were taken at 6.5°N, 177.5°W from World Ocean Atlas 2013 [*Locarnini et al.*, 2013; *Zweng et al.*, 2013] (Figure 5-3).

With the projection of an average late Holocene (<6 ka) $\delta^{18}O$ composition of each planktic foraminifera species to the established calcite $\delta^{18}O$ – depth relationship, calcification depth of each species was estimated to be 70-100 m for *G. sacculifer*, 120-140 m for *P. obliquiloculata*, and 160-200 m depth for *G. tumida* (Figure 5-3c). The predicted depths are slightly deeper than, but largely consistent with, previously reported depth habitats of three species estimated in the center of WPWP; 40-80 m for *G. sacculifer*, 100-130 m for *P. obliquiloculata*, and 140-180 m depth for *G.*

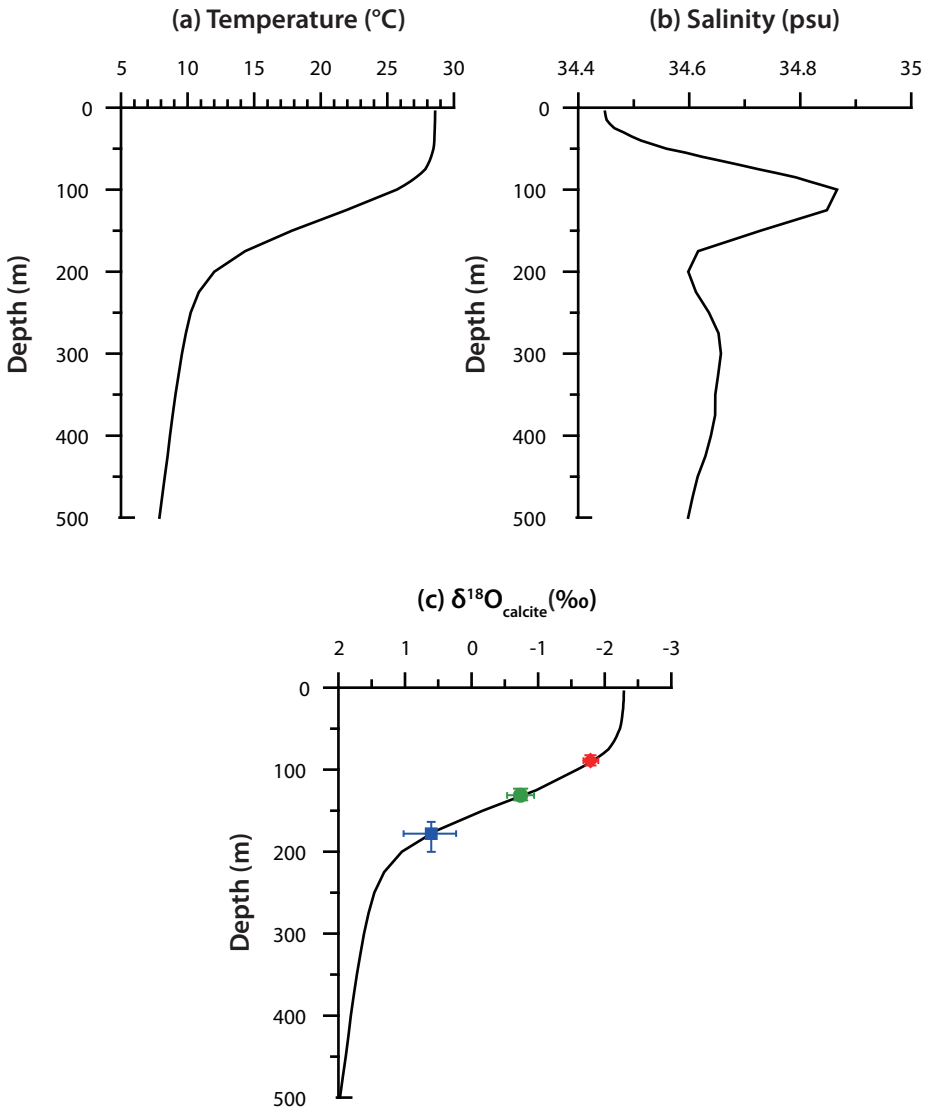

Figure 5-3. Depth profile of annual mean of optimum interpolated (OI) temperature (a) and salinity (b) records provided in World Ocean Atlas 2013 [*Locarnini et al.*, 2013; *Zweng et al.*, 2013]. (c) The estimated calcification depths of three species by comparison of an average $\delta^{18}O$ composition of late Holocene (<6 ka) planktic foraminifera species with the predicted calcite $\delta^{18}O$ (see text for details): *G. sacculifer* (red), *P. obliquiloculata* (green) and *G. tumida* (blue).

tumida [*Sagawa et al.*, 2012].

The calcification temperature (T) of planktic foraminifera is often expressed as Mg/Ca = b × exp(a × T), where a is an exponential constant and b is a pre-exponential constant [*Lea et al.*, 1999; *Nürnberg et al.*, 1996]. However, the effect of seawater salinity on foraminiferal calcite Mg/Ca has been argued as a cause for basin-dependent difference of calibration equation [*Anand et al.*, 2003; *Ferguson et al.*, 2008; *Nürnberg et al.*, 1996]. To avoid such complexity, a generalized equation that account for salinity variation was used to obtain calcification temperature in this study [*Sadekov et al.*, 2009]:

$$\text{Mg/Ca (mmol/mol)} = \exp[0.057(\pm0.012) \times S(\text{psu}) + 0.075(\pm0.006) \times T\ (°C) - 2.56(\pm0.46)],$$

where S and T are seawater salinity and temperature at habitat depth, respectively. The equation was established for *G. sacculifer* and *P. obliquiloculata* in the Western Pacific, but it was also applied to *G. tumida* as there has been no successful establishment of core-top calibration equation for *G. tumida* to date in the Pacific.

The Mg/Ca-derived calcification temperatures of three planktic foraminifera species for the late Holocene (<6 ka) were estimated to be 26.6°C (±0.4), 21.0°C (±0.7), and 16.0°C (±0.8) for *G. sacculifer*, *P. obliquiloculata*, and *G. tumida*, respectively at present. These temperatures are encountered at depths of 90 m, 130 m, and 160 m, respectively, at the study site; thus the Mg/Ca-derived temperature of each species represents that of the mixed layer, upper thermocline, and lower thermocline, respectively (Figure 5-3). These results are consistent with the

aforementioned calcification depths of three species derived from $\delta^{18}O$: 70-100 m for *G. sacculifer*, 120-140 m for *P. obliquiloculata*, and 160-200 m depth for *G. tumida*. Such consistent results indicate reliability of the estimated temperatures in this study.

5.4.2. Change in upper water column structure during the last deglaciation period

Mg/Ca–derived temperatures of the mixed layer and lower thermocline do not change much after 18 ka (Figure 5-2c). In contrast, upper thermocline temperatures were increased as high as 3°C during the last deglaciation period between 18 and 12 ka and were dropped and maintained to the present level since 12 ka (Figure 5-2c). It suggests that the vertical temperature gradient of dwelling depths between *P. obliquiloculata* and *G. sacculifer* was reduced during the 18–12 ka period, but that between *G. sacculifer* and *G. tumida* has not been changed in the same period. The observed trends during the last deglaciation period could have resulted from either increase of temperature at the dwelling depth and/or change in habitat depth of *P. obliquiloculata*.

The increase in deglacial subsurface water temperature could have been attained by the warming of thermocline water mass. Indeed, warming of intermediate water that upwells in the equatorial region is indicated by several observations during the last deglaciation period. Rapid increase of air temperatures was observed as early as 19 ka in the source region (Southern Hemisphere high latitudes) of equatorial intermediate water [*Bostock et al.*, 2013; *Calvo et al.*, 2007]. Concomitant increases of SSTs are also reported in the upwelling regions of East Equatorial Pacific (EEP)

[*Koutavas et al.*, 2002; *Martinez-Boti et al.*, 2015] (Figure 5-4). In addition, $\delta^{18}O$ of benthic foraminifera collected in the EEP at depths influenced by Subantarctic Mode Water and Antarctic Intermediate Water has decreased since 18 ka, simultaneously with rising temperatures in the Antarctica [*Bova et al*., 2015]. Such phenomenon was interpreted as a result of enhanced influence of warmer and less dense Antarctic Intermediate Water produced by melting of sea ice and poleward shift of the southern Westerly winds during the HS1 and YD [*Bova et al*., 2015]. All these observations support a possibility for warming of intermediate water that upwells in the equatorial region.

A hypothesis of sequential warming from deep thermostad water to thermocline water, however, cannot be applied to the study site. If it is the case, lower thermocline temperature, represented by Mg/Ca ratio of *G. tumida*, should have been increased simultaneously with that of the upper thermocline, but it had remained stable throughout the study period (Figure 5-2c). Despite the simultaneous increases of air temperatures [*Parrenin et al.*, 2013], surface ocean temperature [*Lamy et al.*, 2004; *Romero et al.*, 2006], and the intermediate water temperature [*Bova et al.*, 2015; *Pena et al.*, 2013] in the SH at this time, the well-developed thick mixed layer to the north of equator could have prevented the penetration of SH-sourced intermediate water to the upper ocean at the study site.

Interestingly, the difference between $\delta^{18}O$ compositions of *G. sacculifer* and *P. obliquiloculata* was decreased simultaneously with decrease in Mg/Ca temperature difference between them from 18 to 12 ka. It suggests that increase in calcification temperature of *P. obliquiloculata* had been accompanied by shallowing of the maximum population depth of *P. obliquiloculata* during this period. Although *P.*

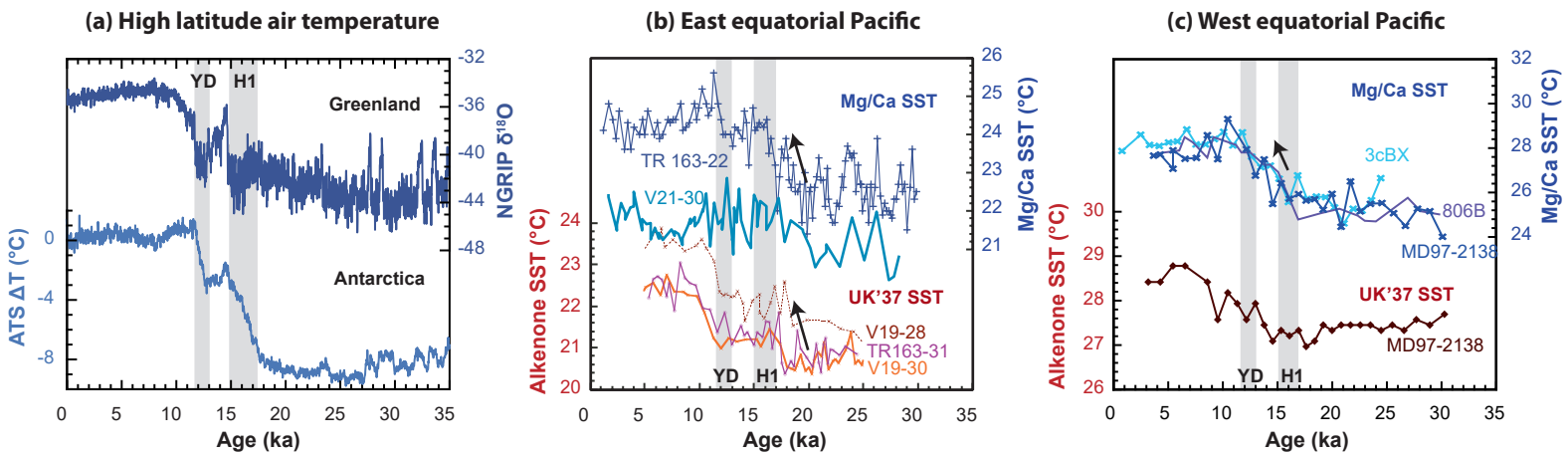

Figure 5-4. Compilation of published dataset showing deglacial warming. (a) Air temperatures from Greenland (NGRIP $\delta^{18}O$ on GICC05 × 1.0063 chronology [*North Greenland Ice Core Project members*, 2004]) and Antarctica ice cores (Antarctic Temperature Stack (ATS) [*Parrenin et al.*, 2013] in degrees Celsius relative to the present day on AICC12 × 1.0063 chronology [*Veres et al.*, 2013]). Foraminifera Mg/Ca and $U^{K'}_{37}$ SST (b) in the east equatorial Pacific [*Dubois et al.*, 2009; *Koutavas et al.*, 2002; *Koutavas and Sachs*, 2008; *Lea et al.*, 2006] and (c) in the west equatorial Pacific [*de Garidel-Thoron et al.*, 2007; *Sagawa et al.*, 2012; *Wara et al.*, 2003].

obliquiloculata occurs in tropical-subtropical subsurface water mainly at a depth range of 60–150 m [*Cléroux et al.*, 2008; *Erez and Honjo*, 1981; *Farmer et al.*, 2007], previous studies indicated wide variations in its habitat depth. In the tropical Pacific, for examples, the maximum population depth range of *P. obliquiloculata* was estimated at 100–140 m from its $\delta^{18}O$ composition in the western Pacific [*Patrick and Thunell*, 1997; *Sagawa et al.*, 2012; this study], but at 30–100 m in the eastern Pacific [*Rincón-Martínez et al.*, 2011]. Especially, depth habitats of *G. sacculifer* and *P. obliquiloculata* were reported being indistinguishable in the tropical eastern Pacific [*Rincón-Martínez et al.*, 2011].

Indistinguishable separation of depth habitats between these two foraminiferal species in the EEP is likely due to the weaker stratification of the upper water column. The density gradient in the EEP region gentler than its western counterpart makes water column structure and vertical zonation of planktic foraminifera unstable since the depth habitat of a foraminifera species primarily depends on density of water column. The separation of depth habitats between species can be lessened in a weakly stratified upper ocean condition [*Caromel et al.*, 2014; *Coxall et al.*, 2000; *Rashid and Boyle*, 2007]. Thus, the depth habitat of *P. obliquiloculata* at the study site could have overlapped with that of *G. sacculifer* under such conditions. This possibility is supported by other thermocline-dwelling species (*Globorotalia menardii* and *Neogloboquadrina dutetrei*) that show similar depth habitat variations across the tropical Pacific [*Patrick and Thunell*, 1997]. The lower thermocline inhabiting species, *G. tumida*, is known to dwell below the photic zone, mostly deeper than 100–150 m depth, and therefore does not show strong spatial variation in the habitat depth [*Rincón-Martínez et al.*, 2011; *Sagawa et al.*, 2012].

Therefore, during the time period between 18 and 12 ka, the increase of calcification temperature of *P. obliquiloculata*, which is unique among others, resulted most likely from shallowing of depth habitat, which suggests the weakly stratified upper water column structure at the study site during the time period between 18 and 12 ka.

5.4.4. Response of central equatorial Pacific to inter-hemispheric thermal asymmetry during the last deglaciation period

The weakening of upper ocean stratification from 18 to 12 ka without associated warming of deep thermocline water could have resulted from the enhanced wind-driven mixing. The study site today is positioned beneath the ITCZ, characterized by high precipitation, weak wind strength and buyout surface watermass. The meridional displacement of the ITCZ from its present position would have exposed the site under the influence of either northeast or southeast Trades, which likely brings about enhanced mixing of surface water column. It also aided to relax the strong water column stratification by placing the site out of intense precipitation zone.

Climate evolution history suggests the southward displacement of the ITCZ during the last deglaciation period. The early warming of SH high latitudes relative to NH counterpart [see *Denton et al.*, 2010 and references therein] resulted in a decreased pole-to-equator temperature gradient in SH. Especially, the interhemispheric thermal asymmetry between SH and NH became intensified significantly during the NH cooling events (i.e., HS1 and YD) [*Barker et al.*, 2009; *Denton et al.*, 2010; *McGee et al.*, 2014; *Stenni et al.*, 2011]. Such strong

asymmetric high latitude thermal forcing induced the southward displacement of the ITCZ through atmospheric teleconnection, which has been documented in many field observations [*Haug et al.*, 2001; *Mohtadi et al.*, 2011; *Montade et al.*, 2015; *Peterson et al.*, 2000] and model simulations (Figure 5-5) [*Gibbons et al.*, 2014; *McGee et al.*, 2014]. These studies documenting southward shift of the ITCZ and strengthening of northeast trade winds during the HS1 and YD strongly suggest the possibility that the ITCZ had been positioned south of the study site during these two episodes. As a result, the study site was likely under the influence of intensified northeast trade winds, which likely led to less stratified upper ocean structure by wind-driven mixing.

The temporal changes in faunal assemblages of planktic foraminifera in the studied core [*Lee*, 2015] supports this interpretation. The foraminifera in the study core are dominated by warm water species (e.g., *G. glutinata*, *G. ruber*, *G. sacculifer*, *P. obliquiloculata*, and *G. rubescens*) for the last 23 kyrs with increasing significance of warm oligotrophic WPWP species (*G. sacculifer* and *P. obliquloculata*) during the Holocene (Figure 5-6). It is noteworthy of the increase in abundance of *G. rubescens* during the last deglaciation period (ca. 18–12 ka) as it is rare in tropical Pacific at present and its high abundance was only reported in a sediment trap (Station P1, ~15°N) and core records (PC17 and PC20, ~21°N) from the subtropical Central Pacific near the Hawaii Islands (Figure 5-1) [*Lee et al.*, 2001; *Thunell and Honjo*, 1981]. The spatial occurrences of *G. rubescens* indicate its preference to more off-equatorial oligotrophic ocean condition. Interestingly, planktic foraminifera assemblages at these subtropical sites also show close resemblance to those at the study site during the last deglaciation period (Figure 5-

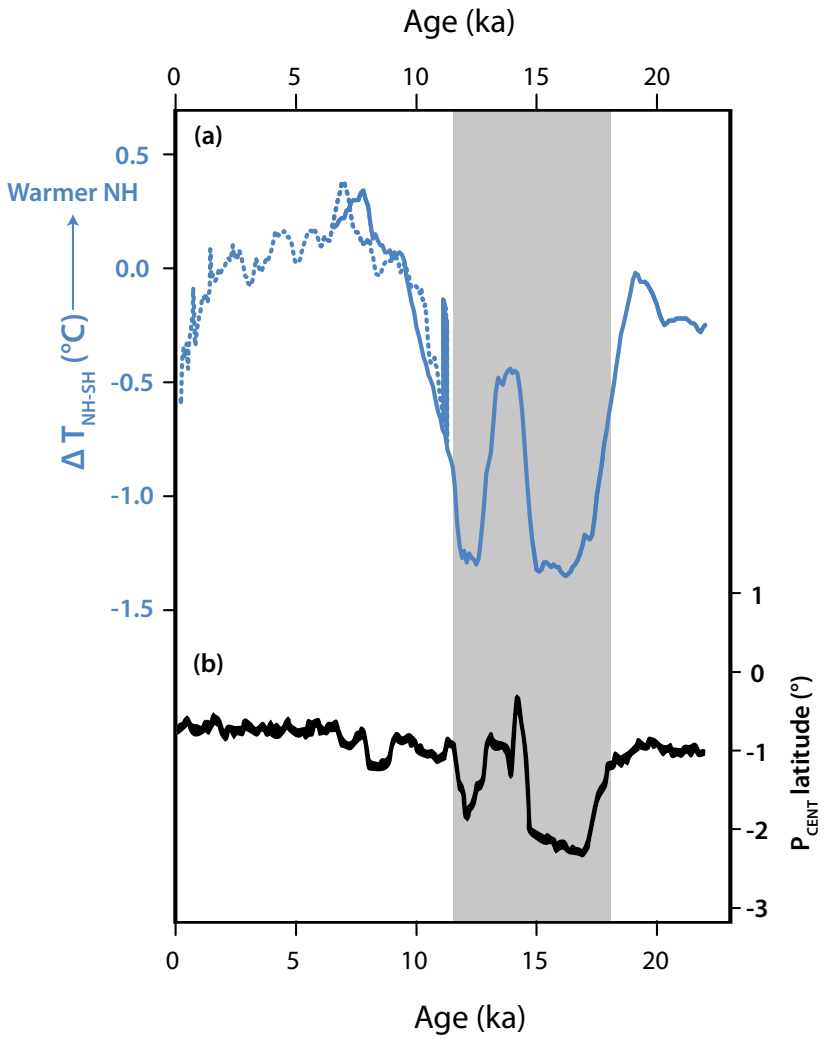

Figure 5-5. Relationship between interhemispheric temperature gradient and ITCZ position (adopted and modified from *McGee et al.* [2014]). (a) Reconstructed inter-hemisphere surface temperature gradients (area-weighted mean NH surface temperature minus area-weighted SH surface temperature), solid line: *Shakun et al.* [2012] and dashed line: *Marcott et al.* [2013]). (b) Changes in mean ITCZ position (P_{CENT}: latitude of maximum precipitation) in the TraCE-21 ka simulation by *McGee et al.* [2014].

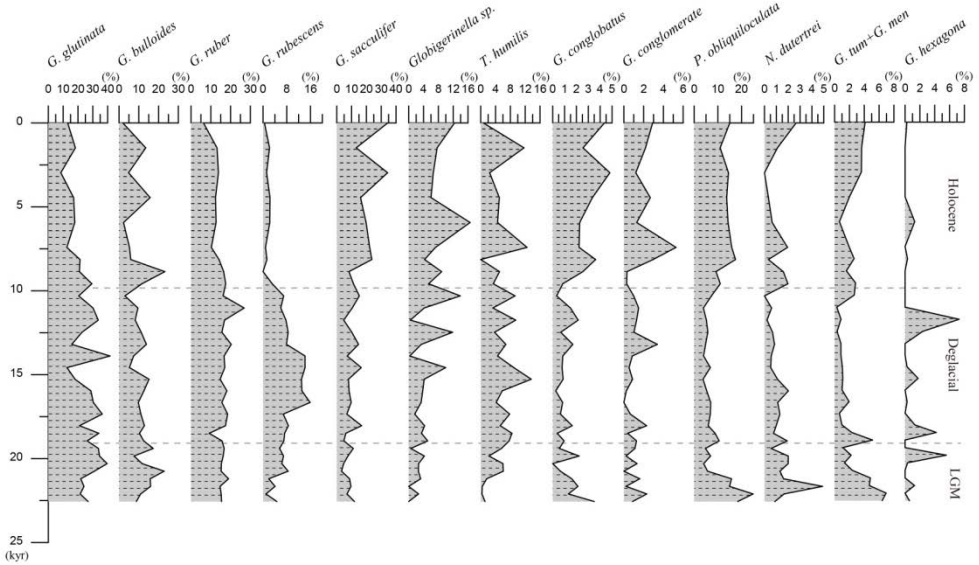

Figure 5-6. Faunal assemblage of planktic foraminifera in MC 931 sediment (modified from *Lee* [2015])

7): dominance of *G. glutinata* and *G. rubescens* with minor contribution of *G. sacculifer*. In contrast, faunal assemblages of the Holocene reveal closer affinity to those of the WPWP region (Figure 5-7). Thus, it can be postulated that the surface ocean condition at the study site during the last deglaciation period was similar to that in North Equatorial Current (NEC) region that is affected by strong northeast trade winds and characterized by weaker upper ocean stratification. To sum up, the surface ocean condition at the study site during the last deglaciation period was under the influence of northeast trade winds and NEC, which can be attributed to displacement of the ITCZ and NECC south to the study site.

The results of this study do not resolve the Bølling-Allerød episode of brief NH warming from HS1 and YD (Figure 5-2c); instead the record shows a broad high temperature bulge between 18 and 12 ka when these three events happened. This is likely due to the low temporal resolution (~1 ka) of the present data not enough to resolve such short term variability. After 12 ka, the upper ocean might have been stratified to the present level by the reduced interhemispheric thermal contrast than the preceding time interval and resultant migration of the ITCZ to its present position. Accordingly, it is interpreted that the present oceanographic and atmospheric conditions of the study site, influenced by the ITCZ and NECC, have been likely established at 12 ka with NH warming.

5.5. Conclusions

Changes in upper ocean temperature and water column structure in the central equatorial Pacific were investigated for the last deglaciation period using Mg/Ca

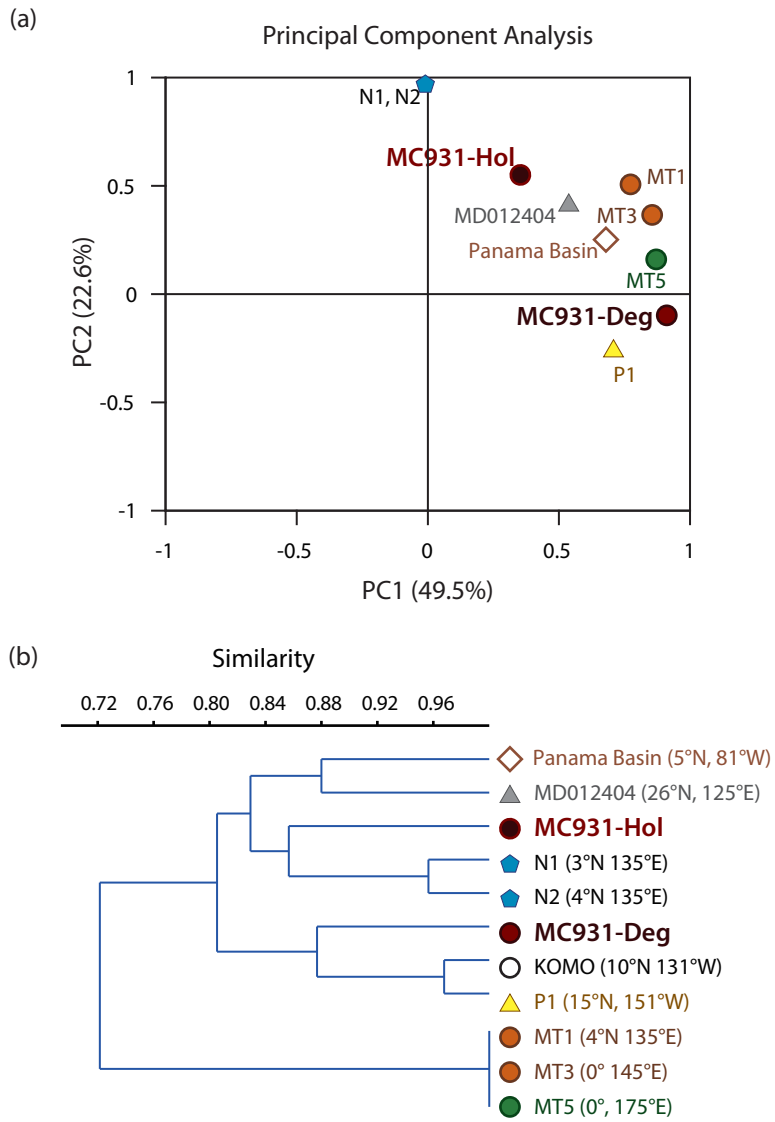

Figure 5-7. (a) Principal component and (b) cluster analyses on foraminifera assemblages determined for tropical and subtropical Pacific sediments. Data are from [*Chang et al.*, 2008; *Kawahata et al.*, 2002; *Lee et al.*, 2001; *Lee*, 2015; *Lee et al.*, 2014; *Thunell and Honjo*, 1981; *Thunell and Reynolds*, 1984; *Yamasaki et al.*, 2008]

and $\delta^{18}O$ compositions of three planktic foraminifera species. Comparison of the measured $\delta^{18}O$ with the predicted calcite $\delta^{18}O$ indicated the calcification depth of 70-100 m for *G. sacculifer*, 120-140 m for *P. obliquiloculata,* and 160-200 m depth for *G. tumida* during the late Holocene: thus Mg/Ca-derived temperatures of each species represents those of the mixed layer, upper thermocline, and lower thermocline, respectively.

Mg/Ca–derived temperatures for the mixed layer and lower thermocline do not change much after 18 ka. In contrast, upper thermocline temperatures had increased as high as 3°C during the last deglaciation period between 18 and 12 ka and has dropped and maintained to the present level since 12 ka. It suggests that the vertical temperature gradient between the dwelling depths of *P. obliquiloculata* and *G. sacculifer* was smaller during the last deglaciation period than before and after without changes in the lower thermocline temperatures. This phenomenon can be explained only with the poor separation of depth habitats between two species, resulted from weakening of water column stratification above the upper part of thermocline.

The observed weakening of stratification at the study site had occurred during the last deglaciation period that includes HS1 and YD, climatic aberrations characterized by NH cooling caused by NH ice sheet collapse and the subsequent weakening of the Atlantic Meridional Overturning Circulation. The NH cooling at these two events was associated with southerly location of the ITCZ due to increased pole to equator temperature gradients in the NH and resultant intensification of northeast trade winds. The faunal assemblage of planktic foraminifera at the study site during the last deglaciation period is similar to those

of North Equatorial Current region influenced by northeast trade winds. It suggests displacement of the ITCZ south to the study site during the deglaciation period. Influence of northeast trade winds and NEC at the site during the last deglaciation period likely had caused relaxed upper water stratification and lessened separation of depth habitats between foraminifera species due to wind-driven mixing. However, low temporal resolution (~1 ka) of the presented data does not allow resolving between the two cooling episodes (HS1 and YD) and a brief warming episode (Bølling-Allerød) in between. This interpretation leads to a conclusion that the ITCZ was positioned south of the study site during the last deglaciation and that the study site was under the influence of northeast trade winds that prevails north of the ITCZ.

CHAPTER 6. SUMMARY AND CONCLUSIONS

Despite the importance of the central equatorial Pacific in the global climate, understanding of ocean environment in the past is highly inadequate because of the paucity of sedimentary archives. By using the sediment cores acquired at the seamounts in the deep-sea basin, evolution of climate and its forcing mechanisms were investigated using various geochemical proxies in biogenic and lithogenic components across the mid-Pleistocene Transition (MPT, 1.2–0.8 Ma) and for the last 23 kyrs in the central equatorial Pacific. The acquisition of sedimentary archives for late Quaternary allows better understanding of changes in mean state of tropical Pacific by comparison with various proxy data available in the center of western Pacific Warm Pool (WPWP) and eastern Pacific Cold Tongue (EPCT).

For the last 600 kyr, eolian mineral dust deposited in the northwest Pacific, represented by a sediment core (12°30’N, 135°00’E) from the Philippine Sea, has been supplied predominantly from the central Asian deserts (e.g., Taklimakan desert). In contrast, eolian mineral dust deposited in a central equatorial Pacific site (5°53’N, 177°26’W) shows Australian/South American affinity before 0.8 Ma but gradually increasing Asian dust contribution after 0.8 Ma. Such change in dust provenance was accompanied by an increased dust flux and decrease in surface productivity and salinity. These changes can be best explained by the southward movement of the Intertropical Convergence Zone (ITCZ) and North Equatorial Counter Current (NECC) and the direct influence of these features on the site after 0.8 Ma. The southward movement of the ITCZ is in phase with the warming trend

observed in upwelling regions of the equatorial Pacific and Atlantic between 0.9 and 0.8 Ma. The southward movement of the ITCZ from 0.9 to 0.8 Ma indicates more significant cooling in the Northern Hemisphere (NH) than in the Southern Hemisphere, which is supportive of the interpretation that the NH ice sheet expanded significantly and stabilized after 0.9 Ma.

For the last deglacial period, water column structure and temperatures were investigated in the central equatorial Pacific (6°40′N, 177°28′W) from a multiple-core by using oxygen isotopic compositions and Mg/Ca ratios of three planktic foraminifer species (*G. sacculifer, P. obliquiloculata*, and *G tumida*) that dwell in mixed layer, upper thermocline, and lower thermocline, respectively.

Contrast to stable Mg/Ca–derived temperatures for mixed layer and lower thermocline since 18 ka, upper thermocline temperatures increased as high as 3°C during the last deglaciation between 18 and 12 ka, and has dropped to the present level of temperature since then. It can be explained by weakening of water column stratification in the upper part of thermocline and shallowing of *P. obliquiloculata* habitat at this time. Such change coincides the period of decreased pole to equator temperature gradients in the SH and following NH cooling events, the Heinrich Stadial 1 (HS1) and Younger Dryas (YD), resulting in intensification of northeast Trades and southward migration of the ITCZ. Intensified wind-driven mixing and reduced precipitation during the last deglacial period likely had caused relatively nutrient-rich surface water condition without a significant surface cooling and migration of *P. obliquiloculata* to shallower depth. This interpretation leads to a conclusion that the ITCZ was placed far south to the study site during the last deglaciation and the study site was influenced by northeast Trades that prevails

north of the ITCZ.

As exemplified by the evolution across the MPT, sea-air interaction (ITCZ movement–cooling/warming of intermediate water source region) forced from the high latitudes could result in the oceanographic change in the central equatorial Pacific. During the last deglaciation, especially during the HS 1 and YD, southward shift of the ITCZ due to NH high latitude thermal forcing exposed the northern part of central equatorial Pacific under the influence of the intensified northeast Trades and created less stratified surface water environments by wind-driven mixing. These results highlight the coupled behavior of ITCZ and surface oceanography in the central equatorial Pacific.

References

An, Z. (2000), The history and variability of the East Asian paleomonsoon climate, *Quaternary Science Reviews*, *19*(1–5), 171-187, doi:10.1016/S0277-3791(99)00060-8.

Anand, P., H. Elderfield, and M. H. Conte (2003), Calibration of Mg/Ca thermometry in planktonic foraminifera from a sediment trap time series, *Paleoceanography*, *18*(2), 1050, doi:10.1029/2002PA000846.

Arnold, E., J. Merrill, M. Leinen, and J. King (1998), The effect of source area and atmospheric transport on mineral aerosol collected over the North Pacific Ocean, *Global and Planetary Change*, *18*(3–4), 137-159, doi:10.1016/S0921-8181(98)00013-7.

Asahara, Y., T. Tanaka, H. Kamioka, and A. Nishimura (1995), Asian continental nature of $^{87}Sr/^{86}Sr$ ratios in north central Pacific sediments, *Earth and Planetary Science Letters*, *133*(1-2), 105-116.

Ashok, K., S. K. Behera, S. A. Rao, H. Weng, and T. Yamagata (2007), El Niño Modoki and its possible teleconnection, *Journal of Geophysical Research: Oceans*, *112*(C11), C11007, doi:10.1029/2006JC003798.

Aston, S. R., R. Chester, L. R. Johnson, and R. C. Padgham (1973), Eolian dust from the lower atmosphere of the eastern Atlantic and Indian Oceans, China Sea and Sea of Japan, *Marine Geology*, *14*(1), 15-28, doi:10.1016/0025-3227(73)90040-6.

Barker, S., P. Diz, M. J. Vautravers, J. Pike, G. Knorr, I. R. Hall, and W. S. Broecker (2009), Interhemispheric Atlantic seesaw response during the last deglaciation, *Nature*, *457*(7233), 1097-1102, doi:10.1038/nature07770.

Barker, S., M. Greaves, and H. Elderfield (2003), A study of cleaning procedures used for foraminiferal Mg/Ca paleothermometry, *Geochemistry, Geophysics, Geosystems*, *4*(9), 8407, doi:10.1029/2003GC000559.

Beaufort, L., T. de Garidel-Thoron, B. Linsley, D. Oppo, and N. Buchet (2003),

Biomass burning and oceanic primary production estimates in the Sulu Sea area over the last 380 kyr and the East Asian monsoon dynamics, *Marine Geology, 201*(1–3), 53-65, doi:10.1016/S0025-3227(03)00208-1.

Bian, Y., Z. Jian, C. Weng, W. Kuhnt, T. Bolliet, and A. Holbourn (2011), A palynological and palaeoclimatological record from the southern Philippines since the Last Glacial Maximum, *Chin. Sci. Bull., 56*(22), 2359-2365, doi:10.1007/s11434-011-4573-1.

Bijma, J., and C. Hemleben (1994), Population dynamics of the planktic foraminifer Globigerinoides sacculifer (Brady) from the central Red Sea, *Deep Sea Research Part I: Oceanographic Research Papers*, *41*(3), 485-510, doi:10.1016/0967-0637(94)90092-2.

Biscaye, P. E. (1965), Mineralogy and Sedimentation of Recent Deep-Sea Clay in the Atlantic Ocean and Adjacent Seas and Oceans, *Geological Society of America Bulletin*, *76*(7), 803-832, doi:10.1130/0016-7606.

Biscaye, P. E., and E. J. Dasch (1971), The rubidium, strontium, strontium-isotope system in deep-sea sediments: Argentine Basin, *Journal of Geophysical Research*, *76*(21), 5087-5096, doi:10.1029/JC076i021p05087.

Blank, M., M. Leinen, and J. M. Prospero (1985), Major Asian aeolian inputs indicated by the mineralogy of aerosols and sediments in the western North Pacific, *Nature*, *314*(6006), 84-86, doi:10.1038/314084a0.

Bory, A. J. M., W. Abouchami, S. J. G. Galer, A. Svensson, J. N. Christensen, and P. E. Biscaye (2013), A Chinese Imprint in Insoluble Pollutants Recently Deposited in Central Greenland As Indicated by Lead Isotopes, *Environmental Science & Technology*, *48*(3), 1451-1457, doi:10.1021/es4035655.

Bory, A. J. M., P. E. Biscaye, A. Svensson, and F. E. Grousset (2002), Seasonal variability in the origin of recent atmospheric mineral dust at NorthGRIP, Greenland, *Earth and Planetary Science Letters*, *196*(3–4), 123-134, doi:10.1016/S0012-821X(01)00609-4.

Bostock, H. C., et al. (2013), A review of the Australian–New Zealand sector of the

Southern Ocean over the last 30 ka (Aus-INTIMATE project), *Quaternary Science Reviews*, *74*, 35-57, doi:10.1016/j.quascirev.2012.07.018.

Bova, S. C., T. Herbert, Y. Rosenthal, J. Kalansky, M. Altabet, C. Chazen, A. Mojarro, and J. Zech (2015), Links between eastern equatorial Pacific stratification and atmospheric CO_2 rise during the last deglaciation, *Paleoceanography*, n/a-n/a, doi:10.1002/2015PA002816.

Boyer, T. P., et al. (2013), *World Ocean Database 2013*, 209 pp., Silver Spring, MD, doi:10.7289/V5NZ85MT.

Broccoli, A. J., K. A. Dahl, and R. J. Stouffer (2006), Response of the ITCZ to Northern Hemisphere cooling, *Geophysical Research Letters*, *33*(1), L01702, doi:10.1029/2005GL024546.

Broecker, W. S., and E. Clark (1999), CaCO3 size distribution: A paleocarbonate ion proxy?, *Paleoceanography*, *14*(5), 596-604, doi:10.1029/1999PA900016.

Cai, M., X. Fang, F. Wu, Y. Miao, and E. Appel (2012), Pliocene–Pleistocene stepwise drying of Central Asia: Evidence from paleomagnetism and sporopollen record of the deep borehole SG-3 in the western Qaidam Basin, NE Tibetan Plateau, *Global and Planetary Change*, *94–95*, 72-81, doi:10.1016/j.gloplacha.2012.07.002.

Calvo, E., C. Pelejero, P. De Deckker, and G. A. Logan (2007), Antarctic deglacial pattern in a 30 kyr record of sea surface temperature offshore South Australia, *Geophysical Research Letters*, *34*(13), L13707, doi:10.1029/2007GL029937.

Caromel, A. G. M., D. N. Schmidt, J. C. Phillips, and E. J. Rayfield (2014), Hydrodynamic constraints on the evolution and ecology of planktic foraminifera, *Marine Micropaleontology*, 106, 69-78, doi:10.1016/j.marmicro.2014.01.002.

Chaisson, W. P., and A. C. Ravelo (2000), Pliocene development of the east-west hydrographic gradient in the equatorial Pacific, *Paleoceanography*, *15*(5), 497-505, doi:10.1029/1999PA000442.

Chang, Y.-P., W.-L. Wang, Y. Yokoyama, H. Matsuzaki, H. Kawahata, and M.-T. Chen (2008), Millennial-Scale Planktic Foraminifer Faunal Variability in the East China Sea during the Past 40000 Years (IMAGES MD012404 from the Okinawa Trough), *Terrestrial, Atmospheric and Oceanic Sciences*, 19(4), 389-401.

Chao, W. C., and B. Chen (2001), The Origin of Monsoons, *Journal of the Atmospheric Sciences*, *58*(22), 3497-3507, doi:10.1175/1520-0469.

Chen, J., G. Li, J. Yang, W. Rao, H. Lu, W. Balsam, Y. Sun, and J. Ji (2007), Nd and Sr isotopic characteristics of Chinese deserts: Implications for the provenances of Asian dust, *Geochimica et Cosmochimica Acta*, *71*(15), 3904-3914, doi:10.1016/j.gca.2007.04.033.

Cheong, C.-s., J.-S. Ryu, and Y.-J. Jeong (2013), Simultaneous multiple collector-ICP-MS measurement of Nd isotopic composition and Sm/Nd ratio in geological reference materials by interference corrections and external calibration using matrix-matched standards, *Geoscience Journal*, *17*(4), 389-395, doi:10.1007/s12303-013-0056-5.

Chester, R., H. Elderfield, J. J. Griffin, L. R. Johnson, and R. C. Padgham (1972), Eolian dust along the eastern margins of the Atlantic Ocean, *Marine Geology*, *13*(2), 91-105, doi:10.1016/0025-3227(72)90048-5.

Chiang, J. C. H., and A. R. Friedman (2012), Extratropical Cooling, Interhemispheric Thermal Gradients, and Tropical Climate Change, *Annual Review of Earth and Planetary Sciences*, *40*(1), 383-412, doi:10.1146/annurev-earth-042711-105545.

Clark, P. U., D. Archer, D. Pollard, J. D. Blum, J. A. Rial, V. Brovkin, A. C. Mix, N. G. Pisias, and M. Roy (2006), The middle Pleistocene transition: characteristics, mechanisms, and implications for long-term changes in atmospheric pCO_2, *Quaternary Science Reviews*, *25*(23–24), 3150-3184, doi:10.1016/j.quascirev.2006.07.008.

Clark, P. U., and D. Pollard (1998), Origin of the Middle Pleistocene Transition by ice sheet erosion of regolith, *Paleoceanography*, *13*(1), 1-9,

doi:10.1029/97PA02660.

Cléroux, C., E. Cortijo, P. Anand, L. Labeyrie, F. Bassinot, N. Caillon, and J.-C. Duplessy (2008), Mg/Ca and Sr/Ca ratios in planktonic foraminifera: Proxies for upper water column temperature reconstruction, *Paleoceanography*, *23*(3), PA3214, doi:10.1029/2007PA001505.

Cole, T. G., and H. F. Shaw (1983), The nature and origin of authigenic smectites in some Recent marine sediments, *Clay Minerals*, *18*(3), 239-252, doi:10.1180/claymin.1983.018.3.02.

Conroy, J. L., K. M. Cobb, J. Lynch-Stieglitz, and P. J. Polissar (2014), Constraints on the salinity–oxygen isotope relationship in the central tropical Pacific Ocean, *Marine Chemistry*, *161*, 26-33, doi:10.1016/j.marchem.2014.02.001.

Corliss, B. H., and C. D. Hollister (1982), A paleoenvironmental model for Cenozoic sedimentation in the central North Pacific, in *The Ocean Floor-Bruce Heezen Commemorative Volume*, edited by R. A. Scrutton and M. Talwani, pp. 277-304, Wiley J., New York, U.S.A.

Coxall, H. K., P. N. Pearson, N. J. Shackleton, and M. A. Hall (2000), Hantkeninid depth adaptation: An evolving life strategy in a changing ocean, *Geology*, 28(1), 87-90, doi:10.1130/0091-7613(2000)28<87:hdaael>2.0.co;2.

Defant, M. J., R. Maury, J.-L. Joron, M. D. Feigenson, J. Leterrier, H. Bellon, D. Jacques, and M. Richard (1990), The geochemistry and tectonic setting of the northern section of the Luzon arc (The Philippines and Taiwan), *Tectonophysics, 183*(1–4), 187-205, doi:10.1016/0040-1951(90)90416-6.

de Garidel-Thoron, T., Y. Rosenthal, F. Bassinot, and L. Beaufort (2005), Stable sea surface temperatures in the western Pacific warm pool over the past 1.75 million years, *Nature, 433*(7023), 294-298, doi:10.1038/nature03189.

de Garidel-Thoron, T., Y. Rosenthal, L. Beaufort, E. Bard, C. Sonzogni, and A. C. Mix (2007), A multiproxy assessment of the western equatorial Pacific hydrography during the last 30 kyr, *Paleoceanography*, *22*(3), PA3204, doi:10.1029/2006PA001269.

DeMaster, D. J. (1981), The supply and accumulation of silica in the marine

environment, *Geochimica et Cosmochimica Acta*, *45*(10), 1715-1732, doi:10.1016/0016-7037(81)90006-5.

deMenocal, P. B. (2004), African climate change and faunal evolution during the Pliocene–Pleistocene, *Earth and Planetary Science Letters*, *220*(1–2), 3-24, doi:10.1016/S0012-821X(04)00003-2.

Denton, G. H., R. F. Anderson, J. R. Toggweiler, R. L. Edwards, J. M. Schaefer, and A. E. Putnam (2010), The Last Glacial Termination, *Science*, *328*(5986), 1652-1656, doi:10.1126/science.1184119.

DiNezio, P. N., and J. E. Tierney (2013), The effect of sea level on glacial Indo-Pacific climate, *Nature Geosci*, *6*(6), 485-491, doi:10.1038/ngeo1823.

Ding, Z., T. Liu, N. W. Rutter, Z. Yu, Z. Guo, and R. Zhu (1995), Ice-Volume Forcing of East Asian Winter Monsoon Variations in the Past 800,000 Years, *Quaternary Research*, *44*(2), 149-159, doi:10.1006/qres.1995.1059.

Dixon, T. H., and R. J. Stern (1983), Petrology, chemistry, and isotopic composition of submarine volcanoes in the southern Mariana arc, *Geological Society of America Bulletin*, *94*(10), 1159-1172, doi:10.1130/0016-7606.

Donguy, J.-R., and G. Meyers (1996), Mean annual variation of transport of major currents in the tropical Pacific Ocean, *Deep Sea Research Part I: Oceanographic Research Papers*, *43*(7), 1105-1122, doi:10.1016/0967-0637(96)00047-7.

Dubois, N., M. Kienast, C. Normandeau, and T. D. Herbert (2009), Eastern equatorial Pacific cold tongue during the Last Glacial Maximum as seen from alkenone paleothermometry, *Paleoceanography*, *24*(4), PA4207, doi:10.1029/2009PA001781.

Dyez, K. A., and A. C. Ravelo (2014), Dynamical changes in the tropical Pacific warm pool and zonal SST gradient during the Pleistocene, *Geophysical Research Letters*, *41*(21), 7626-7633, doi:10.1002/2014GL061639.

Elderfield, H., P. Ferretti, M. Greaves, S. Crowhurst, I. N. McCave, D. Hodell, and A. M. Piotrowski (2012), Evolution of Ocean Temperature and Ice Volume Through the Mid-Pleistocene Climate Transition, *Science*, *337*(6095), 704-

709, doi:10.1126/science.1221294.

Eldin, G., and M. Rodier (2003), Ocean physics and nutrient fields along 180° during an El Niño–Southern Oscillation cold phase, *Journal of Geophysical Research: Oceans*, *108*(C12), 8137, doi:10.1029/2000JC000746.

Erez, J., and S. Honjo (1981), Oxygen and Carbon Isotopes in Foraminifera Comparison of isotopic composition of planktonic foraminifera in plankton tows, sediment traps and sediments, *Palaeogeography, Palaeoclimatology, Palaeoecology*, *33*(1), 129-156, doi:10.1016/0031-0182(81)90035-3.

Fairbanks, R. G., and P. H. Wiebe (1980), Foraminifera and Chlorophyll Maximum: Vertical Distribution, Seasonal Succession, and Paleoceanographic Significance, *Science*, *209*(4464), 1524-1526, doi:10.1126/science.209.4464.1524.

Farmer, E. C., A. Kaplan, P. B. de Menocal, and J. Lynch-Stieglitz (2007), Corroborating ecological depth preferences of planktonic foraminifera in the tropical Atlantic with the stable oxygen isotope ratios of core top specimens, *Paleoceanography*, *22*(3), PA3205, doi:10.1029/2006PA001361.

Feldberg, M. J., and A. C. Mix (2002), Sea-surface temperature estimates in the Southeast Pacific based on planktonic foraminiferal species; modern calibration and Last Glacial Maximum, *Marine Micropaleontology*, *44*(1–2), 1-29, doi:10.1016/S0377-8398(01)00035-4.

Feng, J.-L., L.-P. Zhu, X.-L. Zhen, and Z.-G. Hu (2009), Grain size effect on Sr and Nd isotopic compositions in eolian dust: Implications for tracing dust provenance and Nd model age, *Geochemical Journal*, *43*(2), 123-131, doi:10.2343/geochemj.1.0007.

Ferguson, J. E., G. M. Henderson, M. Kucera, and R. E. M. Rickaby (2008), Systematic change of foraminiferal Mg/Ca ratios across a strong salinity gradient, *Earth and Planetary Science Letters*, *265*(1–2), 153-166, doi:10.1016/j.epsl.2007.10.011.

Ferrat, M., D. J. Weiss, S. Strekopytov, S. Dong, H. Chen, J. Najorka, Y. Sun, S. Gupta, R. Tada, and R. Sinha (2011), Improved provenance tracing of Asian

dust sources using rare earth elements and selected trace elements for palaeomonsoon studies on the eastern Tibetan Plateau, *Geochimica et Cosmochimica Acta*, *75*(21), 6374-6399, doi:10.1016/j.gca.2011.08.025.

Flohn, H. (1981), A hemispheric circulation asymmetry during Late Tertiar, *Geologische Rundschau*, *70*(2), 725-736, doi:10.1007/BF01822146.

Folk, R. L. (1974), *The Petrology of Sedimentary Rocks* Hemphill, Austin, TX.

Ford, H. L., A. C. Ravelo, and P. J. Polissar (2015), Reduced El Niño–Southern Oscillation during the Last Glacial Maximum, *Science*, *347*(6219), 255-258, doi:10.1126/science.1258437.

Gagan, M. K., E. J. Hendy, S. G. Haberle, and W. S. Hantoro (2004), Post-glacial evolution of the Indo-Pacific Warm Pool and El Niño-Southern oscillation, *Quaternary International*, *118–119*, 127-143, doi:10.1016/S1040-6182(03)00134-4.

Gibbons, F. T., D. W. Oppo, M. Mohtadi, Y. Rosenthal, J. Cheng, Z. Liu, and B. K. Linsley (2014), Deglacial $\delta^{18}O$ and hydrologic variability in the tropical Pacific and Indian Oceans, *Earth and Planetary Science Letters*, *387*, 240-251, doi:10.1016/j.epsl.2013.11.032.

Gill, A. E. (1983), An Estimation of Sea-Level and Surface-Current Anomalies during the 1972 El Niño and Consequent Thermal Effects, *Journal of Physical Oceanography*, *13*(4), 586-606, doi:10.1175/1520-0485.

Gingele, F. X., and P. De Deckker (2004), Fingerprinting Australia's rivers with clay minerals and the application for the marine record of climate change, *Australian Journal of Earth Sciences*, *51*(3), 339-348, doi:10.1111/j.1400-0952.2004.01061.x.

Gingele, F. X., P. De Deckker, and C.-D. Hillenbrand (2001), Clay mineral distribution in surface sediments between Indonesia and NW Australia — source and transport by ocean currents, *Marine Geology*, *179*(3–4), 135-146, doi:10.1016/S0025-3227(01)00194-3.

Glaccum, R. A., and J. M. Prospero (1980), Saharan aerosols over the tropical North Atlantic — Mineralogy, *Marine Geology*, *37*(3–4), 295-321,

doi:10.1016/0025-3227(80)90107-3.

Griffin, J. J., H. Windom, and E. D. Goldberg (1968), The distribution of clay minerals in the World Ocean, *Deep Sea Research and Oceanographic Abstracts*, *15*(4), 433-459.

Grousset, F. E., P. E. Biscaye, A. Zindler, J. Prospero, and R. Chester (1988), Neodymium isotopes as tracers in marine sediments and aerosols: North Atlantic, *Earth and Planetary Science Letters*, *87*(4), 367-378, doi:10.1016/0012-821X(88)90001-5.

Grousset, F. E., M. Parra, A. Bory, P. Martinez, P. Bertrand, G. Shimmield, and R. M. Ellam (1998), Saharan wind regimes traced by the Sr–Nd isotopic composition of subtropical Atlantic sediments: last glacial maximum vs. today, *Quaternary Science Reviews*, *17*(4–5), 395-409, doi:10.1016/S0277-3791(97)00048-6.

Harrison, K. G. (2000), Role of increased marine silica input on paleo-pCO_2 levels, *Paleoceanography*, *15*(3), 292-298, doi:10.1029/1999PA000427.

Haug, G. H., K. A. Hughen, D. M. Sigman, L. C. Peterson, and U. Röhl (2001), Southward Migration of the Intertropical Convergence Zone Through the Holocene, *Science*, *293*(5533), 1304-1308, doi:10.1126/science.1059725.

Head, M. J., and P. L. Gibbard (2005), Early-Middle Pleistocene Transitions: an overview and recommendation for the defining boundary, in *Early-Middle Pleistocene Transitions: The Land–Ocean Evidence*, edited by M. J. Head and P. L. Gibbard, pp. 1-18, The Geological Society of London, London, UK.

Held, I. M., and B. J. Soden (2006), Robust Responses of the Hydrological Cycle to Global Warming, *Journal of Climate*, *19*(21), 5686-5699, doi:10.1175/JCLI3990.1.

Hemleben, C., M. Spindler, I. Breitinger, and R. Ott (1987), Morphological and physiological responses of *Globigerinoides sacculifer* (Brady) under varying laboratory conditions, *Marine Micropaleontology*, *12*, 305-324, doi:10.1016/0377-8398(87)90025-9.

Hernández-Almeida, I., F. J. Sierro, I. Cacho, and J. A. Flores (2012), Impact of suborbital climate changes in the North Atlantic on ice sheet dynamics at the Mid-Pleistocene Transition, *Paleoceanography*, *27*(3), PA3214, doi:10.1029/2011PA002209.

Honda, M., S. Yabuki, and H. Shimizu (2004), Geochemical and isotopic studies of aeolian sediments in China, *Sedimentology*, *51*(2), 211-230, doi:10.1111/j.1365-3091.2004.00618.x.

Hovan, S. A., D. K. Rea, and N. G. Pisias (1991), Late Pleistocene Continental Climate and Oceanic Variability Recorded in Northwest Pacific Sediments, *Paleoceanography*, *6*(3), 349-370, doi:10.1029/91PA00559.

Hoyos, C., and P. Webster (2012), Evolution and modulation of tropical heating from the last glacial maximum through the twenty-first century, *Climate Dynamics*, *38*(7-8), 1501-1519, doi:10.1007/s00382-011-1181-3.

Hsu, S.-C., et al. (2012), Dust transport from non-East Asian sources to the North Pacific, *Geophysical Research Letters*, *39*(12), L12804, doi:10.1029/2012GL051962.

Huh, C.-A., J.-L. Peng, and J.-C. Chen (1992), Late Pleistocene pelagic sedimentation in the West Philippine Basin, *Journal of Southeast Asian Earth Sciences*, *7*(2–3), 159-164, doi:10.1016/0743-9547(92)90050-L.

Hyeong, K., J. Kim, T. Pettke, C. M. Yoo, and S.-d. Hur (2011), Lead, Nd and Sr isotope records of pelagic dust: Source indication versus the effects of dust extraction procedures and authigenic mineral growth, *Chemical Geology*, *286*(3-4), 240-251, doi:10.1016/j.chemgeo.2011.05.009.

Hyeong, K., J. Lee, I. Seo, M. J. Lee, C. M. Yoo, and B.-K. Khim (2014), Southward shift of the Intertropical Convergence Zone due to Northern Hemisphere cooling at the Oligocene-Miocene boundary, *Geology*, *42*(8), 667-670, doi:10.1130/g35664.1.

Iwasaka, Y., J. M. Li, G. Y. Shi, Y. S. Kim, A. Matsuki, D. Trochkine, M. Yamada, D. Zhang, Z. Shen, and C. S. Hong (2008), Mass Transport of Background Asian Dust Revealed by Balloon-Borne Measurement: Dust Particles

Transported during Calm Periods by Westerly from Taklamakan Desert, in *Advanced Environmental Monitoring*, edited by Y. Kim and U. Platt, pp. 121-135, Springer Netherlands, doi:10.1007/978-1-4020-6364-0_9.

Jacobsen, S. B., and G. J. Wasserburg (1980), Sm-Nd isotopic evolution of chondrites, *Earth and Planetary Science Letters*, *50*(1), 139-155, doi: 10.1016/0012-821X(80)90125-9.

Jiang, D., and X. Lang (2010), Last Glacial Maximum East Asian Monsoon: Results of PMIP Simulations, *Journal of Climate*, *23*(18), 5030-5038, doi:10.1175/2010JCLI3526.1.

Jiang, F., M. Frank, T. Li, T.-Y. Chen, Z. Xu, and A. Li (2013), Asian dust input in the western Philippine Sea: Evidence from radiogenic Sr and Nd isotopes, *Geochemistry, Geophysics, Geosystems*, *14*(5), 1538-1551, doi:10.1002/ggge.20116.

Jones, C. E., A. N. Halliday, D. K. Rea, and R. M. Owen (1994), Neodymium isotopic variations in North Pacific modern silicate sediment and the insignificance of detrital REE contributions to seawater, *Earth and Planetary Science Letters*, *127*(1-2), 55-66.

Kanayama, S., S. Yabuki, F. Zeng, M. Liu, Z. Shen, L. Liu, F. Yanagisawa, and O. Abe (2005), Size-Dependent Geochemical Characteristics of Asian Dust—Sr and Nd Isotope Compositions as Tracers for Source Identification—, *Journal of the Meteorological Society of Japan. Ser. II*, *83A*, 107–120, doi:10.2151/jmsj.83A.107.

Kao, H.-Y., and J.-Y. Yu (2009), Contrasting Eastern-Pacific and Central-Pacific Types of ENSO, *Journal of Climate*, *22*(3), 615-632, doi:10.1175/2008JCLI2309.1.

Kim, S.-T., and J. R. O'Neil (1997), Equilibrium and nonequilibrium oxygen isotope effects in synthetic carbonates, *Geochimica et Cosmochimica Acta*, *61*(16), 3461-3475, doi:10.1016/S0016-7037(97)00169-5.

Koutavas, A., J. Lynch-Stieglitz, T. M. Marchitto, and J. P. Sachs (2002), El Niño-Like Pattern in Ice Age Tropical Pacific Sea Surface Temperature, *Science*,

297(5579), 226-230, doi:10.1126/science.1072376.

Koutavas, A., and J. Lynch-Stieglitz (2003), Glacial-interglacial dynamics of the eastern equatorial Pacific cold tongue-Intertropical Convergence Zone system reconstructed from oxygen isotope records, *Paleoceanography*, *18*(4), 1089, doi:10.1029/2003pa000894.

Koutavas, A., and J. P. Sachs (2008), Northern timing of deglaciation in the eastern equatorial Pacific from alkenone paleothermometry, *Paleoceanography*, *23*(4), PA4205, doi:10.1029/2008PA001593.

Kug, J.-S., F.-F. Jin, and S.-I. An (2009), Two Types of El Niño Events: Cold Tongue El Niño and Warm Pool El Niño, *Journal of Climate*, *22*(6), 1499-1515, doi:10.1175/2008JCLI2624.1.

Lamy, F., J. Kaiser, U. Ninnemann, D. Hebbeln, H. W. Arz, and J. Stoner (2004), Antarctic Timing of Surface Water Changes off Chile and Patagonian Ice Sheet Response, *Science*, *304*(5679), 1959-1962, doi:10.1126/science.1097863.

Lawrence, K. T., Z. Liu, and T. D. Herbert (2006), Evolution of the Eastern Tropical Pacific Through Plio-Pleistocene Glaciation, *Science*, *312*(5770), 79-83, doi:10.1126/science.1120395.

Le Bouteiller, A., A. Leynaert, M. R. Landry, R. Le Borgne, J. Neveux, M. Rodier, J. Blanchot, and S. L. Brown (2003), Primary production, new production, and growth rate in the equatorial Pacific: Changes from mesotrophic to oligotrophic regime, *Journal of Geophysical Research: Oceans*, *108*(C12), 8141, doi:10.1029/2001JC000914.

Lea, D. W., D. K. Pak, C. L. Belanger, H. J. Spero, M. A. Hall, and N. J. Shackleton (2006), Paleoclimate history of Galápagos surface waters over the last 135,000 yr, *Quaternary Science Reviews*, *25*(11–12), 1152-1167, doi:10.1016/j.quascirev.2005.11.010.

Lee, K. E., N. C. Slowey, and T. D. Herbert (2001), Glacial sea surface temperatures in the subtropical North Pacific: A comparison of $U_{37}^{k'}$, $\delta^{18}O$, and foraminiferal assemblage temperature estimates, *Paleoceanography*, 16(3),

268-279, doi:10.1029/1999PA000493.

Lee, Y. (2015), Paleoenvironment reconstruction of Kuroshio Extension and Central Equatorial Pacific using planktic foraminifera assemblages since the last glacial maximum (LGM), MS thesis, 100 pp, Kyungpook National University, Daegu, Korea (in Korean).

Lee, Y., H. Asahi, H. J. Woo, H. J. Kim, S.-J. Lee, and B.-K. Khim (2014), Seasonal Variation of Planktonic Foraminifera Assemblage in response to Seasonal Shift of Inter-Tropical Convergence Zone in the Northeastern Equatorial Pacific, *Ocean and Polar Research*, 36(4), 437-445 (in Korean).

Lee, Y. C., X. Yang, and M. Wenig (2010), Transport of dusts from East Asian and non-East Asian sources to Hong Kong during dust storm related events 1996–2007, *Atmospheric Environment*, *44*(30), 3728-3738, doi:10.1016/j.atmosenv.2010.03.034.

Leinen, M., J. M. Prospero, E. Arnold, and M. Blank (1994), Mineralogy of aeolian dust reaching the North Pacific Ocean: 1. Sampling and analysis, *Journal of Geophysical Research: Atmospheres*, *99*(D10), 21017-21023, doi:10.1029/94JD01735.

Li, L., Q. Li, J. Tian, P. Wang, H. Wang, and Z. Liu (2011), A 4-Ma record of thermal evolution in the tropical western Pacific and its implications on climate change, *Earth and Planetary Science Letters*, *309*(1–2), 10-20, doi:10.1016/j.epsl.2011.04.016.

Li, Q., B. Li, G. Zhong, B. McGowran, Z. Zhou, J. Wang, and P. Wang (2006), Late Miocene development of the western Pacific warm pool: Planktonic foraminifer and oxygen isotopic evidence, *Palaeogeography, Palaeoclimatology, Palaeoecology*, *237*(2–4), 465-482, doi:10.1016/j.palaeo.2005.12.019.

Li, T., J. Zhao, Q. Nan, R. Sun, and X. Yu (2011), Palaeoproductivity evolution in the centre of the western Pacific warm pool during the last 250 ka, *Journal of Quaternary Science*, *26*(5), 478-484, doi:10.1002/jqs.1471.

Li, Y., and F. Wang (2012), Spreading and salinity change of North Pacific Tropical

Water in the Philippine Sea, *J Oceanogr*, *68*(3), 439-452, doi:10.1007/s10872-012-0110-3.

Lisiecki, L. E., and M. E. Raymo (2005), A Pliocene-Pleistocene stack of 57 globally distributed benthic $\delta^{18}O$ records, *Paleoceanography*, *20*(1), PA1003, doi:10.1029/2004PA001071.

Liu, J. P., K. H. Xu, A. C. Li, J. D. Milliman, D. M. Velozzi, S. B. Xiao, and Z. S. Yang (2007), Flux and fate of Yangtze River sediment delivered to the East China Sea, *Geomorphology*, *85*(3–4), 208-224, doi:10.1016/j.geomorph.2006.03.023.

Liu, T., and Z. Ding (1993), Stepwise coupling of monsoon circulations to global ice volume variations during the late Cenozoic, *Global and Planetary Change*, *7*(1–3), 119-130, doi:10.1016/0921-8181(93)90044-O.

Liu, Z., Y. Zhao, C. Colin, F. P. Siringan, and Q. Wu (2009), Chemical weathering in Luzon, Philippines from clay mineralogy and major-element geochemistry of river sediments, *Applied Geochemistry*, *24*(11), 2195-2205, doi:10.1016/j.apgeochem.2009.09.025.

Locarnini, R. A., et al. (2013), *World Ocean Atlas 2013, Volume 1: Temperature*, 40 pp.

Luo, C., N. M. Mahowald, and J. del Corral (2003), Sensitivity study of meteorological parameters on mineral aerosol mobilization, transport, and distribution, *Journal of Geophysical Research: Atmospheres*, *108*(D15), 4447, doi:10.1029/2003JD003483.

Lurcock, P. C., and G. S. Wilson (2012), PuffinPlot: A versatile, user-friendly program for paleomagnetic analysis, *Geochemistry, Geophysics, Geosystems*, *13*(6), Q06z45, doi:10.1029/2012GC004098.

Mackey, D. J., J. Parslow, H. W. Higgins, F. B. Griffiths, and J. E. O'Sullivan (1995), Plankton productivity and biomass in the western equatorial Pacific: Biological and physical controls, *Deep Sea Research Part II: Topical Studies in Oceanography*, *42*(2–3), 499-533, doi:10.1016/0967-0645(95)00038-R.

Maher, B. A., J. M. Prospero, D. Mackie, D. Gaiero, P. P. Hesse, and Y. Balkanski (2010), Global connections between aeolian dust, climate and ocean biogeochemistry at the present day and at the last glacial maximum, *Earth-Science Reviews*, *99*(1–2), 61-97, doi:10.1016/j.earscirev.2009.12.001.

Mahoney, J. B. (2005), Nd and Sr isotopic signatures of fine-grained clastic sediments: A case study of western Pacific marginal basins, *Sedimentary Geology*, *182*(1–4), 183-199, doi:10.1016/j.sedgeo.2005.07.009.

Mahowald, N. M., J. A. Ballantine, J. Feddema, and N. Ramankutty (2007), Global trends in visibility: implications for dust sources, *Atmospheric Chemistry and Physics*, *7*(12), 3309-3339, doi:10.5194/acp-7-3309-2007.

Marcott, S. A., J. D. Shakun, P. U. Clark, and A. C. Mix (2013), A Reconstruction of Regional and Global Temperature for the Past 11,300 Years, *Science*, *339*(6124), 1198-1201, doi:10.1126/science.1228026.

Martinez-Boti, M. A., G. Marino, G. L. Foster, P. Ziveri, M. J. Henehan, J. W. B. Rae, P. G. Mortyn, and D. Vance (2015), Boron isotope evidence for oceanic carbon dioxide leakage during the last deglaciation, *Nature*, *518*(7538), 219-222, doi:10.1038/nature14155.

Martínez-Garcia, A., A. Rosell-Melé, E. L. McClymont, R. Gersonde, and G. H. Haug (2010), Subpolar Link to the Emergence of the Modern Equatorial Pacific Cold Tongue, *Science*, *328*(5985), 1550-1553, doi:10.1126/science.1184480.

Martínez, I., L. Keigwin, T. T. Barrows, Y. Yokoyama, and J. Southon (2003), La Niña-like conditions in the eastern equatorial Pacific and a stronger Choco jet in the northern Andes during the last glaciation, *Paleoceanography*, *18*(2), 1033, doi:10.1029/2002PA000877.

Masunaga, H., and T. S. L'Ecuyer (2010), Equatorial Asymmetry of the East Pacific ITCZ: Observational Constraints on the Underlying Processes, *Journal of Climate*, *24*(6), 1784-1800, doi:10.1175/2010JCLI3854.1.

McClymont, E. L., and A. Rosell-Melé (2005), Links between the onset of modern Walker circulation and the mid-Pleistocene climate transition, *Geology*,

33(5), 389-392, doi:10.1130/g21292.1.

McClymont, E. L., A. Rosell-Melé, G. H. Haug, and J. M. Lloyd (2008), Expansion of subarctic water masses in the North Atlantic and Pacific oceans and implications for mid-Pleistocene ice sheet growth, *Paleoceanography*, *23*(4), PA4214, doi:10.1029/2008PA001622.

McClymont, E. L., S. M. Sosdian, A. Rosell-Melé, and Y. Rosenthal (2013), Pleistocene sea-surface temperature evolution: Early cooling, delayed glacial intensification, and implications for the mid-Pleistocene climate transition, *Earth-Science Reviews*, *123*, 173-193, doi:10.1016/j.earscirev.2013.04.006.

McGee, D., A. Donohoe, J. Marshall, and D. Ferreira (2014), Changes in ITCZ location and cross-equatorial heat transport at the Last Glacial Maximum, Heinrich Stadial 1, and the mid-Holocene, *Earth and Planetary Science Letters*, *390*, 69-79, doi:10.1016/j.epsl.2013.12.043.

McManus, J. F., R. Francois, J. M. Gherardi, L. D. Keigwin, and S. Brown-Leger (2004), Collapse and rapid resumption of Atlantic meridional circulation linked to deglacial climate changes, *Nature*, *428*(6985), 834-837, doi:10.1038/nature02494.

McPhaden, M. J., and J. Picaut (1990), El Niño-Southern Oscillation Displacements of the Western Equatorial Pacific Warm Pool, *Science*, *250*(4986), 1385-1388, doi:10.1126/science.250.4986.1385.

Merrill, J. T., M. Uematsu, and R. Bleck (1989), Meteorological analysis of long range transport of mineral aerosols over the North Pacific, *Journal of Geophysical Research: Atmospheres*, *94*(D6), 8584-8598, doi:10.1029/JD094iD06p08584.

Ming, J., A. Li, J. Huang, S. Wan, Q. Meng, F. Jiang, and W. Yan (2014), Assemblage characteristics of clay minerals and its implications to evolution of eolian dust input to the Parece Vela Basin since 1.95 Ma, *Chinese Journal of Oceanology and Limnology*, *32*(1), 174-186, doi:10.1007/s00343-014-3066-x.

Mohtadi, M., D. W. Oppo, S. Steinke, J.-B. W. Stuut, R. De Pol-Holz, D. Hebbeln, and A. Luckge (2011), Glacial to Holocene swings of the Australian-Indonesian monsoon, *Nature Geoscience*, *4*(8), 540-544, doi:10.1038/ngeo1209.

Molina-Kescher, M., M. Frank, and E. C. Hathorne (2014), Nd and Sr isotope compositions of different phases of surface sediments in the South Pacific: Extraction of seawater signatures, boundary exchange, and detrital/dust provenance, *Geochemistry, Geophysics, Geosystems*, *15*(9), 3502-3520, doi:10.1002/2014GC005443.

Montade, V., M. Kageyama, N. Combourieu-Nebout, M.-P. Ledru, E. Michel, G. Siani, and C. Kissel (2015), Teleconnection between the Intertropical Convergence Zone and southern westerly winds throughout the last deglaciation, *Geology*, *43*(8), 735-738, doi:10.1130/g36745.1.

Mortlock, R. A., and P. N. Froelich (1989), A simple method for the rapid determination of biogenic opal in pelagic marine sediments, *Deep Sea Research Part A. Oceanographic Research Papers*, *36*(9), 1415-1426, doi:10.1016/0198-0149(89)90092-7.

Mortyn, P. G., and C. D. Charles (2003), Planktonic foraminiferal depth habitat and $\delta^{18}O$ calibrations: Plankton tow results from the Atlantic sector of the Southern Ocean, *Paleoceanography*, *18*(2), n/a-n/a, doi:10.1029/2001PA000637.

Müller, P. J., and R. Schneider (1993), An automated leaching method for the determination of opal in sediments and particulate matter, *Deep Sea Research Part I: Oceanographic Research Papers*, *40*(3), 425-444, doi:10.1016/0967-0637(93)90140-X.

Nagashima, K., R. Tada, H. Matsui, T. Irino, A. Tani, and S. Toyoda (2007), Orbital- and millennial-scale variations in Asian dust transport path to the Japan Sea, *Palaeogeography, Palaeoclimatology, Palaeoecology*, *247*(1–2), 144-161, doi:10.1016/j.palaeo.2006.11.027.

Nagashima, K., R. Tada, A. Tani, Y. Sun, Y. Isozaki, S. Toyoda, and H. Hasegawa

(2011), Millennial-scale oscillations of the westerly jet path during the last glacial period, *Journal of Asian Earth Sciences*, *40*(6), 1214-1220, doi:10.1016/j.jseaes.2010.08.010.

Nakagawa, T., P. E. Tarasov, H. Kitagawa, Y. Yasuda, and K. Gotanda (2006), Seasonally specific responses of the East Asian monsoon to deglacial climate changes, *Geology*, *34*(7), 521-524, doi:10.1130/g21764.1.

Nakai, S. i., A. N. Halliday, and D. K. Rea (1993), Provenance of dust in the Pacific Ocean, *Earth and Planetary Science Letters*, *119*(1-2), 143-157.

Nakano, T., Y. Yokoo, M. Nishikawa, and H. Koyanagi (2004), Regional Sr–Nd isotopic ratios of soil minerals in northern China as Asian dust fingerprints, *Atmospheric Environment*, *38*(19), 3061-3067, doi:10.1016/j.atmosenv.2004.02.016.

North Greenland Ice Core Project members (2004), High-resolution record of Northern Hemisphere climate extending into the last interglacial period, *Nature*, 431(7005), 147-151, doi:10.1038/nature02805.

Nürnberg, D., J. Bijma, and C. Hemleben (1996), Assessing the reliability of magnesium in foraminiferal calcite as a proxy for water mass temperatures, *Geochimica et Cosmochimica Acta*, *60*(5), 803-814, doi:10.1016/0016-7037(95)00446-7.

Paillard, D., L. Labeyrie, and P. Yiou (1996), Macintosh Program performs time-series analysis, *Eos, Transactions American Geophysical Union*, *77*(39), 379-379, doi:10.1029/96EO00259.

Parrenin, F., V. Masson-Delmotte, P. Köhler, D. Raynaud, D. Paillard, J. Schwander, C. Barbante, A. Landais, A. Wegner, and J. Jouzel (2013), Synchronous Change of Atmospheric CO_2 and Antarctic Temperature During the Last Deglacial Warming, *Science*, 339(6123), 1060-1063, doi:10.1126/science.1226368.

Partin, J. W., K. M. Cobb, J. F. Adkins, B. Clark, and D. P. Fernandez (2007), Millennial-scale trends in west Pacific warm pool hydrology since the Last Glacial Maximum, *Nature*, 449(7161), 452-455, doi:10.1038/nature06164.

Patrick, A., and R. C. Thunell (1997), Tropical Pacific sea surface temperatures and upper water column thermal structure during the Last Glacial Maximum, *Paleoceanography*, *12*(5), 649-657, doi:10.1029/97PA01553.

Pena, L. D., S. L. Goldstein, S. R. Hemming, K. M. Jones, E. Calvo, C. Pelejero, and I. Cacho (2013), Rapid changes in meridional advection of Southern Ocean intermediate waters to the tropical Pacific during the last 30 kyr, *Earth and Planetary Science Letters*, *368*, 20-32, doi:10.1016/j.epsl.2013.02.028.

Peterson, L. C., G. H. Haug, K. A. Hughen, and U. Röhl (2000), Rapid Changes in the Hydrologic Cycle of the Tropical Atlantic During the Last Glacial, *Science*, *290*(5498), 1947-1951, doi:10.1126/science.290.5498.1947.

Petschick, R., G. Kuhn, and F. Gingele (1996), Clay mineral distribution in surface sediments of the South Atlantic: sources, transport, and relation to oceanography, *Marine Geology*, *130*(3–4), 203-229, doi:10.1016/0025-3227(95)00148-4.

Pettke, T., A. N. Halliday, C. M. Hall, and D. K. Rea (2000), Dust production and deposition in Asia and the north Pacific Ocean over the past 12 Myr, *Earth and Planetary Science Letters*, *178*(3-4), 397-413.

Pettke, T., A. N. Halliday, and D. K. Rea (2002), Cenozoic evolution of Asian climate and sources of Pacific seawater Pb and Nd derived from eolian dust of sediment core LL44-GPC3, *Paleoceanography*, *17*, 1031, doi:10.1029/2001PA000673.

Philander, S. G., W. J. Hurlin, and A. D. Seigel (1987), Simulation of the Seasonal Cycle of the Tropical Pacific Ocean, *Journal of Physical Oceanography*, *17*(11), 1986-2002, doi:10.1175/1520-0485.

Picaut, J., M. Ioualalen, C. Menkes, T. Delcroix, and M. J. McPhaden (1996), Mechanism of the Zonal Displacements of the Pacific Warm Pool: Implications for ENSO, *Science*, *274*(5292), 1486-1489, doi:10.1126/science.274.5292.1486.

Picaut, J., F. Masia, and Y. du Penhoat (1997), An Advective-Reflective Conceptual

Model for the Oscillatory Nature of the ENSO, *Science*, *277*(5326), 663-666, doi:10.1126/science.277.5326.663.

Pichat, S., W. Abouchami, and S. J. G. Galer (2014), Lead isotopes in the Eastern Equatorial Pacific record Quaternary migration of the South Westerlies, *Earth and Planetary Science Letters*, *388*, 293-305, doi:10.1016/j.epsl.2013.11.035.

Qiu, X., T. Li, F. Chang, Q. Nan, Z. Xiong, and H. Sun (2014), Sea surface temperature and salinity reconstruction based on stable isotopes and Mg/Ca of planktonic foraminifera in the western Pacific Warm Pool during the last 155 ka, *Chinese Journal of Oceanology and Limnology*, *32*(1), 187-200, doi:10.1007/s00343-014-3073-y.

Radenac, M.-H., and M. Rodier (1996), Nitrate and chlorophyll distributions in relation to thermohaline and current structures in the western tropical Pacific during 1985–1989, *Deep Sea Research Part II: Topical Studies in Oceanography*, *43*(4–6), 725-752, doi:10.1016/0967-0645(96)00025-2.

Rao, W., J. U. N. Chen, J. Yang, J. Ji, G. Li, and H. Tan (2008), Sr-Nd isotopic characteristics of eolian deposits in the Erdos Desert and Chinese Loess Plateau: Implications for their provenances, *Geochemical Journal*, *42*(3), 273-282, doi:10.2343/geochemj.42.273.

Rashid, H., and E. A. Boyle (2007), Mixed-Layer Deepening During Heinrich Events: A Multi-Planktonic Foraminiferal $\delta^{18}O$ Approach, *Science*, 318(5849), 439-441, doi:10.1126/science.1146138.

Rasmusson, E. M., and J. M. Wallace (1983), Meteorological Aspects of the El Niño/Southern Oscillation, *Science*, *222*(4629), 1195-1202, doi:10.1126/science.222.4629.1195.

Rateev, M. A., Z. N. Gorbunova, A. P. Lisitzyn, and G. L. Nosov (1969), The distribution of clay minerals in the oceans, *Sedimentology*, *13*(1-2), 21-43, doi:10.1111/j.1365-3091.1969.tb01119.x.

Rea, D. K. (1994), The paleoclimatic record provided by eolian deposition in the deep sea: The geologic history of wind, *Reviews of Geophysics*, *32*(2), 159-

195, doi:10.1029/93RG03257.

Rea, D. K., and S. A. Hovan (1995), Grain size distribution and depositional processes of the mineral component of abyssal sediments: Lessons from the North Pacific, *Paleoceanography*, *10*(2), 251-258, doi:10.1029/94PA03355.

Rea, D. K., and T. R. Janecek (1981), Late cretaceous history of eolian deposition in the mid-pacific mountains, central North Pacific Ocean, *Palaeogeography, Palaeoclimatology, Palaeoecology*, *36*(1–2), 55-67, doi:10.1016/0031-0182(81)90048-1.

Reimer, P. J., et al. (2013), IntCal13 and Marine13 Radiocarbon Age Calibration Curves 0–50,000 Years cal BP, *Radiocarbon*, *55*(4), 1869-1887, doi:10.2458/azu_js_rc.55.16947.

Rincón-Martínez, D., S. Steph, F. Lamy, A. Mix, and R. Tiedemann (2011), Tracking the equatorial front in the eastern equatorial Pacific Ocean by the isotopic and faunal composition of planktonic foraminifera, *Marine Micropaleontology*, *79*(1–2), 24-40, doi:10.1016/j.marmicro.2011.01.001.

Romero, O. E., J.-H. Kim, and D. Hebbeln (2006), Paleoproductivity evolution off central Chile from the Last Glacial Maximum to the Early Holocene, *Quaternary Research*, *65*(3), 519-525, doi:10.1016/j.yqres.2005.07.003.

Rosenthal, Y., E. A. Boyle, and N. Slowey (1997), Temperature control on the incorporation of magnesium, strontium, fluorine, and cadmium into benthic foraminiferal shells from Little Bahama Bank: Prospects for thermocline paleoceanography, *Geochimica et Cosmochimica Acta*, *61*(17), 3633-3643, doi:10.1016/S0016-7037(97)00181-6.

Rosenthal, Y., and G. P. Lohmann (2002), Accurate estimation of sea surface temperatures using dissolution-corrected calibrations for Mg/Ca paleothermometry, *Paleoceanography*, *17*(3), 1044, doi:10.1029/2001PA000749.

Russon, T., M. Elliot, A. Sadekov, G. Cabioch, T. Corrège, and P. De Deckker (2010), Inter-hemispheric asymmetry in the early Pleistocene Pacific warm pool, *Geophysical Research Letters*, *37*(11), L11601,

doi:10.1029/2010GL043191.

Ryan, W. B. F., et al. (2009), Global Multi-Resolution Topography synthesis, *Geochemistry, Geophysics, Geosystems*, *10*(3), Q03014, doi:10.1029/2008GC002332.

Sadekov, A., S. M. Eggins, P. De Deckker, U. Ninnemann, W. Kuhnt, and F. Bassinot (2009), Surface and subsurface seawater temperature reconstruction using Mg/Ca microanalysis of planktonic foraminifera *Globigerinoides ruber*, *Globigerinoides sacculifer*, and *Pulleniatina obliquiloculata*, *Paleoceanography*, *24*(3), PA3201, doi:10.1029/2008PA001664.

Sagawa, T., Y. Yokoyama, M. Ikehara, and M. Kuwae (2012), Shoaling of the western equatorial Pacific thermocline during the last glacial maximum inferred from multispecies temperature reconstruction of planktonic foraminifera, *Palaeogeography, Palaeoclimatology, Palaeoecology*, *346–347*, 120-129, doi:10.1016/j.palaeo.2012.06.002.

Sarnthein, M., and K. Winn (1990), Reconstruction of Low and Middle Latitude Export Productivity, 30,000 Years BP to Present: Implications for Global Carbon Reservoirs, in *Climate-Ocean Interaction*, edited by M. E. Schlesinger, pp. 319-342, Springer Netherlands, doi:10.1007/978-94-009-2093-4_16.

Sato, K., M. Oda, S. Chiyonobu, K. Kimoto, H. Domitsu, and J. C. Ingle Jr (2008), Establishment of the western Pacific warm pool during the Pliocene: Evidence from planktic foraminifera, oxygen isotopes, and Mg/Ca ratios, *Palaeogeography, Palaeoclimatology, Palaeoecology*, *265*(1–2), 140-147, doi:10.1016/j.palaeo.2008.05.003.

Schefuß, E., S. Schouten, J. H. F. Jansen, and J. S. Sinninghe Damste (2003), African vegetation controlled by tropical sea surface temperatures in the mid-Pleistocene period, *Nature*, *422*(6930), 418-421, doi:10.1038/nature01500.

Schneider, T., T. Bischoff, and G. H. Haug (2014), Migrations and dynamics of the

intertropical convergence zone, *Nature*, *513*(7516), 45-53, doi:10.1038/nature13636.

Schubert, S. D., M. J. Suarez, P. J. Pegion, R. D. Koster, and J. T. Bacmeister (2004), On the Cause of the 1930s Dust Bowl, *Science*, *303*(5665), 1855-1859, doi:10.1126/science.1095048.

Seo, I., Y. I. Lee, W. Kim, C. M. Yoo, and K. Hyeong (2015), Movement of the Intertropical Convergence Zone during the mid-pleistocene transition and the response of atmospheric and surface ocean circulations in the central equatorial Pacific, *Geochemistry, Geophysics, Geosystems*, 16, 3973–3981, doi:10.1002/2015GC006077.

Seo, I., Y. I. Lee, C. M. Yoo, H. J. Kim, and K. Hyeong (2014), Sr-Nd isotope composition and clay mineral assemblages in eolian dust from the central Philippine Sea over the last 600 kyr: Implications for the transport mechanism of Asian dust, *Journal of Geophysical Research: Atmospheres*, *119*(19), 11,492-411,504, doi:10.1002/2014JD022025.

Serno, S., G. Winckler, R. F. Anderson, C. T. Hayes, D. McGee, B. Machalett, H. Ren, S. M. Straub, R. Gersonde, and G. H. Haug (2014), Eolian dust input to the Subarctic North Pacific, *Earth and Planetary Science Letters*, *387*, 252-263, doi:10.1016/j.epsl.2013.11.008.

Sexton, P. F., and S. Barker (2012), Onset of 'Pacific-style' deep-sea sedimentary carbonate cycles at the mid-Pleistocene transition, *Earth and Planetary Science Letters*, *321–322*, 81-94, doi:10.1016/j.epsl.2011.12.043.

Shakun, J. D., P. U. Clark, F. He, S. A. Marcott, A. C. Mix, Z. Liu, B. Otto-Bliesner, A. Schmittner, and E. Bard (2012), Global warming preceded by increasing carbon dioxide concentrations during the last deglaciation, *Nature*, *484*(7392), 49-54, doi:10.1038/nature10915.

Shen, Z., X. Li, J. Cao, S. Caquineau, Y. Wang, and X. Zhang (2005), Characteristics of clay minerals in asian dust and their environmental significance, *China Particuology*, *3*(5), 260-264, doi:10.1016/S1672-2515(07)60198-5.

Shi, Y., X. Dai, J. Li, and J. Wang (1997), Origin and significance of clay minerals in the last interglacial loess in Lanzhou area, North-central China, *Marine Geology and Quaternary Geology*, *17*(1), 87-94.

Shi, Z., and X. Liu (2011), Distinguishing the provenance of fine-grained eolian dust over the Chinese Loess Plateau from a modelling perspective, *Tellus B*, *63*(5), 959-970, doi:10.1111/j.1600-0889.2011.00561.x.

Skonieczny, C., et al. (2011), The 7–13 March 2006 major Saharan outbreak: Multiproxy characterization of mineral dust deposited on the West African margin, *Journal of Geophysical Research: Atmospheres*, *116*(D18), D18210, doi:10.1029/2011JD016173.

Sosdian, S., and Y. Rosenthal (2009), Deep-Sea Temperature and Ice Volume Changes Across the Pliocene-Pleistocene Climate Transitions, *Science*, *325*(5938), 306-310, doi:10.1126/science.1169938.

Southon, J., M. Kashgarian, M. Fontugne, B. Metivier, and W. W. S. Yim (2002), Marine reservoir corrections for the Indian Ocean and Southeast Asia, *Radiocarbon*, *44*(1), 167-180.

Siegert, F., G. Ruecker, A. Hinrichs, and A. A. Hoffmann (2001), Increased damage from fires in logged forests during droughts caused by El Nino, *Nature*, *414*(6862), 437-440, doi:10.1038/35106547.

Stancin, A. M., J. D. Gleason, S. A. Hovan, D. K. Rea, R. M. Owen, T. C. Moore Jr, C. M. Hall, and J. D. Blum (2008), Miocene to recent eolian dust record from the Southwest Pacific Ocean at 40°S latitude, *Palaeogeography, Palaeoclimatology, Palaeoecology*, *261*(3–4), 218-233, doi:10.1016/j.palaeo.2007.12.015.

Stancin, A. M., J. D. Gleason, D. K. Rea, R. M. Owen, T. C. Moore Jr, J. D. Blum, and S. A. Hovan (2006), Radiogenic isotopic mapping of late Cenozoic eolian and hemipelagic sediment distribution in the east-central Pacific, *Earth and Planetary Science Letters*, *248*(3–4), 840-850, doi:10.1016/j.epsl.2006.06.038.

Stenni, B., et al. (2011), Expression of the bipolar see-saw in Antarctic climate

records during the last deglaciation, *Nature Geoscience*, *4*(1), 46-49, doi:10.1038/ngeo1026.

Stuiver, M., and P. J. Reimer (1993), Extended ^{14}C data base and revised CALIB 3.0 ^{14}C age calibration program, *Radiocarbon*, *35*, 215-230.

Sun, D. (2004), Monsoon and westerly circulation changes recorded in the late Cenozoic aeolian sequences of Northern China, *Global and Planetary Change*, *41*(1), 63-80, doi:10.1016/j.gloplacha.2003.11.001.

Sun, D., J. Bloemendal, D. K. Rea, J. Vandenberghe, F. Jiang, Z. An, and R. Su (2002), Grain-size distribution function of polymodal sediments in hydraulic and aeolian environments, and numerical partitioning of the sedimentary components, *Sedimentary Geology*, *152*(3–4), 263-277, doi:10.1016/S0037-0738(02)00082-9.

Sun, J., M. Zhang, and T. Liu (2001), Spatial and temporal characteristics of dust storms in China and its surrounding regions, 1960–1999: Relations to source area and climate, *Journal of Geophysical Research: Atmospheres*, *106*(D10), 10325-10333, doi:10.1029/2000JD900665.

Tanaka, T. Y., and M. Chiba (2006), A numerical study of the contributions of dust source regions to the global dust budget, *Global and Planetary Change*, *52*(1-4), 88-104, doi:10.1016/j.gloplacha.2006.02.002.

Tanaka, T. Y., Y. Kurosaki, M. Chiba, T. Matsumura, T. Nagai, A. Yamazaki, A. Uchiyama, N. Tsunematsu, and K. Kai (2005), Possible transcontinental dust transport from North Africa and the Middle East to East Asia, *Atmospheric Environment*, *39*(21), 3901-3909, doi:10.1016/j.atmosenv.2005.03.034.

Tang, Z., T. Li, F. Chang, Q. Nan, and Q. Li (2013), Paleoproductivity evolution in the West Philippine Sea during the last 700 ka, *Chinese Journal of Oceanology and Limnology*, *31*(2), 435-444, doi:10.1007/s00343-013-2117-z.

Thunell, R. C., and S. Honjo (1981), Planktonic foraminiferal flux to the deep ocean: Sediment trap results from the tropical Atlantic and the central Pacific,

Marine Geology, 40(3), 237-253, doi:10.1016/0025-3227(81)90142-0.

Thunell, R. C., and L. A. Reynolds (1984), Sedimentation of Planktonic Foraminifera: Seasonal Changes in Species Flux in the Panama Basin, *Micropaleontology*, 30(3), 243-262, doi:10.2307/1485688.

Tian, J., P. Wang, R. Chen, and X. Cheng (2005), Quaternary upper ocean thermal gradient variations in the South China Sea: Implications for east Asian monsoon climate, *Paleoceanography*, *20*(4), PA4007, doi:10.1029/2004PA001115.

Tian, Y., B. P. Kohn, S. Hu, and A. J. W. Gleadow (2015), Synchronous fluvial response to surface uplift in the eastern Tibetan Plateau: Implications for crustal dynamics, *Geophysical Research Letters*, *42*(1), 29-35, doi:10.1002/2014GL062383.

Timmermann, A., S. J. Lorenz, S. I. An, A. Clement, and S. P. Xie (2007), The Effect of Orbital Forcing on the Mean Climate and Variability of the Tropical Pacific, *Journal of Climate*, *20*(16), 4147-4159, doi:10.1175/JCLI4240.1.

Vecchi, G. A., A. Clement, and B. J. Soden (2008), Examining the Tropical Pacific's Response to Global Warming, *Eos, Transactions American Geophysical Union*, *89*(9), 81-83, doi:10.1029/2008EO090002.

Vecchi, G. A., and B. J. Soden (2007), Global Warming and the Weakening of the Tropical Circulation, *Journal of Climate*, *20*(17), 4316-4340, doi:10.1175/JCLI4258.1.

Vecchi, G. A., B. J. Soden, A. T. Wittenberg, I. M. Held, A. Leetmaa, and M. J. Harrison (2006), Weakening of tropical Pacific atmospheric circulation due to anthropogenic forcing, *Nature*, *441*(7089), 73-76, doi:10.1038/nature04744.

Veres, D., et al. (2013), The Antarctic ice core chronology (AICC2012): an optimized multi-parameter and multi-site dating approach for the last 120 thousand years, *Climate of the Past*, 9(4), 1733-1748, doi:10.5194/cp-9-1733-2013.

Wan, S., Z. Yu, P. D. Clift, H. Sun, A. Li, and T. Li (2012), History of Asian eolian input to the West Philippine Sea over the last one million years, *Palaeogeography, Palaeoclimatology, Palaeoecology, 326–328*, 152-159, doi:10.1016/j.palaeo.2012.02.015.

Wang, B., R. Wu, and K. M. Lau (2001), Interannual Variability of the Asian Summer Monsoon: Contrasts between the Indian and the Western North Pacific–East Asian Monsoons*, *Journal of Climate*, *14*(20), 4073-4090, doi:10.1175/1520-0442.

Wang, B., and Y. Wang (1999), Dynamics of the ITCZ–Equatorial Cold Tongue Complex and Causes of the Latitudinal Climate Asymmetry, *Journal of Climate*, *12*(6), 1830-1847, doi:10.1175/1520-0442(1999)012<1830:DOTIEC>2.0.CO;2.

Wang, J., X. Fang, E. Appel, and C. Song (2012), Pliocene–Pleistocene Climate Change At the NE Tibetan Plateau Deduced From Lithofacies Variation In the Drill Core SG-1, Western Qaidam Basin, China, *Journal of Sedimentary Research*, *82*(12), 933-952, doi:10.2110/jsr.2012.76.

Wang, Y. J., H. Cheng, R. L. Edwards, Z. S. An, J. Y. Wu, C.-C. Shen, and J. A. Dorale (2001), A High-Resolution Absolute-Dated Late Pleistocene Monsoon Record from Hulu Cave, China, *Science*, 294(5550), 2345-2348, doi:10.1126/science.1064618.

Wara, M. W., M. L. Delaney, T. D. Bullen, and A. C. Ravelo (2003), Possible roles of pH, temperature, and partial dissolution in determining boron concentration and isotopic composition in planktonic foraminifera, *Paleoceanography*, *18*(4), 1100, doi:10.1029/2002PA000797.

Wara, M. W., A. C. Ravelo, and M. L. Delaney (2005), Permanent El Niño-Like Conditions During the Pliocene Warm Period, *Science*, *309*(5735), 758-761, doi:10.1126/science.1112596.

Watkins, J. M., A. C. Mix, and J. Wilson (1998), Living planktic foraminifera in the central tropical Pacific Ocean: articulating the equatorial ‘cold tongue’ during La Niña, 1992, *Marine Micropaleontology*, *33*(3–4), 157-174,

doi:10.1016/S0377-8398(97)00036-4.

Webster, P. J. (1994), The role of hydrological processes in ocean-atmosphere interactions, *Reviews of Geophysics*, *32*(4), 427-476, doi:10.1029/94RG01873.

Woodhead, J. D. (1989), Geochemistry of the Mariana arc (western Pacific): Source composition and processes, *Chemical Geology*, *76*(1–2), 1-24, doi:10.1016/0009-2541(89)90124-1.

Wurster, C. M., M. I. Bird, I. D. Bull, F. Creed, C. Bryant, J. A. J. Dungait, and V. Paz (2010), Forest contraction in north equatorial Southeast Asia during the Last Glacial Period, *Proceedings of the National Academy of Sciences*, *107*(35), 15508-15511, doi:10.1073/pnas.1005507107.

Xie, R. C., and F. Marcantonio (2012), Deglacial dust provenance changes in the Eastern Equatorial Pacific and implications for ITCZ movement, *Earth and Planetary Science Letters*, *317–318*, 386-395, doi:10.1016/j.epsl.2011.11.014.

Xu, Z., T. Li, S. Wan, Q. Nan, A. Li, F. Chang, F. Jiang, and Z. Tang (2012), Evolution of East Asian monsoon: Clay mineral evidence in the western Philippine Sea over the past 700 kyr, *Journal of Asian Earth Sciences*, *60*, 188-196, doi:10.1016/j.jseaes.2012.08.018.

Yeh, S.-W., J.-S. Kug, B. Dewitte, M.-H. Kwon, B. P. Kirtman, and F.-F. Jin (2009), El Nino in a changing climate, *Nature*, *461*(7263), 511-514, doi:10.1038/nature08316.

Yumimoto, K., K. Eguchi, I. Uno, T. Takemura, Z. Liu, A. Shimizu, and N. Sugimoto (2009), An elevated large-scale dust veil from the Taklimakan Desert: Intercontinental transport and three-dimensional structure as captured by CALIPSO and regional and global models, *Atmospheric Chemistry and Physics*, *9*(21), 8545-8558, doi:10.5194/acp-9-8545-2009.

Yunev, O. A., J. Carstensen, S. Moncheva, A. Khaliulin, G. Ærtebjerg, and S. Nixon (2007), Nutrient and phytoplankton trends on the western Black Sea shelf in response to cultural eutrophication and climate changes, *Estuarine, Coastal*

and Shelf Science, *74*(1–2), 63-76, doi:10.1016/j.ecss.2007.03.030.

Zhang, J., P. Wang, Q. Li, X. Cheng, H. Jin, and S. Zhang (2007), Western equatorial Pacific productivity and carbonate dissolution over the last 550 kyr: Foraminiferal and nannofossil evidence from ODP Hole 807A, *Marine Micropaleontology*, *64*(3–4), 121-140, doi:10.1016/j.marmicro.2007.03.003.

Zhang, X. Y., R. Arimoto, and Z. S. An (1997), Dust emission from Chinese desert sources linked to variations in atmospheric circulation, *Journal of Geophysical Research: Atmospheres*, *102*(D23), 28041-28047, doi:10.1029/97JD02300.

Zhang, X. Y., R. Arimoto, and Z. S. An (1999), Glacial and interglacial patterns for Asian dust transport, *Quaternary Science Reviews*, *18*(6), 811-819, doi:10.1016/S0277-3791(98)00028-6.

Zweng, M. M., et al. (2013), *World Ocean Atlas 2013, Volume 2: Salinity*, 39 pp.

국문초록

신생대 제 4기 동안의 서태평양 난수역의 해양학적 특성과 대기순환 복원

중앙태평양 적도 해역은 서태평양 난수역과 동태평양 용승대의 경계부에 해당하여 적도태평양의 해양학적 환경을 이해하는 데 매우 중요한 위치에 있음에도 불구하고 퇴적물 기록의 부재로 과거 기후에 대해 알려진 바가 거의 없다. 본 연구에서는 신생대 제 4기 동안 서태평양 난수역의 동쪽 경계부에서의 고해양학적 환경 변화와 그 기작을 살펴보기 위하여 북서태평양 및 중앙태평양 적도해역에서 퇴적물 기록을 획득하였다. 대기와 표층 해양의 상호작용을 파악하기 위하여, 풍성 기원 입자의 기원지와 생물 기원 퇴적물의 구성 성분을 함께 분석하였다.

북서태평양 필리핀 해(12° 30’ N, 135° 00’ E)의 퇴적물 기록에 따르면, 중앙 아시아의 사막 지대 (예: 타클라마칸 사막)에서 기원한 광물 입자가 지난 60만 년 동안 공급된 것으로 판단된다. 필리핀 해가 계절풍의 영향이 강한 지역임에도 불구하고 동아시아가 아닌 중앙아시아의 영향이 나타나는 것은 탁월풍이 가장 중요한 황사 운반 기작이며 중앙아시아 기원 광물 입자의 조성이 북태평양 전역에 나타날 것임을 시사한다. 이러한 결과는 현재 중앙태평양 적도해역(5° 53’ N, 177° 26’ W)에 퇴적된 풍성기원 입자 조성과도 일치하나, 0.8 Ma 이전에 적도 해역에 퇴적된 광물입자는 호주와

남아메리카 기원과 유사한 조성을 나타냈다. 0.8 Ma에 풍성기원입자의 주된 기원지가 남반구에서 북반구로 변화함과 동시에, 해양에서는 표층 염도와 생산성이 급격히 감소하고 풍성기원입자의 유입량이 증가하였다. 이러한 대기-해양의 변화는 적도수렴대와 북적도반류가 연구해역으로 남하하면서 발생한 결과로 해석되며, 북동무역풍이 남동무역풍에 비해 강화되었음을 시사한다. 북동무역풍의 상대적 강화는 북반구의 적도-극지역의 열적 구배가 증가한 결과로, 중기플라이스토세 전환기 (Mid-Pleistocene Transition) 동안 북반구의 빙하가 상대적으로 크게 발달하였을 가능성을 지지한다.

마지막 해빙기 동안 중앙태평양 적도해역(6° 40′ N, 177° 28′ W)의 수층구조 변화를 알아보기 위해 혼합층, 상부수온약층, 하부수온약층에 각각 서식하는 부유성 유공충 *G. sacculifer*, *P. obliquiloculata*, *G. tumida*의 안정산소동위원소 조성과 Mg/Ca 조성을 분석하였다. 표층과 하부수온약층의 수온은 18 ka 이후 안정적으로 유지된 반면, 해빙기의 18-12 ka 기간에 상부수온약층의 수온이 상승하였고 이후 다시 하강하여 현재와 비슷한 조성이 유지되었다. 이는 해당 시기 표층 바람의 세기가 증가하여 성층 구조가 약화되어 유공충 종들 간 서식 깊이가 혼합되어 나타난 결과로 보인다. 이러한 변화는 해빙기에 남반구의 온난화가 빨리 진행되고 북반구의 차별적 냉각 사건들이 발생하면서 북동무역풍이 강화되고 적도수렴대가 연구해역보다 남쪽에 위치하게 되면서 발생하였을 것으로 여겨진다. 중기플라이스토세 전환기와 지난 해빙기의 기록으로 볼 때,

중앙태평양 적도 해역의 해양학적 변화는 남북반구의 열적 변화에 의한 대기순환 변화에 크게 영향을 받음을 알 수 있다.

주요어 : 고해양학, 홍적세, 적도수렴대, 적도태평양, 기후변화
학 번 : 2011-30917